Running-in of Rolling Contacts

The research described in this thesis was undertaken at the Laboratory for Surface Technology and Tribology, Faculty of Engineering Technology, University of Twente, Enschede, The Netherlands. The research was funded largely by SKF Engineering and Research Centre B.V., Nieuwegein, The Netherlands, through project number N97329 (Engineering Surface Topography; numerical and experimental design) Part B running-in and partly by STW, the Dutch Technology Foundation, through project number TET.5120 (Contactless detection and monitoring of micro- and macro-wear using imaging methods).

Samenstelling promotiecommissie:

Prof.dr.ir. H.J. Grootenboer, Universiteit Twente, CTW, voorzitter and secretaris
Prof.dr.ir. D.J. Schipper, Universiteit Twente, CTW, promotor
Prof.dr.ir. R. Akkerman, Universiteit Twente, CTW
Prof.dr.ir. P.P.L. Regtien, Universiteit Twente, EWI
Prof.dr. P. Vergne, INSA-Lyon, Frankrijk
Prof.dr. M.C. Elwenspoek, Universiteit Twente, EWI
Dr.ir. A. van Beek, Technische Universiteit Delft

Jamari, J. 2006.
Running-in of Rolling Contacts
ISBN: 90-365-2314-1
Keywords: running-in, rolling, contact mechanics, surface topography, asperity.

e-mail: j.jamari@gmail.com

Printed by Wöhrmann Printing Service, Zutphen, The Netherlands.

RUNNING-IN OF ROLLING CONTACTS

PROEFSCHRIFT

ter verkrijging van
de graad van doctor aan de Universiteit Twente,
op gezag van de rector magnificus,
prof.dr. W.H.M. Zijm,
volgens besluit van het College voor Promoties,
in het openbaar te verdedigen
op woensdag 19 april 2006 om 15.00 uur

door

Jamari
geboren te Rembang
Java, Indonesië

Dit proefschrift is goedgekeurd door de promotor:

Prof.dr.ir. D.J. Schipper

aan Galuh

Contents

Nomenclature

This section presents the general nomenclature used in this thesis. Certain specialized terminology is defined locally.

Roman symbols

a	semi-minor radius of the contact area	[m]
A	area of contact	[m^2]
b	semi-major radius of the contact area	[m]
c_a	fully plastic contact area ratio to its critical value	[-]
c_h	hardness factor	[-]
C_m	deformation criterion	[-]
d	separation	[m]
D	deformation and texturing term	[-]
D_d	deformation degree	[-]
e	eccentricity of the ellipse	[-]
err_z	error in height measurement	[m]
E	equivalent elasticity modulus for combined surfaces	[Pa]
E_1	elasticity modulus of surface 1	[Pa]
E_2	elasticity modulus of surface 2	[Pa]
$\mathbf{E}(e)$	complete elliptic integral of the second kind	[-]
F_p	maximum coefficient of friction contribution	[-]
$g(y)$	modified height density	[-]
h	cut-off height	[m]
$h(x,y)$	measured surface height	[m]
$h'(x,y)$	surface height as an output of contact model	[m]
$h''(x,y)$	surface height as an output of wear model	[m]
H	hardness of material	[Pa]
H_m	measured mean contact pressure	[Pa]
k	shear yield stress	[Pa]
K, K_v	maximum contact pressure factor	[-]
$\mathbf{K}(e)$	complete elliptic integral of the first kind	[-]
l	lubricant effectiveness	[-]
L	lubrication factor	[-]

L_x	contact area diameter in principal x direction	[m]
L_y	contact area diameter in principal y direction	[m]
m_b	crystallographic factor of bulk	[-]
m_s	crystallographic factor of surface	[-]
n	work-hardening coefficient	[-]
N	number of asperities	[-]
p	mean contact pressure	[Pa]
p_c	initial contact pressure	[Pa]
p_m	maximum contact pressure	[Pa]
p_x	pixel size in x direction	[m]
p_y	pixel size in y direction	[m]
p_0	maximum Hertzian pressure	[Pa]
p_0^e	elastic limit of Hertzian pressure	[Pa]
p_0^s	maximum Hertzian pressure at shakedown	[Pa]
$p(0)$	effective maximum contact pressure	[Pa]
P	normal force or load	[N]
P_s	nominal shakedown pressure	[Pa]
R	effective radius of contacting surfaces	[m]
R_1	radius of surface 1	[m]
R_2	radius of surface 2	[m]
R_a	center line average (c.l.a.) surface roughness	[m]
R_{ai}	initial center line average surface roughness	[m]
R_m	mean effective radius	[m]
R_q	root mean square surface roughness	[m]
R_x	effective radius in principal x direction	[m]
R_y	effective radius in principal y direction	[m]
s	sliding distance	[m]
S	solid material factor	[-]
t	time	[s]
t_i	incubation time	[s]
T	transitions term	[-]
V	volume	[m^3]
V_+	sum velocity, $V_+ = V_1 + V_2$	[ms^{-1}]
w_b	bulk deformation	[m]
y	surface height	[m]
Y	yield strength	[Pa]
z	surface height	[m]

Greek symbols

α	dimensionless semi-axis of contact ellipse in principal x direction	[-]
α_{hys}	hysterisis loss factor	[-]
β	dimensionless semi-axis of contact ellipse in principal y direction	[-]
δ_0	interference at shakedown	[m]
Δ_0	initial interference	[m]
Δ_{opt}	‘equilibrium’ surface roughness	[m]

ε	contact model convergence criterion	[-]
ε_r	running-in model convergence criterion	[-]
$\phi(z)$	Gaussian surface height distribution	[-]
γ	dimensionless interference parameter of elliptical contact	[-]
η	lubricant inlet viscosity	[Pas]
η_s	asperity density, = N/A	[m^{-2}]
κ_x	curvature in principal x direction	[m]
κ_y	curvature in principal y direction	[m]
λ	ellipse ratio, = R_x/R_y	[-]
λ_i	specific oil film thickness	[-]
μ	coefficient of friction	[-]
μ_{max}	maximum coefficient of friction	[-]
ν	Poisson's ratio	[-]
σ	root mean square surface roughness	[m]
τ_0	initial surface shear strength	[Pa]
τ_b	shear strength of bulk	[Pa]
τ_s	shear strength of surface	[Pa]
ψ_s	plasticity index	[-]
ψ_s^*	'working' plasticity index	[-]
ψ_2^*	plasticity index of soft surface	[-]
ω	interference or approach	[m]
ω_1	limit of the first yield interference	[m]
ω_2	limit of the fully plastic interference	[m]

Subscripts and superscripts

1, 2	surface 1, 2
a	asperity
c	critical
e	elastic
ep	elastic-plastic
max	maximum
p	plastic
u	unloading
x	*x* direction
y	*y* direction

Abbreviations

AF	Abbott-Firestone model
BL	Boundary Lubrication
c.l.a.	center line average
CEB	Chang-Etsion-Bogy model

EHL	Elastohydrodynamic Lubrication
FEM	Finite Element Method
GT	Greenwood-Tripp model
GW	Greenwood-Williamson model
HL	Hydrodynamic Lubrication
JG	Jackson-Green model
KE	Kogut-Etsion model
ML	Mixed Lubrication
r.m.s.	root mean square
ZMC	Zhao-Maietta-Chang model

Chapter 1

Introduction

1.1. Tribology and rolling contact

In almost every aspect of our daily lives we meet some manifestation of tribology. Gripping, holding, sliding, brushing, machinery works, friction between skin and clothes, et cetera all demonstrate the impact of tribology. Tribology is defined as the science and technology of interacting surfaces in relative motion and of related subjects and practices. The nature and consequence of the interactions that take place at the interface control friction and wear. Friction and wear are not material properties; they are system properties, depending on the materials used and on the operational (contact) conditions. During the interactions, forces are transmitted, mechanical energy is converted, physical and chemical natures of the interacting materials are altered. The essence of tribology can be constituted by understanding the nature of the interactions and solving the technological problems associated with the interfacial phenomena. Rolling contacts is one of the most used solution to control friction and wear of a load carrying interface in which two bodies are separated by rolling elements.

Consider two nonconforming bodies which touch at a single point, *O*, see Fig. 1.1. During rolling of two surfaces relative to each other, any relative motion can be regarded as a combination of sliding, spinning and rolling [1]. Sliding or slip is the relative velocity between the two bodies or surfaces at the contact point *O* in the tangent plane. The spinning is the relative angular velocity between the two bodies about the common normal through *O*, and rolling is the relative angular velocity between the two bodies about an axis lying in the tangent plane.

Friction in rolling contacts can be classified into [2]: (a) Free rolling, (b) Rolling subjected to traction, (c) Rolling in conforming grooves and (d) Rolling around curves. Whenever rolling occurs, free rolling friction must occur, whereas (b), (c) and (d) occur separately or in combination, depending on the particular situation. The wheel of a car involves (a) and (b), whereas in a radial ball bearing, as shown in Fig. 1.2, (a), (b) and (c) are involved, and in a thrust ball bearing (a), (b), (c) and (d) occur. Rolling friction is the

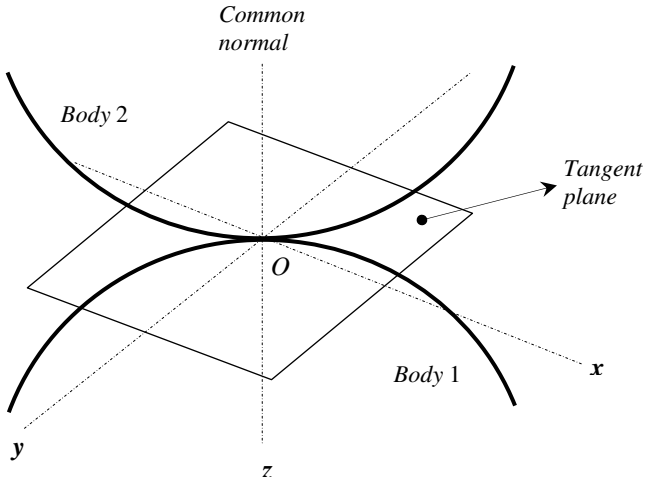

FIGURE 1.1: *The coordinate system for two non-conforming bodies.*

resistance to motion which takes place when a surface is rolled over another surface. The term rolling friction is usually restricted to bodies of nearly perfect (continuous) shapes with very low surface roughness. With hard materials the coefficient of rolling friction between a cylinder or spherical body against itself or a flat body generally is in the range of 10^{-5} to 5 x 10^{-3}. In comparison, the coefficient of sliding friction of dry sliding bodies ranges typically

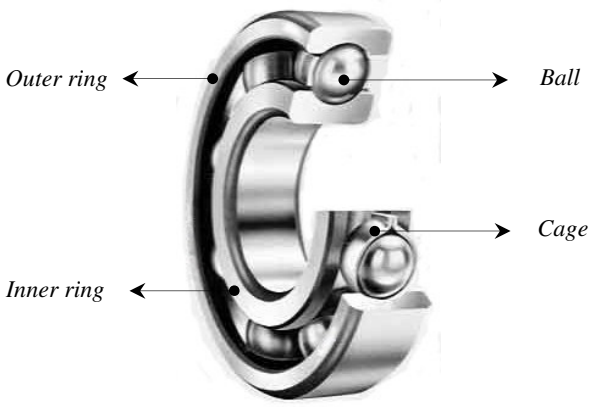

FIGURE 1.2: *Example of radial ball bearing.*

from 0.1 to sometimes a value much larger than 1 [3]. If the contact of two non-conforming bodies was a point, pure rolling conditions would prevail. However, in most cases, the contact region is elastically or plastically deformed, so the contact is made over an area. As a result, pure rolling takes place at only a very small number of points, but a combination of

rolling with a small degree of sliding or slip takes place at all other points. The sliding resistance at the interface has to be overcome and to achieve this slipping and rolling, friction must be present [4]. Rolling friction can be caused through several causes; however, slip is the most dominant.

Roughness is an important parameter in rolling contacts with respect to friction and wear. The perfection of rolling geometry can be reduced by roughness, so that micro-slip may occur at roughness level. Plastic deformation of the asperities also causes energy losses during rolling motion. The friction force is lower for smooth surfaces than for rough surfaces and in almost every case the friction of a rolling contact device drops during running-in.

1.2 Running-in of lubricated systems

1.2.1 Running-in wear definition and process

When two surfaces are loaded for the first time and moved relatively to one another, changes in the condition of both surfaces generally occur. These changes are usually a combination of many things, such as the alignment of axes, shape changes, changes in surface roughness, and the equalizing of various mechanical and chemical properties between the moving surfaces, such as the micro-hardness, which is produced by selective work hardening or the formation of oxide layers and other boundary layers. All these changes are adjustments to minimize energy flow, whether mechanical or chemical, between the moving surfaces [5]. The changes which occur between start-up and steady state are associated with running-in (also called breaking-in or wearing-in). Although in terms of conservation, wear is always undesirable, running-in wear is encouraged rather than avoided.

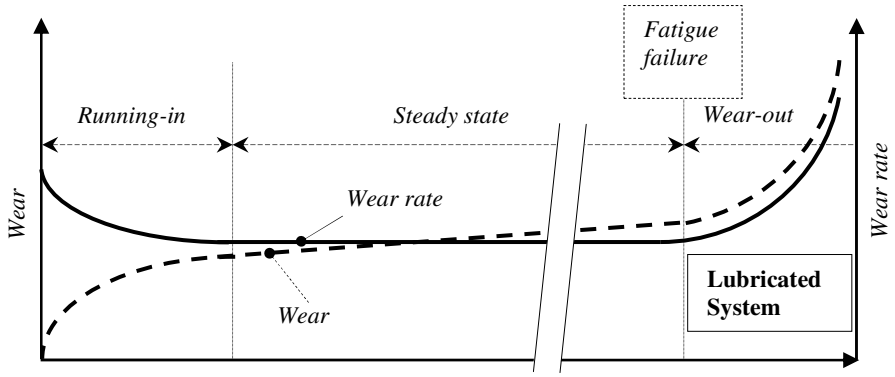

FIGURE 1.3: *Schematic representation of the wear behavior as a function of time, number of overrollings or sliding distance of a contact under constant operating conditions.*

GOST (former USSR) Standard defines running-in as: “The change in the geometry of the sliding surfaces and in the physicomechanical properties of the surface layers of the material during the initial sliding period, which generally manifests itself, assuming constant external conditions, in a decrease in the frictional work, the temperature, and the wear rate” [6]. Summer-smith [7] defines running-in as: “The removal of high spots in the contacting surfaces by wear or plastic deformation under controlled conditions of running giving improved conformability and reduced risk of film breakdown during normal operation”. Running-in occurs in the first period in the life-time of a rolling or sliding contact of a lubricated system, which is schematically shown in Fig. 1.3.

Prior to running-in, the various pairs of contacting surfaces in, for instance, a new engine are not ‘mated together’. There may be a slight initial misalignment and there will certainly be ‘high spots’ on all surfaces. Initially the clearances will be small and therefore the cooling flow or oil is low and this, together with the initial higher friction, leads to operating temperatures higher than normal. During the running-in period, the high spots left from the final machining process are reduced by plastic flow, voids are filled and overall shapes are matched. The higher temperatures usually cause higher wear rates, but as the surfaces become smoother and the more prominent asperities are flattened, the wear rate falls to a steady state. There are two dominant mechanisms in the running-in period; plastic deformation and mild wear [8]. The plastic deformation mechanism is similar to roller burnishing; the asperities literally get squashed down. The change of the surface topography can be the amplitude and/or the texture depending on the load and moving direction. The higher asperities are rubbed off. This mechanism is also called truncating or censoring the height distribution. Frictional losses usually decrease during this period and contact clearances increase, thus reducing the surface temperatures. The wear rate decreases until it reaches the normal steady-state wear rate for the design contact pairs. The wear rate during running-in, even when misalignments are minimal, is higher than during normal running.

After the running-in period, of which duration is invariably depending on the tribo-system, the full service conditions can be applied without any sudden increase in wear rate. The load carrying capacity reaches to its operating design. The steady low wear rate regime is maintained for the designed operational life. The term steady state is defined as the condition of a given tribo-system in which the average dynamic coefficient of friction, wear rate, and other specific parameters have reached and maintained a relatively constant level [9].

The wear rate may rise again once the operating time becomes sufficiently long for a fatigue process to occur in the upper layers of the loaded surface. A significant contribution to material loss driven by cyclic loading is started. The particles from such a fatigue wear process are characteristically much larger than the small fragments associated with adhesive or abrasive wear [10]. This form of wear generates a ‘pitted’ surface (pitting failure). Once the wear particles due to fatigue wear accumulate the surface, it will wear-out i.e. total failure occurs.

1.2.2 Running-in friction

The friction and the change of the average roughness behavior during the life-time of a rolling/sliding contact are schematically presented in Fig. 1.4. There are two phases during

the running-in period, i.e. Phase I and Phase II. In Phase I, the coefficient of friction strongly decreases and the change in surface topography shows similarities with the decrease of the center line average roughness, R_a, value. As was mentioned previously, the plastic deformation is the main factor in changing the surface topography. In Phase II, there is only a slight decrease in the coefficient of friction as well as in the reduction of R_a for quite some time. In this phase mild wear is considered due to the removal of boundary layers formed by a reaction of the additives and oxygen in the lubricant and the contacting metal surfaces.

Schipper [11] studied the running-in effect on the frictional behavior of lubricated concentrated contacts, which can be represented in generalized Stribeck curves, as shown in Fig. 1.5. The coefficient of friction, μ, is plotted as a function of the lubrication number, $(\eta V_+)/p$ or H, in a logarithmic scale. η is the lubricant inlet viscosity, V_+ is the sum velocity and p is the mean contact pressure. During the running-in period, the decrease in the micro-geometry increases the hydrodynamic action.

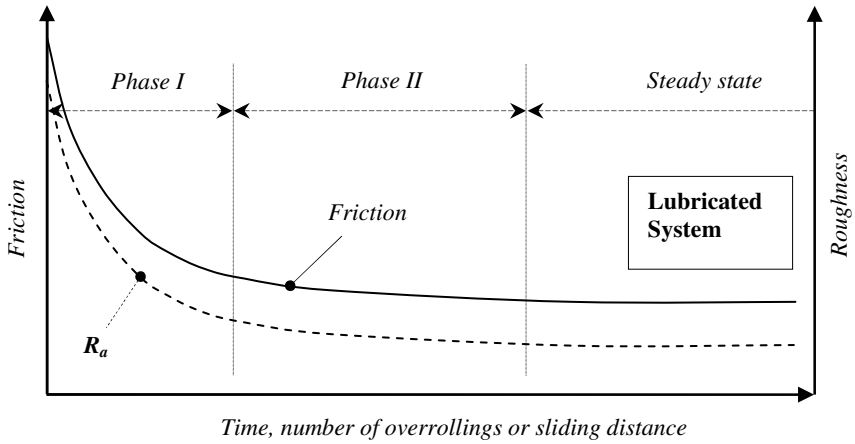

FIGURE 1.4: *Schematic representation of friction and the change of roughness as a function of time, number of overrollings or sliding distance of a contact under constant operating conditions.*

The succeeded running-in increases the load carrying capacity, i.e. increases the hydrodynamic action hence decreases the friction at constant operational conditions. For the low pressure situation (Fig 1.5a), running-in manifests itself by shifting the mixed lubrication (ML) regime to lower values of the lubrication number, H and by decreasing the coefficient of friction. The change in micro-geometry affects the coefficient of friction in the boundary lubrication (BL) regime to lower values. The same shifts are found for the high pressure situation, except that the minimum coefficient of friction, at the transition from mixed lubrication to elasto-hydrodynamic lubrication (E(HL)) regime, shifts to higher values.

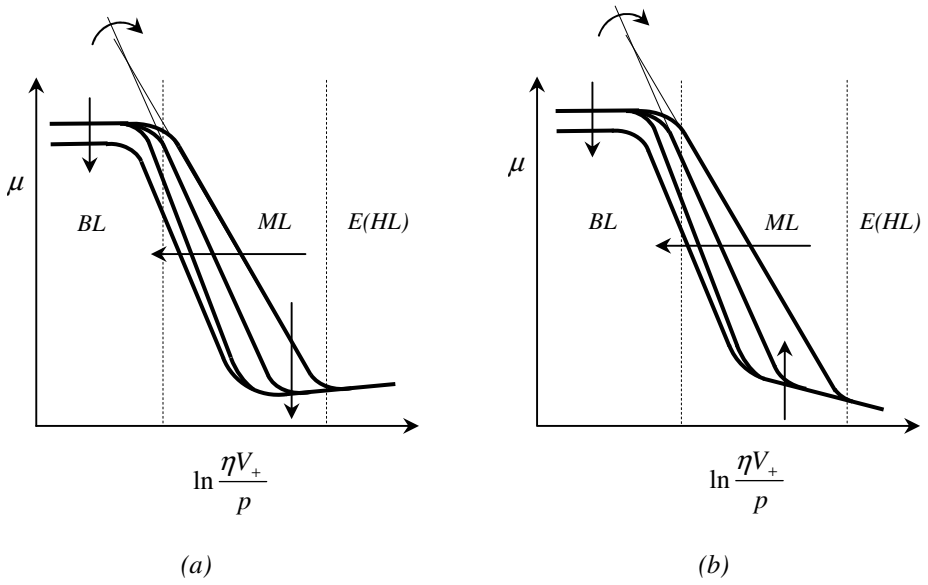

FIGURE 1.5: *Running-in effect at: (a) low pressure and (b) high pressure* [11].

1.3 Objective of this thesis

Running-in is an effective way of matching two contacting components in a functional situation of rolling and/or sliding. As mentioned in the previous section there are many parameter changes during running-in, chemically or mechanically. However, the change of the micro-geometry due to wear or plastic deformation is dominant.

Two historical terms are particularly associated with running-in: asperity truncation and elastic shakedown. In asperity truncation, most studies have been done on modeling the surface statistically. The shape change of the amplitude distribution curve after the running-in has taken place is shown in Fig. 1.6. One would expect the change of the statistical surface parameters such as average roughness, root-mean-square roughness, peak-to-valley height, slope, et cetera during running-in. However, the change of the surface topography is in fact not only the height distribution (one dimension) but change in three dimensions in order to conform to each other. Elastic shakedown is the process in which a surface which initially yields plastically during running-in, eventually reaches an elastic shakedown limit in which the behavior of the near-surface layer is no longer plastic, but has reached a condition which is sufficient to support contact pressure elastically.

In most of the contacting engineering surfaces, the coefficient of friction and wear are decreased due to the running-in process. Plastic deformation leads to the increase of the contacting area and as a result, the mean contact pressure decreases or the load carrying capacity is increased. It is worth noting that if the plastic deformation occurs macroscopically, the change of the roller diameter in roller bearing for instance, there will be a failure of functionality. But if the plastic deformation occurs microscopically, i.e. on

roughness level, the functionality performance of the machine components will be increased.

The objective of this thesis is to predict the process roughness of the surface after the running-in period of rolling contact deterministically. The running-in process is complicated, the number of variables involved are numerous. This thesis will focus only on the prediction of the plastic deformation of the micro-geometry of the contacting metal surfaces which operate in the near or pure rolling situation.

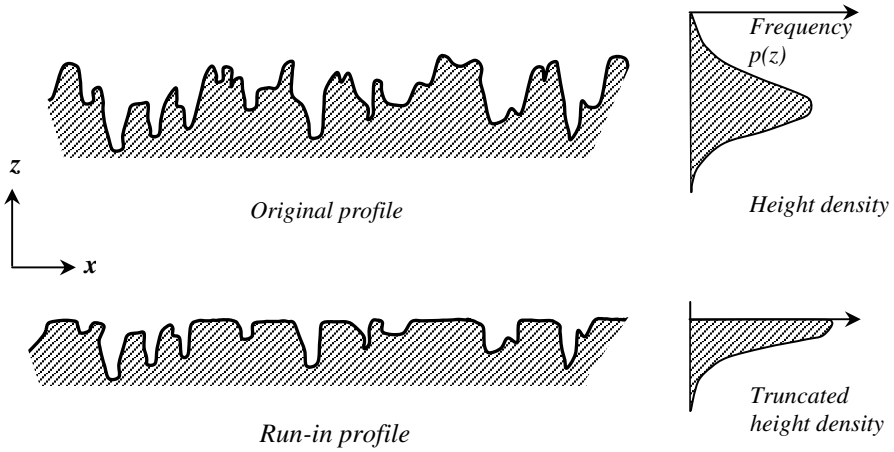

FIGURE 1.6: *Effect of running-in on the surface profile, reproduced from* [5].

1.4 Outline

A brief background and the objective of this thesis have been stated in this chapter. The next chapter will give a review of the available literature on the study of running-in both theoretically and experimentally. An extensive explanation about the background of this work is given in this chapter.

In Chapter 3 an asperity contact model is presented. A new elastic-plastic or elastoplastic contact model is developed as a foundation for the running-in model. Some experiments have been performed in order to validate the developed contact model. A further investigation on the contact model has been extended to the contact of rough surfaces deterministically in Chapter 4. Some approaches have been applied to define an asperity on real surfaces. In this chapter the criteria of surface flattening are developed, there are three types of deformation on the real contact of surfaces: asperity deformation, bulk deformation or a combination of asperity and bulk deformation. Attention is paid only to the deformation of the asperity as the main effect of the running-in process. To validate the rough surface contact model, experiments are performed.

In Chapter 5 the running-in model will be presented. The developed contact model in Chapter 3 and 4 is used to build the running-in model in which the contact situations

change in time. The theoretical results in this chapter will be compared to the experimental results. Finally, conclusions are drawn and recommendations are given in Chapter 6.

References

[1] Johnson, K.L., 1985, *Contact Mechanics*, Cambridge University Press.
[2] Halling, J., 1976, *Introduction to Tribology*, Wykeham Publication Ltd., London.
[3] Bhushan, B., 1999, *Principles and Applications of Tribology*, John Wiley & Sons Inc., New York.
[4] Rabinowicz, E., 1995, *Friction and Wear of Materials*, John Wiley.
[5] Whitehouse, D.J., 1994, *Handbook of Surface Metrology*, Institute of Physics Publishing.
[6] Kraghelsky, V., Dobychun, M.N. and Kombalov, V.S., 1982, *Friction and Wear Calculation Methods*, Pergamon Press, Oxford.
[7] Summer-smith, J.D., 1994, *An Introductory Guide to Industrial Tribology*, Mechanical Engineering Publications Limited, London.
[8] Whitehouse, D.J., 1980, "The effect of surface topography on wear," *Fundamentals of Tribology,* edited by Suh and Saka, MIT, pp. 17 – 52.
[9] Blau, P.J., 1989, *Friction and Wear Transitions of Materials,* Noyes, Park Ridge, NJ.
[10] Williams, J.A., 1994, *Engineering Tribology,* Oxford University Press.
[11] Schipper, D.J., 1988, Transitions in the Lubrication of Concentrated Contacts, PhD Thesis, University of Twente, Enschede, The Netherlands.

Chapter 2

Running-in: a literature survey

2.1. Introduction

Running-in is categorized as the first part of the life-time period of rolling or sliding contacts. Friction and wear mechanisms occurring during the running-in process have been briefly presented in the previous chapter. Chapter 2 presents the changes in a tribo-system during the running-in process in more detail, based on a literature survey. Although the subject is somewhat vague, numerous investigations have been conducted to study running-in. Most studies are based on experiments in order to get an impression of the running-in behavior. The experimental work done by Hirn in 1854 is probably the first study on running-in [1]. The effect of running-in upon bearing friction was discovered and it pointed out that lubricated bearing must be run continuously for a certain time before a steady value of friction is attained. However, the running-in process is a complicated phenomenon related to surface texture, geometry, film formation, chemical and physical properties of materials in contact, lubricant or additives, operating conditions and so on and is not well understood yet.

The following sections describe published articles on running-in. Articles based on experiments on running-in are presented in Section 2.2 and 2.3. The changes in surface micro-geometry after running-in are explored in Section 2.2. Section 2.3 focuses on the factors influencing the effectiveness of running-in. Section 2.4 deals with the theoretical works published on running-in. The available running-in models are reviewed. A summary is given at the end of this chapter.

2.2 Changes in surface micro-geometry

As discussed in Chapter 1, the initial surface topography is one of the most important factors influencing the running-in process. Various researchers studied the effect of the initial surface topography on the running-in performance. Sreenath and Raman [2] showed that the initial surface roughness is the most influencing factor in the conformity between

cylinder liner and piston rings of an internal combustion engine. Anderson *et al.* [3] found that the initial surface roughness strongly influences the initial dynamic coefficient of friction and the running-in distance required. The coefficient of friction is reduced from a level typical for boundary lubrication to a level typical for full film lubrication.

Rowe *et al.* [4] performed a basic investigation of surface topography changes during running-in of grease-lubricated plain bearings. It was shown that the initial surface roughness of the hard shaft is the governing factor, whilst the initial topography of the softer member has less effect on the running-in equilibrium roughness. If the difference in hardness of the two contact surfaces is large, cutting and ploughing will take place easily and requires therefore the roughness value of the hard surface to be as small as possible [5]. To study the effect of surface topography on running-in, most of the literature considers one surface to be relatively smooth and hard running against a deformable rough surface. Only a few articles study the contact between two deformable rough surfaces on running-in. For example, Chou & Lin [6] used the same hardness of rollers and discs to study the effect of roughness and running-in on oil-lubricated line-contacts. Results show that running-in increases the roughness of smooth rollers but decreases the roughness of rough rollers.

The changes of some surface parameters during running-in have been compared by Stout *et al*. [7], Whitehouse [8] and Foucher *et al.* [9] as shown in Fig. 2.1. The average peak curvature is the parameter which changes most rapidly as the load increases. The common type of height parameters such as R_a and R_q do not change quickly. It was suggested that the most relevant and straightforward approach to quantify wear during running-in is to quote both the skewness and a profile height parameter. The skewness is used for quantifying the change of the shape of height distribution.

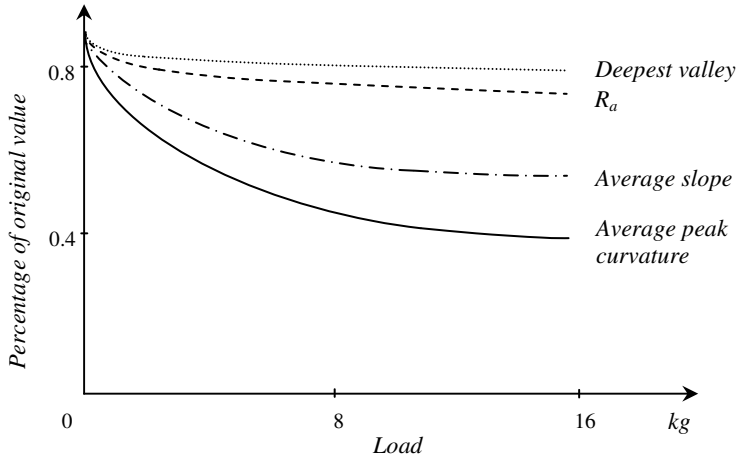

FIGURE 2.1: *Variation of surface parameters as a function of load during running-in, after* [8].

The surface finishing methods have significant contribution to friction and wear during running-in. It was shown by [10, 11] that by suitable modification of the surface

topography, keeping the average roughness, R_a, constant, friction can be reduced. Plateaued surfaces have a shorter running period than non-plateaued surfaces [12, 13]. Running-in performance can also be increased by modifying the lay direction of the surfaces [14-16]. Surface roughness with a transversely oriented pattern gives a lower friction than the other roughness patterns (longitudinal or oblique). This phenomenon is caused by an increase in oil film thickness with transverse roughness compared to the longitudinal roughness [17, 18].

The effects of waviness and roughness on the running-in of lubricated contacts have been studied by Wu & Zheng [19]. Running-in changes the roughness but hardly changes the surface wavelength. An appropriate surface waviness is necessary for the formation of an oil film between parallel sliders. Pawlus [20, 21] studied some connections between the cylinder surface micro-geometry and functional parameters of the piston ring-cylinder assembly during running-in. From the results, it was concluded that cylinder wear during running-in mainly depends on both the roughness height and the shape of the roughness profile distribution.

The change of the initial surface roughness and friction as a function of running-in time was explored in more detail by Wang *et al.* [22]. In their experiments, a two disk machine was employed to perform the rolling and sliding tests. A new optical technique method has been applied to measure the roughness of the running surface in real-time [23]. Results showed that the rougher the initial surface, the larger the ratio of roughness change (Fig 2.2a). This is different from the presumption that the final or process roughness after running-in depends mainly on the operational conditions such as material, temperature, lubrication contaminant and so on instead of on the initial roughness [24, 25]. However, the final friction forces with surfaces of different initial average roughness, R_{ai}, have similar values after running-in. This indicates that the surfaces have similar effects on lubrication due to their degree of conformity after running-in.

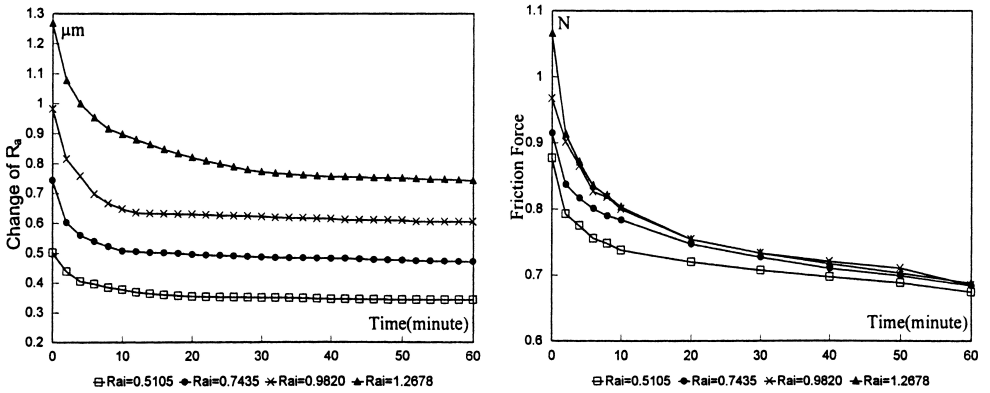

(a) *(b)*

FIGURE 2.2: *Variation of R_a and friction force as a function of running-in time for different initial roughnesses (slip ratio* 0.6 *and Hertzian pressure* 0.22 *GPa), after Wang et al.* [22].

The plasticity index is also used as a criterion for evaluating the effects of surface topography during running-in [19, 26]. A random isotropic surface with a very low average asperity slope and very low plasticity index demonstrate no run-in characteristics.

2.3 Effective running-in

The mechanism governing the formation of asperities during running-in is a complex process and is formed by the action of periodic factors and numerous random effects [24]. Plastic deformation, fatigue damage and in some cases micro-cutting, scuffing and ploughing occurs. If the hardness of the contacting pairs differ the softest of the mating surfaces undergoes most change, and during running-in its roughness changes so that it approximates the roughness of hard surface, until certain equilibrium is attained.

Kragelsky [24] presented some factors influencing the effectiveness of running-in. All these factors are interconnected so it is difficult to study their effects on running-in separately. However, the main factors influencing the effectiveness of running-in are load and velocity, the initial physicomechanical of the materials and the lubricant.

2.3.1 The influence of load and velocity

In practical situations running-in takes place by increasing the load and velocity continuously or stepwise. The load has a significant effect on the quality and duration of running-in. By increasing the load during the initial period of running-in the proportion of plastic deformation of a thin surface layer increases [24]. This leads to an increase of the overall work done, heat evolved and energy absorption. High mechanical stresses arise from an increase in pressure in the contact area. The quality of a run-in surface is improved by increasing the contact pressure to a value not exceeding a certain critical contact pressure. Increasing the contact pressure beyond its critical value will lead to severe wear. Kelly & Critchlow [27] concluded that the dominant effect of enhancing the loads and temperatures which lubricated surfaces can resist without severe wear prior to running-in, is reduction of surface roughness.

Cavatorta & Cusano [28] showed that the smoothening of surfaces is increased by increasing the pressure. For higher velocities a more negative skewness is produced. However, the optimal pressure/velocity run-in procedures were shown to depend on the operating conditions. The range of running velocities is always related to the formation of a surface layer which prevents severe wear [29, 30]. Under high velocity severe wear resistance improvement can be obtained only if there is significant smoothening of the rough surfaces.

Wang *et al*. [22] investigated the effect of the sliding/rolling ratio on the change of surface roughness during running-in. It was shown that the change in R_a is not straightforward with the change of the sliding/rolling ratio. The change in R_a increases with the increase in the sliding/rolling ratio for low sliding/rolling values but it decreases with the increase in the sliding/rolling ratio for high sliding/rolling values, see Fig. 2.3. The change in roughness relates to wear loss of the materials. The amount of wear will be larger when there is a small amount of sliding at the surface than when the surface is run under pure rolling. The sliding action downgrades the lubrication effect and increases the shear

stresses. However, the wear loss is smaller under a higher sliding/rolling ratio in the high sliding/rolling ratio region. In this region the wear mechanism is different from the low sliding/rolling ratio region. Oxidation is dominant and the thin oxide layer formed on the surface can act as a solid lubricant and protect the surface. Schipper *et al.* [31] studied the effect of the travel mode of the motion on the running-in behavior of lubricated concentrated contacts. It was shown that the gradual change of the surface roughness is strongly dependent on the motion mode and the lubrication regime. If the contact operates in the boundary lubrication regime, the influence of the motion mode becomes minimal.

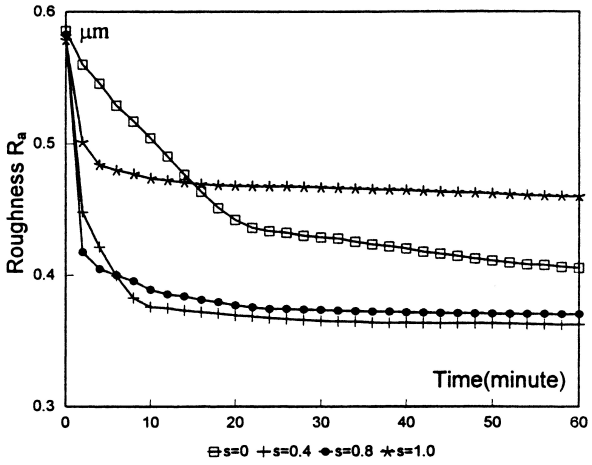

FIGURE 2.3: *Variation in R_a as a function of time for different sliding/rolling ratios (combined velocity* 2 *m/s, load* 4 *kg and Hertz pressure* 0.22 *GPa)* [22].

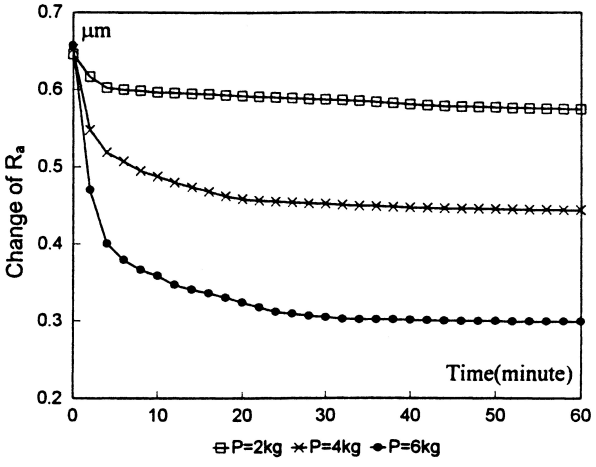

FIGURE 2.4: *Variation in R_a as a function of time under different normal loads* [22].

The smoothening process of rough surfaces by increasing the load has also been presented in [22]. The surfaces started with almost the same surface roughness and ended with different roughness values as a function of the load, see Fig 2.4. The larger the applied load the lower the surface roughness after running-in. It is reasonable that more flattening is induced by a higher load which is beneficial for decreasing the contact pressure.

2.3.2 The influence of lubricants and additives

Under unchanged contact conditions, the presence of lubricants and additives has a significant effect on the change in micro-geometry during running-in [24]. Significant shortening of the running-in time and smoothening of the surface can be achieved by using polymer additives in the oil. The polymer changes due to rupture by mechanical action, and the surface active substances react with the fresh metal surface and plasticizes the thin layer.

Rowe *et al.* [4] evaluated the performance of greases with extreme pressure and solid-lubricant additives on running-in of plain bearings. Tests on grease-lubricated bearings showed that the surface is progressively smoothed as running proceeds, however, after a few hours it breaks down. Similar greases with a chlorinated extreme-pressure compound additive give the same smoothening but breakdown is prevented. By using Molybdenum Disulphide (MoS_2) similar no-failure results were obtained but the initial smoothing was retarded. The influence of MoS_2 was also studied by Braithwaite *et al.* [32] on the mechanism of piston-ring wear during the running-in process. It was concluded that the use of MoS_2 additive is effective in modifying the mechanism of wear during running-in so that metal-to-metal contact is reduced and the change in surface topography is achieved mainly by plastic deformation rather than by adhesive or an abrasive wear process which mainly occurs when using conventional break-in oil. MoS_2 has great resistance to penetration and, at the same time, facilitates sliding and thus promotes the reduction of surface asperities by plastic deformation rather than by shearing.

The use of a running-in compound which is added to the fuel was found to shorten the running-in time without any harmful effects. This study was applied to the running-in of a locomotive diesel engine in an attempt to improve the resistance to scuffing or severe wear [33]. Murakami *et al.* [34] used a Dibenzyl Disulphide (DBDS) additive to study the significance of tribochemical effects on running-in in four-ball testing. Results showed that oxide films and Sulphur compounds are formed and the rubbing surface becomes extremely smooth.

Although lubricant has a significant effect on shortening the running-in time, a careful choice must be taken in order to get an optimum for the running-in process. The performance of the lubricant and in particularly the additives depends mainly on the contact temperature [9]. Another aspect of the lubricant during running-in is the oil film thickness. Khurshudov *et al.* [35] studied the effect of oil film thickness on the wear rate. For the initial value of the specific oil film thickness, λ_i (oil film thickness over roughness ratio) < 0.5 causes both a high wear rate and a high surface roughness of the contacting surfaces. The increase of the λ_i value from 0.5 to 0.75 causes a significant decrease of wear rate and a steady-state roughness for both contacting surfaces. Further increase of λ_i above 0.75 does not affect the wear rate and roughness significantly anymore. This is because of their appreciable separation by an EHL film.

2.4 Modeling running-in

2.4.1 The model of Blau

From published work Blau [36] collected numerous examples of running-in experiments, which resulted in sliding coefficient of friction versus time behavior graphs, and own laboratory experiments in order to be able to develop a physical realistic and useful running-in model [37]. A survey of literature revealed eight common forms of friction versus sliding time curves (Fig. 2.5). Some of the possible occurrences and causes related to each type of friction curve illustrated in Fig. 2.5 are indicated in Table 2.1.

The friction curve most observed in experiments on the running-in bearings is curve *f* in Fig. 2.5. One possible mechanism in this curve is the crystallographic reorientation of near-surface microstructures during the early stages of running. Once a preferred crystal texture is achieved, a steady state micro-structural resistance to running direction is acquired. The micro-geometry conformity also contributes much in lowering the coefficient of friction in this friction-curve behavior. However, at extreme heavy loads, a given initial surface finish may have much less contribution, since the first running of a heavily loaded component could remove all traces of the initial surface roughness.

The basic shape of the transition curves as shown in Fig. 2.5 is a starting point for developing a semi-empirical running-in model. The model can be represented in its simple form as a product of two factors:

$$\mu(t) = L(t)S(t) \tag{2.1}$$

where $\mu(t)$ is the time-dependent coefficient of friction, $L(t)$ is the time-dependent lubrication factor, and $S(t)$ is the time-dependent contribution of the solid materials in contact. Each factor in the model is further broken down into a form which permits the magnitude and rate of change in the different frictional contributions to be incorporated.

The lubrication factor modifies the contribution of the friction of solids in contact and its value ranges between 0 and 1. If the lubricant is absent or fails to prevent solid contact, $L(t) = 1$. If the lubrication chosen for the system works well from the start and continues to do so, $L(t)$ may taken as a constant value, typically between 0.001 to 0.1. The time dependence of the lubrication factor $L(t)$ during running-in is written more generally:

$$L(t) = \frac{1}{1+l} \tag{2.2}$$

and l is the lubricant effectiveness:

$$l = l_0 e^{-At} \tag{2.3}$$

where l_0 is the initial lubricant effectiveness, A is a rate constant, and t is the running time. If the lubrication effectiveness l is 0, then the $L(t) = 1$. The effectiveness of the lubricant decreases if A is positive.

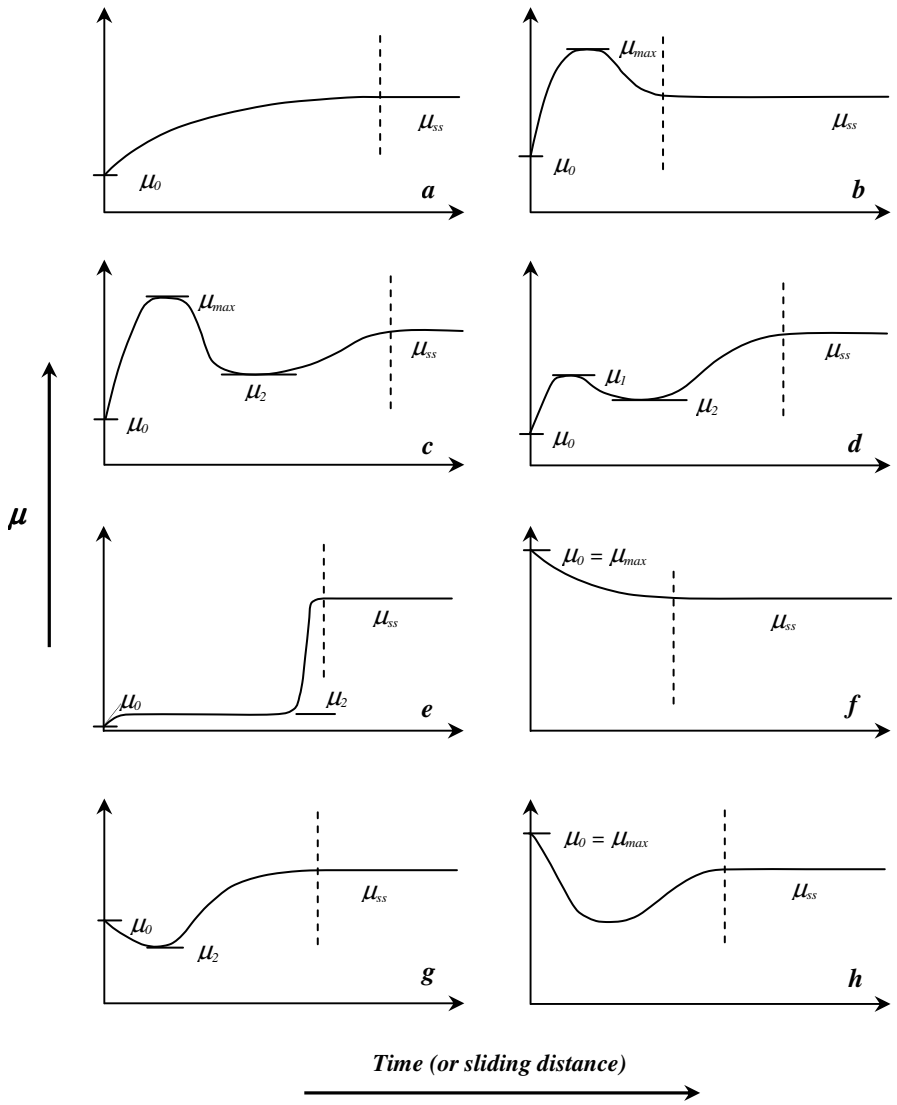

FIGURE 2.5: *Eight commonly observed forms of initial frictional behaviour as a function of time or sliding distance, after Blau* [36].

TABLE 1.1: *Possible causes for friction break-in curve shapes, after* [38].

Type	Occurrence	Possible cause(s)
a	Contaminant surfaces.	A thin film of lubricious contaminant is worn off the sliding surface(s).
b	Boundary-lubricated metals.	Surfaces wear in; initial wear rate is high until the sharpest asperities are worn off and the surface becomes smoother.
c	Unlubricated oxidized metals, often observed in ferrous or ferrous/nonferrous pairs.	Wear-in, as in **b**, but with the subsequent development of a debris layer or excessive transfer of material.
d	Same as type **c**.	Similar to **c**, but the initial oxide film may be more tenacious and protective.
e	Coated systems; also, systems in which wear is controlled by subsurface fatigue processes.	Wear-through of a coating; or subsurface fatigue cracks grow until debris is first produced (the debris creates third bodies), which induce a rapid transition in friction
f	Clean, pure metals.	Changes in crystallographic orientation in near-surface layers reduce their shear strength and lower the friction.
g	Graphite on graphite; metal on graphite.	Creation of a thin film during running-in; debris or transfer produces a subsequent rise in friction.
h	Hard coatings on ceramics.	Roughness changes, then a fine-grained debris layer forms.

In this simple model, the lubricant factor is treated as being independent of the solid bodies' behavior. Clearly, when the surface roughness changes during sliding, the film thickness to roughness ratio will be affected, which, in turn, affects the regime of lubrication, therefore the changes in the solids could ultimately affect $L(t)$.

The time-dependent contribution of the solid materials $S(t)$ to the friction can be represented as follows:

$$S(t) = D + T + V \tag{2.4}$$

where D is the initial deformation and texturing term, T is the transitions term, and V is the magnitude of the variability in the coefficient of friction which can derive from any source.

Based on the consideration that the friction is governed by the properties of the softer material of the two mating surfaces the initial deformation and texturing term is defined as:

$$D = C\left(\frac{\tau_s}{\tau_b}\right)\left(\frac{m_b}{m_s}\right) \tag{2.5}$$

where τ_s and τ_b are the shear strengths of the work-hardened surface and bulk material, respectively; m_s and m_b are the crystallographic factors for the surface and bulk material, respectively; and C is a constant derived from considerations of the contact area. Another possible form of D which relates the rate of change in friction to work-hardening coefficient n, by a system-dependent constant m is:

$$D = \mu_{\max}\left\{1 - \left(\frac{\tau_{\max} - \tau_0}{\tau_{\max}}\right)\left[1 - \exp(-nm/t)\right]\right\} \tag{2.6}$$

where μ_{max} is the maximum coefficient of friction after break-in, τ_{max} is the maximum surface shear stress, τ_0 is the initial surface shear stress and t is the running time. It is suggested by Blau that the user of the model should use the D form, because it is most descriptive of the physical situation encountered.

The transition term T is designed to account for longer term, non-induced changes in the friction force, those that may require an incubation period. One example is the development of subsurface fatigue damage, which eventually results in the production of wear particles, which in turn cause a rapid transition to three-body contact. The T form for modeling the friction curve of type ***e*** in Fig. 2.5 is:

$$T = \left(\frac{F_p}{2}\right)\left\{1 + \left[\frac{t - t_i}{\left(\left|t - t_i\right|^b + 1\right)^{1/b}}\right]\right\} \tag{2.7}$$

in which F_p is the maximum coefficient of friction contribution of the transition process, t_i is the incubation time to the midpoint of the transition and b is a rate constant for

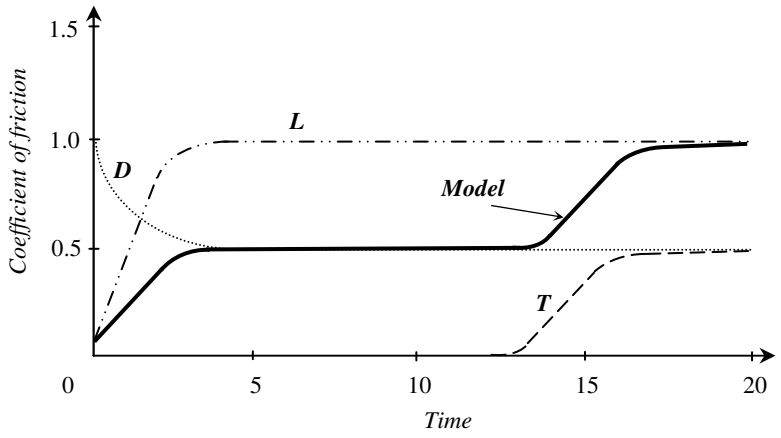

FIGURE 2.6: *Illustration of how Equation* (2.7) *can be used to model longer term transitions in frictional behavior, after Blau* [38].

determining how fast the transition occurs. Finally, several kinds of frictional behavior can be represented by summing up contributions of the various terms and factors after the proper time scales and magnitudes of contributory processes have been determined. The combined effect of individual terms and factors in the production of the type of curve in Fig. 2.5**e** is illustrated in Fig. 2.6. By using various combinations of *L*, *D* and *T* terms, all the curve shapes in Fig. 2.5 can be produced.

The *V* term in Eq. (2.4) is the variation term indicating the contribution to the amplitude of the instantaneous coefficient of friction from any of several interfacial and instrumental factors. A 'frictional noise' for instance can produce a spurious line in the coefficient of friction.

It can be summarized that a simple generalized model of Blau is able to generate the various types of frictional transitions including the running-in friction. However, the model may be applied to a frictional system behavior globally rather than to study the local micro-geometry changes which affect the global frictional behavior.

2.4.2 The model of Kapoor *et al.*

In static contact situations in which the contact pressure is lower than the elastic limit or yield stress, a material element will return to its original geometry once the load has been removed. If the contact pressure is larger than the elastic limit then some material will undergo plastic flow. There are two significant consequences with respect to this situation; residual stresses will develop and the material may strain-harden so increase its effective yield stress [39].

In repeated contact situations, the developed residual stresses will increase the yield stress for the subsequent loading. These residual stresses are essentially protective, together with any effects of strain-hardening and geometric changes which may ensure that the repeated contact is still in the elastic regime. This process is referred to as shakedown. Shakedown is the process in which a cyclically loaded structure or material element deforms plastically at the first loading and finally achieves a steady state in which the response is perfectly elastic [40]. The influence of residual stresses in promoting shakedown was governed by the Melan's theorem [41] which states: "If any system of self-equilibrating residual stresses can be found which, in combination with the stresses due to the repeated load, do not exceed yield at any time, then elastic shakedown will take place". These processes are illustrated in Fig 2.7.

The response of the structure is entirely elastic for loading up to the elastic limit (Fig. 2.7a). The plastic flow is encountered when applying the load above the elastic limit. The shakedown process takes place and the structure responses to the elastic steady-state. The upper limit for this behavior is shown as elastic shakedown limit in Fig. 2.7b. When increasing the load, the plastic flow is encountered, even in the steady-state condition. If the load is below the plastic shakedown limit (Fig.2.7c) a closed cycle of plastic deformation occurs. In this stage plastic flow occurs at two instances in each load cycle but there is no net accumulation of deformation. However, if the load lies above the plastic shakedown limit, then an open cycle of plastic deformation occurs and the material accumulates small increments of plastic deformation in each loading cycle or ratcheting (Fig.2.7d).

Kapoor & Johnson [42] consider running-in as a shakedown process. They hypothesize that due to plastic flow in early passages of a body, the shape and height of

asperities at the surface will be modified as such that, in steady state, the load will be carried purely elastically in order to model running-in. This approach has been used extensively to different applications [40, 43]. A rough surface of 2D cylindrical asperities of equal radii

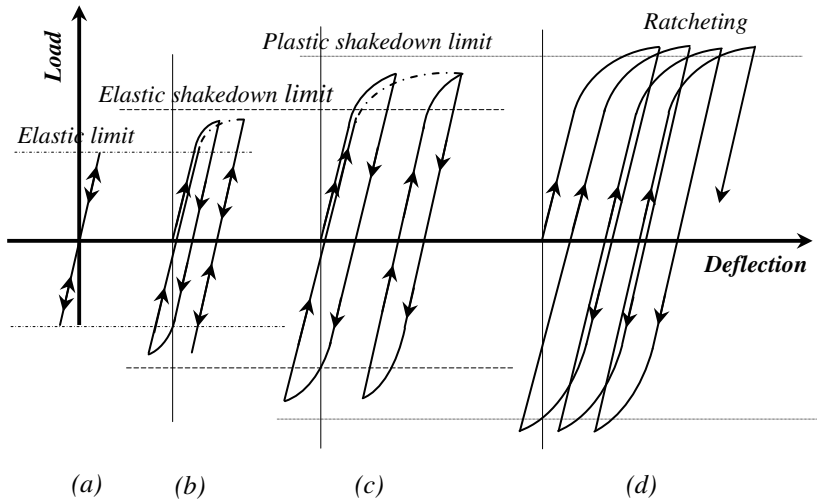

FIGURE 2.7: *Response of a structure or material element to cyclic loading* [39].

and following a Gaussian distribution is considered. This surface is slid by a hard regular surface which has 2D cylindrical asperities of equal height and radii. A unit event is introduced as a basis of the model. The unit event is taken to be that of the cylinder asperities pushing against each other when passing as is shown in Fig.2.8a. During an elastic contact, contact pressure rising from zero at point *A* to a maximum at *B* and failing to zero at *D* with semi-contact width *a* (Fig.2.8b). Above a critical value of Δ_0, the pressure p_0 exceeds the elastic limit p_0^e whereupon the shakedown mechanisms, such as developing residual stresses, geometry changes and strain hardening occur. The deformed asperities adopt a shape which supports the contact pressure at the shakedown limit throughout the interaction (Fig.2.8c).

Based on the shakedown hypothesis [43] a constant *C* is defined by:

$$C = \left(\frac{p_0{}^s}{E} \right)^2 \left[2 \ln \frac{4E}{p_0{}^s} - 1 \right] \tag{2.8}$$

where v is the Poisson's ratio, p_0^s is the shakedown pressure for the given friction conditions as shown in Fig. 2.9, where k is the shear yield stress and the equivalent elastic modulus of the two surfaces is given by $1/E = [(1-v_1^2)/E_1 + (1-v_2^2)/E_2]$.

Considering surface 1 as a rigid regular surface and surface 2 as a deformable Gaussian surface, the modified distribution $g(y)$ of surface 2 after shakedown (in steady state) is represented by:

$$g(y) = 1.46\eta^2 \exp\left[-\frac{1}{2}\left(\frac{d}{\sigma} + \frac{R_1 C}{\sigma}\eta\right)^2\right] \tag{2.9}$$

where

$$\eta = \frac{0.277(R_1 C/\sigma)}{1.05(R_1 C/\sigma) + (d/\sigma) - (y/\sigma)}$$

R_1 is the radii of surface 1, d is the separation between the surfaces, σ is the standard deviation of peak heights of surface 2, C is as defined in Eq. (2.8), and y is the new height of the deformed asperity. It must be remembered that the modification of heights is possible only when $(\Delta_0/RC) > 1$, where $1/R = 1/R_1 + 1/R_2$ and R_2 is the radii of surface 2.

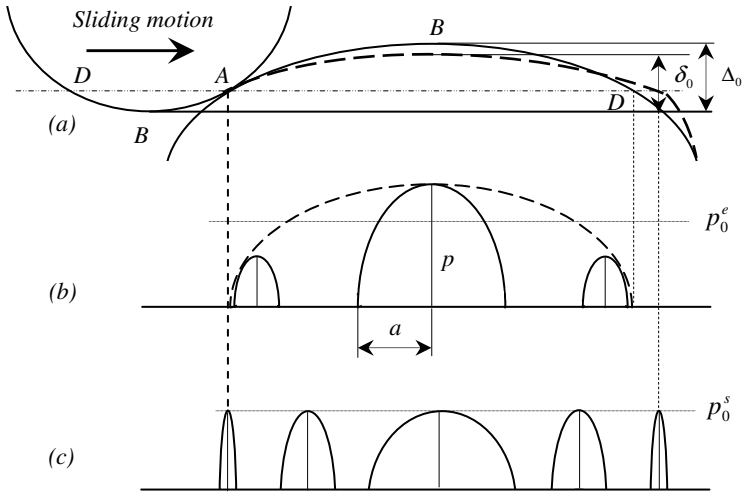

FIGURE 2.8: *(a) The unit event (b) Variation of pressure and semi-contact width on undeformed profile and (c) Variation of pressure on shakedown profile* [42].

The range of y for which equation (2.9) is valid is:

$$\left(\frac{d}{\sigma}\right) + \frac{1}{1+t}\left(\frac{R_1 C}{\sigma}\right) \le \left(\frac{y}{\sigma}\right) \le \left(\frac{d}{\sigma}\right) + \left(\frac{R_1 C}{\sigma}\right) \tag{2.10}$$

where t is the ratio of the radius R_1 of the non-deforming asperity to the radius R_2 of the deforming asperity. The asperities remain undeformed and the distribution unchanged in the range y:

$$\left(\frac{y}{\sigma}\right)=\left(\frac{d}{\sigma}\right)+\frac{1}{1+t}\left(\frac{R_1 C}{\sigma}\right) \tag{2.11}$$

whereupon

$$g(y)=\frac{1}{\sqrt{2\pi}}\exp\left[-\frac{1}{2}\left(\frac{y}{\sigma}\right)^2\right] \tag{2.12}$$

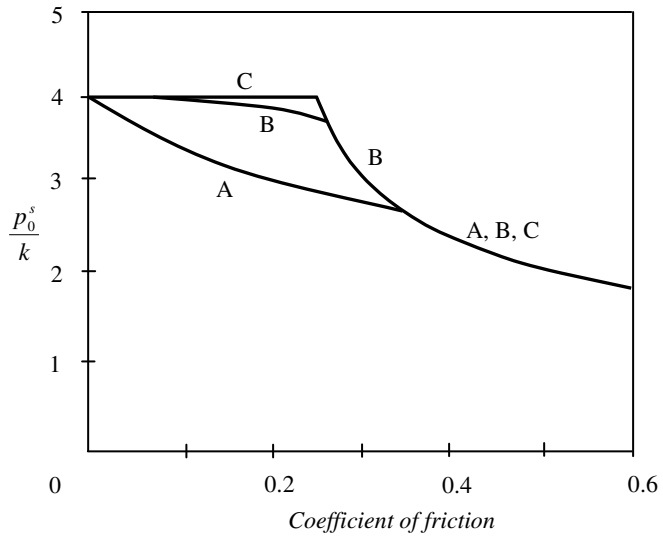

FIGURE 2.9: *Shakedown limits to be used in Equation* (2.8)*,* [42]*:*
A Lateral asperity (perpendicular to sliding)
B Longitudinal asperity (parallel to sliding)
C Kinematic hardening for both the lateral and longitudinal asperity

The new distribution of asperity heights is completely defined by equations (2.9) to (2.12) which depend only on the non-dimensional separation (d/σ) and the non-dimensional group (R_1C/σ).

The proposed model was validated by the experimental results [44] as is shown in Fig. 2.10. In that experiment a bead blasted mild steel pad was pressed against an oil lubricated rotating hard steel which had been finely ground. The experimental results fit satisfactorily in spite of the fact that the surface roughness of the specimen was isotropic, while the theory was developed for linear roughness.

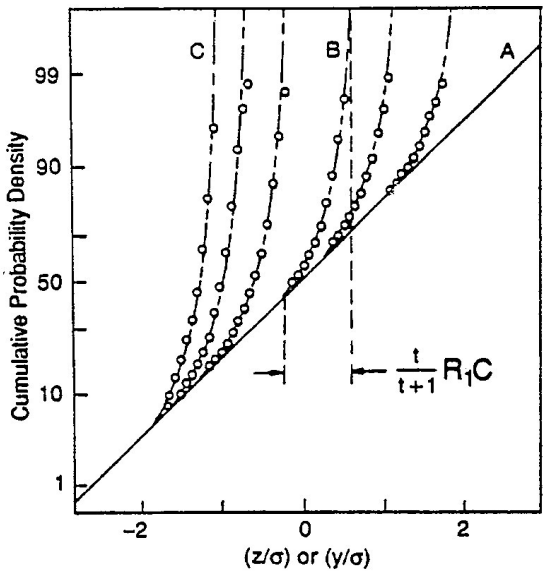

FIGURE 2.10: *Modification of peak heights: — is the original Gaussian distribution, -- is the modified distribution for t = 0.5, 1, 2, and ○ experimental results* [42].

The model has been extended to the more realistic situation in which the hard surface is also randomly rough and the asperity heights follow a Gaussian distribution, but their radii remain constant [45]. The non-dimensional nominal pressure at shakedown for point contact was derived as:

$$\overline{P}_s \equiv \frac{\left(P_s / p_0{}^s\right)}{NR_1\sigma_1} = \left(\frac{9\pi^{5/2}}{16\sqrt{2}}\right)\frac{1}{\psi_s{}^2}\int_{d/\sigma_1}^{h/\sigma_1}\left\{1+\left(\frac{4}{3\pi}\right)^2\psi_s{}^2\left(\frac{z}{\sigma_1}-\frac{h}{\sigma_1}\right)\right\}^{3/2} e^{-z^2/2\sigma_1} d\left(\frac{z}{\sigma_1}\right) + \left(\frac{9\pi^3}{32}\right)\frac{1}{\psi_s{}^2}\left[1-erf\left(\frac{h}{\sqrt{2}\sigma_1}\right)\right] \tag{2.13}$$

where

$$\frac{1}{\psi_s{}^2} = \left(\frac{p_0{}^s}{E}\right)^2 \frac{R_1}{\sigma_1} \tag{2.14}$$

P_s is the nominal shakedown pressure, $p_0{}^s$ is the asperity shakedown pressure, N is the number of asperities per unit area, R_1 is the radius of hard asperities, ψ_s is the plasticity index, h is the cut-off height of hard asperities and σ_1 is the r.m.s. roughness of hard asperities. Eq. (2.13) has been evaluated numerically and the resulting values of the

nominal shakedown pressure are plotted against the value of ψ_s in Fig. 2.11 for various values of h/σ_1.

The process of running-in can be interpreted by referring to Fig. 2.11. Initially, the softer surface has asperities with radius R_2 and r.m.s. height σ_2. A 'working' plasticity index ψ_s^* in repeated sliding was introduced to take into account the changes in those quantities as:

$$\psi_s^* = \frac{E}{p_0^{\,s}}\left(\frac{\sigma}{R}\right)^{1/2} \tag{2.15}$$

where $R = R_1R_2/(R_1+R_2)$ and $\sigma = (\sigma_1^2+\sigma_2^2)^{1/2}$.

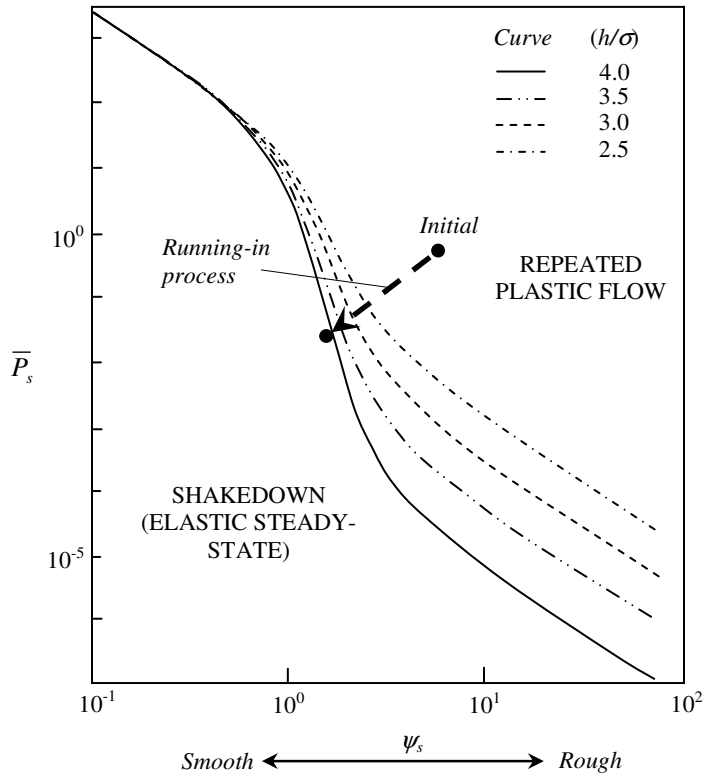

FIGURE 2.11: *Shakedown map for rough surfaces (one hard, the other soft) in sliding contact, after Kapoor et al.* [45].

In the first sliding pass, the system can be represented by a point somewhere in Fig. 2.11 with coordinates ψ_s^* and P_s. If the point lies below the shakedown curve, then the load is carried purely elastically without any change in the softer surface topography. However, if

the point lies above the shakedown curves, plastic flow will occur during sliding and the softer asperities will deform. R_2 will increase and σ_2 will decrease such that ψ_2* will reduce. The run-in (shakedown) state will be reached if, and only if, the curve in Fig. 2.11 is crossed with R_2 less than infinity and σ_2 greater than 0. If $R_2 = \infty$ and $\sigma_2 = 0$ (i.e. when the soft surface has become flat and thus is capable of carrying its maximum load) the point still lies to the right of the shakedown curves, then running-in will not lead to the conditions of elastic sliding and the steady state will be one of repeated plastic deformation.

The model of Kapoor is promising with respect to running-in, however, there is a shortcoming, the radius of the asperities is assumed to be equal, and that should be taken into consideration for the improvement of the model for real rough surfaces.

2.4.3 Other models

Based on a statistical approach King *et al*. [46] consider truncating functions of triangular and Gaussian shape to obtain the run-in height distribution, but there is no theoretical basis for the choice of the truncating functions or its standard deviation. Other approaches have been applied by researchers for modeling running-in other than the statistical approach. Masouros *et al.* [47] and Kumar *et al*. [48] used polynomial analytical expressions, Lin & Cheng [49] and Hu *et al.* [50] used a dynamic system approach and Shirong & Gouan [51] used scale-independent fractal parameters. Liang *et al.* [52] used a numerical approach based on the elastic contact stress distribution of a three-dimensional real rough surface while Liu *et al*. [53] used an elastic-perfectly plastic contact model.

Kragelsky *et al.* [24, 54] described several approaches to model running-in. One of them considers the conditions necessary to reach the optimum, 'equilibrium' surface roughness Δ_{opt}, at which friction will be the lowest:

$$\Delta_{opt} = \frac{16\tau_0^{1.25}[(1-\nu^2)/E]^{0.75}}{p_c^{0.5}\alpha_{hys}^{1.25}} \tag{2.16}$$

where τ_0 is the shear strength of the asperities, p_c is the initial contact pressure, α_{hys} is the hysteresis loss factor (change in strength properties as a result of sliding) which is determined by uniaxial tension and compression experiments, ν is Poisson's ratio, and E is the elastic modulus.

Recently, Jeng and co-workers have developed a model which describes the change of surface topography of general surfaces during running-in [55]. Principally, the model is based on the wear model of Sugimura *et al*. [56] and the distribution translatory system of Johnson [57]. The Johnson's translatory system transforms the surface height of a non-Gaussian surface into that of a Gaussian surface.

2.5 Summary

Studies on running-in have been performed for many years, however, due to the complexity of its phenomena many problems have not been solved yet. A review of the theoretical and

experimental published work regarding running-in has been presented in this chapter. The following points have been observed from this literature review:

1. There are two dominant mechanisms during running-in of lubricated contacts process, i.e. plastic deformation due to normal loading and mild wear. These mechanisms are associated with the change of the initial surface topography. Running-in only changes the surface roughness but hardly change the surface wavelength. If the initial surface roughness is very smooth it will end up to a rougher one and conversely, if the initial surface roughness is quite rough it will end up a smoother one as running-in proceeds.
2. Most studies, both theoretical and experimental, consider contacts between hard smooth surfaces against soft rough surfaces in sliding motion.
3. Increasing loads is the most effective way to accelerate running-in, however, by increasing the loads severe wear occurs easily. In order to reduce severe wear, lubricants and additives are most frequently used.
4. Statistical approaches have been used widely for modeling running-in and the Gaussian distribution is always assumed.

Therefore the main aspects of this thesis will be focused on the normal loading of lubricated metal to metal surfaces for the 'pure' rolling contact situation.

Due to the fact that the change of the micro-geometry is dominant, many efforts have been made in order to study the behavior of the micro-geometry changes by applying a contact model. From the literature it can be concluded that there is no model which predicts the surface topography changes during running-in at roughness level deterministically. In the present work, a model which predicts the process roughness of real surfaces as running-in proceeds will be developed. It is clear that the contact model is crucial in developing such a model and therefore the asperity contact model as well as the asperity deformation model will be developed.

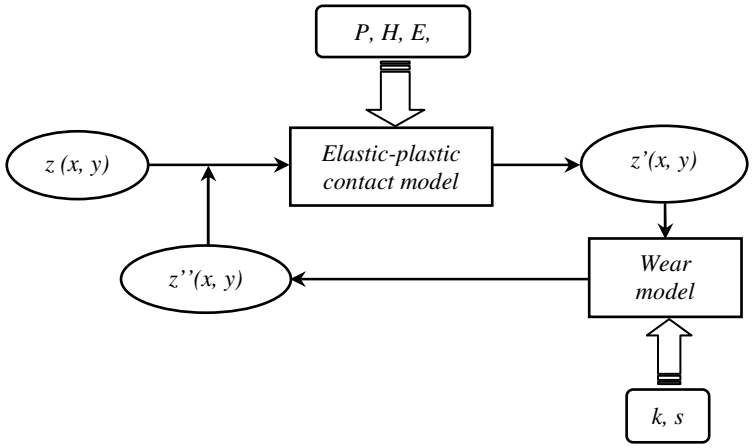

FIGURE 2.12: *Schematic illustration of the proposed running-in model.*

Fig. 2.12 shows schematically the proposed running-in model. In this model the initial (measured) surface geometry, $z(x,y)$, will be used as an input for the elastic-plastic contact model and $z'(x,y)$ and $z''(x,y)$ will be the output of surface geometries after applying the elastic-plastic contact model and wear model respectively. For calculating with the elastic-plastic contact model the applied load, P, the material hardness, H, the elasticity modulus, E, et cetera are needed. The wear coefficient, k, and sliding distance, s, are necessary to calculate $z''(x,y)$ with the wear model. $z''(x,y)$ is now used as input for the elastic-plastic contact model until a near steady-state or process roughness is obtained. The surface topography changes during the running-in process for a certain number of cycles or sliding distances may then be predicted by using this model.

This thesis focuses on the changes of local micro-geometry in 'pure' rolling contacts; therefore the wear model in Fig. 2.12 is neglected. As a basis of the proposed running-in model, the elastic-plastic asperity contact model, which incorporates the elastic, elastoplastic and fully plastic contact situation, will be presented in the following chapter.

References

[1] Dowson, D., 1998, *History of Tribology*, Second Edition, Professional Engineering Publishing, London.

[2] Sreenath, A.V. and Raman, N., 1976, "Running-in wear of a compression ignition engine: Factors influencing the conformance between cylinder liner and piston rings," *Wear* **38**, pp. 271 – 289.

[3] Anderson, P., Juhanko, J., Nikkila, A.P. and Lintula, P., 1996, "Influence of topography on the running-in of water-lubricated silicon carbide journal bearings," *Wear* **201**, pp. 1 – 9.

[4] Rowe, G.W., Kalizer, H., Trmal, G. and Cotter, A., 1975, "Running-in of plain bearings," *Wear* **34**, pp. 1 – 14.

[5] So, H. and Lin, R.C., 1999, "The combined effects of ZDDP, surface texture and hardness on the running-in of ferrous metals," *Tribology International* **32**, pp. 243 – 253.

[6] Chou, C.C. and Lin, F.J., 1997, "Tribological effects of roughness and running-in on oil-lubricated line contacts," *Proceedings of the Institution of Mechanical Engineers part J Journal of Engineering Tribology* **211**, pp. 209 – 222.

[7] Stout, K.J., Whitehouse, D.J. and King, T.G., 1977, "Analytical techniques in surface topography and their application to a running-in experiment," *Wear* **43**, pp. 99 – 115.

[8] Whitehouse, D.J., 1994, *Handbook of Surface Metrology*, Institute of Physics Publishing.

[9] Foucher, D., Flamand, L. and Berthe, D., 1981, "Running-in of lubricated Hertzian contacts," *The Running-In Process in Tribology, Proceedings of the 8th Leeds-Lyon Symposium on Tribology,* edited by Dowson, Taylor, Godet and Berthe, Butterworths, London, pp. 58 – 61.

[10] Prujanski, L.Y., 1979, "A study of surface wearing ability in relations to some technological factors: II. Effect of the method of surface finishing and running-in," *Wear* **54**, pp. 355 – 369.

[11] Lugt, P.M., Severt, R.W.M., Fogelström, J. and Tripp, J.H., 2001, "Influence of surface topography on friction, film breakdown and running-in in the mixed lubrication regime," *Proceedings of the Institution of Mechanical Engineers part J Journal of Engineering Tribology* **215**, pp. 519 – 533.

[12] Jeng, Y.R., 1996, "Impact of plateaued surfaces on tribological performance," *Tribology Transaction* **39**, pp. 354 – 361.

[13] Visscher, M., Dowson, D. and Taylor, C.M., 1998, "The profile development of a twin-land oil-control ring during running-in," *ASME-Journal of Tribology* **120**, pp. 616 – 621.

[14] Jeng, Y.R., 1990, "Experimental study of the effects of surface roughness on friction," *Tribology Transactions* **33**, pp. 402 – 410.

[15] Horng, J.H., Lin, J.F. and Lee, K.Y., 1994, "The effect of surface irregularities on tribological behavior of steel rollers under rolling-sliding contact," *ASME-Journal of Tribology* **116**, pp. 209 – 218.

[16] Katoh, J., Satoh, T., Kamikubo, F. and Mizuhara, K., 2001, "Analysis of running-in process under lubricated conditions using combined time-space plot and three-dimensional bearing curves," *Tribology Transaction* **44**, pp. 104 – 110.

[17] Prakash, J. and Czichos, H., 1983, "Influence of surface roughness and its orientation on partial elastohydrodynamic lubrication of rollers," *ASME-Journal of Tribology* **105**, pp. 591 – 597.

[18] Jeng, Y.R. and Hamrock, B.J., 1987, "The effect of surface roughness on elastohydrodynamically lubricated point contact," *ASLE Transactions* **30**, pp. 531 – 538.

[19] Wu, C. and Zheng, L., 1991, "Effects of waviness and roughness on lubricated wear related to running-in," *Wear* **147**, pp. 323 – 334.

[20] Pawlus, P., 1994, "A study on the functional properties of honed cylinders surface during running-in," *Wear* **176**, pp. 247 – 254.

[21] Pawlus, P., 1997, "Change of cylinder surface topography in the initial stage of engine life," *Wear* **209**, pp. 69 – 83.

[22] Wang, W., Wong, P.L. and Zhang, Z., 2000, "Experimental study of the real time in surface roughness during running-in for PEHL contacts," *Wear* **244**, pp. 140 – 146.

[23] Wang, W., Wong, P.L., Luo, J.B. and Zhang, Z., 1998, "A new optical technique for roughness measurement on moving surface," *Tribology International* **31**, pp. 281 – 287.

[24] Kragelsky, I.V., Dobychun, M.N. and Kombalov, V.S, 1982, "Running-in and equilibrium roughness," *Friction and Wear Calculation Methods,* Pergamon Press, Oxford, pp. 297 – 316.

[25] Booser, E.R., 1983, *Handbook of Lubrication*, CRC Press, Boca Raton.

[26] Zhou, R.S. and Hashimoto, F., 1995, "A new rolling contact surface and "no run-in" performance bearings," *ASME-Journal of Tribology* **117**, pp. 166 – 170.

[27] Kelly, D.A. and Critchlow, G.W., 1992, "Running-in and the enhancement of scuffing resistance," *Proceedings of the Institution of Mechanical Engineers* **C206**, pp. 425 – 429.

[28] Cavatorta, M.P. and Cusano, C., 2000a, "Running-in of aluminimum/steel contacts under starved lubrication, part I: Surface modifications," *Wear* **242**, pp. 123 – 132.

[29] Cavatorta, M.P. and Cusano, C., 2000b, "Running-in of aluminimum/steel contacts under starved lubrication, part II: Effects on scuffing," *Wear* **242**, pp. 133 – 139.

[30] King, T.G. and Stout, K.J, 1981, "Surface finish and running-in effects on friction in lubricated sliding," *The Running-In Process in Tribology, Proceedings of the 8th Leeds-Lyon Symposium on Tribology,* edited by Dowson, Taylor, Godet and Berthe, Butterworths, London, pp. 103 – 110.

[31] Schipper, D.J., Vroegop, P.H. and de Gee, A.W.J., 1994, "Influence of the reciprocating sliding on the running-in of lubricated concentrated contacts," *Proceeding of the 4th International Tribology Conference, Austrib '94 Vol.* **1**, pp. 219 – 226.

[32] Braithwaite, E.R., Greene, A.B. and Train, B.M., 1999, "The influence of MoS_2 on the mechanism of piston-ring wear during the running-in process," *Industrial Lubrication and Tribology* **51**, 6, pp. 274 – 286.

[33] Maki, J. and Aho, K., 1981, "Development of a running-in procedure for a locomotive diesel engine," *The Running-In Process in Tribology, Proceedings of the 8th Leeds-Lyon Symposium on Tribology,* edited by Dowson, Taylor, Godet and Berthe, Butterworths, London, pp. 147 – 152.

[34] Mukarami, T., Sakai, T., Yamamoto, Y. and Hirano, F., 1981, "Tribochemical aspects of the running-in processes in four-ball testing," *The Running-In Process in Tribology, Proceedings of the 8th Leeds-Lyon Symposium on Tribology,* edited by Dowson, Taylor, Godet and Berthe, Butterworths, London, pp. 210 – 220.

[35] Khurshudov, A.G., Drozdov, Y.N. and Kato, K., 1995, "Transitional phenomena in the lubricated heavily loaded sliding contact of ceramics and steel," *Wear* **184**, pp. 179 – 186.

[36] Blau, P.J., 1981, "Interpretations of the friction and wear break-in behaviour of metal in sliding contact," *Wear* **71**, pp. 29 – 43.

[37] Blau, P.J., 1987, "A model for run-in and other transitions in sliding friction," *ASME-Journal of Tribology* **109**, pp. 537 – 544.

[38] Blau, P.J., 1996, "Running-in and other friction transitions," *Friction Sciences and Technology,* Marcel Dekker, New York, pp. 251 - 283.

[39] Kapoor, A. and Williams, J.A., 1994, "Shakedown limits in sliding contacts on a surface-hardened half-space," *Wear* **172**, pp. 197 – 206.

[40] Kapoor, A. and Johnson, K.L., 1992, "Effect of changes in contact geometry on shakedown of surfaces in rolling/sliding contact," *Int. Journal of Mech. Sci*. **34**, pp. 223 – 239.

[41] Melan, E., 1938, "Der Spannungszustand eines "Henky-Mises'schen" Kontinuums bei veranderlicher Belastung," *Sitzungsberichte der Akademie der Wissenschaften Wien, Ser. 2A,* **147**, pp. 73 – 87.

[42] Kapoor, A. and Johnson, K.L., 1992, "Steady state topography in repeated boundary lubricated sliding," *Proceedings 19th Leeds-Lyon Symposium on Tribology, Leeds*, Elsevier, Amsterdam. pp. 81 – 90.

[43] Johnson, K.L. and Shercliff, H.R., 1992, "Shakedown of 2-D asperities in sliding contact," *Int. Journal of Mech. Sci*. **34**, pp. 375 – 394.

[44] Williamson, J.B.P., Pullen, J. and Hunt, R.T., 1969, "The shape of solid surfaces," in Ling, F. (ed.), *Surface Mechanics*, ASME, New York.

[45] Kapoor, A., Williams, J.A. and Johnson, K.L., 1994, "The steady state sliding of rough surfaces," *Wear* **175**, pp. 81 – 92.

[46] King, T.G., Watson, W. and Stout, K.J., 1978, "Modelling the micro-geometry of lubricated wear," *Proc. 4th Leeds-Lyon Symp.,* MEP, London, pp. 333 – 343.

[47] Masouros, G., Dimarogonas, A. and Lefas, K., 1977, "A model for wear and roughness transients during the running-in of bearings," *Wear* **45**, pp. 375 – 382.

[48] Kumar, R., Prakash, B. and Sethuramiah, A., 2002, "A systematic methodology to characterize the running-in and steady-state processes," *Wear* **252**, pp. 445 – 453.

[49] Lin, J.Y. and Cheng, H.S., 1989, "An analytical model for dynamic wear," *ASME-Journal of Tribology* **111**, pp. 468 – 474.

[50] Hu, Y.Z., Li, N. and Tonder, K., 1991, "A dynamic system model for lubricated sliding wear and running-in," *ASME-Journal of Tribology* **113**, pp. 499 – 505.

[51] Shirong, G. and Gouan, C., 1999, "Fractal prediction models of sliding wear during the running-in process," *Wear* **231**, pp. 249 – 255.

[52] Liang, X., Kaiyuan, J., Yongqing, J. and Darong, C., 1993, "Variations in contact stress distribution of real rough surfaces during running-in," *ASME-Journal of Tribology* **115**, pp. 602 – 606.

[53] Liu, Z., Neville, A. and Reuben, R.L., 2001, "Analyzing elastic-plastic real rough surface contact in running-in," *Tribology Transactions* **44**, pp. 428 – 436.

[54] Kraghelsky, I.V. and Kombalov, V.S., 1969, "Calculation of value of stable roughness after running-in," *Wear* 1**4**, pp. 137 – 140.

[55] Jeng, Y.R., Lin, Z.W. and Shyu, S.H., 2004, "Changes of surface topography during running-in process," *ASME-Journal of Tribology* **126**, pp. 620 – 625.

[56] Sugimura, J., Kimura, Y. and Amino, K., 1987, "Analysis of the topography changes due to wear–Geometry of the running-in process," *JSLE* **31**(11), pp. 813 – 820.

[57] Johnson, N.L., 1949, "Systems of frequency curves generated by methods of translation," *Biometrika* **36**, pp. 149 – 176.

Chapter 3

Elastic-plastic single asperity contact

3.1. Introduction

When two engineering surfaces are pressed together there will always be some contact deformation. Depending on the scale considered, this contact deformation can be categorized as macro-contact or micro-contact. The contact between a heavily loaded roller and the inner and outer race ways in a rolling-element bearing, for example, can be analyzed as a macroscopic contact.

Most engineering surfaces are rough on micro-scale. High points or micro-protrusions, usually called asperities, exist on all engineering solid surfaces, see Fig. 3.1. In non-lubricated or boundary lubrication systems, when such surfaces are loaded against each other, the actual contact takes place at these asperities. The real contact area is the sum of the areas of the contacting asperities, therefore, the ratio between the real contact area and the apparent (nominal) contact area will be small. During the contact of two surfaces, contact will initially occur at a limited amount of asperities to support the normal load.

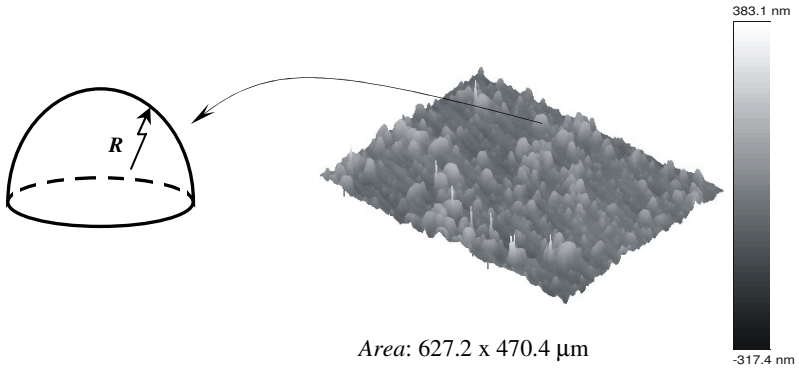

FIGURE 3.1: *Engineering surface and its asperities.*

The number of asperities in contact becomes larger as the normal load is increased. Deformation occurs in the region of contacts spots, establishing stresses which oppose the applied load. Depending on the load carried by the asperities and its mechanical properties, the asperities may deform elastic, elastic-plastic or fully plastic. The local stresses at the contact spots are much higher than the nominal stresses. Therefore local plastic deformation is usually found in the contact of two rough surfaces. The asperities on the solid bodies are sometimes considered to be spherically shaped with different sizes so that the contact of two surfaces can be reduced to the study of an array of spherical contacts deforming at their tips [1].

In the study of friction, wear and lubrication, knowledge about the deformation state of the surface asperities becomes very important. Understanding the relationship between local contact properties and surface topography can lead to the specification of optimized surface topography and manufacturing processes with respect to the functional task of the surface. Accurate modeling and study of the deformation behavior of contacting asperities are important on both micro and macro scale. Understanding the contact mechanics, the mechanism of friction, wear, lubrication, frictional heating and electrical contact resistance, et cetera rely upon the study of asperity contact. Furthermore, the elastic-plastic asperity contact model can be applied to predict the behavior of powder compaction [2]. In attempting to predict the deformation behavior of the contacting bodies, a developed elastic-plastic asperity based contact model is presented in this chapter. This developed asperity contact model can be applied to both macroscopic geometry and microscopic contacts. At first, overview of the elastic, fully plastic and elastic-plastic contact models published in literature are given in Section 3.2, Section 3.3 and Section 3.4, respectively. In order to verify the proposed models, an experimental investigation was done and it is presented in Section 3.5. In Section 3.6, a new developed elastic-plastic asperity contact model which incorporates the purely elastic, elastic-plastic and fully plastic regime is derived. The next section deals with the unloading contact of asperities, and finally concluding remarks are presented at the end of the chapter.

3.2 Elastic contact

Modeling the contact between surfaces based on the asperity approach was pioneered by Greenwood and Williamson (*GW* model) in 1966 [3]. The contact between a plane and a nominally flat surface covered with a large number of asperities, which, at least near their summits, are spherical, was considered. In their analysis the following assumptions were used:

1. The asperity distribution is isotropic.
2. All asperities are spherical near their summits.
3. Asperity summits have a uniform radius R, but their heights vary randomly.
4. The interactions among contacting asperities are neglected.
5. Only the asperities deform during the contact and there is no bulk deformation.

Analysis of the contact of two curved bodies can be reduced to the analysis of a single asperity contact with a rigid smooth flat as is schematically shown in Fig. 3.2. In this case, the interference ω is an important variable which measures the extent of asperity deformation. The contact variables, such as contact pressure and contact area of the asperity

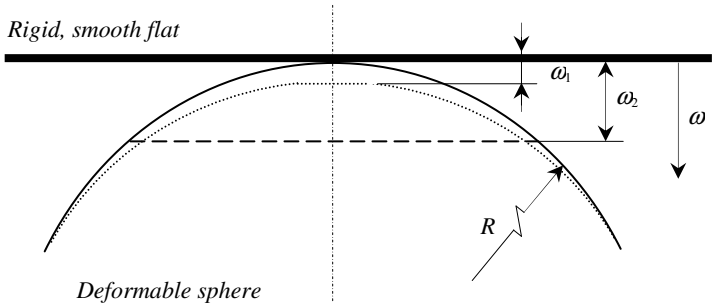

FIGURE 3.2: *Contact of a single asperity with a rigid smooth flat.*

will be derived in terms of this interference. Three modes of deformation: elastic, elastic-plastic and fully plastic will be introduced as ω increases.

When ω is sufficiently small or a low load is applied, the asperity deforms elastically. In this range the deformations involved are reversible: if the load between the contacting asperities is removed they return to their original shape. Analysis of elastic contact is according to Hertz [4] and such contact is referred to as Hertzian contact. Hertzian analysis is based on the following assumptions: (1) the surfaces are continuous, smooth and non-conforming; (2) the strains are small; (3) each solid can be considered as an elastic half-space in the proximity of the contact region; and (4) the surfaces are frictionless. For the elastic contact situation, the contact area A_e, the contact load P_e and the mean contact pressure p_e according to the Hertz theory are:

$$A_e = \pi R \omega \tag{3.1}$$

$$P_e = \frac{4E}{3} R^{0.5} \omega^{1.5} \tag{3.2}$$

$$p_e = \frac{4E}{3\pi}\left(\frac{\omega}{R}\right)^{0.5} \tag{3.3}$$

where the effective or composite curvature is:

$$\frac{1}{R} = \frac{1}{R_1} + \frac{1}{R_2} \tag{3.4}$$

and the effective modulus is:

$$\frac{1}{E} = \frac{1-\nu_1^{\,2}}{E_1} + \frac{1-\nu_2^{\,2}}{E_2} \tag{3.5}$$

The parameters R, E and v are the reduced radius, Young's modulus of elasticity and the Poisson's ratio, respectively; subscripts 1 and 2 denote the two bodies in contact.

It was shown by Tabor [5] that initial yield occurs when the maximum Hertz contact pressure reaches $p_m = 0.6H$, or, the average contact pressure $p_e = 0.4H$ where H is the hardness of the softer material in contact. For a more general representation Chang, Etsion and Bogy (*CEB* model) [6] correlate the maximum contact pressure at the point of initial yielding with the hardness by:

$$p_m = KH \tag{3.6}$$

where K is the maximum contact pressure factor. The maximum contact pressure is equal to $1.5p_e$ so that by substituting this relation and Eq. (3.6) into Eq. (3.3) yields the critical interference $\omega_{1\text{-}CEB}$ at the inception of plastic deformation:

$$\omega_{1-CEB} = \left(\frac{\pi KH}{2E}\right)^2 R \tag{3.7}$$

A similar approach was used by Zhao, Maietta and Chang (*ZMC* model) [7] to derive the critical interference based on the mean contact pressure instead of the maximum contact pressure. A constant k was introduced as the mean contact pressure factor. The critical interference $\omega_{1\text{-}ZMC}$ according to *ZMC* is:

$$\omega_{1-ZMC} = \left(\frac{2\pi kH}{4E}\right)^2 R \tag{3.8}$$

Kogut and Etsion (*KE* model) [8] used the K value from [9] (see Appendix A) and the critical interference $\omega_{1\text{-}KE}$ is defined by:

$$\omega_{1-KE} = \left(\frac{\pi K_{KE} H}{2E}\right)^2 R \tag{3.9}$$

where

$$K_{KE} = 0.454 + 0.41v \tag{3.10}$$

v and H are the Poisson's ratio and the hardness of the material which yields first respectively.

Recently, Jackson and Green (*JG* model) [10] derived the critical interference based on the von Mises criteria for stresses, $\omega_{1\text{-}JG}$, (see Appendix A) as:

$$\omega_{1-JG} = \left(\frac{\pi CY}{2E}\right)^2 R \tag{3.11}$$

where

$$C = 1.295\exp(0.736\nu) \tag{3.12}$$

and Y is the yield strength of the softer material.

3.3 Fully plastic contact

If the load of the contacting asperities is increased significantly, such that the deformations become irreversible, the contact operates in the fully plastic contact regime. The basic plastic contact model, which is known as the profilometric model or surface micro-geometry model, was introduced in 1933 by Abbott and Firestone (*AF* model) [11]. In this model the plastic contact area A_{AF} of a rough surface against a rigid smooth flat is assumed to be equal to the intersection of the flat with the original undeformed profile of the asperity:

$$A_{AF} = 2\pi R\omega \tag{3.13}$$

The mean pressure over the contact area is the flow pressure or the indentation hardness H and remains constant so that the contact load P_{AF} is equal to the contact area multiplied by the mean contact pressure, or:

$$P_{AF} = 2\pi R\omega H \tag{3.14}$$

CEB [6] proposed an elastic-plastic micro-contact model on the basis of the volume conservation of plastically deformed asperities. The *CEB* model assumes that the mean contact pressure in the fully plastic contact regime is equal to KH instead of H as used in the *AF* model. Hence, the plastic contact area A_{CEB} according to the *CEB* model is:

$$A_{CEB} = \pi R\omega\left(2 - \frac{\omega_{1-CEB}}{\omega}\right) \tag{3.15}$$

and the plastic contact load P_{CEB} is:

$$P_{CEB} = \pi R\omega\left(2 - \frac{\omega_{1-CEB}}{\omega}\right)KH \tag{3.16}$$

Another fully plastic model has been presented recently by Jackson and Green [10]. Because this model incorporate expressions from elastic-plastic to fully plastic contact regime the exploration of this model will be discussed further in the next section.

3.4 Elastic-plastic contact

The elastic-plastic contact regime is defined as the regime in which, due to the contact loading conditions, the deformations of the contacting asperities stay in between the pure

elastic and fully plastic deformation mode. Analysis of Johnson [12] shows that for the indentation of a sphere on a plane, the contact load increases about 360 times from the point of initial yielding to the fully plastic regime, or $P/P_c \approx 360$ where P_c is the load at which initial yield occurs. Based on the analysis of plastic spherical indentation, Francis [13] found that the fully plastic regime starts when the contact area is about 113 times the contact area at which first yield occurs, or $A/A_c \approx 113$. These analyses suggest that the elastic-plastic or elastoplastic regime, the transition regime from the fully elastic to the fully plastic, is extensive and cannot be neglected. This is the shortcoming of the *CEB* model in which the elastic-plastic regime is neglected.

Zhao *et al.* [7] introduced the *ZMC* model and defined the second transition from the elastic-plastic to the fully plastic contact regime in terms of the contact interference ω, namely $\omega_{2\text{-}ZMC}$ which is defined by:

$$\omega_{2-ZMC} = 54\omega_{1-ZMC} \tag{3.17}$$

The mean contact pressure in the elastic-plastic regime was:

$$p_{ZMC} = H - H(1-k)\left[\frac{\ln(\omega_{2-ZMC}) - \ln(\omega)}{\ln(\omega_{2-ZMC}) - \ln(\omega_{1-ZMC})}\right] \tag{3.18}$$

where H is the hardness of the softer material, k is the hardness coefficient, $\omega_{1\text{-}ZMC}$ is the first transition as defined by Eq. (3.8) and $\omega_{2\text{-}ZMC}$ is the second transition as defined in Eq. (3.17). Based on the already-known formulation of the contact area in the elastic and fully plastic contact regime as was introduced by Hertz and the *AF* model, respectively, *ZMC* derived the contact area A_{ZMC} in the elastic-plastic regime. In order to smooth the contact area transition from Eq. (3.1) to Eq. (3.13) a cubic polynomial was used which lead to:

$$A_{ZMC} = \pi R\omega\left[1 - 2\left(\frac{\omega - \omega_{1-ZMC}}{\omega_{2-ZMC} - \omega_{1-ZMC}}\right)^3 + 3\left(\frac{\omega - \omega_{1-ZMC}}{\omega_{2-ZMC} - \omega_{1-ZMC}}\right)^2\right] \tag{3.19}$$

The elastic-plastic contact load P_{ZMC} is expressed simply by multiplication of the mean contact pressure and the contact area as:

$$P_{ZMC} = p_{ZMC}A_{ZMC} \tag{3.20}$$

Vu-Quoc *et al.* [14] studied the elastic-plastic contact of two identical spheres, which by symmetry is equivalent to that of one sphere in contact with a frictionless rigid plane by finite element method (FEM) calculations. However, their analysis is restricted to the contact situation where the mean contact pressure never exceeded 2.3 times the yield strength of the material. *KE* [8] employed similar FEM calculations covering from the elastic to the inception of the fully plastic contact regime of a sphere in contact with a rigid flat. In the *KE* model the second transition from the elastic-plastic to the fully plastic regime $\omega_{2\text{-}KE}$ was proposed as:

$$\omega_{2-KE} = 110\omega_{1-KE} \tag{3.21}$$

According to this model the mean contact pressure p_{KE} in the elastic-plastic regime is obtained by applying curve fitting from the FEM results and is expressed as follows:

$$\begin{aligned} \frac{p_{KE}}{Y} &= 1.19\left(\frac{\omega}{\omega_{1-KE}}\right)^{0.289} \qquad \text{for} \quad 1 \le \frac{\omega}{\omega_{1-KE}} \le 6 \\ \frac{p_{KE}}{Y} &= 1.61\left(\frac{\omega}{\omega_{1-KE}}\right)^{0.117} \qquad \text{for} \quad 6 \le \frac{\omega}{\omega_{1-KE}} \le 110 \end{aligned} \tag{3.22}$$

The dimensionless elastic-plastic contact area and contact load was derived empirically by using the same method, i.e. FEM calculations. Results are expressed in Eqs. (3.23) and (3.24) respectively:

$$\begin{aligned} \frac{A_{KE}}{A_{c-KE}} &= 0.93\left(\frac{\omega}{\omega_{1-KE}}\right)^{1.136} \qquad \text{for} \quad 1 \le \frac{\omega}{\omega_{1-KE}} \le 6 \\ \frac{A_{KE}}{A_{c-KE}} &= 0.94\left(\frac{\omega}{\omega_{1-KE}}\right)^{1.146} \qquad \text{for} \quad 6 \le \frac{\omega}{\omega_{1-KE}} \le 110 \end{aligned} \tag{3.23}$$

$$\begin{aligned} \frac{P_{KE}}{P_{c-KE}} &= 1.03\left(\frac{\omega}{\omega_{1-KE}}\right)^{1.425} \qquad \text{for} \quad 1 \le \frac{\omega}{\omega_{1-KE}} \le 6 \\ \frac{P_{KE}}{P_{c-KE}} &= 1.40\left(\frac{\omega}{\omega_{1-KE}}\right)^{1.263} \qquad \text{for} \quad 6 \le \frac{\omega}{\omega_{1-KE}} \le 110 \end{aligned} \tag{3.24}$$

where $A_{c\text{-}KE}$ is the contact area according to Eq. (3.1) and $P_{c\text{-}KE}$ is the corresponding contact load, Eq. (3.2), at $\omega = \omega_{1\text{-}KE}$. The KE model is not restricted to specific material or geometry and applicable as a general solution.

Jackson and Green [10] also used FEM calculations to study the elastic-plastic contact of a hemispherical body against a rigid flat. Interestingly, a continuous fitting function was found to capture the whole way from the purely elastic to the fully plastic conditions, whereas in the *KE* model there are discontinuities. In contradiction to the *KE* model, the *JG* model accounts for the geometry and material effects. It was stated that the most notable effect is that the predicted hardness is not a material constant as suggested by Tabor [5]; the hardness changes with the evolving contact geometry and the material properties. The analysis of the *JG* model surpasses the *KE* model deeply into the fully

plastic regime and is valid until a/R = 0.412, where a is the contact radius and R is the undeformed radius of the sphere. Regarding to tribological applications this range is acceptable. The contact area and contact load from the pure elastic to the fully plastic contact state are formulated empirically in the *JG* model. The contact area, A_{JG}, is defined by:

$$\begin{aligned} \frac{A_{JG}}{A_{c-JG}} &= \frac{\omega}{\omega_{1-JG}} && \text{for} \quad 1 \le \frac{\omega}{\omega_{1-JG}} \le 1.9 \\ \frac{A_{JG}}{A_{c-JG}} &= \frac{\omega}{\omega_{1-JG}} \left(\frac{\omega}{1.9\omega_{1-JG}} \right)^{B} && \text{for} \quad \frac{\omega}{\omega_{1-JG}} \ge 1.9 \end{aligned} \tag{3.25}$$

with

$$B = 0.14 \exp\left(\frac{23Y}{E} \right) \tag{3.26}$$

In Eq. (3.25) $A_{c\text{-}JG}$ is the critical contact area according to Eq. (3.1) at $\omega = \omega_{1\text{-}JG}$ where $\omega_{1\text{-}JG}$ is the critical interference as was defined in Eq. (3.11). The contact load is defined by:

$$\begin{aligned} \frac{P_{JG}}{P_{c-JG}} &= \left(\frac{\omega}{\omega_{1-JG}} \right)^{1.5} && \text{for } 1 \le \frac{\omega}{\omega_{1-JG}} \le 1.9 \\ \frac{P_{JG}}{P_{c-JG}} &= \left\{ \exp\left[-0.25 \left(\frac{\omega}{\omega_{1-JG}} \right)^{5/12} \right] \right\} \left(\frac{\omega}{\omega_{1-JG}} \right)^{1.5} \\ &\quad + \frac{4H_G}{CY} \left\{ 1 - \exp\left[-\frac{1}{25} \left(\frac{\omega}{\omega_{1-JG}} \right)^{5/9} \right] \right\} \left(\frac{\omega}{\omega_{1-JG}} \right) && \text{for} \quad \frac{\omega}{\omega_{1-JG}} \ge 1.9 \end{aligned} \tag{3.27}$$

where

$$\frac{H_G}{Y} = 2.84 \left\{ 1 - \exp\left[-0.82 \left(\frac{\pi CY}{2E} \sqrt{\frac{\omega}{\omega_{1-JG}}} \left(\frac{\omega}{1.9\omega_{1-JG}} \right)^{B/2} \right)^{-0.7} \right] \right\} \tag{3.28}$$

and the other parameters were defined as was discussed earlier.

Summarizing, there are three regimes of deformation in the contact between asperities, namely, pure elastic, fully plastic and elastoplastic or elastic-plastic. The analysis

of Hertz [4] is well adopted and widely used by many researchers for the elastic contact case. However, the analysis of the fully plastic as well as the elastic-plastic regime is still in progress. Many investigations have been devoted to predict their behavior and most of them are theoretically based. In order to verify the proposed models as were mentioned previously, experimental investigation is needed. The behavior of the mean contact pressure, the contact area and the contact load will be explored experimentally in the next section. The mean contact pressure is determined simply by dividing the contact load by the contact area. Some models have expressed the mean contact pressure explicitly, however, in the *KE* model there is a difference between the mean contact pressure equation, Eq. (3.22), and the contact load, Eq. (3.24), divided by contact area, Eq. (3.23), as can be seen in Fig. 3.3. In the following contact analyses the latter is used.

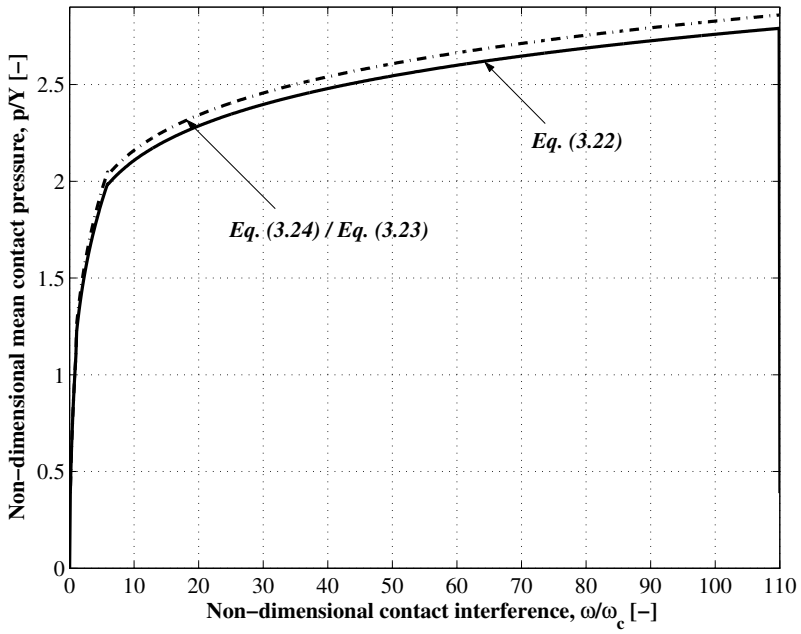

FIGURE 3.3: *The difference in mean contact pressure of the KE model.*

3.5 Experiment

3.5.1 Fully plastic contact experiment

Experiments were performed on a pin-on-disk machine. A photographical impression of the pin-on-disk machine can be seen in Appendix D. The flat specimen (SiC ceramic) was firmly mounted on a disk and was held statically to apply simple normal loading. The pin of the tester was replaced by a sphere specimen holder. The holder was made from steel and

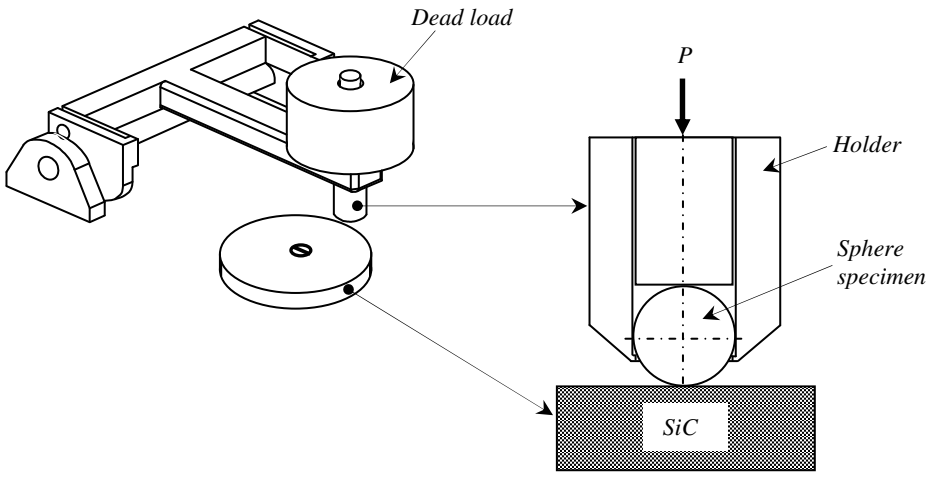

FIGURE 3.4: *Setup of the asperity normal indentation.*

was designed in such a way that the hemispherical form is maintained as shown in Fig. 3.4. The maximal load which could be applied to this setup was 600 N.

3.5.1.1 Specimens

Copper spheres (H = 1.2 GPa, E = 120 GPa and ν = 0.35) with a diameter of 3 mm were used as specimens to perform the experiments. The hard flat specimen used was a SiC ceramic (H = 28 GPa, E = 430 GPa and ν = 0.17). The copper specimens were as-received without annealing and having a center line average roughness R_a of about 0.15 μm. The average roughness of the flat specimen was 0.09 μm.

Most of the proposed asperity contact models assume an elastic perfectly plastic (no-strain hardening) material behaviour, therefore the same material properties were used in this experiment. To be sure that there is no strain hardening effect of the copper spheres used, hardness measurements were done before and after a compression test. The Vicker's hardness before compression was 1.15 GPa and after compression at a/R = 0.3 was 1.2 GPa where a is the contact radius and R is the initial radius of the Copper sphere. This shows that the specimens used did not show a strain hardening effect.

In order to get more accurate results experiments were also performed with another material. Aluminium spheres (H = 0.28 GPa, E = 75.2 GPa, ν = 0.345) with a diameter of 6 mm were used and the hard flat specimen used was SiC. The results of the aluminium experiments, see Appendix B, are similar to the results of the copper specimens, therefore in the following section the analysis is done for copper only.

3.5.1.2 Matching and stitching

In most situations it is not possible to get an accurate or detailed image of a complete cross section of the contact area. For an accurate image of the cross section a high lateral

resolution is needed and as a result only small areas can be measured. A new measuring technique has been developed to overcome this problem (see Appendix C).

The developed contact area from the plastic compression of the sphere is wider than one single measurement of the optical profiler. Therefore, a matching and stitching procedure is needed to get the measurement results more precisely.

3.5.1.3 Experimental details

Before doing any tests, the spherical and flat specimens were cleaned with acetone and dried in air. To reduce the effect of friction, the contact region was lubricated. The load was applied to the sphere specimen for 30 seconds and then removed. Prior to measuring the fully plastic contact area, again the sphere was cleaned and dried.

An optical interference microscope was used to measure the plastic contact area. In this step the matching and stitching procedure was employed. A special holder, by which one is able to rotate and translate the sphere specimen, was designed to make the matching and stitching procedure easier. After taking all the images, the matching and stitching calculation was done separately by a personal computer. It must be noted that to be able to compare the change of the sphere accurately before and after loading, this measurement procedure has to be conducted for the undeformed sphere as well.

3.5.1.4 Experimental results

As mentioned previously, to obtain results of a single experiment, several steps must be followed. Eleven copper sphere specimens were used to perform the tests. Figure 3.5 shows a typical matching and stitching result of the plastic deformation of a sphere after compression. Five images have been matched and stitched to cover the total track along the diameter of the plastic contact area at P = 490 N. According to the *JG* model, the dimensionless normal load in this case was $P/P_{c\text{-}JG}$ = 1923, so far into the fully plastic regime. As can be seen in Fig. 3.5(a), the matching and stitching of the images results into an almost straight total image (no zig-zag but in line images) which implies that the translation and rotation specimen holder table works very well. Missing data points were found in the images at the start and at the end of the contact region. This is caused by bad reflection of the surfaces as can be seen more clearly in the profile plot in Fig. 3.5(b). At the edge of the contact, the sudden change of the geometry results in a high slope.

The experimental results of the plastic contact area as a function of the contact interference, along with the theoretical model predictions of *AF*, *CEB* and *JG*, are presented in Fig. 3.6. Here, the plastic contact area was measured by measuring the contact radius from the plastic deformation trace as shown in Fig. 3.5(b). To determine the plastic interference, the maximum difference between the 'before' and 'after' compression profile was measured. Based on the deformed profile the undeformed (before) profile was calculated by the already-known sphere radius and two points in the profile references, namely the first and the end images. As can be seen, the experimental results agree well to the *AF* and *CEB* model. According to Eq. (3.15) for a very small $\omega_{c\text{-}CEB}/\omega$ (very high load) the *AF* and *CEB* model almost coincide. The measured plastic contact area is almost equal to $2\pi R\omega$ as predicted by the *AF* model. The experimental results (the dashed line represents

the best fit of the experimental data) show a slightly higher contact area as a function of the interference than predicted by the *AF* model. This difference is caused by the measurement method as described before. The plastic deformation is not as perfect as a truncation by a rigid flat, but there is a slight crown at the centre of the contact, as can be observed in Fig. 3.5(b). The same phenomena have also been shown by the work of Johnson [15]. The crown is symmetrical around the centre indicating that the pressure distribution was also symmetrical. The *JG* model predicts a smaller contact area than that of the *AF* and the *CEB* model for low values of the interference (low loads) and the contact area increases more gradually as the interference (load) increases compared to the *AF* and the *CEB* model. The deviation of the *JG* model to the *AF* and the *CEB* model is larger for high loads.

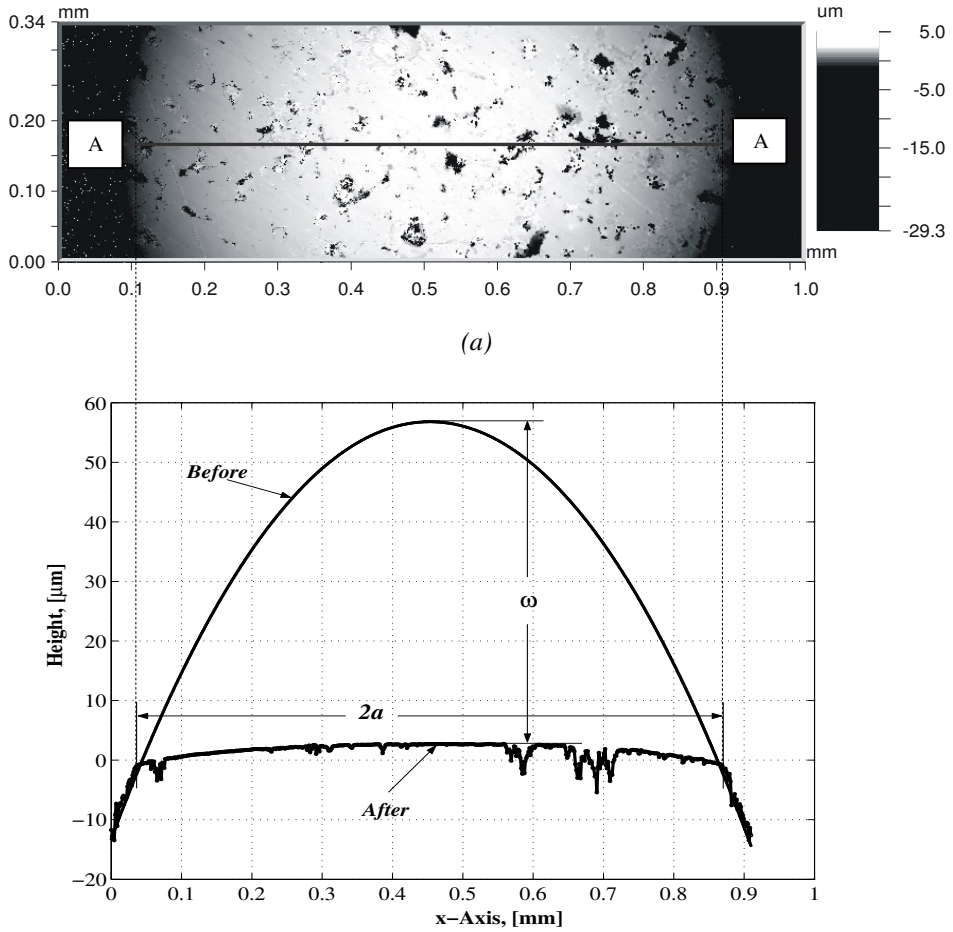

FIGURE 3.5: *Plastic deformed copper sphere, R = 1.5 mm and P = 490 N. Deformed track along the diameter after matching and stitching of 5 images (a) and its A-A profile (b).*

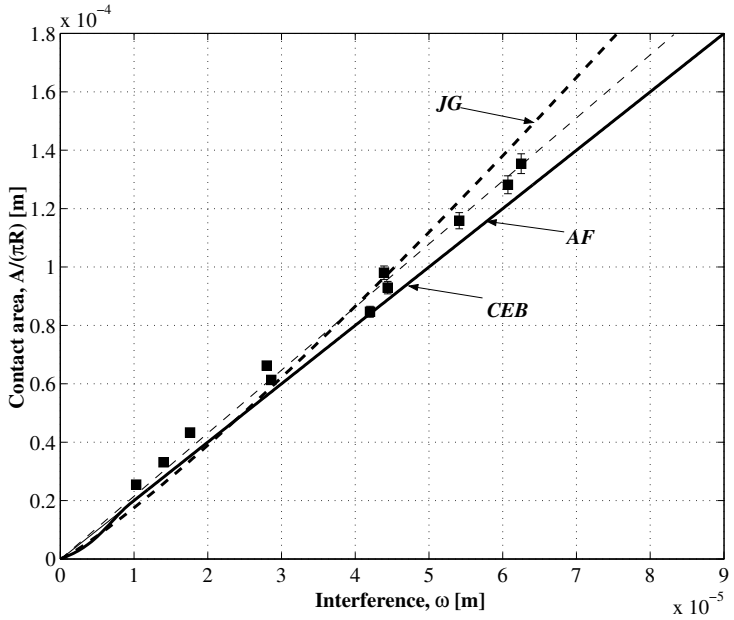

FIGURE 3.6: *Plastic contact area vs interference.* ■ *experimental data.*

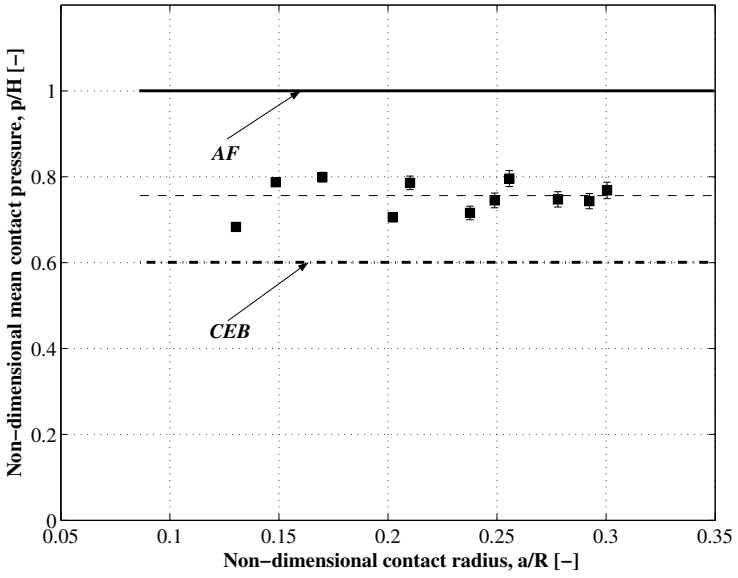

FIGURE 3.7: *Non-dimensional mean contact pressure plotted against the non-dimensional contact radius a/R.* ■ *experimental data.*

The behavior of the mean contact pressure as a function of the non-dimensional plastic contact radius is plotted in Fig. 3.7. It shows that for all the loading cases the mean contact pressure remains constant at a value of about 0.75*H*. The present observations can be compared to previously published work. The work of Johnson [15] for instance, studied the deformation of the contact between two equal work-hardened copper spheres (radius 63.5 mm). Results showed that the mean contact pressure in the fully plastic regime is constant for about 0.79*H*. The experimental results of Chaudhri [16] showed a constant value of the mean contact pressure for about 0.68*H* in the fully plastic regime in the case of the indentation of a copper sphere (radius 1.5 mm) against a hard sapphire flat. The comparison between these investigations [15, 16] and the proposed models can be seen in detail in Appendix B. These measurements compare very well with those made in the present research of this thesis.

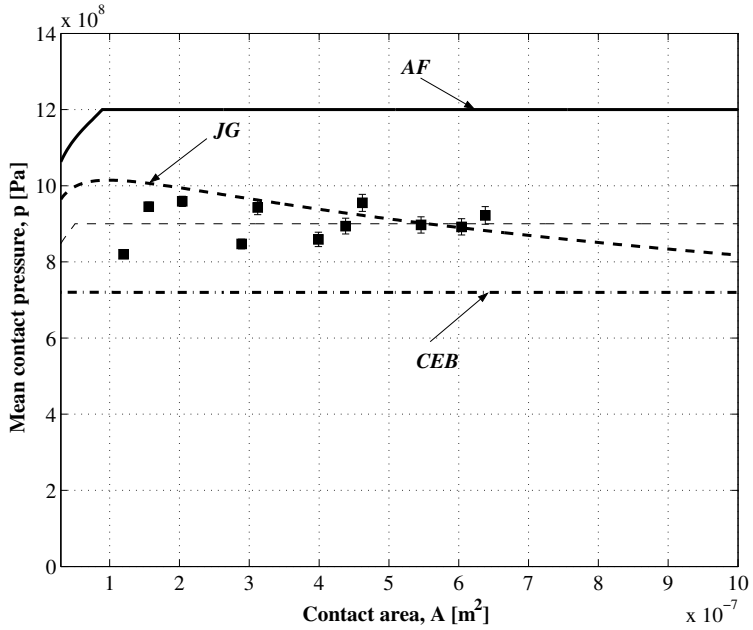

FIGURE 3.8: *Mean contact pressure vs contact area.* ■ *experimental data.*

The non-dimensional mean contact pressures of the present experimental results, however, are in between the values predicted by the *AF* model and the *CEB* model. A more quantitative comparison between the experimental and predicted mean contact pressure as a function of the contact area of the available models based on the experimental conditions as used in the present experiment is presented in Fig. 3.8. As can be seen, the theoretical model of *JG* predicts a higher mean contact pressure for the lower contact area (lower load) and underestimates the mean contact pressure for the higher contact area (higher load) region. The present experiment shows an almost constant mean contact pressure for the whole measured contact area. According to Tabor [5], as a first approximation, the fully

plastic yielding of the indentation of a hard sphere against a deformable half-space occurs when the mean contact pressure p

$$p = cY = c_h H \tag{3.29}$$

where c is nearly a constant and has a value of about 3 and c_h is a hardness constant. If it is assumed that the hardness is equal to 3 times the yield strength Y then c_h has a value of about 1. Interestingly, the *AF* model predicts fairly well the experimental results when the

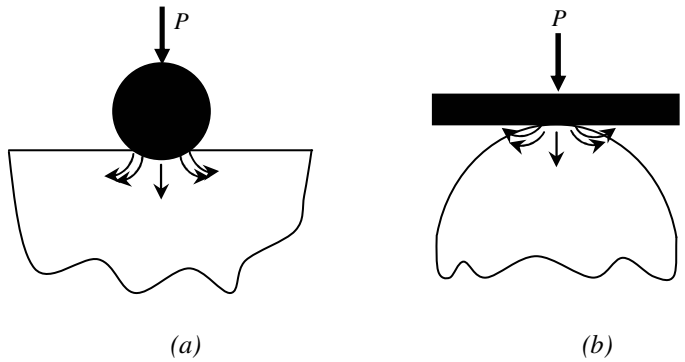

FIGURE 3.9: *Behavior of a hard sphere indenting a deformable half-space (a) and a hard flat indenting a deformable sphere (b).*

mean contact pressure is equal to $0.75H$ (shown by the dashed line) or the c_h value of Eq. (3.29) is 0.75. This contradicts the most widely used value for the fully plastic contact regime i.e. the mean contact pressure is simply equal to its hardness value or $c_h = 1$. Indentation experiments by Tabor [5] for instance, used a hard spherical indenter against a deformable half-space but in the present experiment a deformable sphere is indented by a hard flat. Intuitively, for a very high load these two cases will pronounce a different behavior with respect to the deformation as schematically shown in Fig. 3.9. In the first case the displaced material in the indented half-space is confined by the elastic bulk of the half-space and the hard spherical indenter. This situation will produce a higher mean contact pressure so increases the coefficient value c_h in Eq. (3.29). But in the second case the displaced material of the deformable sphere is free to expand radially in the edge of the contact and the contact radius increases as the load increases.

Figure 3.10 presents the results of the contact area as a function of the normal contact load. Again, the present experimental results lie along the straight line for $p = 0.75H$ (dashed line) of the *AF* model. The *CEB* model overestimates the contact area as a function of the contact load which contradicts to Fig. 3.6 when it is plotted as a function of the contact interference. This is caused by the mean contact pressure predicted by the *CEB* model which is lower than the actual one. The same phenomenon also occurs with the *AF* model where the mean contact pressure is predicted to be higher. Depending on the material properties, the *JG* model predicts the contact area as a function of the load differently.

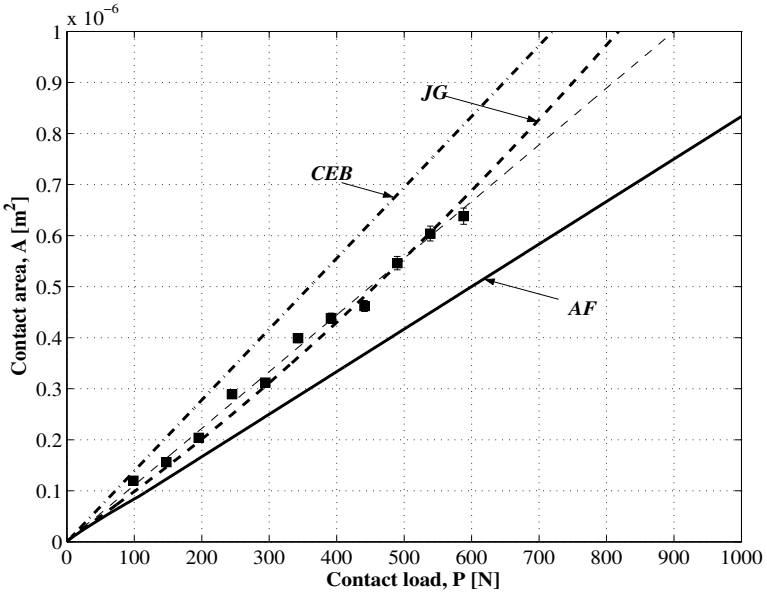

FIGURE 3.10: *Contact area as a function of normal load.*
■ *experimental data.*

However, the *JG* model tends to overestimate the contact area as the load increases. The difference will be more pronounced for higher loads. This overestimation is caused by the decrease of the mean contact pressure as predicted by the model.

3.5.2 Elastic-plastic contact experiment

In this section the experimental elastic-plastic contact data of Tabor [5] and Chaudhri [17] is used. Tabor's experiment was performed by indenting a work-hardened mild steel (Y = 0.75 GPa, E = 200 GPa and v = 0.33) by a hard spherical indenter of 10 mm diameter. The indentation experiment of Chaudhri used phosphor-bronze (H = 2.72 GPa, E = 115 GPa and v = 0.35) and brass (H = 1.8 GPa, E = 115 GPa and v = 0.35) spheres of 3.175 mm diameter and a sapphire (H = 190 GPa, E = 430 GPa and v = 0.26) plate. In Chaudhri's experiment, the contact area was measured directly. The sphere was compressed between a load cell and a transparent sapphire plate so that the contact area could be measured directly by a microscope [18]. A schematic diagram of this method can be seen in Appendix B.

Figure 3.11 shows the indentation pressure under elastic, elastic-plastic and fully plastic conditions which is correlated on a non-dimensional plot of p/H as a function of Ea/HR where p, H, E, a and R are the variables as was mentioned previously. With a hard spherical indenter of Tabor, the mean contact pressure starts to deviate from the elastic curve (Hertz) at a value of $p \approx 0.4H$ at $Ea/HR \approx 0.92$ and gradually rises until it reaches the value of about H at $Ea/HR \approx 14.3$. The plastic compression of deformable brass sphere by a hard flat of Chaudhri [17], shows the same phenomena as the data fit to the experimental data of Tabor. However, for the case of a phosphor-bronze sphere indented by a hard flat,

different results are shown. Up to the first yield points ($Ea/HR \approx 0.92$) the mean contact pressure stays the same, but as the load increases, the data starts to deviate from Tabor's results. Different from Tabor's results the maximum contact pressure which is reached in this test is about $0.79H$.

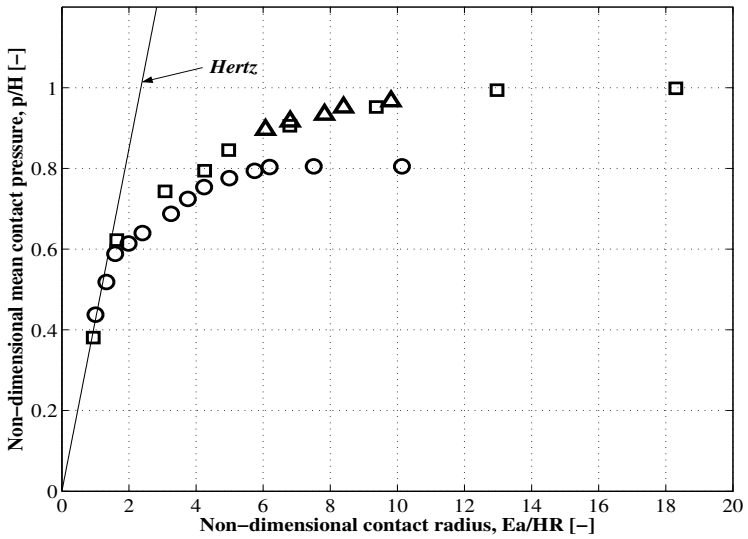

FIGURE 3.11: *Non-dimensional mean contact pressure vs non-dimensional contact radius. Experiments: □ steel, Tabor* [5]*; ○ phosphor-bronze and Δ brass, Chaudhri* [17].

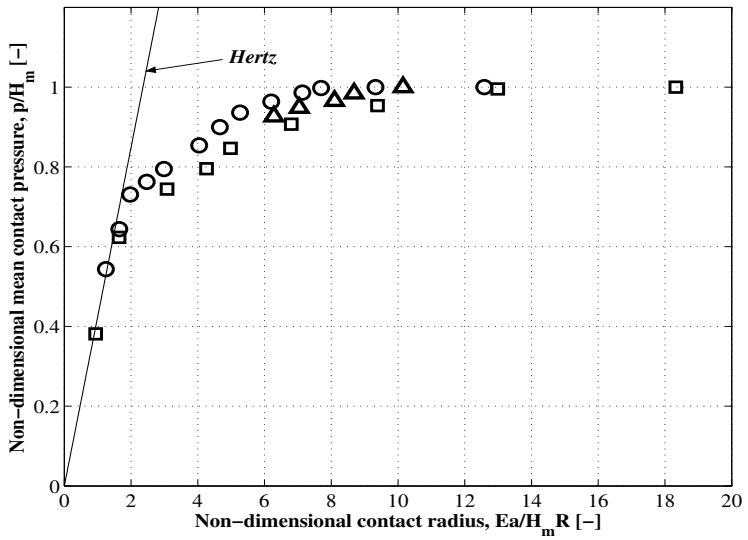

FIGURE 3.12: *Non-dimensional mean contact pressure vs non-dimensional contact radius. Symbols have the same meaning as in Figure* 3.11.

Interestingly, when the measured mean contact pressure H_m ($p = H_m$) value in the fully plastic regime is used for the non-dimensional value, instead of the hardness H, all the experimental data spreads closely in one line as is shown in Fig. 3.12. This suggests that the maximum contact pressure which can be reached for a deformable sphere against a hard flat is material dependent. Based on this, in the analysis of the elastic-plastic contact the maximum mean contact pressure will be used instead of the hardness which is most frequently used by the proposed elastic-plastic asperity contact models.

Comparison of the proposed elastic-plastic contact models with the experimental data of Phosphor-bronze of Chaudhri [17] is presented in Fig. 3.13 and 3.14. From Fig. 3.13 it can be seen that the *ZMC* model predicts the mean contact pressure as a function of the contact area best among the other models. The *KE* model predicts p/H_m value better in the beginning of the elastic-regime but as the plasticity is more involved, the model starts to deviate from the experimental results. Since the *JG* model is based on the yield stress Y and the yield stress of the phosphor-bronze is not provided, an assumption is made. The yield stress of $H_m/2.8$ and $H_m/3$ are assumed. For the both assumed yield stress values, the *JG* model largely underestimates the mean contact pressure as a function of the contact area. The deviation from the experimental data becomes larger as the contact area increases. In addition, the effect of the assumed yield stress is very significant in predicting the mean contact pressure as can be seen from Fig. 3.13.

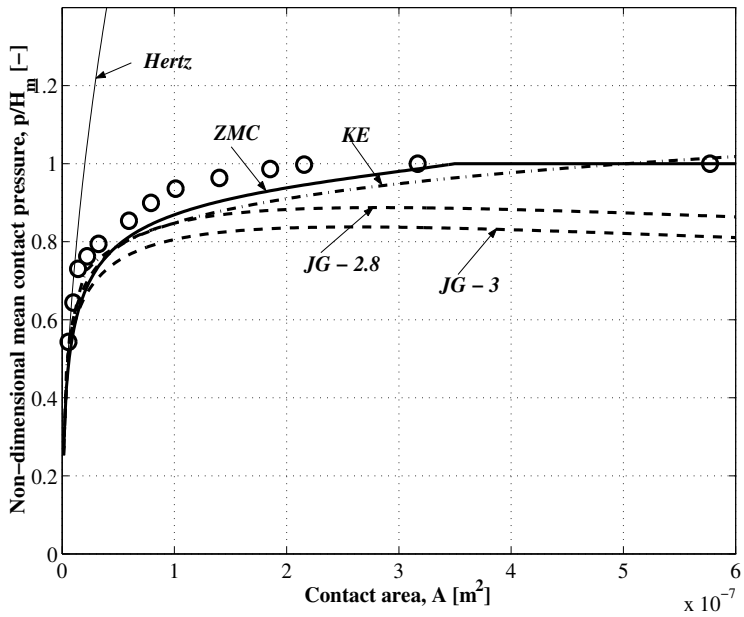

FIGURE 3.13: *Non-dimensional mean contact pressure as a function of contact area.* ○ *experimental data of phosphor-bronze, Chaudhri* [17].

The experimental data reaches its maximum for the contact pressure quickly as the contact area increases. Analysis of these data suggests that the *ZMC* model can predict the

mean contact pressure better when the criteria of the onset of fully plasticity $\omega_{2\text{-}ZMC}$ as defined in Eq. (3.17) is set lower. The criteria used by the *ZMC* model in determining $\omega_{2\text{-}ZMC}$ are based on the experimental data analysis of Johnson [12] where a deformable half-space is indented by a hard sphere.

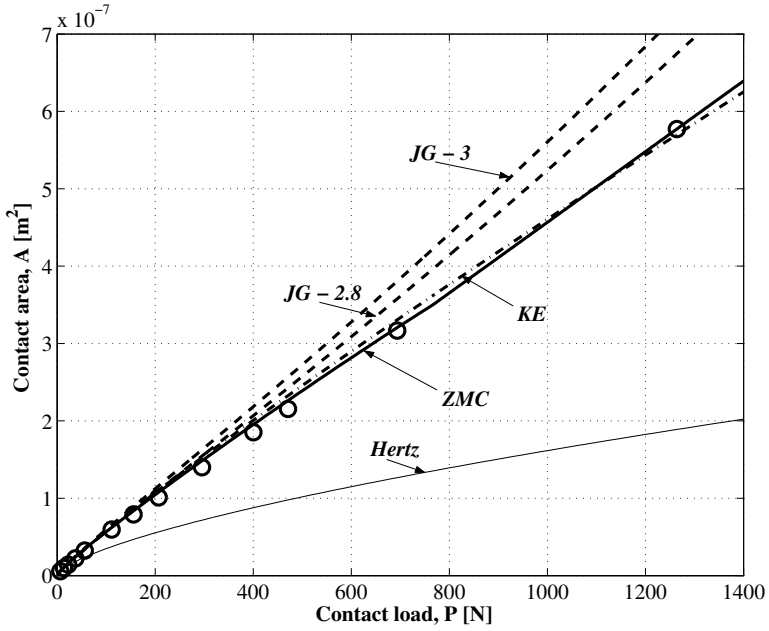

FIGURE 3.14: C*ontact area as a function of contact load. ○ experimental data of phosphor-bronze, Chaudhri* [17].

Figure 3.14 presents the calculated contact area from the proposed models as a function of the contact load. In this graph the difference of the model prediction is not clear for loads below 200 N. For loads higher than this value the difference is more pronounced and it can be seen that the *ZMC* model can predict very well. As it is expected the Hertz analysis dramatically underestimates the contact area as the load increases because the analysis is elastic. The *KE* model predicts a higher contact area than the experimental data for loads below about 1100 N but predicts a lower contact area for loads higher than this value. For the assumed yield stress values, the *JG* model overestimates the contact area for all loading cases.

Another comparison of experimental data of brass by Chaudhri [17] and steel by Tabor [5] with the proposed modification on the elastic-plastic contact model, Eq. (3.29), can be seen in Appendix B. In Appendix B, the yield stress is assumed to be $H_m/2.8$ for the *JG* model.

As a summary, by modifying the mean contact pressure at the fully plastic contact regime as formulated in Eq. (3.29) the *ZMC* approach in the elastic-plastic contact regime and the *AF* approach in the fully plastic contact regime predict best among the other

models. Based on these analyses a new elastic-plastic contact model will be developed in the next section.

3.6 A new developed elastic-plastic asperity contact model

The surface textures of most of the engineering surfaces are oriented with the direction of the relative motion of cutting tools to the workpieces. Different processing methods will produce different asperity radii of curvature, and therefore different ellipticity ratios of the micro-contacts are formed. The profile of the asperities generally contains various curvatures for various directions. In accordance to these facts, several models have been proposed to extend the isotropic asperity contact model into an anisotropic asperity contact model. Horng [19], for instance, extended the *CEB* model and Jeng and Wang [20] extended the *ZMC* model for the elliptical contact situation.

Even though the results of McCool [21] showed that for anisotropy rough surfaces with a random distribution of asperity radii differ negligibly from those of the isotropic one, for the deterministic contact situation the ellipticity of the contact cannot be simplified, especially when studying the change of the micro-geometry. In this thesis the micro-geometric change of the surface after unloading is the main topic. Therefore, the elliptical contact situation will be considered for the analysis.

3.6.1 Elliptic elastic contact

Figure 3.15 shows the general situation of the contact between two elastic bodies.

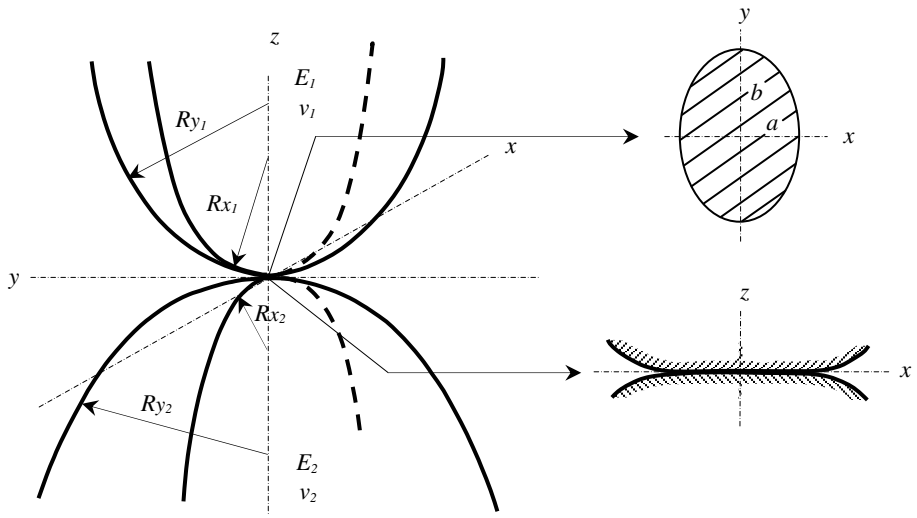

FIGURE 3.15: *Geometry of contraformal contact.*

Eccentricity of the ellipse e is defined as:

$$e^2 = 1 - \left(\frac{a}{b}\right)^2, \qquad a < b \tag{3.30}$$

where a and b denote the semi-minor and semi-major radius of the elliptic contact area. The mean effective radius R_m is represented as:

$$\frac{1}{R_m} = \frac{1}{R_x} + \frac{1}{R_y} = \frac{1}{R_{x1}} + \frac{1}{R_{x2}} + \frac{1}{R_{y1}} + \frac{1}{R_{y2}} \tag{3.31}$$

where R_x and R_y are the effective radii of curvature in principal x and y direction; subscripts 1 and 2 indicate body 1 and body 2, respectively.

From the theory of elasticity, the maximum contact pressure p_o, the semi-major contact ellipse radius b and the interference of an asperity ω can be written as [12]:

$$p_0 = \frac{3}{2} p = \frac{3P}{2\pi ab} \tag{3.32}$$

$$b = \left[\frac{3\mathbf{E}(e) P R_m}{\pi E (1 - e^2)}\right]^{1/3} \tag{3.33}$$

$$\omega = \frac{2\mathbf{K}(e)}{\pi}\left[\frac{\pi(1-e^2)}{4\mathbf{E}(e)R_m}\right]^{1/3}\left(\frac{3P}{4E}\right)^{2/3} \tag{3.34}$$

where

$$\left(\frac{a}{b}\right)^2 = \frac{\mathbf{E}(e)}{\mathbf{K}(e) + \dfrac{R_x}{R_y}\left[\mathbf{K}(e) - \mathbf{E}(e)\right]}$$

p is the mean contact pressure, P is the contact load, a is the semi-minor radius of the elliptic contact area, E is the effective elastic modulus as was defined in Eq. (3.5) and R_x and R_y are the effective radii of curvature as defined in Eq. (3.31). $\mathbf{K}(e)$ and $\mathbf{E}(e)$ are the complete elliptic integrals of the first and second kind, respectively:

$$\mathbf{K}(e) = \int_0^{\pi/2} (1 - e^2 \sin^2 \varphi)^{-0.5} d\varphi \tag{3.35}$$

$$\mathbf{E}(e) = \int_0^{\pi/2} (1 - e^2 \sin^2 \varphi)^{0.5} d\varphi \tag{3.36}$$

The elastic contact area A_e and the contact load P_e can be expressed in terms of the contact interference ω by combining Eqs. (3.32), (3.33) and (3.34):

$$A_e = \left[\frac{\mathbf{E}(e)}{\mathbf{K}(e)(1-e^2)^{0.5}} \right] 2\pi R_m \omega \tag{3.37}$$

$$P_e = \left[\frac{\pi \mathbf{E}(e)^{0.5}}{2\mathbf{K}(e)^{1.5}(1-e^2)^{0.5}} \right] \frac{4\sqrt{2}}{3} E R_m{}^{0.5} \omega^{1.5} \tag{3.38}$$

Eqs. (3.37) and (3.38) contain elliptical integrals, whose values must be found from tables. Approximations for the complete elliptic integrals have been introduced, for example, by Reussner [22] and Moes [23].

According to [22, 23], the semi-minor radius of the contact area a, the semi-major radius of the contact area b and the elastic interference ω are defined as:

$$a = \alpha \left(\frac{3PR_m}{2E} \right)^{1/3} \tag{3.39}$$

$$b = \beta \left(\frac{3PR_m}{2E} \right)^{1/3} \tag{3.40}$$

$$\omega = \gamma \left(\frac{9P^2}{32E^2 R_m} \right)^{1/3} \tag{3.41}$$

where α, β and γ, according to Moes [23], are

$$\alpha = \kappa^{1/3} \left[\frac{2}{\pi} \mathbf{E}(m) \right]^{1/3} \tag{3.42}$$

$$\beta = \kappa^{-2/3} \left[\frac{2}{\pi} \mathbf{E}(m) \right]^{1/3} \tag{3.43}$$

$$\gamma = \kappa^{2/3} \left[\frac{2}{\pi} \mathbf{E}(m) \right]^{-1/3} \frac{2}{\pi} \mathbf{K}(m) \tag{3.44}$$

In Eqs. (3.42)-(3.44) κ, $\mathbf{E}(m)$ and $\mathbf{K}(m)$ are defined by:

$$\kappa \approx \left[1+\sqrt{\frac{\ln(16/\lambda)}{2\lambda}}-\sqrt{\ln 4}+0.16\ln\lambda\right]^{-1} \quad for\ \ 0<\lambda\le 1 \tag{3.45}$$

$$\mathbf{E}(m) \approx \frac{\pi}{2}(1-m)\left[1+\frac{2m}{\pi(1-m)}-0.125\ln(1-m)\right] \tag{3.46}$$

$$\mathbf{K}(m) \approx \frac{\pi}{2}(1-m)\left[1+\frac{2m}{\pi(1-m)}\ln\left(\frac{4}{\sqrt{1-m}}\right)-0.375\ln(1-m)\right] \tag{3.47}$$

where $m = 1 - \kappa^2$ and the curvature ratio λ

$$\lambda = \frac{R_x}{R_y} \tag{3.48}$$

Combining Eqs. (3.39), (3.40) and (3.41), the contact area and the contact load can be presented in terms of ω as:

$$A_e = 2\pi R_m \omega \frac{\alpha\beta}{\gamma} \tag{3.49}$$

$$P_e = \frac{4\sqrt{2}}{3} E R_m^{0.5}\left(\frac{\omega}{\gamma}\right)^{1.5} \tag{3.50}$$

The mean contact pressure p_e is simply expressed in terms of ω by dividing Eq. (3.50) by Eq. (3.49):

$$p_e = \frac{2}{3} p_m = \frac{2\sqrt{2}}{3\pi}\frac{E}{\alpha\beta}\left(\frac{\omega}{R_m\gamma}\right)^{0.5} \tag{3.51}$$

Substituting Eq. (3.6) into Eq. (3.51) yields the critical interference ω_1:

$$\omega_1 = \frac{\pi^2}{2}\alpha^2\beta^2\gamma R_m \frac{K_v^{\,2} H^2}{E^2} \tag{3.52}$$

where K_v is a hardness coefficient related to the Poisson's ratio v as was defined in Eq. (3.10). Recently, [24] have derived K_v based on the von Mises shear strain energy criterion (see Appendix A) as:

$$K_v = 0.4645 + 0.3141v + 0.1943v^2 \tag{3.53}$$

However, the difference between Eq. (3.10) and Eq. (3.53) is small.

3.6.2 Elliptic fully plastic contact

Based on the experimental results of a deformable sphere in contact with a hard flat in the fully plastic contact regime, the mean contact pressure is not equal to the hardness but lower. For a more general representation the mean contact pressure in the fully plastic regime can be related to the hardness as:

$$p_p = c_h H \tag{3.54}$$

where c_h is the hardness coefficient for the fully plastic contact regime.

It was shown in Fig. 3.6 that in the fully plastic contact regime the contact area is simply a truncation of the undeformed asperity geometry as was postulated by [11]. For the elliptical contact situation this can be expressed as:

$$\omega = \frac{a^2}{2R_x} = \frac{b^2}{2R_y} \tag{3.55}$$

Rearranging and substituting Eq. (3.55) into $A = \pi ab$ yields the contact area in the fully plastic A_p:

$$A_p = 2\pi\sqrt{R_x R_y}\,\omega \tag{3.56}$$

The contact load P_p is equal to the contact area multiplied by the mean contact pressure, or

$$P_p = 2\pi\omega\sqrt{R_x R_y}\,c_h H \tag{3.57}$$

The solid expression for the onset of fully plastic interference ω_2 is not known, therefore it is estimated. A simple analysis is done based on the contact load. At $\omega = \omega_2$, the contact load is equal to Eq. (3.57). At the same time, the contact load had it been elastic as would be equal to Eq. (3.50). Therefore, the following inequality can be established:

$$\frac{4\sqrt{2}}{3} E R_m^{0.5} \left(\frac{\omega_2}{\gamma}\right)^{1.5} > 2\pi\omega_2\sqrt{R_x R_y}\,c_h H \tag{3.58}$$

Eq. (3.58) can be rewritten as:

$$\omega_2 > \left(\frac{\pi^2}{2}\alpha^2\beta^2\gamma\frac{R_m}{E^2}K_v{}^2 H^2\right)\left(\frac{3}{2}\frac{\gamma}{\alpha\beta}\frac{\sqrt{R_x R_y}}{R_m}\frac{c_h}{K_v}\right)^2 \tag{3.59}$$

Substituting Eq. (3.42) to (3.48) and Eq. (3.52) into Eq. (3.59) yields:

$$\omega_2 > \left(\frac{3\kappa}{2} \frac{\mathbf{K}(1-\kappa^2)}{\mathbf{E}(1-\kappa^2)} \frac{1+\lambda}{\sqrt{\lambda}} \frac{c_h}{K_v} \right)^2 \omega_1 \tag{3.60}$$

Fig. 3.16 depicts the plot of Eq. (3.60) in terms of λ. The onset of full plasticity based on this equation is strongly affected by the plastic hardness coefficient c_h. For the same value of $K_v = 0.6$, the onset of full plasticity for $c_h = 1$ is about 25 and for $c_h = 0.8$ this is about 16 for λ in the range 0.75 to 1.

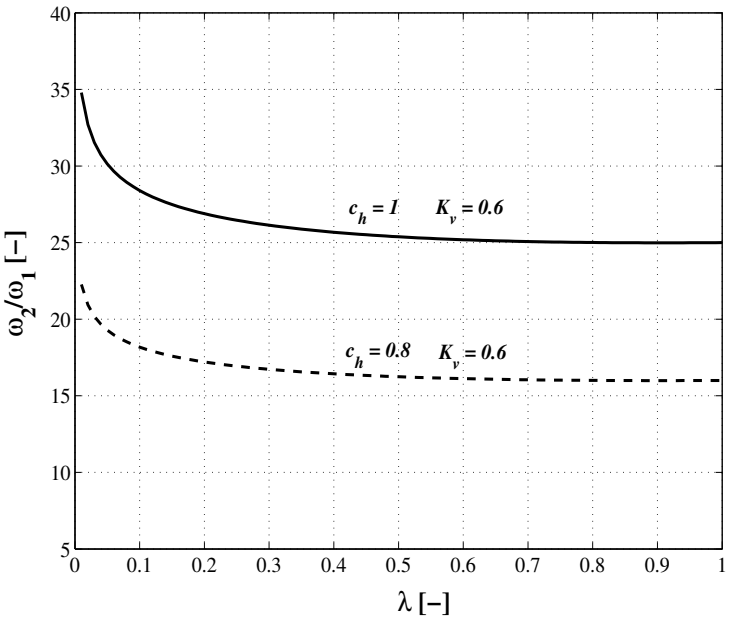

FIGURE 3.16: *Onset of full plasticity as a function of the ellipticity ratio* λ *of Equation* (3.60).

The minimum value of ω_2 may also be further estimated using experimental results. The fully plastic regime of a half-space indented by a rigid sphere according to Francis [13], starts at $A/A_c = 113.2$ and according to Johnson [12] full plasticity starts at $Ea/YR \approx 40$ or $P/P_c \approx 360$. Based on the experimental results of Chaudhri *et al.* [17] and Tabor [5] for the contact problem of a deformable sphere and a rigid flat, the fully plastic contact regime (as indicated by a constant mean contact pressure) starts at $A/A_c \approx 40$ for phosphor-bronze, 90 for brass and 160 for steel according to the *JG* model. Or in general:

$$\frac{A}{A_c} = c_A \tag{3.61}$$

Substituting Eqs. (3.49) and (3.56) into Eq. (3.61) and rearranging results:

$$\frac{\omega_2}{\omega_1} = c_A \frac{R_m}{\sqrt{R_x R_y}} \frac{\alpha\beta}{\gamma} \tag{3.62}$$

Using Eqs. (3.42) - (3.48) and substituting into Eq. (3.62) yields:

$$\frac{\omega_2}{\omega_1} = c_A \frac{\sqrt{\lambda}}{1+\lambda} \frac{1}{\kappa} \frac{\mathbf{E}(1-\kappa^2)}{\mathbf{K}(1-\kappa^2)} \tag{3.63}$$

Fig. 3.17 shows the plot of the onset of fully plastic contact as a function of the ellipticity ratio λ based on Eq. (3.63). It can be seen that for the range of λ of 0.55 to 1, ω_2/ω_1 is almost constant at a value of about 45 for c_A = 90. For the next analysis this value will be used.

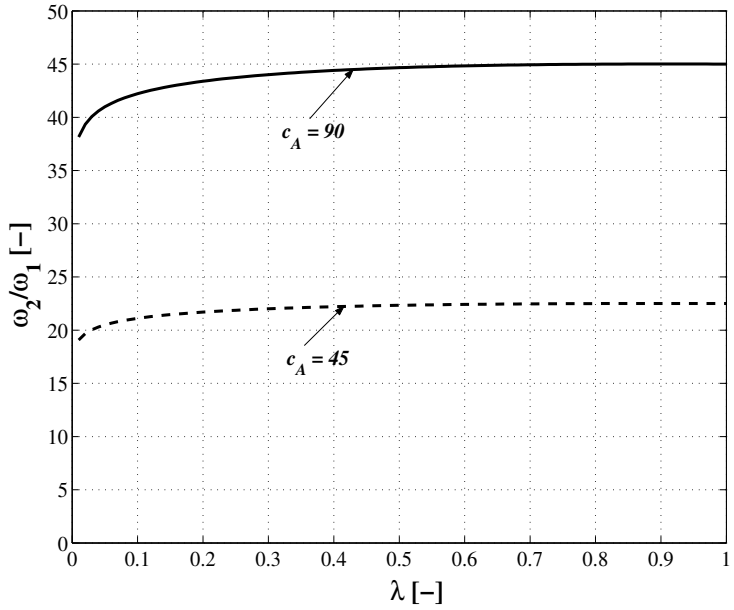

FIGURE 3.17: *Onset of full plasticity as a function of the ellipticity ratio* λ *of Equation* (3.63).

3.6.3 Elliptic elastic-plastic contact

Since the modified *ZMC* model predicts the contact behavior in the elastic-plastic regime best among the other contact models, the approaches used by the *ZMC* model will be used to analyze the elliptic elastic-plastic contact problem.

Based on a statistical analysis of spherical indentations, Francis [13] presented the dependence of the mean contact pressure p_{ep} on ω for the elastic-plastic contact situation, which may be analogously characterized by a logarithmic function, as follows:

$$p_{ep} = a_1 + a_2 \ln\left(\frac{\omega}{r}\right) \tag{3.64}$$

where a_1 and a_2 are two constants to be determined, and r is the circular contact radius. Since the area of elliptical contact $A = \pi ab$, the elliptical contact radius can be represented as $(ab)^{1/2}$. Substituting this relation into Eq. (3.64) results:

$$p_{ep} = a_1 + a_2 \ln\left(\frac{\omega}{\sqrt{ab}}\right) \tag{3.65}$$

At the critical interference ω_1, Eq. (3.65) can be expressed in the form:

$$\frac{2}{3} K_v H = a_1 + a_2 \ln\left(\frac{\omega_1}{\sqrt{ab}}\right) \tag{3.66}$$

and at the inception of full plasticity ω_2:

$$c_h H = a_1 + a_2 \ln\left(\frac{\omega_2}{\sqrt{ab}}\right) \tag{3.67}$$

By simultaneously solving Eqs. (3.66) and (3.67), the parameters a_1 and a_2 can be determined in terms of the properties of the contact:

$$a_1 = c_h H - \frac{H\left(c_h - \frac{2}{3} K_v\right)}{\ln \omega_2 - \ln \omega_1} \ln\left(\frac{\omega_2}{\sqrt{ab}}\right) \tag{3.68}$$

$$a_2 = \frac{H\left(c_h - \frac{2}{3} K_v\right)}{\ln \omega_2 - \ln \omega_1} \tag{3.69}$$

Substituting Eqs. (3.68) and (3.69) into (3.65) gives the mean contact pressure in the elastic-plastic deformation region as follows:

$$p_{ep} = c_h H - H\left(c_h - \frac{2}{3} K_v\right) \frac{\ln \omega_2 - \ln \omega}{\ln \omega_2 - \ln \omega_1} \tag{3.70}$$

Zhao *et al.* [7] proposed a relation of the elastic-plastic contact area as a function of ω. The relation was modeled by using a polynomial expression to join the expression of the contact area at $\omega = \omega_1$ and $\omega = \omega_2$ smoothly. A 'template' cubic polynomial function is defined as:

$$y = 3x^2 - 2x^3 \tag{3.71}$$

By this function all four boundary conditions: $A_{ep} = A_e$, $dA_{ep}/d\omega = dA_e/d\omega$ at $\omega = \omega_1$ and $A_{ep} = A_p$, $dA_{ep}/d\omega = dA_p/d\omega$ at $\omega = \omega_2$ are satisfied. The transformation involves translating and scaling ω so that $\omega = \omega_1$ and $\omega = \omega_2$ correspond to $x = 0$ and $x = 1$, respectively, where:

$$x = \frac{\omega - \omega_1}{\omega_2 - \omega_1} \tag{3.72}$$

The expression of A_{ep} after scaling is:

$$A_{ep} = A_e + (A_p - A_e)\left[3\left(\frac{\omega - \omega_1}{\omega_2 - \omega_1}\right)^2 - 2\left(\frac{\omega - \omega_1}{\omega_2 - \omega_1}\right)^3\right] \tag{3.73}$$

Substituting Eqs. (3.49) and (3.56) into Eq. (3.73) gives the relation between the elastic-plastic contact area A_{ep} in terms of contact interference ω as:

$$A_{ep} = 2\pi R_m \omega \frac{\alpha\beta}{\gamma} + \left(2\pi\sqrt{R_x R_y}\,\omega - 2\pi R_m \omega \frac{\alpha\beta}{\gamma}\right)\left[3\left(\frac{\omega - \omega_1}{\omega_2 - \omega_1}\right)^2 - 2\left(\frac{\omega - \omega_1}{\omega_2 - \omega_1}\right)^3\right] \tag{3.74}$$

The elastic-plastic contact load P_{ep} is defined using Eqs. (3.70) and (3.74), $P_{ep} = p_{ep}A_{ep}$, as:

$$P_{ep} = A_{ep}\left[c_h H - H\left(c_h - \frac{2}{3}K_v\right)\frac{\ln\omega_2 - \ln\omega}{\ln\omega_2 - \ln\omega_1}\right] \tag{3.75}$$

Examples of the application of the developed new elliptic elastic-plastic contact model are presented in Fig 3.18 and 3.19 in which the non-dimensional mean contact pressure, $p/(c_h H)$, is plotted as a function of the non-dimensional contact area, A/A_c, and the non-dimensional contact area as a function of the non-dimensional contact load, P/P_c, respectively. It can be seen from the figures that the proposed elastic-plastic contact model fits very well with the experimental results of Chaudhri [17]. In these cases, the coefficient of hardness $c_h = 0.805$ and the contact area constant $c_A = 40$ for phosphor-bronze and $c_h = 0.967$ and $c_A = 90$ for brass. This suggests that those constants are material dependent.

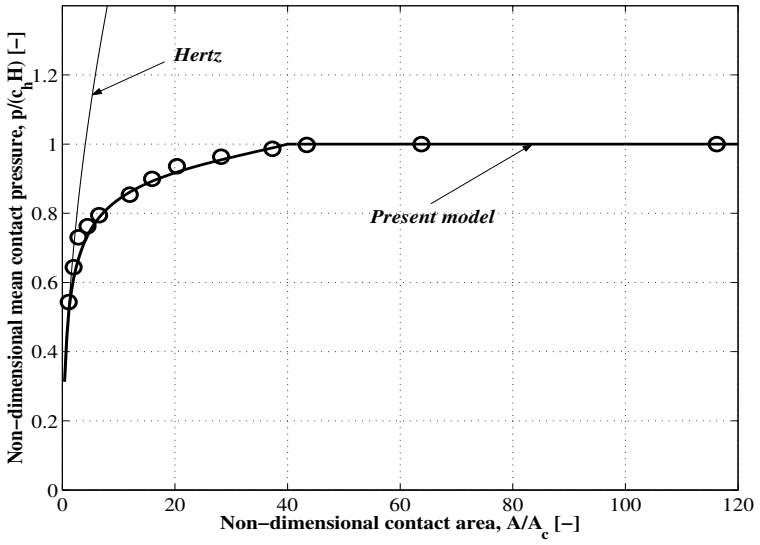

(a)

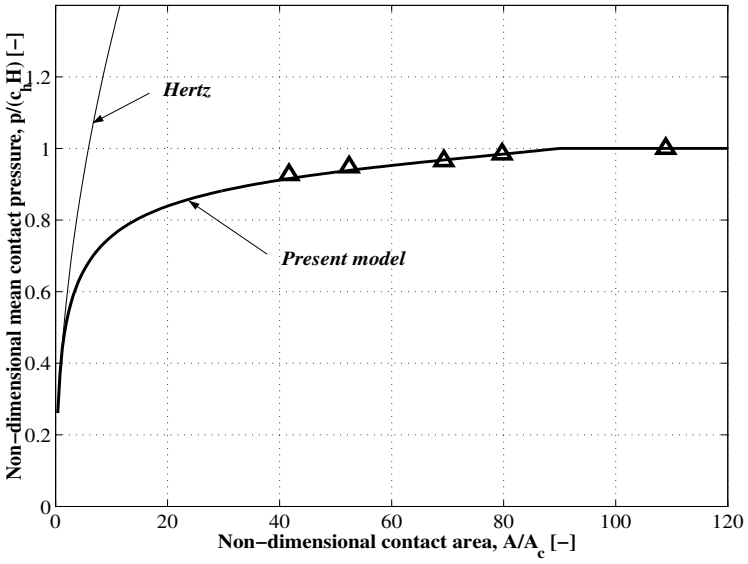

(b)

FIGURE 3.18: *Non-dimensional mean contact pressure vs non-dimensional contact area. Experiments: (a) ○ phosphor-bronze and (b) Δ brass of Chaudhri* [17].

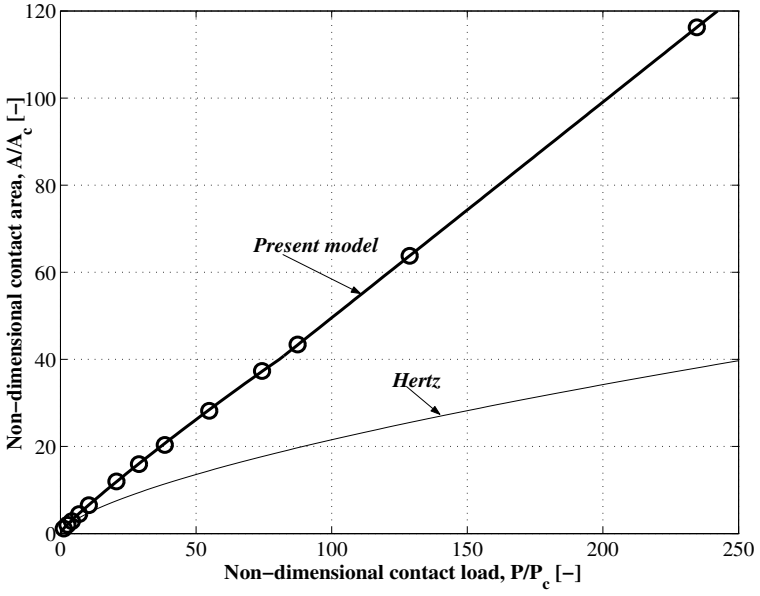

(a)

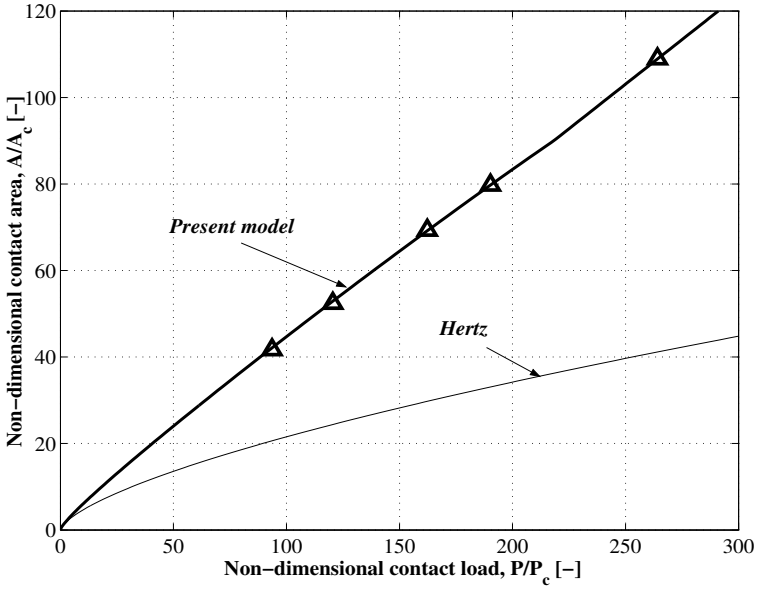

(b)

FIGURE 3.19: *Non-dimensional contact area vs non-dimensional contact load. Experiments: (a) ○ phosphor-bronze and (b) Δ brass of Chaudhri* [17].

3.7 Unloading of elastic-plastic asperity contact model

The same as for the loading of an elastic-plastic contacting asperity, the unloading does have three different contact regimes i.e. elastic, elastic-plastic and fully plastic. The plastic deformation results in a permanent change of the asperity which in fact is the main issue of this study. Therefore, attention will be paid to the completed unloading process rather than studying all the unloading stages itself. The study will focus on the residual contact interference and the residual contact area. Due to the fact that there is not much literature concerning this topic, the unloading contact behavior will be developed.

3.7.1 Elastic contact unloading

It is widely accepted that the elastic unloading process is assumed to follow the Hertzian analysis. Therefore, in the elastic contact regime there is no difference between loading and unloading contact behavior. Consequently, the residual contact interference, ω_{ue} and the residual contact area A_{ue} are:

$$\omega_{ue} = 0 \tag{3.76}$$

$$A_{ue} = 0 \tag{3.77}$$

3.7.2 Fully plastic contact unloading

In the fully plastic contact regime the elastic recovery is very small. This is also confirmed by the experimental results, see for example Fig. 3.5b. From this figure the elastic recovery interference is about 3% of the contact interference. Therefore, it is reasonable to assume that the elastic part is negligible in the fully plastic regime. Accordingly, all the contact parameters for the fully plastic contact loading can be used for the unloading analysis.

The residual contact interference, ω_{up} and the residual contact area A_{up} in the fully plastic regime are:

$$\omega_{up} = \omega_p \tag{3.78}$$

$$A_{up} = A_p \tag{3.79}$$

where ω_p and A_p are the contact interference and contact area in the fully plastic regime during loading, respectively.

Experimental results of the plastic deformation and plastic contact area, along with the model prediction of Eqs. (3.78) and (3.79), are presented in Fig. 3.20 and Fig. 3.21 as a function of the contact load. In these figures, since the contact pressure in the fully plastic regime depends on the constant c_h, the contact load is normalized by the factor $c_h P_c$ where P_c is the contact load at $\omega = \omega_1$. The same specimens as were used previously in Sub-

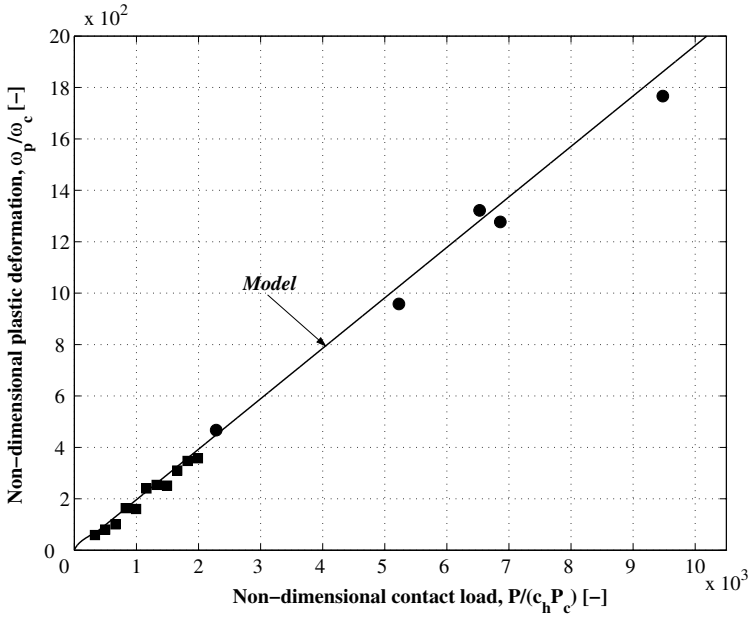

FIGURE 3.20: *Non-dimensional plastic deformation vs non-dimensional contact load in the fully plastic contact regime. Experimental results:* ■ *copper and* ● *aluminium.*

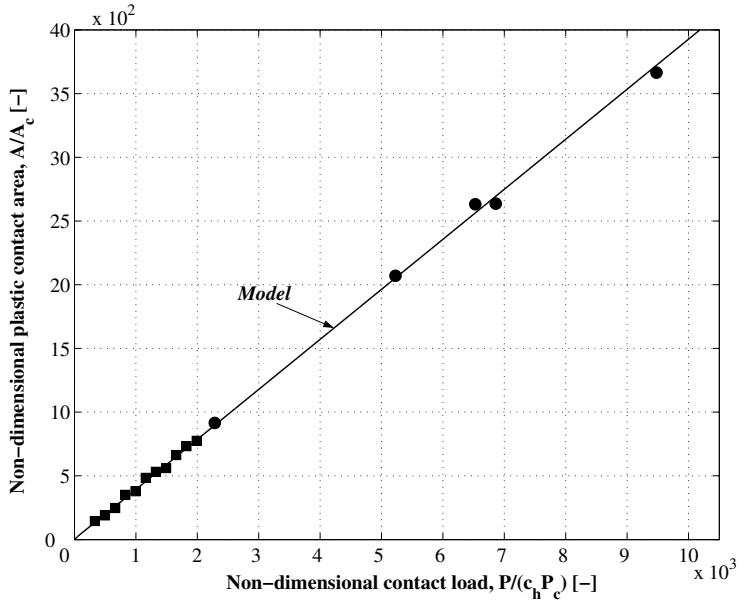

FIGURE 3.21: *Non-dimensional plastic contact area vs non-dimensional contact load in the fully plastic contact regime. Experimental results:* ■ *copper and* ● *aluminium.*

section 3.5.1 were used in the present experiments. The constant c_h for copper is 0.75 and for aluminium is 0.71. A very good correlation is observed from these figures. The model predicts the plastic deformation and the plastic contact area accurately for both materials far into the fully plastic contact regime, $P/(c_h P_c) = 9450$.

3.7.3 Elastic-plastic contact unloading

From the available literature about the unloading contact behaviour all of research was devoted to the elastic-plastic contact situation [14, 25 and 26]. Vu-Quoc [14, 25] proposed the plastic interference $\omega_{p\text{-}VQ}$ and the plastic contact area $A_{p\text{-}VQ}$ on the basis of FEM calculations as:

$$\omega_{p-VQ} = \omega_{\max} - \frac{\left(a_{e-\max}\right)^2}{\left(C_R\right)^2 R} \tag{3.80}$$

$$A_{p-VQ} = \pi\left(C_a\left(P_{\max} - P_Y\right)\right)^2 \tag{3.81}$$

where ω_{max}, $a_{e\text{-}max}$ and P_{max} are the contact interference, the contact area radius and the contact load, respectively, from which the unloading is started. C_R and C_a are constants which are dependent on the asperity properties and P_Y is the load at the yield point. The model seems to be simple, however to determine the constants, extra effort is needed such as FEM calculations or experimental analysis. Furthermore, this model was applied for relatively low loads and for a certain material. As was shown by experimental results, the elastic part is reduced as the load increases, but from Eq. (3.80) by taking a constant value of C_R, the elastic deformation increases quadratically as the contact area radius increases.

Li *et al*. [26], also based on a FEM analysis, developed the unloading contact model for the contact of a rigid sphere with an elastic-perfectly plastic half-space and an elastic-perfectly plastic sphere with a rigid plane. In their model, the load-displacement relationship for the unloading situation is expressed by:

$$\frac{P}{P_Y} = \frac{P_{\max}}{P_Y} - \left(\frac{R_{\max}}{R}\right)^{0.5}\left[\left(\frac{\omega_{\max}}{\omega_c}\right)^{1.5} - \left(\frac{\omega}{\omega_c}\right)^{1.5}\right] \tag{3.82}$$

where P_{max} and ω_{max} are the maximum load and the corresponding maximum interference during the loading-unloading cycle, R_{max} is the radius of curvature at the maximum load and P_Y is the load at the critical interference ω_c. As can be seen in Eq. (3.82) it is difficult to analyze the unloading contact situation, i.e. for determining the R_{max}. Compared to the Vu-Quoc *et al.* model, this model reduces the number of the unknown constants. The residual or plastic deformation of the asperity $\omega_{p\text{-}Li}$ can be obtained from Eq. (3.82) by substituting the value at the final loading, i.e. when $P = 0$:

$$\omega_{p-Li} = \omega_c \left(\left(\frac{\omega_{\max}}{\omega_c} \right)^{1.5} - \frac{P_{\max}}{P_c} \left(\frac{R_{\max}}{R} \right)^{-0.5} \right)^{2/3} \tag{3.83}$$

Figure 3.22 shows the plot of loading a phosphor-bronze sphere [17], see Section 3.5.2, by the developed model of section 3.6 and the unloading process for P_{max} at $\omega/\omega_c = 25$ by Li *et al.* model as a function of the non-dimensional contact interference ω/ω_c. Li *et al.* [26] suggest the value for R_{max} to be $2.15R$. It should be noted that this value depends on the load or interference. According to Johnson [12] the value of R_{max} is $2R$ in the fully plastic contact regime when there is no pile-up and sinking in adjacent to the perimeter of the contact area and R_{max} is R for the elastic contact situation. In order to obtain a more precise value for R_{max} for the elastic-plastic unloading contact model, an experimental investigation should be conducted.

The present experimental work uses the same procedure as was mentioned in Section 3.5. In this case, two equal hardened steel spheres (H = 7.55 GPa, E = 210 GPa and v = 0.3) with a diameter of 20 mm were compressed in the Tensile Testing Machine (see Appendix D). A typical result after the unloading of such spheres is shown in Fig. 3.23. In this figure, a load of 77330 N was applied to the equal spheres in contact for about 30 seconds and then removed. Compared to the results of Fig. 3.5b, the profile in this figure is much smoother. This is because the average roughness R_a value of the hardened steel sphere is about 0.01 μm whiles the R_a value in Fig. 3.5b is about 0.15 μm.

Residual or plastic deformation is determined by fitting a curve along the experimental results which maintain the continuity from the elastic, elastic-plastic and fully plastic contact regimes. Two types of polynomial functions are employed for this method in the elastic-plastic contact regime. According to this, the plastic deformation ω_{uep} in the elastic-plastic regime is expressed by:

$$\begin{aligned} \omega_{uep} &= \omega_1 \left[a_1 \left(\frac{\omega}{\omega_1} \right)^2 - a_2 \left(\frac{\omega}{\omega_1} \right) + a_3 \right] && \text{for} \quad \omega_1 \le \omega \le a_b \omega_1 \\ \omega_{uep} &= \omega_1 \left[-b_1 \left(\frac{\omega}{\omega_1} \right)^3 + b_2 \left(\frac{\omega}{\omega_1} \right)^2 - b_3 \left(\frac{\omega}{\omega_1} \right) + b_4 \right] && \text{for} \quad a_b \omega_1 \le \omega \le \omega_2 \end{aligned} \tag{3.84}$$

where ω_1 and ω_2 are the critical interference for the first yield and the critical interference for the fully plastic situation, respectively. The constant a_1 = 23/1521, a_2 = 46/1521, a_3 = 23/1521, b_1 = 523/1248000, b_2 = 4567/62400, b_3 = 1039/390, b_4 = 1532/39 and $a_b = 40\omega_1$. Based on the experimental investigation of Johnson [12], the fully plastic contact regime is reached when P/P_c is about 360 to 400 for spherical asperities indentations. In the present analysis the value of P/P_c = 400 was used, or $\omega_2 = 80\omega_1$.

It is difficult to find the relation between the plastic contact area and the plastic deformation; however, as soon as there is plastic deformation as can be seen in Fig. 3.23, the plastic contact area formed is nearly the plastic contact area in the loading condition. Therefore, the plastic contact area A_{uep} can be expressed as:

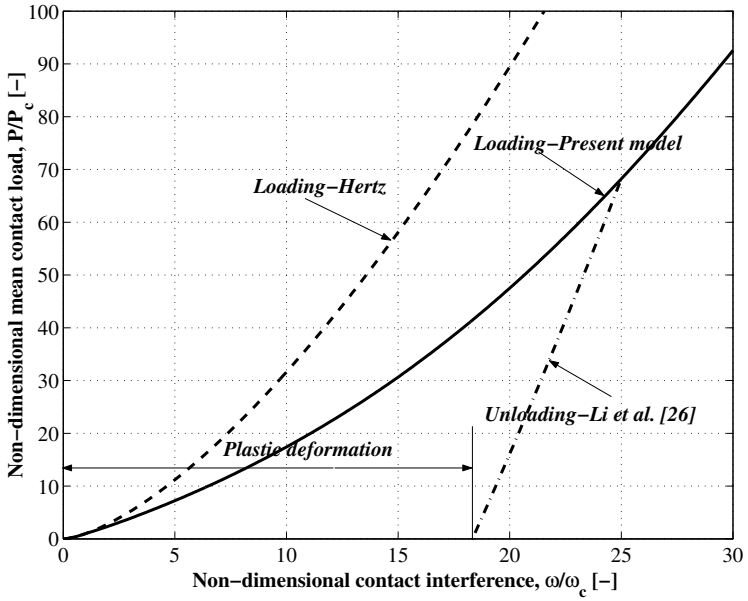

FIGURE 3.22: *Non-dimensional load versus non-dimensional interference curves during loading-unloading of a sphere against a rigid flat.*

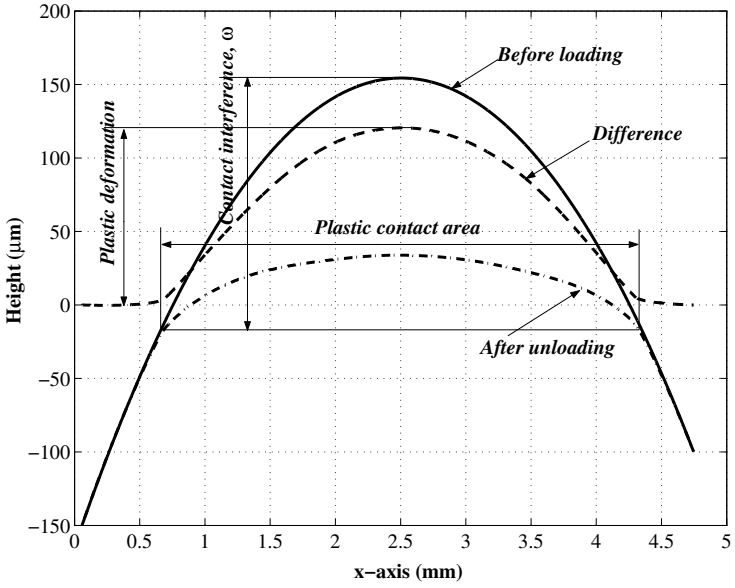

FIGURE 3.23: *Measured plastic deformation and plastic contact area after unloading of two equal hardened steel spheres with a diameter of* 20 *mm at* P = 77330 *N,* R_a = 0.01 μ*m.*

$$A_{uep} = A_{ep} \tag{3.85}$$

where A_{ep} is the contact area in the elastic-plastic regime during loading.

Figure 3.24 shows the measured values obtained with the experiment described, along with the expression for the plastic deformation of Eq. (3.84). In these experiments, hardened steel, mild steel and aluminium were used. For the mild steel and aluminium ridge shaped asperities were used. The curvature of the ridge shaped asperities were determined based on the volume conservation method, see Chapter 4. As can be seen, the theoretical model (plastic deformation) predicts the trend of the experimental results very well. The plastic deformation starts from zero in the elastic contact regime and steadily grows as the load increases until there is almost no elastic recovery in the fully plastic regime. Conversely, the elastic recovery grows as the load increases from zero until it reaches a maximum value at a certain load and then decreases until almost zero in the fully plastic contact regime.

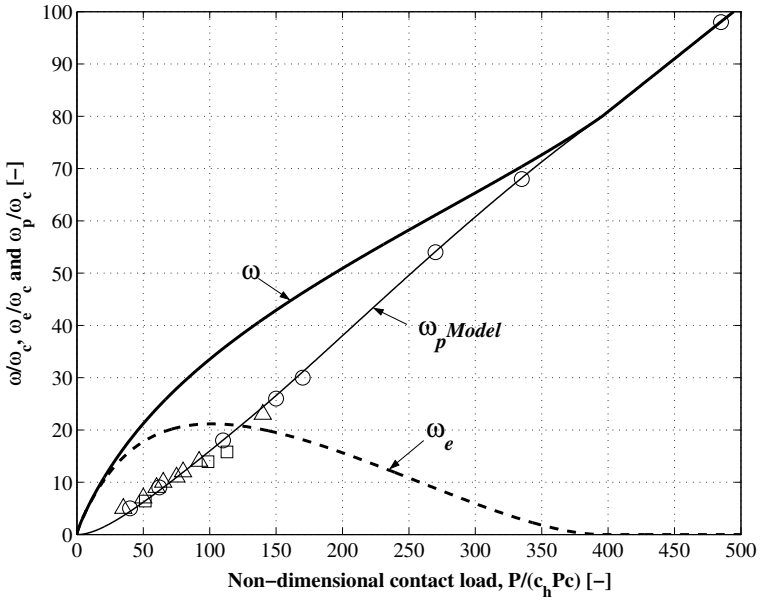

FIGURE 3.24: *Non-dimensional plastic deformation as a function of non-dimensional contact load in the elastic-plastic contact regime. Experimental results: □ hardened steel, Δ mild steel (ridge) and ○ aluminium (ridge).*

A comparison of the non-dimensional plastic contact area measured and predicted by Eq. (3.85) or Eq. (3.74) is shown in Fig. 3.25. The results are plotted against the non-dimensional contact load $P/(c_h P_c)$. The theoretical model, as can be seen, predicts the remaining plastic contact area fairly well. The model overestimates the measurement results a little bit, however, when the degree of plasticity increases, the accuracy of the model

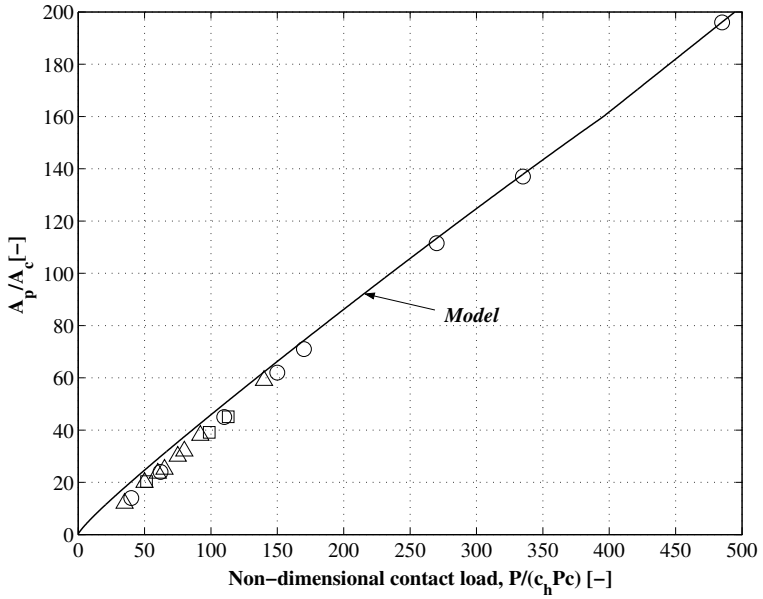

FIGURE 3.25: *Plastic contact area as a function of contact load in the elastic-plastic contact regime. □ hardened steel, Δ mild steel (ridge) and ○ aluminium (ridge).*

prediction increases. The reason for the lower measured plastic contact area is that during unloading there is a small elastic recovery and as a consequence there is a decrease in the diameter of the contact area after unloading.

3.8 Concluding remarks

An elastic-plastic single asperity contact model has been studied in this chapter. The published elastic-plastic asperity contact models have been reviewed. In order to verify the proposed models from literature, experiments were conducted. From the experimental results it is concluded that there is no agreement between the measured and the theoretical predictions. Therefore, a new single asperity contact model has to be developed.

A new contact model has been developed by making use of the knowledge gained by the experimental investigations. To make it more general, the model is presented for the elliptical contact condition. Two constants have been introduced, c_h the coefficient for the hardness in the fully plastic contact regime and c_A the coefficient for the full plasticity contact area in determining the interference where the full plasticity begins. It was shown that the mean contact pressure in the fully plastic contact regime is lower than the hardness of the material as proposed by most of the asperity contact models. There is no significant difference in determining the critical interference from the elastic to the elastic-plastic contact regime (ω_1) for all the proposed contact models; however, the difference in the transition from the elastic-plastic to the fully plastic contact regime (ω_2) is very significant.

Experiments suggest that (ω_2) depends on the asperity contact properties. In the fully plastic contact regime the contact area is simply a truncation of the asperities.

Since the change of the asperity geometry is the main topic in this thesis, the model is extended for the unloading condition. A simple expression for the unloading of the elastic-plastic asperity contact model has been developed. The unloading model predicts the plastic deformation and the plastic contact area.

In Chapter 4 the elastic-plastic single asperity contact model which has been developed (loading and unloading) is applied to the multi asperity contact situation.

References

[1] Bhushan, B., 1996, "Contact mechanics of rough surfaces in tribology: single asperity contact," *Applied Mechanics Reviews* **49**, pp. 275 – 298.

[2] Fleck, N.A., 1995, "On the cold compaction of powders," *J. Mech. Phys. Solids* **43**, pp. 1409 – 1431.

[3] Greenwood, J.A. and Williamson, J.B.P., 1966, "Contact of nominally flat surfaces," *Proc. R. Soc London* **A295**, pp. 300 – 319.

[4] Hertz, H., 1882, *Uber die beruhrung fester elastische korper und uber die harte (On the contact of rigid elastic solids and on hardness),* Verhandlungen des Vereins zur Beforderung des Gewerbefleisses, Leipzig, Nov 1882 (For English translation see Miscellaneous Papers by H. Hertz*,* Eds Jones and Schott, Macmillan, London, 1896).

[5] Tabor, D., 1951, *The Hardness of Metals,* Oxford University Press, UK.

[6] Chang, W.R., Etsion, I. and Bogy, D.B., 1987, "An elastic-plastic model for the contact of rough surfaces," *ASME-Journal of Tribology* **109**, pp. 257 – 263.

[7] Zhao, Y., Maietta, D.M. and Chang, L., 2000, "An asperity microcontact model incorporating the transition from elastic deformation to fully plastic flow," *ASME-Journal of Tribology* **122**, pp. 86 – 93.

[8] Kogut, L. and Etsion, I., 2002, "Elastic-plastic contact analysis of a sphere and a rigid flat," *ASME-Journal of Applied Mechanics* **69**, pp. 657 – 662.

[9] Chang, W.R., Etsion, I. and Bogy, D.B., 1988, "Static friction coefficient model for metallic rough surfaces," *ASME-Journal of Tribology* **110**, pp. 57 – 63.

[10] Jackson, R.L. and Green, I., 2005, "A finite element study of elasto-plastic hemispherical contact against a rigid flat," *ASME-Journal of Tribology* **127**, pp. 343 – 354.

[11] Abbott, E.J. and Firestone, F.A., 1933, "Specifying surface quality – A method based on accurate measurement and comparison," *Mech. Eng. (Am. Soc. Mech. Eng.)* **55**, pp. 569.

[12] Johnson, K.L., 1985, *Contact Mechanics,* Cambridge University Press, Cambridge, UK.

[13] Francis, H.A., 1976, "Phenomenological analysis of plastic spherical indentation," *ASME-Journal of Engineering Material Technology* **98**, pp. 272 – 281.

[14] Vu-Quoc, L., Zhang, X. and Lesburg, L., 2000, "A normal force-displacement model for contacting spheres accounting for plastic deformation: Force-driven formulation," *ASME-Journal of Applied Mechanics* **67**, pp. 363 – 371.

[15] Johnson, K.L., 1968, "An experimental determination of the contact stresses between plastically deformed cylinders and spheres," Engineering Plasticity, Cambridge University Press, Cambridge, pp. 341 – 361.

[16] Chaudhri, M.M., 1987, "The plastic deformation of single asperities by hard flats," Inst. Mech. Eng. Conference Publications **C158**, pp. 1003 – 1012.

[17] Chaudhri, M.M., Hutchings, I.M. and Makin, P.L., 1984, "Plastic compression of spheres," *Philosophical Magazine A* **49**, pp. 493 – 503.

[18] Chaudhri, M.M. and Yoffe, E.H., 1981, "The area of contact between a small sphere and a flat surface," *Philosophical Magazine A* **44**, pp. 667 – 675.

[19] Horng, J.H., 1998, "An elliptic elastic-plastic asperity microcontact model for rough surfaces," *ASME-Journal of Tribology* **120**, pp. 82 – 88.

[20] Jeng, Y.R. and Wang, P.Y., 2003, "An elliptic microcontact model considering elastic, elastoplastic, and plastic deformation," *ASME-Journal of Tribology* **125**, pp. 232 – 240.

[21] McCool, J.I., 1986, "Predicting microfracture in ceramics via a microcontact model," *ASME-Journal of Tribology* **108**, pp. 380 – 386.

[22] Reussner, H., 1977, Druckflächenbelastung und Oberflächen verschiebung im Wälzcontact von Rotationskörpen, PhD Thesis, University of Karlsruhe, Germany (in German).

[23] Moes, H., 2000, Lubrication and Beyond – University of Twente Lecture Notes code 115531, University of Twente, Enschede, The Netherlands.

[24] Lin, L.P. and Lin, J.F., 2005, "An elastoplastic microasperity contact model for metallic materials," *ASME-Journal of Tribology* **127**, pp. 666 – 672.

[25] Vu-Quoc, L. and Zhang, X., 1999, "An elasto-plastic contact force-displacement model in the normal direction: Displacement-driven version," *Proc. R. Soc London* **A455**, pp. 4013 – 4044.

[26] Li, L.-Y., Wu, C.-Y. and Thornton, C., 2002, "A theoretical model for the contact of elastoplastic bodies," *Proc. Instn. Mech. Engrs. Part C* **216**, pp. 421 – 431.

Chapter 4

Deterministic elastic-plastic multi asperity contact

4.1. Introduction

All engineering surfaces found in nature are observed to be rough at microscopic scale and never perfectly smooth. Irregularities or roughness of the solid surfaces can be formed by either of the following methods: fracture of solids; machining; thin-film deposition; and solidification of liquids [1]. The roughness often appears randomly and disorderly and does not seem to follow any particular structural pattern which contributes to the complexity of the surface geometrical structure. The effect of roughness is very significant in studying contact mechanics, friction, wear, lubrication, electrical contact resistance, noise and vibration, et cetera [2].

Several attempts have been made to model the rough surfaces, for instance an asperity based model as was presented in the previous chapter, in order to study the effect of the roughness for a certain application further. In this chapter the developed elastic-plastic single asperity contact model in Chapter 3 is extended to study the behavior of the elastic-plastic rough surface contact deterministically. In this case, a rough surface is represented by an array of asperities (multi asperity approach). The roughness or asperity deformation without bulk deformation is a point of interest in this thesis (running-in); therefore, this will be used as a boundary of the operating contact condition. However, there is no criterion available by which one is able to distinguish in which condition the contacting surfaces will deform: in the surface asperities only, in the bulk only (asperity persistence) or in a combination of asperity and bulk deformation. For this purpose, a criterion is proposed theoretically and is presented in Section 4.2. In Section 4.3 the experimental validation of the proposed criterion in Section 4.2 is given. By having the criteria to determine the contact deformation of rough surfaces on asperity level only, analysis of the contact of rough surfaces deterministically can be performed readily. Deterministic contact of surfaces is explored in Section 4.4. In this section, the modeling of contacts between rough surfaces published in literature is reviewed and a new developed rough surface contact model is presented. Experimental validation of the rough surface contact model is given in Section 4.5. Finally, concluding remarks are given in Section 4.6.

4.2 Surface asperities and bulk deformation

When two surfaces are loaded against each other, contact will initially occur at a limited amount of asperities of different shapes and sizes to support the normal load. The number of the contacting asperities becomes larger as the normal load is increased, as well as the contact deformation. If the deformation is in the same order as the topography of the surfaces, the response to the normal load may be strongly related to the height and size of the asperities. An elastic-plastic material plasticity may be initiated either in the surface asperities or in the bulk depending on the contact condition. This problem is of particular interest to tribologists and engineers with respect to the functional properties of the devices. Or in another words, depending on the desired functional performance, the contacting surfaces condition may be designed. In this section, the study of the deformation behavior of the contacting surfaces will be presented. The study will focus on the contact of rough curved surfaces, since in practical engineering applications, this contact is most frequently observed, such as the contact of a ball on the race way of ball bearings, ball screws, ball joints, et cetera.

4.2.1 Overview of the asperities and bulk deformation models

In the Hertz theory [3], the contact of two elastic bodies is based on the assumption that their surfaces are topographically smooth. However, when roughness is present, the qualitative behavior is clear and there are two scales of size in such a problem [4]: (i) the bulk or nominal contact dimensions and elastic deformation according to the Hertz theory and (ii) the height and spatial distribution of the roughness or asperities. Quantitative study of this problem has been conducted by Greenwood and Tripp (*GT* model) [5] by analyzing the elastic contact of rough spheres. The analysis of [5] is based on the work of Greenwood and Williamson [6] where the rough surfaces are assumed to be covered with spherical asperities and the height of the asperities is represented by a well-defined statistical distribution function. Similar approaches have been used by Lo [7] to analyze the contact behaviour of two parallel rough cylinders. Different to the previous studies, Mikic and Roca [8] studied the contact problem of two rough spherical surfaces based on the plasticity theory.

Most of the developed contact models are devoted to the calculation of the real contact area or load carrying capacity and the sub-surface stresses. The deformation behaviour of the contacting surfaces is rarely explored, especially during the unloading. Recently, Rajendrakumar and Biswas [9] have studied the deformation response of the contact between a two-dimensional rough surface and a smooth cylinder by using complex variable analysis. A map which can be used as a design guide for predicting the deformation responses – asperity, bulk or a combination between asperity and bulk deformation of the contacting surfaces, was constructed. However, the map was based upon a simple two-dimensional configuration of the contact problem and there is no experimental verification for the proposed model. The asperities were represented by simple uniformly spaced cylinders of the same radius and height.

4.2.2 Contact of rough curved surfaces

In the case of the contact between a smooth sphere and a flat rough surface, true contact is not made continuously over the circular contact area envisaged by the Hertz theory, but through an archipelago of small discrete islands roughly clustered within a circular region. Therefore, true contact pressure is discontinuous, very high within the contact region and falling to zero in between the contact islands. In the present analysis the *GT* model is used for convenience.

According to the *GT* model the asperities are assumed to have spherical caps of uniform radius β, whose heights above a mean datum have a statistical distribution $\phi(z)$, deform elastically and independently following the Hertzian theory. The contact load P required to compress an individual asperity by an amount of ω_a is given by:

$$P_a = \frac{4}{3} E\beta^{1/2}\omega_a^{3/2} \tag{4.1}$$

E is the effective elastic modulus as was defined in Eq. (3.5). If such a nominally flat rough surface is in contact with a smooth flat surface at a separation d, the effective pressure p between them is:

$$p = \frac{4}{3}\eta_s E\beta^{1/2}\int_d^\infty (z-d)^{3/2}\phi(z)dz \tag{4.2}$$

where η_s is the asperity density i.e. the number of asperity per unit area N/A_0.

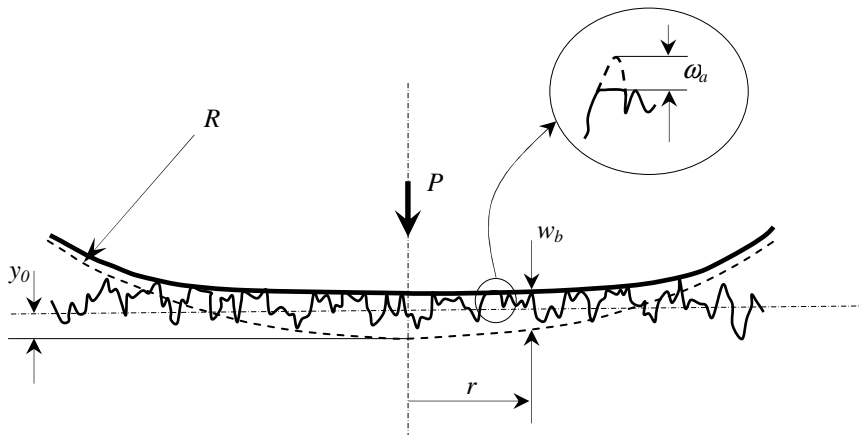

FIGURE 4.1: *Contact of a nominally flat rough surface with a smooth sphere, after* [4] *and* [5].

The geometry of the contact of a rough surface with a smooth sphere is shown in a diagram in Fig. 4.1. A datum is taken at the mean level of the rough surface. For the sphere, the profile of the undeformed sphere relative to the datum is defined by:

$$y = y_0 - \frac{r^2}{2R} \tag{4.3}$$

When the contacting surfaces start to be compressed there will be deformations in the asperities ω_a and a deformation of the bulk w_b, hence the separation between the two surfaces is given by:

$$d(r) = w_b(r) - y(r) = -y_0 + \frac{r^2}{2R} + w_b(r) \tag{4.4}$$

If the asperity deformation is assumed to be elastic, substituting of Eq. (4.4) into Eq. (4.2) yields the effective pressure at radius r as:

$$p(r) = \frac{4}{3}\eta_s E \beta^{1/2} \int_d^\infty \{z_s - d(r)\}^{3/2} \phi(z_s) dz_s \tag{4.5}$$

where z_s is the height of the asperity summit above the datum. The bulk deformation w_b is related to the effective pressure $p(r)$ by the equations for the axi-symmetric deformation of an elastic half-space [4] and is written as:

$$w_b(r) = \frac{4}{\pi E} \int_0^a \frac{t}{t+r} p(t) \mathbf{K}(k) dt \tag{4.6}$$

where **K** is the first kind complete elliptical integral with argument k:

$$k = \frac{2(rt)^{1/2}}{r+t} \tag{4.7}$$

By using iterative numerical techniques, Greenwood and Tripp [5] solved Eqs. (4.4), (4.5) and (4.6) to find the effective pressure distribution $p(r)$. The solution depends upon two independent non-dimensional parameters α and μ:

$$\alpha = R_{qs} \left(\frac{16RE^2}{9P^2} \right)^{1/3} \tag{4.8}$$

$$\mu = \frac{8}{3}\eta_s R_{qs} (2R\beta)^{1/2} \tag{4.9}$$

where R_{qs} is the r.m.s. roughness of the summits, R is the radius of the sphere. E is the reduced elasticity modulus, P is the normal load, η_s is the number of asperity per unit area and β is the radius of the asperities.

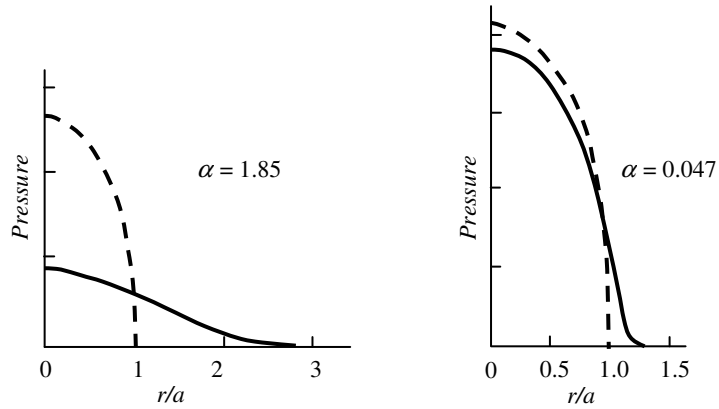

FIGURE 4.2: *Effective pressure distribution and effective contact area (solid line) of the contact of a nominally flat rough surface with a smooth sphere, after [4] and [5]. Dashed line is based on the Hertz theory (smooth surfaces).*

The pressure distributions calculated by *GT* [5] for two different values of α are shown in Fig. 4.2. It can be seen that for small values of α, the asperity deformation is small compared to the bulk deformation, whereupon the pressure distribution is close to the Hertz theory. The effect of asperities becomes significant when α is large where the contact pressure is reduced and is spread over a wider area than according to the Hertz theory.

Figure 4.3 shows the fraction of the central effective pressure $p(0)$ and the maximum Hertzian pressure p_0 as a function of the parameter α for two values of μ which bracket most practical engineering surfaces. It is clear from Fig. 4.3 that the parameter α is the primarily governing factor to predict the effect of surface roughness on the effective contact pressure, while the detailed geometry of the surface expressed by the parameter μ has a secondary effect. The effective pressure decreases as the roughness increases, and consequently, the ratio of the deformation of the asperities to the bulk increases. This contact problem has been analyzed by Mikic and Roca [8] by assuming that the asperity deforms plastically. However, results showed that the difference between their theory and the *GT* theory is small.

For the unloading case it is, of course, interesting to evaluate the plastic deformation of the contacting surfaces. In general, for smooth surfaces initial yielding occurs when the maximum or central Hertz pressure equals:

$$p_{0-y} = KH \tag{4.10}$$

Tabor [10] proposed that the value K in Eq. (4.10) is to be 0.6. Other researchers found that the K value depends on the Poisson's ratio v, see Section 3.2. However, the difference of the K value between the proposed models is small. For given contact conditions one is able to predict the contact deformation behavior. If the effective maximum or central pressure is larger than KH, bulk plastic deformation occurs and if the effective central pressure is lower than KH, plastic deformation may happen at asperity level. A plot of this map as a function of the surface roughness will be given along with the experimental results in the next section.

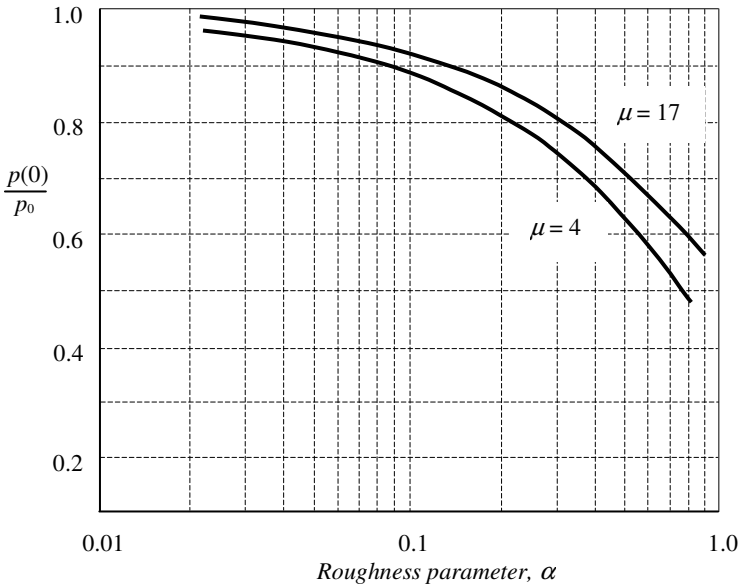

FIGURE 4.3: *Ratio of central effective pressure to maximum Hertz pressure as a function of roughness parameter α and μ, after* [4] *and* [5].

4.3 Experiment on the surface asperity and bulk deformation

4.3.1 Specimens

Hardened steel spheres (H = 7.5 GPa, E = 210 GPa and v = 0.3) with a diameter of 10 mm were used as a hard smooth spherical indenter. The deformable flat specimens used were made from aluminium (H = 0.24 GPa, E = 75.2 GPa and v = 0.34) and brass (H = 1.2 GPa, E = 105 GPa and v = 0.34). The sphere specimens have a center line average roughness R_a of about 0.01 μm and the average roughness of the flat specimens varied from about 0.1 to 2.5 μm.

4.3.2 Experimental details

The matching and stitching procedure (see Sub-section 3.5.1 and Appendix C) is utilized in these experiments. Experiments were performed on a setup as shown in Fig. 4.4. The maximum load which could be applied to this setup was about 30 N. Before doing any test, the spherical and flat specimens were cleaned with acetone and dried in air.

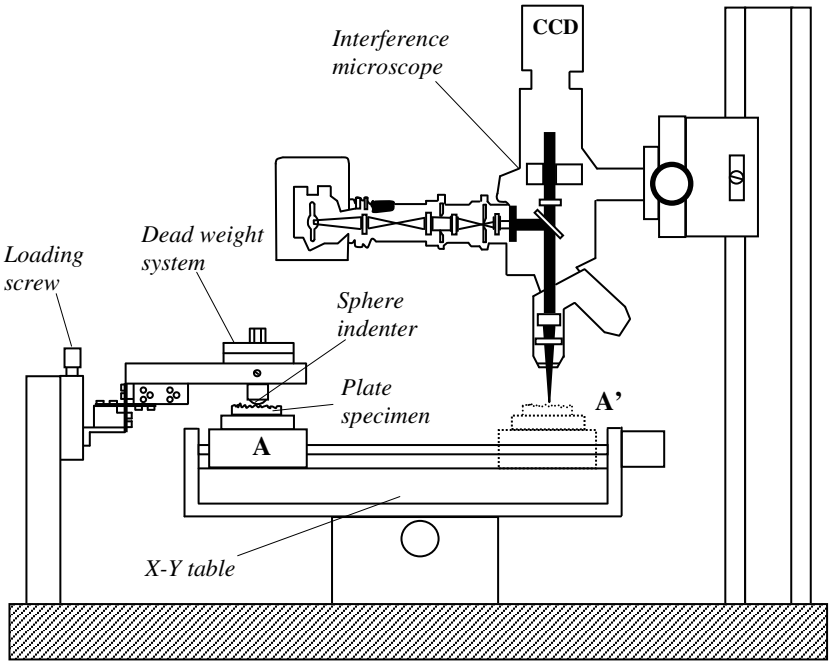

FIGURE 4.4: *Experimental setup.*

An optical interference microscope was used to measure the three-dimensional surface roughness. An X-Y table which is controlled by stepper motors was employed to position the flat specimen from the loading position (position **A**) to the surface measuring position (position **A'**) and the other way around. The measurement sequence is as follows. First, the flat surface was measured under the optical interference microscope. The number of the stitching images which should be taken depends on the predicted contact area and the chosen magnification of the interferometer. After finishing the surface measurement in position **A'** the flat surface was moved to the loading position **A**. In this loading position the statically mounted sphere specimen was moved down by the loading screw and subsequently loaded by the dead weight load system. To reduce the effect of friction, the contact region was lubricated. The load was applied to the sphere specimen for 30 seconds and then unloaded. Prior to measuring the after loading contact area with the optical interference microscope, again the spherical and flat specimens were cleaned and dried. After taking all the surface images data, the matching and stitching calculation was performed separately by a personal computer.

4.3.3 Experimental results

4.3.3.1 Experiment on aluminium surfaces

Figure 4.5 shows the measurements' results of the aluminium flat surfaces before and after an experiment for load = 4 N, $\alpha = 0.86$ and $\mu = 6$. The matching and stitching results of this surface can be seen in Fig. 4.6a. It is clear from Fig. 4.6 that bulk deformation occurs as indicated by the different datum of the difference image following the shape of the spherical indenter. Figure 4.6b shows this phenomenon more clearly. As can be seen, the asperities are almost undeformed, whereas it is clear that the bulk is deformed. This is referred to as asperity persistence in which the plastic deformation of the asperity is very small compared to the bulk deformation.

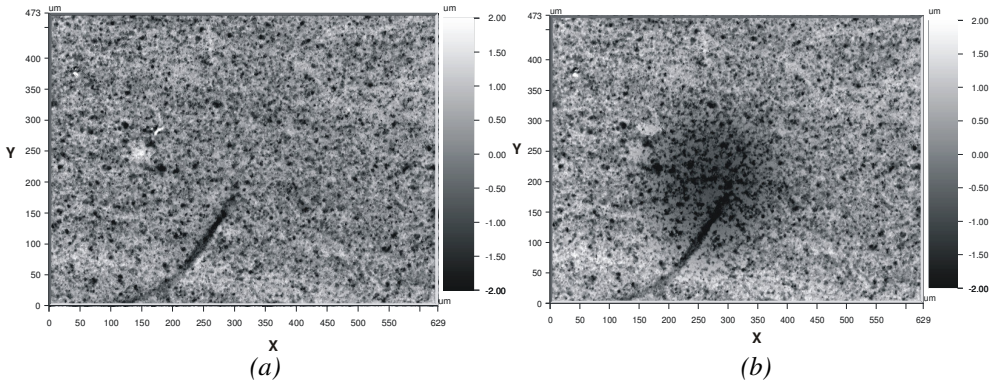

(a) *(b)*

FIGURE 4.5: *Surface measurements of an aluminium flat surface, load = 4 N, $\alpha = 0.86$ and $\mu = 6$. (a) Before experiment and (b) after experiment.*

Figure 4.7 shows the example of the matching and stitching in the experimental results where deformation takes place both in the asperities and bulk. In this case, the asperities and bulk deformation are comparable, therefore, in the difference image (Fig. 4.7a) the shape of the bulk deformation as in Fig. 4.6a is present, along with the local shape like archipelago which corresponds to the difference of the asperities deformation.

An example of experimental results of plastic deformation on asperity level without any bulk plastic deformation of the aluminium surface is shown in Fig. 4.8. Here, the bulk deformation is not present as can be seen in the difference image of Fig. 4.8a. The deformation takes place in the asperities only.

For all the experimental results, it can be seen that the matching and stitching performance is very good. The presence of a small scatter in the difference profile is due to the noise of the measurement. However, the important information or the global shape of the difference profile is very clear so that the plastic deformation behavior can be evaluated easily. It should be noted here that for all the present experiments, the value of σ_s was taken from the combined roughness of the surface [11], $R_q = (R_{q1}^2 + R_{q2}^2)^{1/2}$, where R_{q1} and R_{q2} are the r.m.s. roughness of surface 1 and surface 2, respectively. The parameters η_s

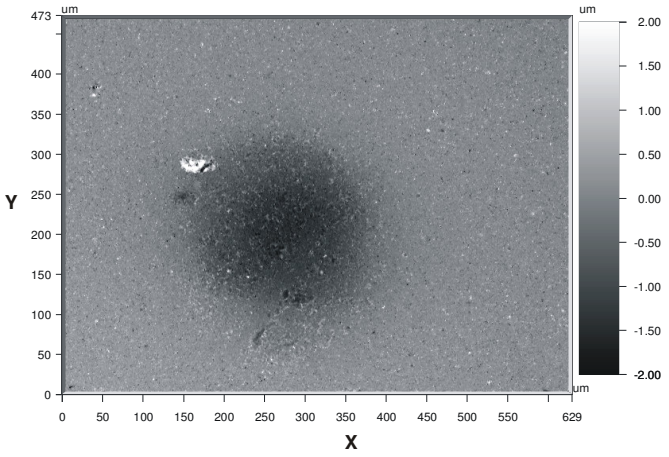

(a)

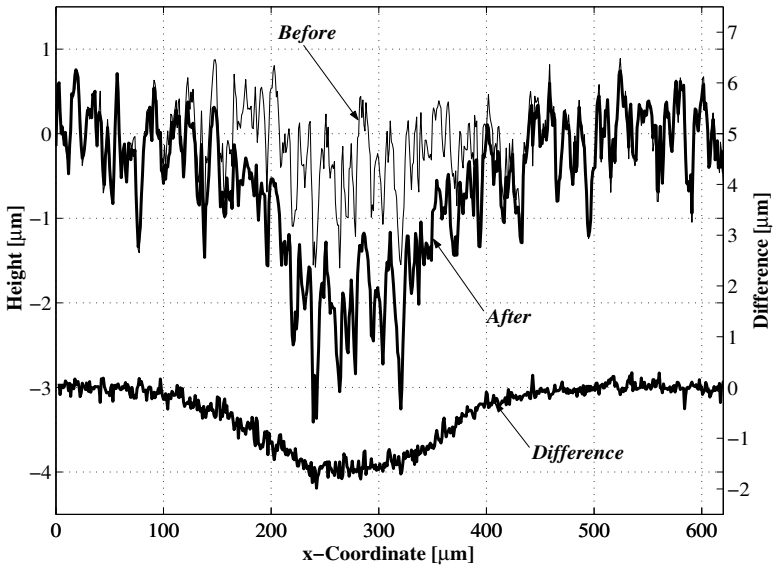

(b)

FIGURE 4.6: *Matching and stitching results of an aluminium surface, load* = 4 *N,* $\alpha = 0.86$ *and* $\mu = 6$*. (a) Difference* 3*D image of Figure* 4.5 *and (b) Profile at y* = 200 μm*.*

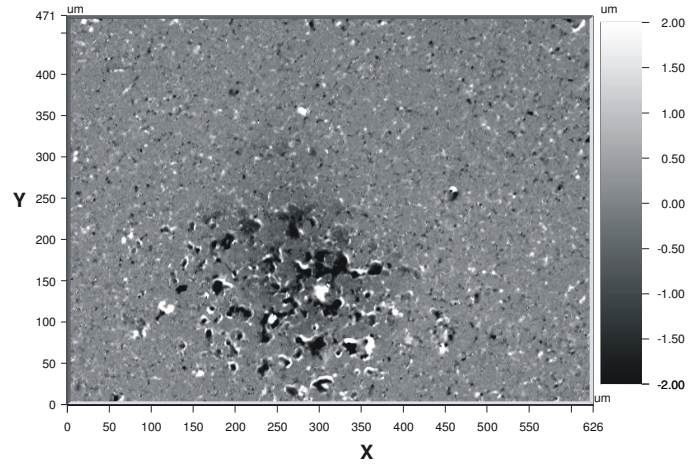

(a)

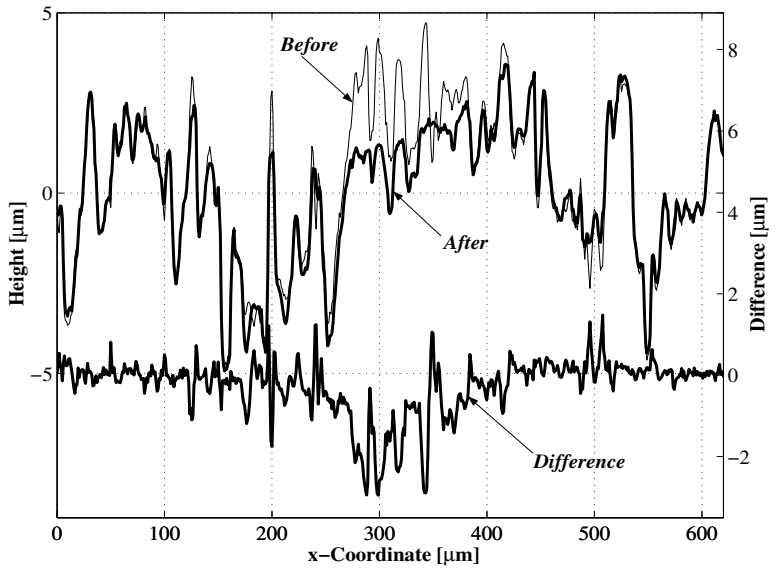

(b)

FIGURE 4.7: *Matching and stitching results of an aluminium surface, load* = 4 *N,* $\alpha = 2.7$ *and* $\mu = 10$*. (a) Difference* 3*D image and (b) Profile at y* = 158 μm*.*

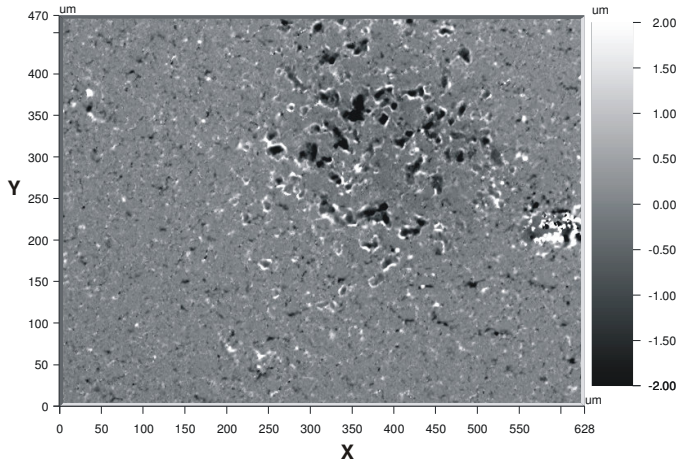

(a)

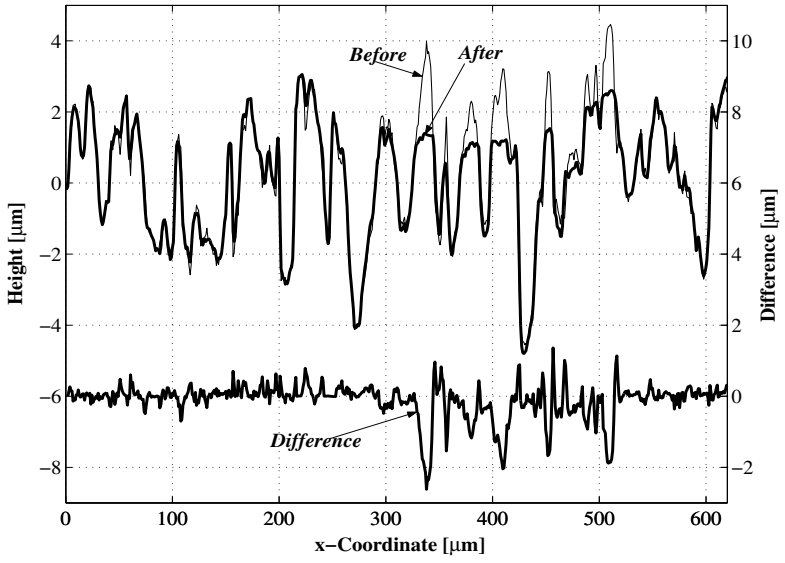

(b)

FIGURE 4.8: *Matching and stitching results of an aluminium surface, load = 4 N, $\alpha = 2.84$ and $\mu = 12$. (a) Difference 3D image and (b) Profile at y = 320 μm.*

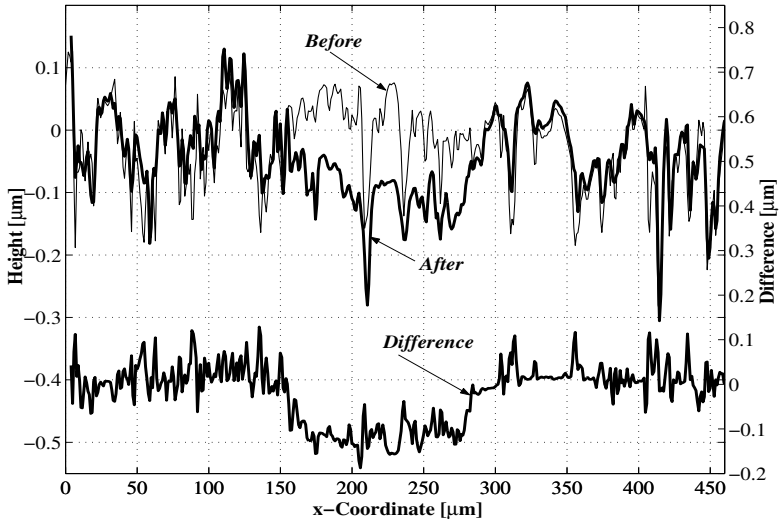

FIGURE 4.9: *Matching and stitching results of a brass surface, load* = 12 *N,* $\alpha = 0.09$ *and* $\mu = 11$.

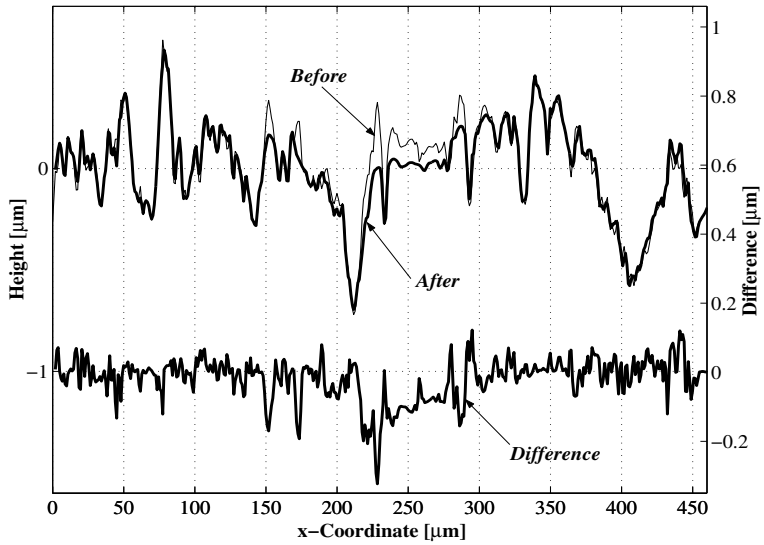

FIGURE 4.10: *Profile of the matching and stitching results of a brass surface, load* = 12 *N,* $\alpha = 0.2$ *and* $\mu = 13$.

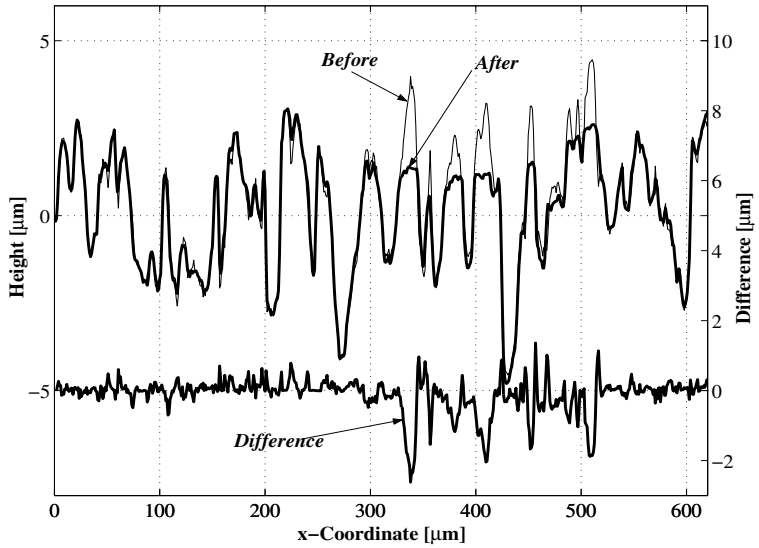

FIGURE 4.11: *Profile of the matching and stitching results of a brass surface, load* = 12 *N,* $\alpha = 0.5$ *and* $\mu = 7$.

and β were calculated based on a 'nine point summit' [12] in order to determine the parameter μ.

4.3.3.2 Experiment on brass surfaces

Similar results were also found for the brass surfaces. Example results of the matching and stitching results for bulk deformation, combined bulk and asperity deformation and asperity deformation are shown in Fig. 4.9, Fig. 4.10 and Fig. 4.11, respectively.

4.3.4 Discussion

Experimental results showed that even for the same Hertzian contact pressure the plastic deformation state behaves differently depending on the roughness of the surfaces. The parameter α increases proportionally to the roughness of the surfaces, and as a result, the central effective pressure decreases. According to Eq. (4.10), plasticity of the bulk surface takes place when this central effective pressure is larger than the constant K times the hardness of the flat surface H. The experimental results presented are in line with the theoretical prediction of α in Eq. (4.8) and the central effective pressure curves of Fig. 4.3. It is unimportant whether the asperities deform elastically [5] or plastically [8] in this statistical approach.

The results also showed the minor effect of the parameter μ. For bulk deformation of brass as was shown in Fig. 4.9, for instance, the parameter $\mu = 11$ corresponds to the fraction of the central effective pressure and the maximum Hertz pressure $p(0)/p_0$ of about

0.925 (α = 0.09). If the parameter μ is taken to be 4, the ratio $p(0)/p_0$ = 0.9 and when the parameter μ is equal to 17, the ratio $p(0)/p_0$ = 0.93 for the same α. Indeed, the difference in the ratio $p(0)/p_0$ becomes larger when the two extremes of the parameter μ are taken as the parameter α increases, however, the difference is not that dramatic.

Many experiments were performed in order to gain more insightful results for a certain range of surface roughness. These results are plotted in Fig. 4.12 for constructing the plastic deformation indentation behavior map where the ratio $p(0)/H$ (instead of p_0/H) is plotted as a function of the surface roughness R_q. In this figure the points Al_A, Al_B , Al_{AB}, Br_A, Br_{AB} and Br_B correspond with the contact condition locations of aluminium and brass as was shown in Fig. 4.6 to Fig. 4.8 and Fig. 4.9 to Fig. 4.11 (the index *A*, *B* and *AB* refer to asperity, bulk and combined asperity-bulk plastic deformation, respectively). The ratio of the non-dimensional effective maximum contact pressure $p(0)/H$ reaches the value larger than 1 which contradicts the indentation results of Tabor [9]. This is because the calculation of the effective maximum contact pressure is based on the elastic contact theory. The map shows that for contact conditions located above the ratio $p(0)/H$ = 0.6, bulk plastic deformation is observed, whilst below the ratio $p(0)/H$ = 0.6, asperity deformation is attained for the whole range of the surface roughness tested. The plastic deformation of both the asperity and the bulk is observed for the contact conditions near the line $p(0)/H$ = 0.6.

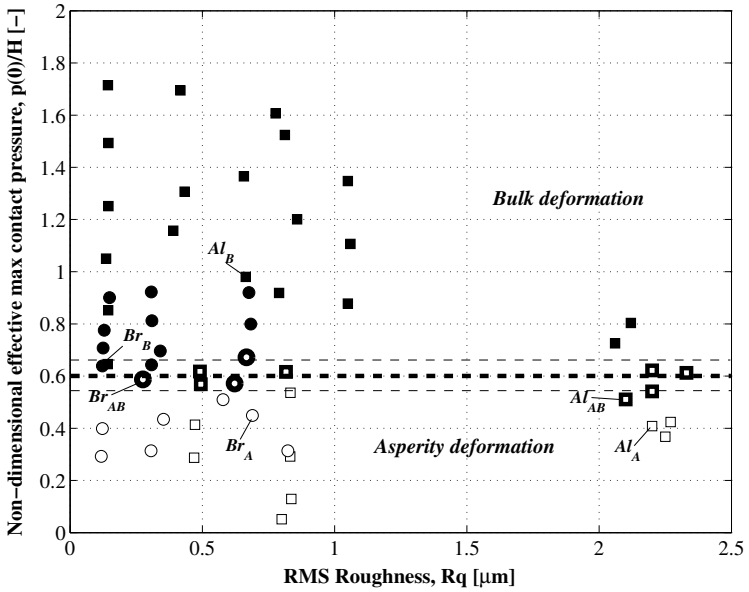

FIGURE 4.12: *Plastic deformation behavior of the contact between a rough surface and a smooth curved body. Square symbols are for aluminium and circle symbols are for brass where the full filled symbols indicating bulk deformation, the open symbols indicate asperity deformation and the half-filled symbols represent a combined deformation of the asperity and the bulk.*

For practical engineering purposes it is very convenient to build an expression in determining the value of the ratio $p(0)/p_0$ instead of using the graph in Fig. 4.3. Since the parameter μ has a secondary effect on the ratio $p(0)/p_0$ and for $\mu = 4$ and $\mu = 17$ brackets most of the engineering surfaces a curve was found to fit the data as:

$$\frac{p(0)}{p_0} = 1 - \exp\left(-\frac{2}{3\alpha^{3/5}}\right) \tag{4.11}$$

where α is as defined in Eq. (4.8). It was discussed earlier that if $p(0)/H$ is larger than 0.6, bulk deformation does occur and for values of $p(0)/H$ lower than 0.6, asperity deformation prevails, therefore, criterion can be made for the asperity deformation to occur as:

$$C_m = \frac{p(0)}{H} = \frac{p_0}{H}\left[1 - \exp\left(-\frac{2}{3\alpha^{3/5}}\right)\right] < K \tag{4.12}$$

where K is the hardness coefficient in which the first yield occurs and p_0 is the maximum Hertzian contact pressure:

$$p_0 = \left(\frac{16PE^2}{\pi^3 R^2}\right)^{1/3} \tag{4.13}$$

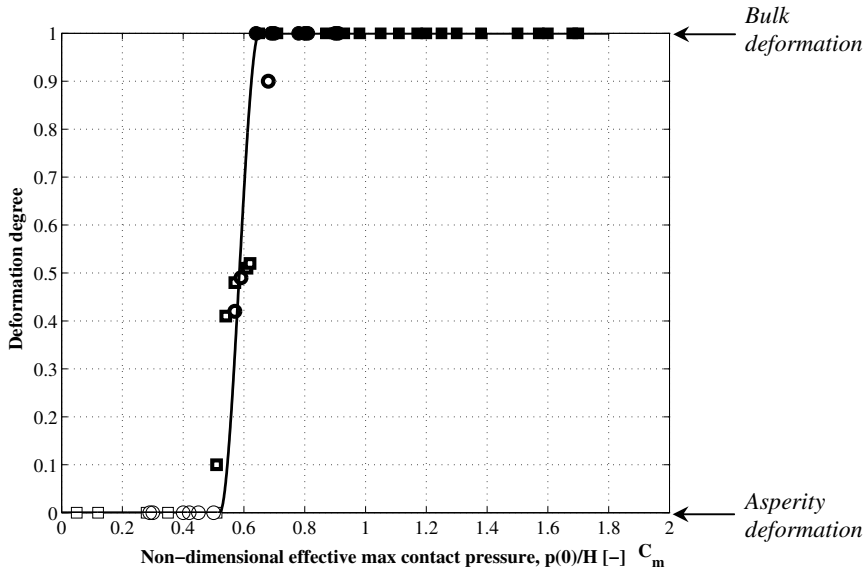

FIGURE 4.13: *Deformation degree of the contact between a rough surface and a smooth curved body. Symbols have the same meaning as in Figure 4.12.*

If the analysis of Fig. 4.12 is taken carefully, there is a relatively large regime where plastic deformation takes place in both the asperities and the bulk. This regime start from the value of about $p(0)/H = 0.52$ to $p(0)/H = 0.65$ as is bracketed by the thin dashed lines. In the plot of Fig. 4.12 there is no variation between $p(0)/H$ along with the variation of R_q in deformation mode (asperity versus bulk deformation) as is indicated by the straight line. This is because the parameter R_q has been calculated inclusively in $p(0)$. It is very convenient to introduce the degree of deformation mode as another criterion as is shown in Fig. 4.13. The degree of deformation, D_d, is defined as follows:

$$\begin{aligned} D_d &= 0 && \text{for} \quad C_m \le 0.52 \\ D_d &= 3\left(\frac{C_m - 0.52}{0.13}\right)^2 - 2\left(\frac{C_m - 0.52}{0.13}\right)^3 && \text{for} \quad 0.52 < C_m \le 0.65 \\ D_d &= 0 && \text{for} \quad C_m > 0.65 \end{aligned} \tag{4.14}$$

where C_m is as defined in Eq. (4.12). The expression for the mixed-deformation mode as is presented in Eq. (4.14) was chosen in order to have continuity in the transitions. If plastic deformation takes place on asperity level only, the degree of deformation is 0, if plastic deformation solely occurs in the bulk, the degree of deformation equals 1, but if plastic deformation takes place in both the asperities and the bulk, the degree of deformation varies from 0 to 1 depending on the proportion of the plastic deformation between asperity and bulk, which is controlled by C_m (= $p(0)/H$).

4.3.5 The effect of thickness

In 1948, Moore [13] demonstrated the remarkable persistence of surface asperities for the line contact situation. Moore pressed a highly polished hard steel roller against a face-turned copper plate. The copper had previously been work hardened so that it was not capable of much additional work hardening and therefore an additional hardness of the asperities due to turning was not expected. Moore showed that even for very high loads the ridges in the copper remained clearly visible in the indentation profile as discussed in the previous section for the circular contact situation.

Milner and Rowe [14] performed an experiment where a ‘penny-shaped’ rough surface specimen is compressed between smooth anvils, for which bulk plastic flow implies that every element of the specimen deforms plastically. Depending on the relative hardness, the asperities were either flattened or ‘pressed into’ the smooth surface.

Based on the work of Moore [13] and Milner and Rowe [14], Greenwood and Rowe [15] performed an experiment to study the effect of the thickness on the flattening of surface asperities under bulk plastic flow. In their experiment, a rough flat surface of a cylinder (R_a = 1 μm) was pressed against a hard smooth steel (R_a = 0.03 μm) anvil. Profiles of the deformed surface after 10% compression of tall and ‘penny-shaped’ cylinders were compared which implied different specimen thickness. In both cases, there is a bulk dented area around the center of the contact. However, the degree of asperity deformation is different. According to Eq. (E.8) in Appendix E, the maximum contact pressure occurs at

the center of the contact; therefore, the deformation of the bulk surface is higher around the contact center. If there is no sticking in the contact interface and the coefficient of friction is not zero, the required mean contact pressure decreases as the thickness of the blank increases, see Figure 4.14. This behavior becomes more pronounced as the coefficient of friction increases. Up to a certain value of the coefficient of friction, the assumption of pure sliding is invalid as the sticking mechanism start to occur. Greenwood and Rowe [15] explained that a degree of flattening of the asperities for a thin 'penny-shaped' cylinder occurs because the plastic deformation extends to the surface, while for the thick or tall cylinder, the plastic deformation still occurs in the bulk (below the surface), therefore, the asperities persist.

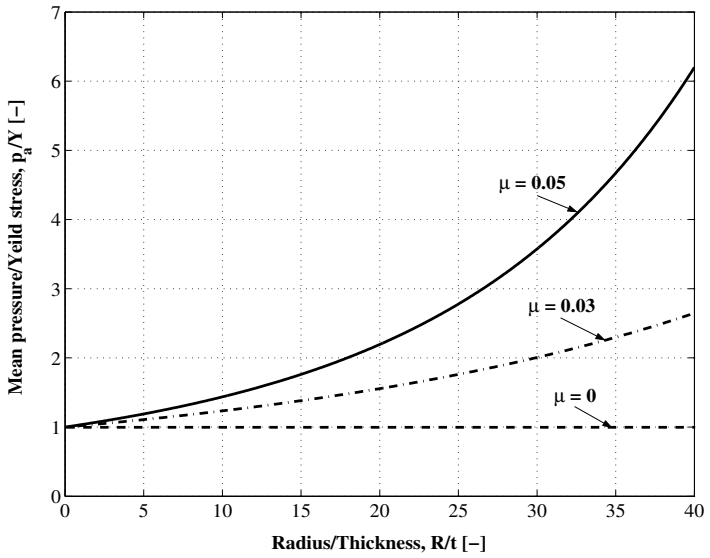

FIGURE 4.14: *Non-dimensional mean pressure as a function of non-dimensional thickness of compression of a blank specimen.*

Kimura and Childs [16] studied the asperity deformation under bulk plastic straining conditions based on the velocity field analysis theoretically. The asperities were modeled by an array of ridges. It was found that the ratio of the real contact area to the nominal contact area, which implies the degree of asperity flattening, is sensitive to the thickness t of the specimen when $t/\lambda < 15$ in which λ is the wavelength of the surface ridges.

Summarizing, the effect of the material or specimen thickness on the flattening of surface asperities described in literature, were studied based on bulk plastic flow or very high load. This idea is not of interest in the present study, since bulk deformation is avoided. However, it is also interesting to study the effect of the material thickness on the deformation behavior as was discussed in the previous section.

Experiments were done in the same setup and in the same material as was described in Sub-sections 4.3.1 and 4.3.2. For the aluminium two samples were used with a

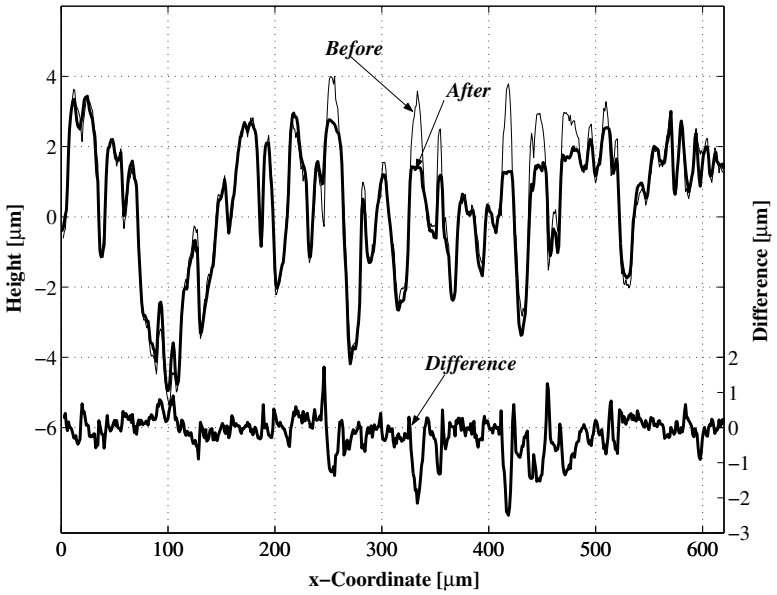

FIGURE 4.15: *Matching and stitching results of an aluminium surface, t = 0.3 mm, load = 4 N, α = 3.8 and C_m = 0.52.*

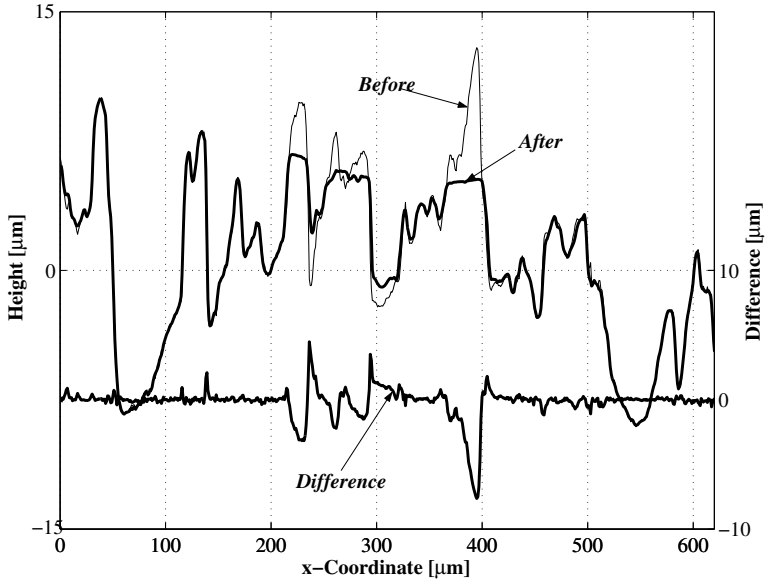

FIGURE 4.16: *Matching and stitching results of an aluminium surface, t = 10 mm, load = 4 N, α = 6.2 and C_m = 0.41.*

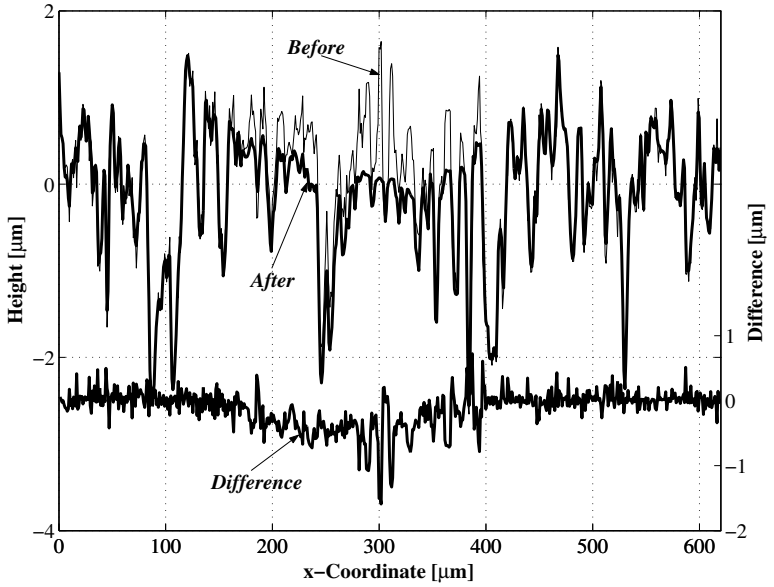

FIGURE 4.17: *Matching and stitching results of a brass surface, t = 0.05 mm, load = 40 N, α = 0.26 and C_m = 0.8.*

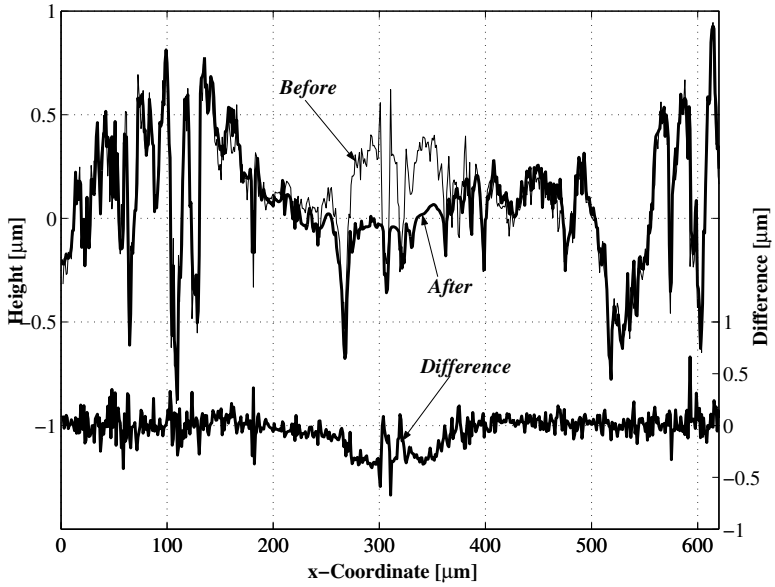

FIGURE 4.18: *Matching and stitching results of a brass surface, t = 8 mm, load = 40 N, α = 0.22 and C_m = 0.83.*

thickness of 0.3 mm and 10 mm and for the brass samples of 0.05 mm and 8 mm thickness were used. Results of the experiments studying the effect of thickness on the deformation mode are presented in Figs. 4.15 and 4.16 for aluminium surfaces and Figs. 4.17 and 4.18 for Brass surfaces. As can be seen, all the parameters involved follow the criteria discussed in Sub-section 4.3.4, Eq. (4.12), where the thickness parameter is not considered. It can be concluded that for the contact between a rough surface against a smooth spherical body without bulk plastic straining conditions, there is no thickness effect.

4.4 Deterministic elastic-plastic multi asperity contact model

In this section, the new developed elliptic elastic-plastic single asperity contact as was presented in Section 3.6 will be extended to the multi asperity or deterministic rough surface contact. Bulk deformation is not considered in the analysis, because the topic of this thesis is running-in due to surface roughness change.

4.4.1 Overview of the contact models of rough surfaces

The interest in modeling the contact of rough surfaces is very high because of its importance with respect to many tribological problems. This can be seen in the review papers of Bhushan [17], Liu *et al.* [18] and Adams and Nosonovsky [19]. Most of the models consider a hard perfectly smooth surface in contact with a deformable rough surface.

Roughness always exists on the surfaces. Perfectly smooth surfaces are very rare in nature. A surface is composed of large number length scales that are superimposed on each other [20]. Although surface roughness is intrinsic, measured roughness is extrinsic, depending on the sampling lengths and intervals of the measuring devices. The complex nature of roughness, together with elastic-plastic deformation, strain hardening, asperity interaction, et cetera, will contribute to the difficulty of modeling the contact of rough surfaces. However, several attempts have been conducted in this field.

Modeling the contact of rough surfaces was pioneered by Greenwood and Williamson [6]. In their model a nominal flat surface is assumed to be composed with spherical asperities of the same radius, and the height of the asperities is represented by a well-defined statistical distribution function (i.e. Gaussian). The contact analysis is based on the Hertz theory [3] where the asperities deform elastically. This basic elastic asperity-based contact model has been extended to the contact of rough curved surfaces [5], the contact of two nominally flat rough surfaces with misaligned asperities [21], the contact of rough surfaces considering the distribution of radii of the asperities [22] and elliptic paraboloidal surfaces [23]. However, the aforementioned models are devoted to the elastic contact situation. The basic plastic contact model which is known as the profilometric model or surface micro-geometry model has been introduced by Abbott and Firestone [24]. Based on experimental results, Pullen and Williamson [25] proposed a volume conservation model for the fully plastic contact of a rough surface. Kucharski *et al.* [26] confirmed this model by the finite element analysis. In order to bridge the two extreme deformation models, elastic and fully plastic, Chang *et al.* (*CEB* model) [27] developed an elastic-plastic contact model of rough surfaces based on volume conservation of the plastically deforming

asperities. In the *CEB* model there is no transition regime from the elastic to the fully plastic contact regime, while Johnson [4] showed, based on the analysis of the indentation of a sphere on a flat, that there is a long transition regime from the point of initial yielding to the fully plastic state. Therefore, Zhao *et al.* (*ZMC* model) [28] proposed a new elastic-plastic contact model of rough surfaces which includes this transition by mathematical smoothing expressions to incorporate the elastic and fully plastic contact parameters. Kogut and Etsion (*KE* model) [29] performed a detailed finite element analysis on the elastic-plastic contact of a sphere and a rigid flat and then extended this to the contact of rough surfaces [30]. The empirical coefficients for the dimensionless relations for contact load, contact area and mean contact pressure as a function of contact interference have been provided. However, the analysis is limited up to the onset of the fully plastic state. Similar work has been done recently by Jackson and Green (*JG* model) [31, 32]. Because the surface textures of most of the engineering surfaces are oriented with the direction of the relative motion of cutting tools to the surface, the different ellipticity ratios of the micro-contacts are formed according to the surface forming method. Several models have been proposed to extend the elastic-plastic isotropic contact model of rough surfaces into an anisotropic one. Horng [33], for instance, has extended the *CEB* model to the elliptical contact situation. Similar approaches have been performed by Jeng and Wang [34] in extending the *ZMC* model.

Most of the above statistical models can predict important trends on the effect of surface properties on the real contact area, however, its usefulness is limited by, for example, the simplified assumption about asperity geometry, height distribution and the difficulty in determining the statistical roughness parameters. With the advent of computer technology, a measured profile can be digitalized and used for contact simulation. Webster and Sayles [35] used the matrix inversion method and Rajendrakumar and Biswas [9] used the complex variables method to simulate the rough line contact situation. For the elastic contact of three-dimensional rough surfaces, numerical analyses have been done by many investigators such as Liang and Linqing [36], Ren and Lee [37] and Chang and Gao [38]. In these models, the contact between a smooth and a rough surface is modeled by considering asperities as bars. Equations which relate the elastic displacement of an asperity to the pressure imposed are applied.

Majumdar and Bhushan [39] and Bhushan and Majumdar [40] have developed an elastic-plastic contact model of rough surface based on fractal geometry. The idea comes due to the fact that the surface roughness parameters depend strongly on the resolution of the measuring instrument or any other form of filtering. By using the fractal geometry there is no scale dependence of the surface roughness, however, not all surfaces have fractal properties.

Summarizing, there are many studies devoted to model the contact of rough surfaces. However, much of the published models have assumed qualitative results such as Gaussian distribution of the roughness heights rather than a real measured distribution. Some models have been proposed to analyze the contact of rough surfaces deterministically by employing numerical methods. However, there are some shortcomings such as computational cost and the incorporation of contact deformation regimes. Most of the numerical contact models of rough surfaces consider elastic deformation; there are few models which include plastic deformation. It is difficult to gain a model considering the elastic-plastic deformation contact regime. In the present study, contact of rough surfaces is analyzed based on measured real surfaces. An analytical approach is used; hence the

calculation cost is reduced significantly. All the contact deformation regimes, elastic, elastic-plastic and plastic are considered in the analysis. The details of the method are described in the next section.

4.4.2 Deterministic contact model of rough surfaces

In a real rough surface, the asperities are not perfectly following certain shape geometry like spherical or paraboloidal, instead protrude randomly in the three-dimensional space. The radius of each asperity is not the same and in many cases the height distribution of the asperities does not follow the Gaussian distribution as is used by most of the statistical contact models of rough surfaces. In the present study, rough surfaces are modeled by an array of asperities with different radii and heights. Details of this deterministic model will be discussed further in the following sub-sections.

4.4.2.1 Asperity determination

The three-dimensional (3D) surface roughness data are obtained by an interference microscope as was shown in Fig. 4.4. The data contains a discrete presentation of the 3D surface roughness over a certain area depending on the measuring apparatus capability. These data will be processed to determine the asperities' location and geometry by using a certain method. There are several methods to evaluate the asperity parameters such as the nine-point summit method [12], volume conservation method [41], et cetera.

Greenwood [12] introduced a way to calculate the asperity properties using the peak or summit method. A summit is defined as a local surface height higher than its neighboring points. This leads to the definition of peak (4.19a), five-point summit (4.19b) and nine-point summit (4.19c). To minimize the probability of detecting a 'false summit' the nine-point summit definition is used.

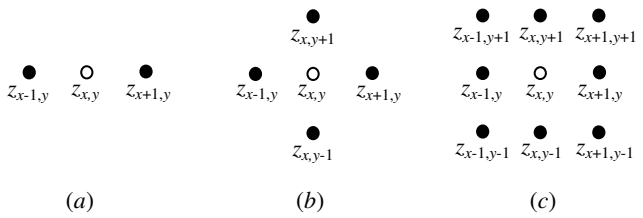

FIGURE 4.19: *Summit definitions.*

Based on these definitions the curvatures of the summit are defined as:

$$\kappa_x = \frac{1}{\beta_x} = \frac{z_{x-1,y} - 2z_{x,y} + z_{x+1,y}}{p_x{}^2} \tag{4.15}$$

$$\kappa_y = \frac{1}{\beta_y} = \frac{z_{x,y-1} - 2z_{x,y} + z_{x,y+1}}{p_y{}^2} \tag{4.16}$$

where κ and β are the curvature and the radius of asperity, respectively. The index x indicates the x-direction and the index y for y-direction. p_x and p_y are the pixel size or sample length in x-direction and y-direction, respectively. This method has been used extensively, for instance, to analyze the tribological aspects of the deepdrawing process [42], friction and wear of ceramics [43] and mixed lubrication of line contacts [44].

Masen *et al.* [45] proposed a method to define the asperity geometry by fitting the micro-contacts with paraboloids using the least square method. Masen [46] and de Rooij [41] used a volume conservation model for determining the contact geometry of the asperities. In this method, the micro-contacts of real rough surfaces are fitted by elliptical paraboloids where the initial volume of the micro-contacts is conserved as well as the area of contacts. Details of this method can bee seen in Appendix F. The curvatures of the elliptical paraboloid using this method are expressed as:

$$\kappa_x = 4\pi \frac{V}{A^2} \frac{L_y}{L_x} \tag{4.17}$$

$$\kappa_y = \kappa_x \left(\frac{L_x}{L_y} \right)^2 \tag{4.18}$$

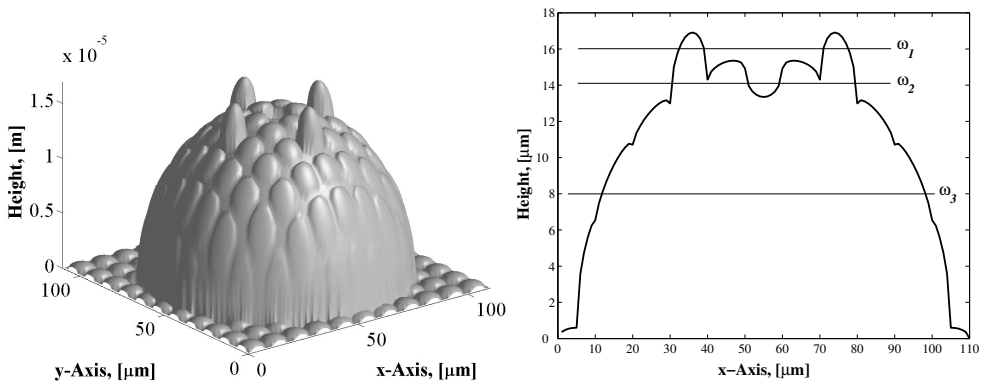

FIGURE 4.20: *3D surface asperities and its centered x-profile.*

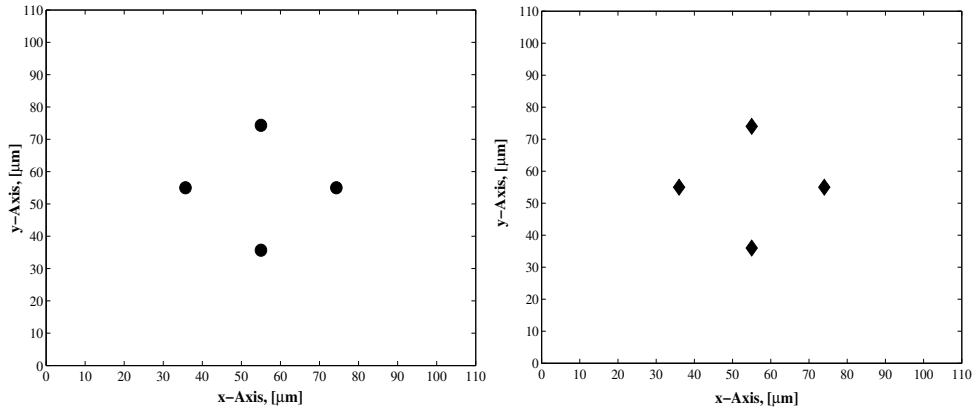

(*a*) (*b*)

FIGURE 4.21: *Location of the asperities for* $\omega = \omega_1$ *in Figure* 4.20*, (a) volume conservation method, (b) summit method.*

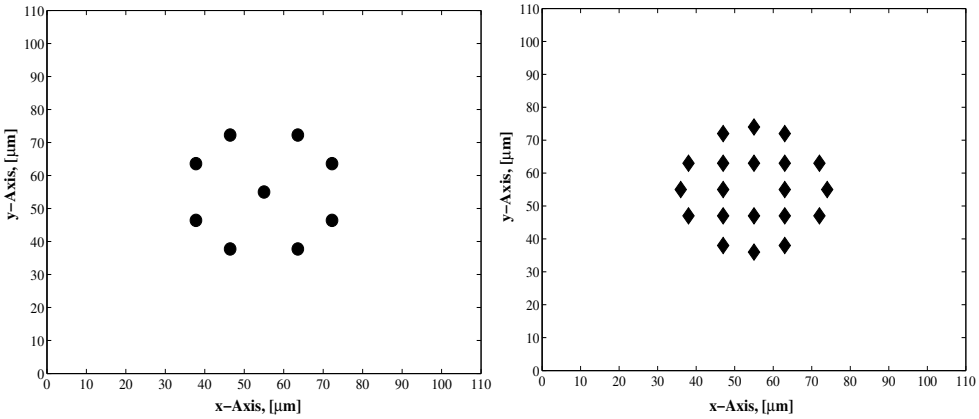

(*a*) (*b*)

FIGURE 4.22: *Location of the asperities for* $\omega = \omega_2$ *in Figure* 4.20*, (a) volume conservation method, (b) summit method.*

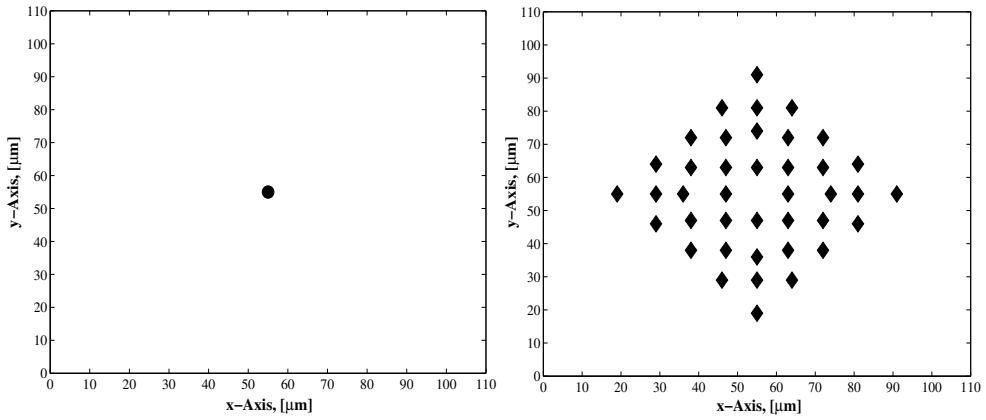

(*a*) (*b*)

FIGURE 4.23: *Location of the asperities for* $\omega = \omega_3$ *in Figure* 4.20*, (a) volume conservation method, (b) summit method.*

where V is the volume from the measured micro-contacts, A is the cross-sectional area of the micro-contacts and L_x and L_y is the length or diameter of the cross-sectional micro-contact area in x- and y-direction, respectively. The asperity geometry depends on the indentation or interference ω, and the location of the asperity is determined from the weighted center of the cross-sectional contact area. The curvatures change as the interference changes whilst in the summit method the geometry of the asperity is constant. This behavior is illustrated in Fig. 4.20 to Fig. 4.23. As can be seen from the figures, there is a clear difference between the summit method and the volume conservation method. The number of asperities in contact (micro-contacts) changes as the interference changes. In the summit method this number always increases, see Figs. 4.21b, 4.22b and 4.23b, and the geometry of the asperities in contact does not depend on the interference. For the volume conservation method, this number changes depending on the surface geometry, see Figs. 4.21a, 4.22a and 4.23a, and the geometry and location of the asperities in contact depend on the interference. For $\omega = \omega_3$ for example, there are 40 asperities in contact according to the summit method whilst for the volume conservation method this is only 1 large asperity. It is clear from Fig. 4.20 that the volume conservation method is much better than the summit method for $\omega = \omega_3$. This concludes that the summit method represents the micro-contacts well only for the very small interference whilst in the volume conservation method the micro-contacts are represented well for all interference; therefore, in the present study the latter is used.

After determining the asperity curvatures, Eqs. (4.17) and (4.18), another important parameter in the deterministic contact model is the asperity height. According to [41] the height of the asperity is determined from the maximum pixel height from the measured surface data within the cut-off contact area regime as is schematically shown in Fig. 4.24. When all the locations, the curvatures (or radii) and the heights of the asperities are determined, the calculation with the deterministic contact model can start.

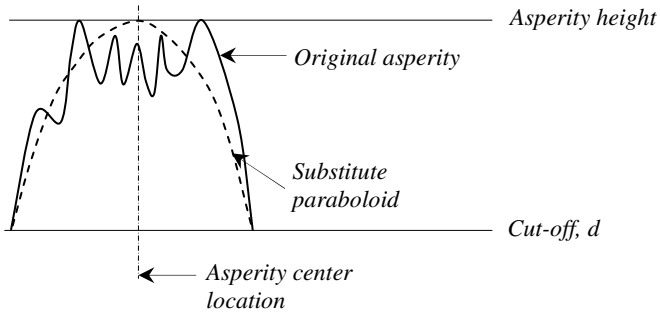

FIGURE 4.24: *Asperity height determination.*

4.4.2.2 Modeling procedure

The iterative procedure for analyzing the contact of rough surfaces based on the volume conservation method is shown schematically in Fig. 4.25. The 3D data of the contacting surfaces, $z(x,y)$, are taken from the roughness measurement apparatus. The material properties such as elasticity modulus E, Poisson's ratio v and hardness H of the surfaces are assumed to be the same as the bulk. To bring these surfaces into contact, load must be applied. In the present study, analysis of the contact is based on the separation; therefore, the load is calculated from the separation. For this purpose, a separation is given as an initial guess. At this separation, there will be a number of asperities in contact (micro-contacts). Subsequently, all the contact input parameters such as curvature, height and location of each asperity in contact are determined as was discussed previously.

Given all the contact input parameters, the contact load, the contact area, et cetera can be calculated readily from the analysis of a single asperity as was presented in Section 3.6.

Summation of all the micro-contact loads gives the macro-contact load (input load), therefore, an iterative procedure is applied by changing the separation until the difference between summation of all the micro-contacts and macro-contact load reach a certain criterion, ε. When the criterion is satisfied the iteration loop is stopped and the contact parameters such as load, contact area, plastic deformation, et cetera for each asperity are taken from the last separation.

The roughness data obtained by the optical interferometer normally suffer from measurement errors. One of the errors is in the spots with high local surface slopes where the interferometer is not able to measure. This type of spots is referred to as 'missing points'. Another error is the unnaturally local surface heights which are so-called 'spikes'. Due to these errors, the measured roughness data should be preprocessed before they can be used for input of the contact model. The heights of the missing points are estimated by applying an interpolation method from their correctly measured neighboring points [42]. It is not easy to remove the 'spikes' error because it is not clear whether it is a measurement error or a real measurement result. The removal of these is normally done by filtering the surface with heights less than three times the r.m.s. roughness for the lower limit and more than three times the r.m.s. roughness for the upper limit.

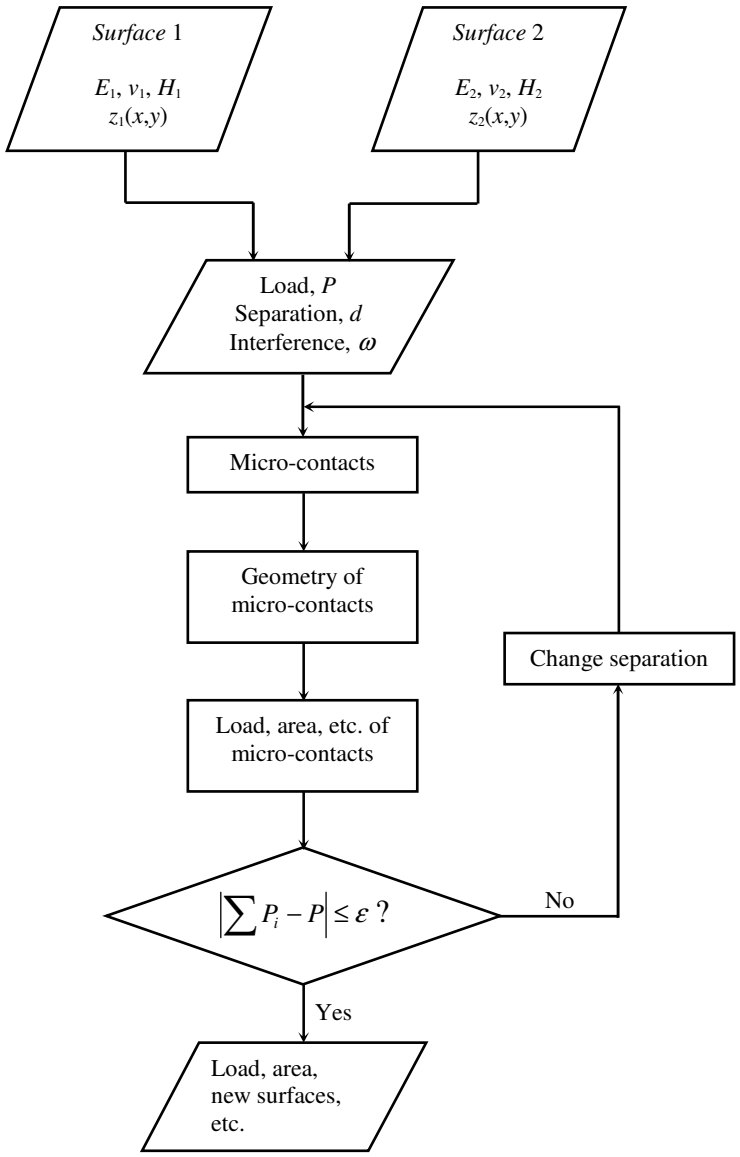

FIGURE 4.25: *Flow diagram of the volume conservation method contact calculation of rough surfaces.*

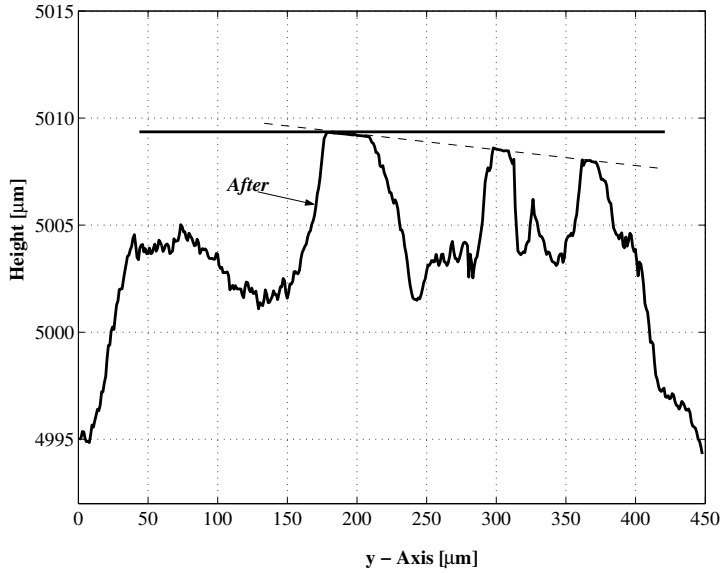

FIGURE 4.26: *Profile of the contact between a smooth flat against a rough ball when the center of the ball is on the left-side of the 'true' one.*

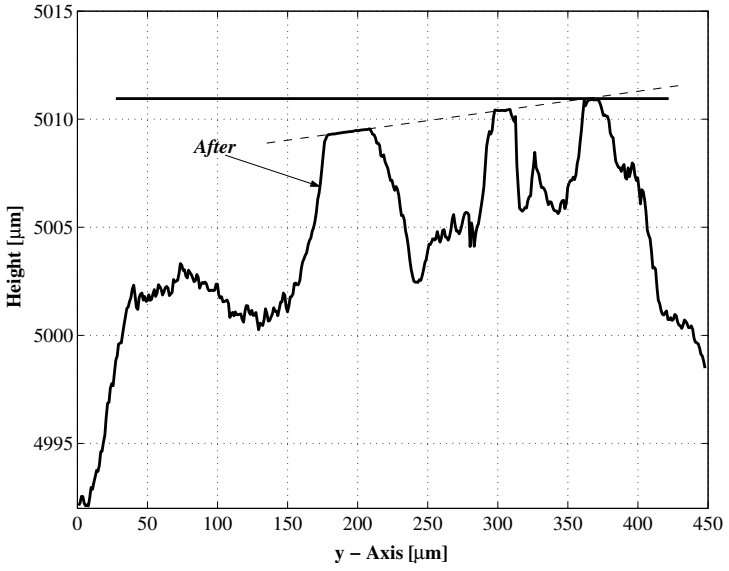

FIGURE 4.27: *Profile of the contact between a smooth flat against a rough ball when the center of the ball is on the right-side of the 'true' one.*

One of the most important topics in modeling the contact of rough surfaces deterministically is to determine the location of the contacting bodies. As an example, the contact of a rough flat surface with a smooth spherical surface will be used for explanation. In this contact situation, the coordinate of the sphere in contact with the flat should be determined properly before applying the rough surfaces contact model. For this purpose, an iterative method is introduced. It is relatively difficult to estimate the location of the center of the ball indenter based on the deforming flat surface. Therefore, the contact problem as was presented in Fig. 4.1 is converted into an equivalent one. In this case, the geometrical contact of a smooth ball against a rough surface is now converted into the contact of a smooth flat against a rough ball surface. Figure 4.26 shows the *y*-profile deformation results of a rough ball after being in contact with a hard smooth flat (thick solid line). As can be seen, the magnitude of the deforming asperities is not flat but follows the straight line (thin dashed line) with a positive value of the slope, which means that the 'true' center of the ball indenter is somewhere on the right-side from the present position or the position of the present indenter is on the left-side of the 'true' one. Similarly, when the present position of the ball indenter is in the right-side of the 'true' one, as is shown in Fig. 4.27, the magnitude of the plastic deforming asperities follows the straight line with a positive value of the slope. By changing the point location iteratively for *x* and *y* directions, the coordinate of the contact center of the ball indenter can be determined. This is indicated by the flat magnitude of the plastic deformation of the asperities.

4.5 Experiment on the deterministic contact of rough surfaces

4.5.1 Experimental procedures

A hard and smooth curved surface in contact with a deformable nominally flat rough surface is used in the present experiments. A hardened steel sphere (H = 7.5 GPa, E = 210 GPa and ν = 0.3) with a diameter of 10 mm and the average roughness R_a = 0.01 μm was used as a hard smooth surface and aluminium (H = 0.24 GPa, E = 75.2 GPa and ν = 0.34) plates were used as deformable flat surfaces. Several contact conditions were applied by changing the flat surface for different roughness.

The setup and procedures of the experiment are basically the same as the experiment in studying the surface asperity and bulk deformation as was discussed in Sub-section 4.3.2.

4.5.2 Experimental results

Two surfaces were used to perform the experiments. The first, Surface A, has asperities with relatively low density, r.m.s. roughness of about 5 μm. The second surface, Surface B, has a higher asperity density and the r.m.s. roughness of this surface is about 1.4 μm. A load of 1 N has been applied for each contact loading case. Areas of the surfaces are presented only near the region of the contact.

4.5.2.1 Experimental results of surface A

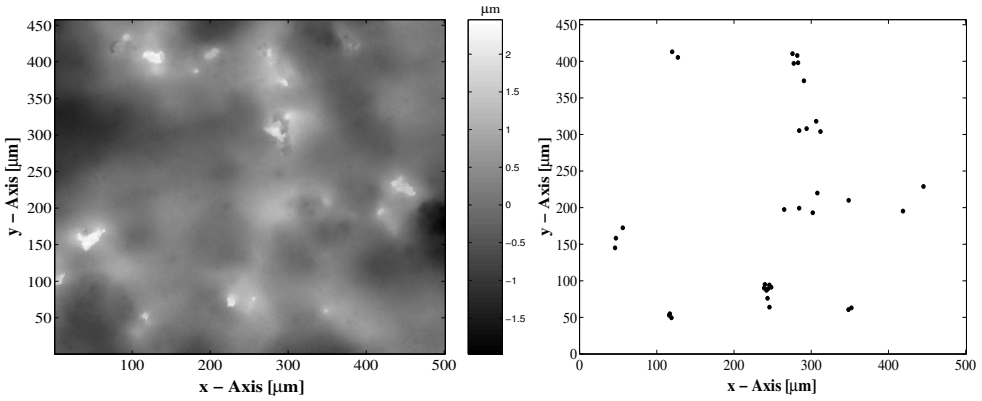

(*a*) (*b*)

FIGURE 4.28: *Initial Surface A (a) and location (not size) of the corresponding contact asperities according to the volume conservation method (b).*

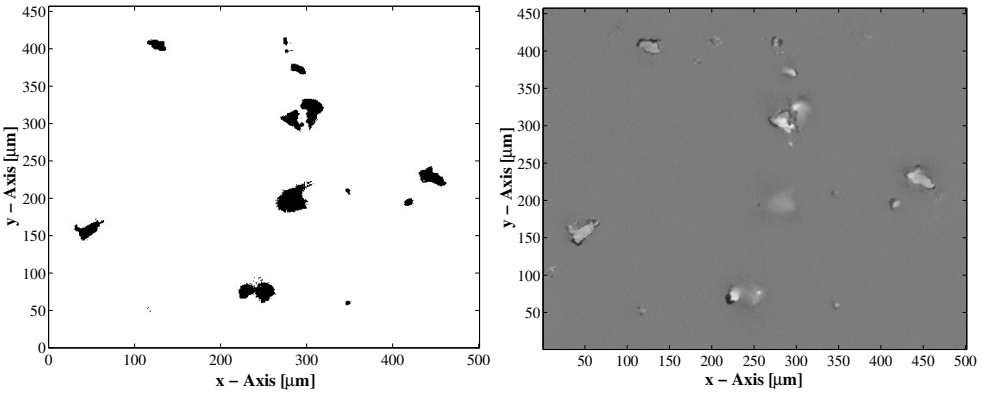

(*a*) (*b*)

FIGURE 4.29: *Contact area of Surface A: (a) present model and (b) experiment.*

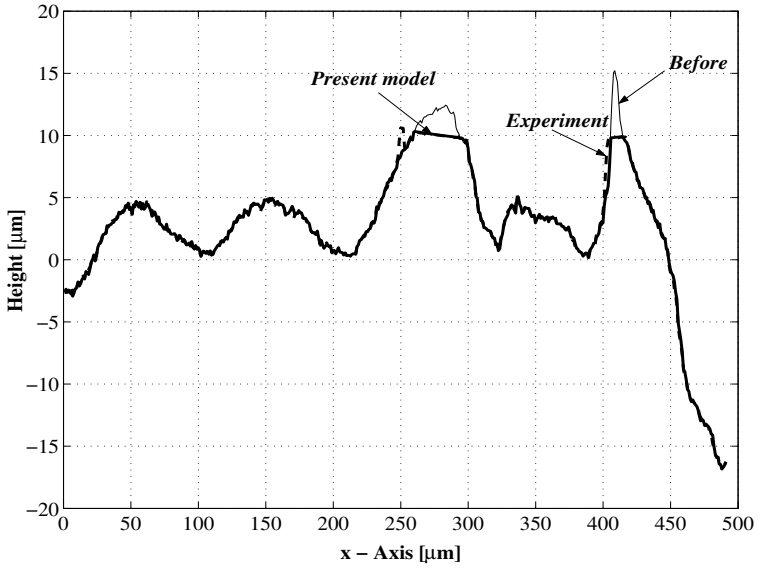

(*a*)

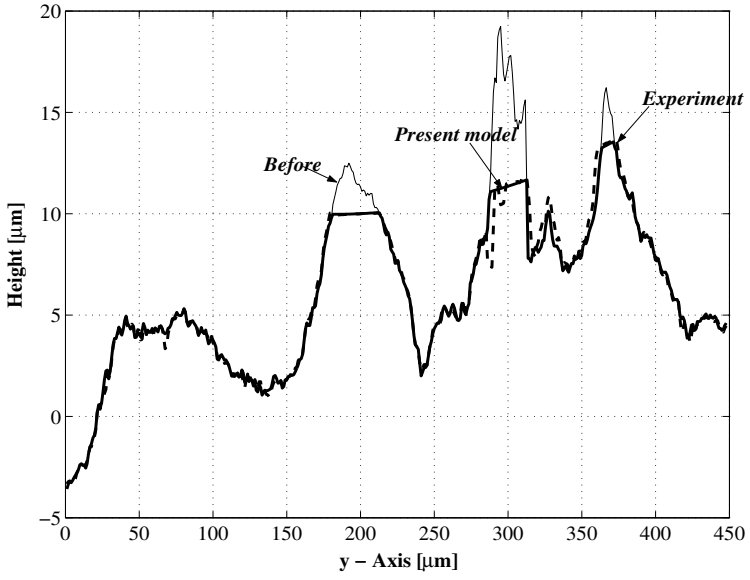

(*b*)

FIGURE 4.30: *Profile of the matching and stitching of Surface A: (a) x-profile at y* = 195 *μm and (b) y-profile at x* = 288 *μm.*

4.5.2.1 Experimental results of surface B

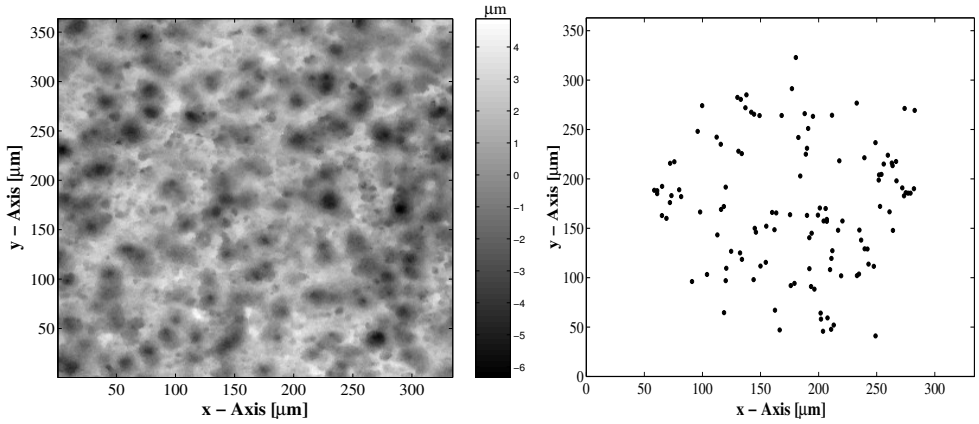

(*a*) (*b*)

FIGURE 4.31: *Initial Surface B (a) and location (not size) of the corresponding contact asperities according to the volume conservation method (b).*

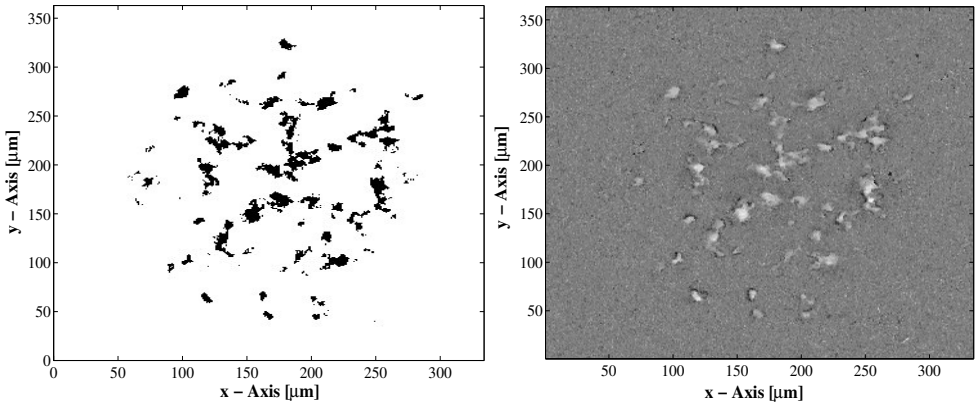

(*a*) (*b*)

FIGURE 4.32: *Contact area of Surface B: (a) present model and (b) experiment.*

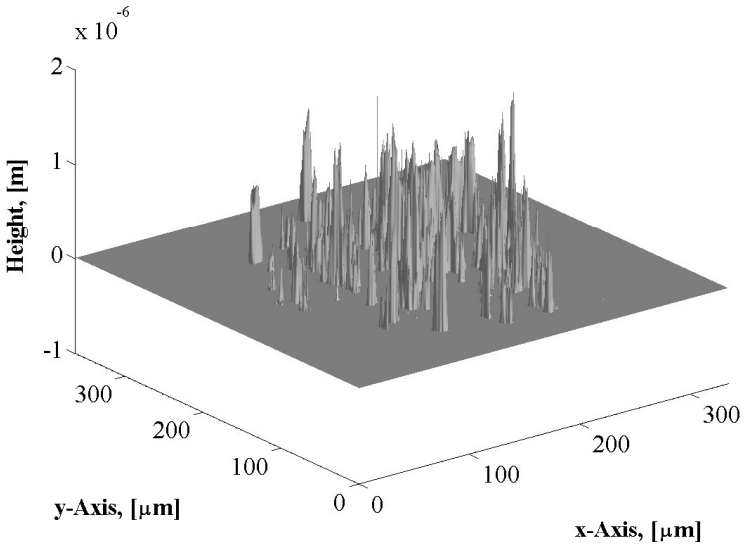

(a)

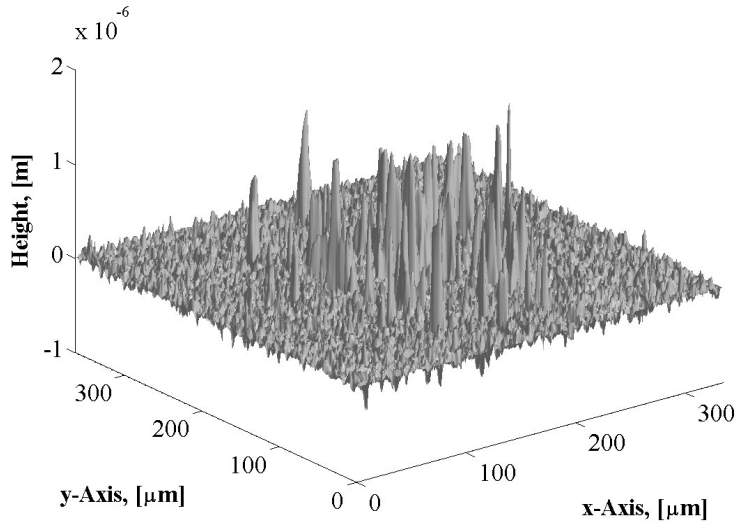

(b)

FIGURE 4.33: *3D difference image of Surface B: (a) present model and (b) experiment.*

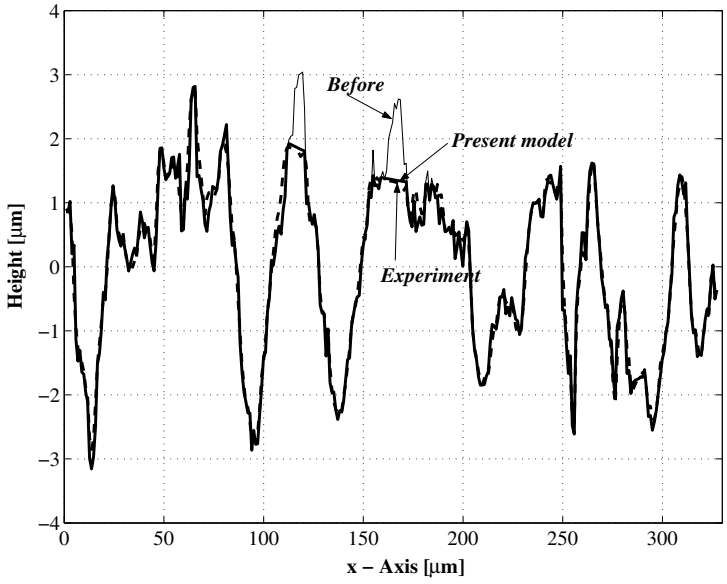

(*a*)

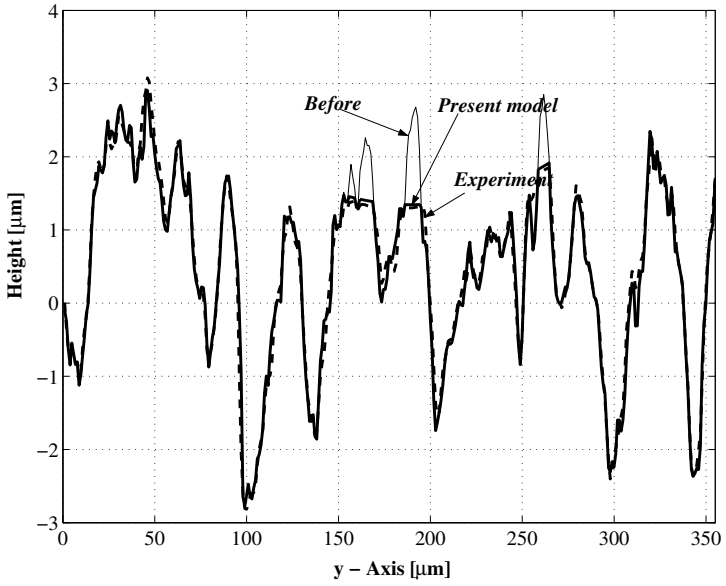

(*b*)

FIGURE 4.34: *Profile of the matching and stitching of Surface B: (a) x-profile at y* = 195 *μm and (b) y-profile at x* = 171 *μm.*

4.5.3 Discussion

Both Surface A and B are made from aluminium, the same material was used for the single asperity experiments in the fully plastic regime (Appendix B). From Appendix B it was found that the c_h value for this material is about $0.71H$. This value is used in the present experiments for the contact of rough surfaces. Another value which is used is the coefficient for the ratio between fully plastic and initial yield deformation c_A of 160.

Figure 4.28a depicts the input surface for the rough surface contact model. The value of σ of this surface is 5 μm and together with 1 N load gives an α value of about 16.28 (Eq. (4.8)). According to the criterion in Eq. (4.12) results a value of C_m = 0.152 which is much smaller than 0.6, so that this surface will deform on asperity level. Another input of the contacting surface is the smooth spherical surface of radius 5 mm. For the determined separation of 1 N load, micro-contacts are formed and the location of these micro-contacts is shown in Fig. 4.28b in which they are indicated by points.

Figure 4.29a presents the results of the rough surface contact simulation for calculating the micro-contact areas. When comparing this figure with Fig. 4.28b, it gives the impression of the geometries of the asperities. Some asperities are small and others are much bigger. Figure 4.29b shows the difference image of the matching and stitching results of the surface in Fig. 4.28a before and after indentation. There is a variation in magnitude of plastic deformation of the asperities; consequently, the images look different in scale according to its plastic deformation. However, the cross-sectionals of the plastic deformations, which imply the contact areas, are clearly observed. The difference in the cross-sectional contact areas between Figs. 4.29a and 4.29b is very small, indicating that the prediction of the developed contact model is very good.

Figure 4.30 demonstrates the prediction and the experimental results of the change in surface topography. The results confirm the prediction of the mode of deformation very well in which the deformation takes place on asperity level. It is also shown that the prediction of the present model of the change of the surface topography is very good.

Similar results are found in the contacting Surface B with a smooth sphere, see Fig. 4.31 to Fig. 4.34. The α value of this surface is about 4.56 and the C_m value is about 0.3, meaning that the surface will deform on asperity level. The asperity density of this surface is higher than Surface A, therefore, locations of the asperities are close to each other. The contact area and the asperity deformation of the micro-contacts are well predicted by the model. Figure 4.33 demonstrates the details of the difference image of the model prediction and the measured one in three-dimensional. In Fig. 4.33b there are values in locations where no contact occurs. This may be caused by the experimental noise, however, the real deformation is distinctive. As can be seen in Fig. 4.34, there is a small difference in the magnitude of plastic deformation. This difference may be caused by the ‘spikes’ of the surface which contribute to the value of the separation or the error in determining the height of the asperities in contact. However, the difference is relatively small compared to the total deformation. In general, it can be concluded that the proposed contact model for the deterministic static contact of rough surfaces works very well.

4.6 Concluding remarks

A theoretical and experimental investigation was carried out to study the deformation behavior of the contact between a real rough surface and a smooth ball. The experimental results confirmed the theoretical prediction very well. The main finding of the present work is that the surface roughness is the primal factor in controlling the deformation behavior of contacting surfaces. For a given Hertzian contact pressure situation, the deformation behavior differs significantly. For the purpose of engineering application, a formula is developed to predict the deformation behavior of contacting engineering surfaces. If the ratio $p(0)/H$ is larger than 0.6, bulk deformation occurs and if the ratio $p(0)/H$ is lower than 0.6, asperity deformation takes place. Combination between asperity and bulk deformation occurs at the ratio $p(0)/H \approx 0.6$.

Preliminary study of the contact of single asperity has been extended to the deterministic multi-asperity contact model for rough surfaces. In this study the surface bulk deformation is excluded in the analysis, therefore, the previous criterion is applied to determine the deformation mode of contacting surfaces. Surface asperities are modeled by an array of elliptic paraboloids in which the unit event of a single paraboloid contact is analyzed using the elastic-plastic elliptical contact model as was developed in the previous chapter. Results showed that the theory of the developed model predicts the contact area and the asperity deformation of the static contact of rough surfaces very well.

This elliptic elastic-plastic deterministic static contact model of rough surfaces will be extended to the dynamic contact situation in Chapter 5.

References

[1] Majumdar, A. and Bhushan, B., 1995, "Characterization and modeling of surface roughness and contact mechanics," *Hanbook of Micro/Nano Tribology,* edited by Bharat Bhushan, CRC Press, Boca Raton, FL.

[2] Thomas, T.R., 1999, *Rough Surfaces*, Imperial College Press, London.

[3] Timoshenko, S. and Goodier, J.N., 1951, *Theory of Elasticity*, McGraw-Hill Book Company Inc., New York.

[4] Johnson, K.L., 1985, *Contact Mechanics*, Cambridge Univ. Press, Cambridge, UK.

[5] Greenwood, J.A. and Tripp, J.H., 1967, "The elastic contact of rough spheres," *ASME-Journal of Applied Mechanics* **34**, pp. 153 – 159.

[6] Greenwood, J.A. and Williamson, J.B.P., 1966, "Contact of nominally flat surfaces," *Proc. R. Soc London* **A295**, pp. 300 – 319.

[7] Lo, C.C., 1969, "Elastic contact of rough cylinders," *Int. Journal of Mech. Sci.* **11**, pp. 105 – 115.

[8] Mikic, B.B. and Roca, R.T., 1974, "A solution to the contact of two rough spherical surfaces," *ASME-Journal of Applied Mechanics* **96**, pp. 801 – 803.

[9] Rajendrakumar, P.K. and Biswas, S.K., 1997, "Deformation due to contact between a two-dimensional rough surface and a smooth cylinder," *Tribology Letters* **3**, pp. 297 – 301.

[10] Tabor, D., 1951, *The Hardness of Metals*, Oxford University Press, UK.

[11] Greenwood, J.A., Johnson, K.L. and Matsubara, E., 1984, "A surface roughness parameter in Hertz contact," *Wear* **100**, pp. 47 – 57.

[12] Greenwood, J.A., 1984, "A unified theory of surface roughness," *Proc. R. Soc London* **A393**, pp. 133 – 157.

[13] Moore, A.J.W., 1948, "Deformation of metals in static and in sliding contacts," *Proc. R. Soc London* **A195**, pp. 231 – 249.
[14] Milner, D.R. and Rowe, G.W., 1962, "Fundamentals of solid-phase welding," *Metallurgical Reviews* **7**, pp. 433 – 480.
[15] Greenwood, J.A. and Rowe, G.W., 1965, "Deformation of asperities during bulk plastic flow," *Journal of Applied Physics* **36**, pp. 667 – 668.
[16] Kimura, Y. and Childs, T.H.C., 1999, "Surface asperity deformation under bulk plastic straining conditions," *Int. Journal of Mech. Sci.* **41**, pp. 283 – 307.
[17] Bhushan, B., 1998, "Contact mechanics of rough surfaces in tribology: Multiple asperity contacts," *Tribology Letters* **4**, pp. 1 – 35.
[18] Liu, G., Wang, Q.J. and Lin, C., 1999, "A survey of current models for simulating the contact between rough surfaces," *Tribology Transactions* **42**, pp. 581 – 591.
[19] Adams, G.G. and Nosonovsky, M., 2000, "Contact modeling – Forces," *Tribology International* **33**, pp. 431 – 442.
[20] Bhushan, B., 1995, *Handbook of Micro/Nanotribology*, CRC Press, Boca Raton, FL.
[21] Greenwood, J.A. and Tripp, J.H., 1970-71, "The contact of two nominally flat rough surfaces," *Proc. Instn. Mech. Engrs.* **185**, pp. 625 – 633.
[22] Hisakado, T., 1974, "Effect of surface roughness on contact between solid surfaces," *Wear* **28**, pp. 217 – 234.
[23] Bush, A.W., Gibson, R.D. and Thomas, T.R., 1975, "The elastic contact of a rough surface," *Wear* **35**, pp. 87 – 111.
[24] Abbott, E.J. and Firestone, F.A., 1933, "Specifying surface quality – A method based on accurate measurement and comparison," *Mech. Engr.* **55**, p. 569.
[25] Pullen, J. and Williamson, J.B.P., 1972, "On the plastic contact of rough surfaces," *Proc. R. Soc London* **A327**, pp. 159 – 173.
[26] Kucharski, S., Klimczak, T., Polijaniuk, A. and Kaczmarek, J., 1994, "Finite element model for the contact of rough surfaces," *Wear* **177**, pp. 1 – 13.
[27] Chang, W.R., Etsion, I. and Bogy, D.B., 1987, "An elastic-plastic model for the contact of rough surfaces," *ASME-Journal of Tribology* **109**, pp. 257 – 263.
[28] Zhao, Y., Maietta, D.M. and Chang, L., 2000, "An asperity microcontact model incorporating the transition from elastic deformation to fully plastic flow," *ASME-Journal of Tribology* **122**, pp. 86 – 93.
[29] Kogut, L. and Etsion, I., 2002, "Elastic-plastic contact analysis of a sphere and a rigid flat," *ASME-Journal of Applied Mechanics* **69**, pp. 657 – 662.
[30] Kogut, L. and Etsion, I., 2003, "A finite element based elastic-plastic model for the contact of rough surfaces," *Tribology Transactions* **46**, pp. 383 – 390.
[31] Jackson, R.L. and Green, I., 2005, "A finite element study of elasto-plastic hemispherical contact against a rigid flat," *ASME-Journal of Tribology* **127**, pp. 343 – 354.
[32] Jackson, R.L. and Green, I., 2003, "A statistical model of elasto-plastic asperity contact of rough surfaces," *Proceedings of STLE/ASME Joint Tribology Conference* **TRIB-102**.
[33] Horng, J.H., 1998, "An elliptic elastic-plastic asperity microcontact model for rough surfaces," *ASME-Journal of Tribology* **120**, pp. 82 – 88.
[34] Jeng, Y.R. and Wang, P.Y., 2003, "An elliptic microcontact model considering elastic, elastoplastic and plastic deformation," *ASME-Journal of Tribology* **125**, pp. 232 – 240.
[35] Webster, M.N. and Sayles, R., 1986, "A numerical model for the elastic frictionless contact of real rough surfaces," *ASME-Journal of Tribology* **108**, pp. 314 – 320.
[36] Liang, X. and Linqing, Z., 1991, "A numerical model for the elastic contact of three-dimensional real rough surfaces," *Wear* **148**, pp. 91 – 100.
[37] Ren, N. and Lee, S.C., 1993, "Contact simulation of three-dimensional rough surfaces using moving grid method," *ASME-Journal of Tribology* **115**, pp. 597 – 601.
[38] Chang, L. and Gao, Y., 1999, "A simple numerical method for contact analysis of rough surfaces," *ASME-Journal of Tribology* **121**, pp. 425 – 432.

[39] Majumdar, A. and Bhushan, B., 1991, "Fractal model of elastic-plastic contact between rough surfaces," *ASME-Journal of Tribology* **113**, pp. 1 – 11.
[40] Bhushan, B. and Majumdar, A., 1992, "Elastic-plastic contact model of bifractal surfaces," *Wear* **153**, pp. 53 – 64.
[41] de Rooij, M.B., 2005, Handout Solids and Surfaces, University of Twente, Enschede, The Netherlands.
[42] de Rooij, M.B., 1998, Tribological Aspects of Unlubricated Deepdrawing Processes, PhD Thesis, University of Twente, Enschede, The Netherlands.
[43] Pasaribu, H.R., 2005, Friction and Wear of Zirconia and Alumina Ceramics Doped with CuO, PhD Thesis, University of Twente, Enschede, The Netherlands.
[44] Faraon, I.C., 2005, Mixed Lubricated Line Contacts, PhD Thesis, University of Twente, Enschede, The Netherlands.
[45] Masen, M.A., de Rooij, M.B. and Schipper, D.J., 2005, "Micro-contact based modelling of abarasive wear," *Wear* **258**, pp. 339 – 348.
[46] Masen, M.A., 2004, Abrasive Tool Wear in Metal Forming Processes, PhD Thesis, University of Twente, Enschede, The Netherlands.

Chapter 5

Running-in of rolling contacts

5.1. Introduction

Most of mechanical components with surface contacts during operation have a running-in period for enhancing the surface contact conformity conditions before they reach a steady-state operation. Changes in the surface topography, friction, temperature and wear rate are commonly observed shortly after the start of the contact between fresh solid surfaces. The properties of two mating surfaces are continuously and monotonously changing during this initial stage of the operation. These changes are advantageous when the running-in process succeeds, i.e. the degree of conformity increases so that the performance of the contacting components improves. In other cases, due to some contact conditions, the better degree of the conformity is not attained, which leads to the failure of the contacting components soon after the initial contact operation. This failure is referred to as run-out.

Obviously, running-in is beneficial for engineers. Therefore a lot of work has been done to study the running-in, as was presented in Chapter 2. However, fundamental studies which attempt to investigate the detailed process of the running-in period phenomena are relatively rare. Rather, many researches which have been conducted focused on the steady-state conditions that follow instead of studying the transition process prior to it. Running-in plays an important role in friction and wear of tribology systems during the steady-state period. Ignoring the running-in aspects means overlooking the important clues to the evolution of conjoint processes which leads to the final long-term steady-state friction and wear behavior.

The term running-in is related to the terms breaking-in and wearing-in. The extensive discussion and definition about these terms can be found in [1]. Generally, running-in has been connected to the process by which contacting machine parts improve in conformity, surface topography and frictional compatibility during the initial stage of use. This leads to a very wide definition and is applicable to a broad spectrum of mechanical contact problems. Running-in is still a vast problem area in which much investigation remains to be done. Running-in is very complex; however, based on the literature review in Chapter 2, plastic deformation and mild wear are the dominant mechanisms during running-

in. In case of a rolling contact situation plastic, deformation will be dominant. There are two types of the tribological transition of running-in [2], namely, induced running-in and non-induced or natural running-in. Induced running-in is referred to when the operator applies a specified set of procedures in order to gain the desired surface condition after running-in of certain contacting components. Whilst non-induced or natural running-in occurs as the system 'ages' without changing the operating contact conditions such as increasing the load, velocity et cetera. For non-induced running-in, the performance of running-in is mostly determined by the finished surface topography from the manufacturing process.

In this chapter, the change of surface topography due to plastic deformation of the non-induced running-in of a rolling contact will be studied. On the basis of the developed elastic-plastic elliptical contact model in Chapter 3 and the deterministic contact model of rough surfaces in Chapter 4, the surface topography changes during running-in for a rolling contact is modeled in Section 5.2. Before modeling the rolling situation, repeated contact without rolling is studied in this section. In Section 5.3 a procedure, which will be used to perform the experiments to verify the proposed model, is presented. Section 5.4 gives the experimental results along with the proposed model prediction. Discussion of the results is also presented in this section. Conclusions are given in the last section.

5.2 Modeling running-in of rolling contacts

Most of the running-in models available in literature, e.g. [3-8], are devoted to running-in with respect to wear during sliding motion. The models are designed to predict the change of the macroscopic wear volume or the standard deviation of the surface roughness rather than the change of the surface topography locally during the running-in process. Frictional behavior during running-in has been modeled by Blau [9] semi-empirically, however, the model is more phenomenological, since there are many constants introduced in order to portray the shape of the friction curves globally. In the present study, the change of the surface topography during running-in is analyzed deterministically and is concentrated on the pure rolling contact situation.

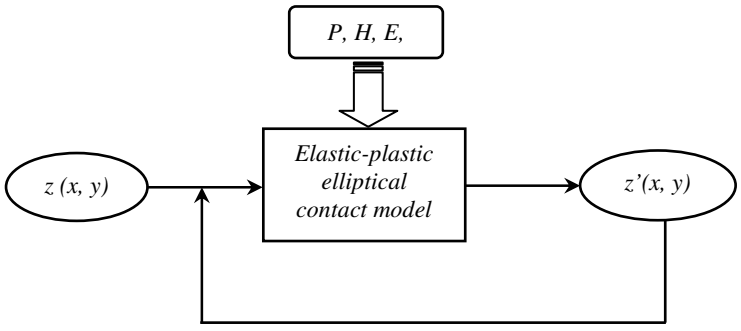

FIGURE 5.1: *Schematic illustration of the repeated contact model.*

There are several types of repeated contacts such as: (1) repeated contact of the contacting bodies by loading-unloading in normal direction (z-direction) without changing the contact position in the contact plane which is referred to as repeated stationary contact, (2) repeated sliding contact and (3) repeated rolling contact. This study focuses on the repeated rolling contact. However, this type of repeated contact is principally based on repeated stationary contact; therefore the repeated stationary contact is evaluated before modeling of the repeated rolling contact.

Basically, for repeated stationary and rolling contacts, the model is built upon the model as was discussed in the last section of Chapter 2. Here, the wear model part is excluded so that the schematic model as was illustrated in Fig. 2.12, results into the model as schematically presented in Fig. 5.1. Details of the proposed model are discussed in the next sub-sections.

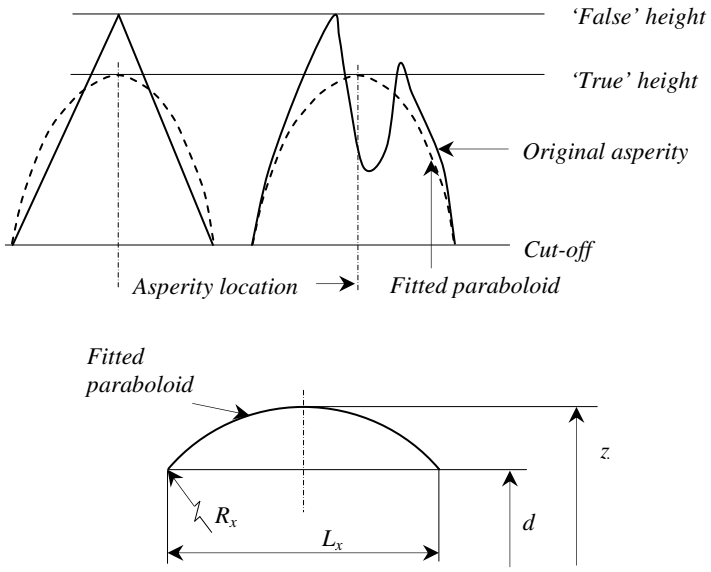

FIGURE 5.2: *Asperity height determination.*

In the following analysis of the elliptic elastic-plastic contact model, the method to determine the asperity height is presented in Fig. 5.2. Instead of using the maximum height within the micro-contact area, the asperity height, z, is determined based on the calculated radius in x direction R_x and the diameter of the cross-sectional elliptical contact area in x direction L_x as:

$$z = d + \frac{\left(\frac{L_x}{2}\right)^2}{2R_x} \tag{5.1}$$

where d is the contact separation.

5.2.1 Repeated stationary contact

In general, the repeated contact model is similar to the deterministic contact of rough surfaces as was presented in Chapter 4. Therefore, the procedures used for the proposed repeated contact model are also similar.

The flow diagram of the repeated stationary contact model is presented in Fig. 5.3. The 3D measured surface topography $z_1(x,y)$ and $z_2(x,y)$ are used as an input for the contacting surfaces. The surface topography $z'_1(x,y)$ and $z'_2(x,y)$ of the contacting surfaces are the output from the deterministic elastic-plastic contact model. These outputs are used as the input for the next loading cycle. The condition where there is no plastic deformation anymore, i.e. there is no difference between the subsequent input and output values of the surface topography by following certain running-in criterion ε_r, is referred as the run-in condition.

5.2.2 Rolling contact

Many studies have been conducted to analyze the rolling contact mechanism. Based on the work of Merwin and Johnson [10], Bhargava *et al.* [11-14] modeled the rolling contact situation by finite element analysis. A rigid cylinder rolling on an elastic-perfectly plastic half-space is simulated by translating a Hertzian pressure distribution over a finite element mesh representing a semi-infinite body. The pressure distribution is applied incrementally at the first contact point and translated incrementally to the end of the rolling distance and then unloaded. For each consecutive cycle the same procedure is repeated by applying the pressure distribution incrementally, translating it incrementally, and unloading it. The changes in surface topography, which are represented by the deformed nodes on the finite element mesh, have been shown by the model. However, there are several things which need to be discussed further. Firstly, the pressure distribution is kept Hertzian even when plasticity occurs. Secondly, the deformation at the first point of contact and at the end of contact is higher than in the other part of the track, which is unrealistic and there is no experimental validation of the proposed model. Furthermore, since the analyses involve elastic-plastic finite element calculation and are solved in an iterative manner, considerable computational effort is required. To overcome the computational cost some methods were introduced [15-19] so that the computational efficiency is increased although they are still essentially numerical or non-analytic in nature.

According to Johnson [20] rolling is defined as the relative angular velocity between the two bodies about an axis lying in the tangent plane. Depending on the forces acting in the contacting bodies, rolling can be classified as free rolling and tractive rolling. Free rolling is use to describe a rolling motion in which there is no slip and the tangential force at the contacting point is zero. The term tractive rolling is used when the tangential force in the point of contact is not zero or slip is present. The present study is focused on the free rolling motion only.

The free or pure rolling does not contain a tangential force and therefore this type of motion can be modeled by multiple-indentation of one body to another body with changing the indentation position. To mimic the pure rolling contact motion the range or the position distance between one indentation to the next indentation should be as small as

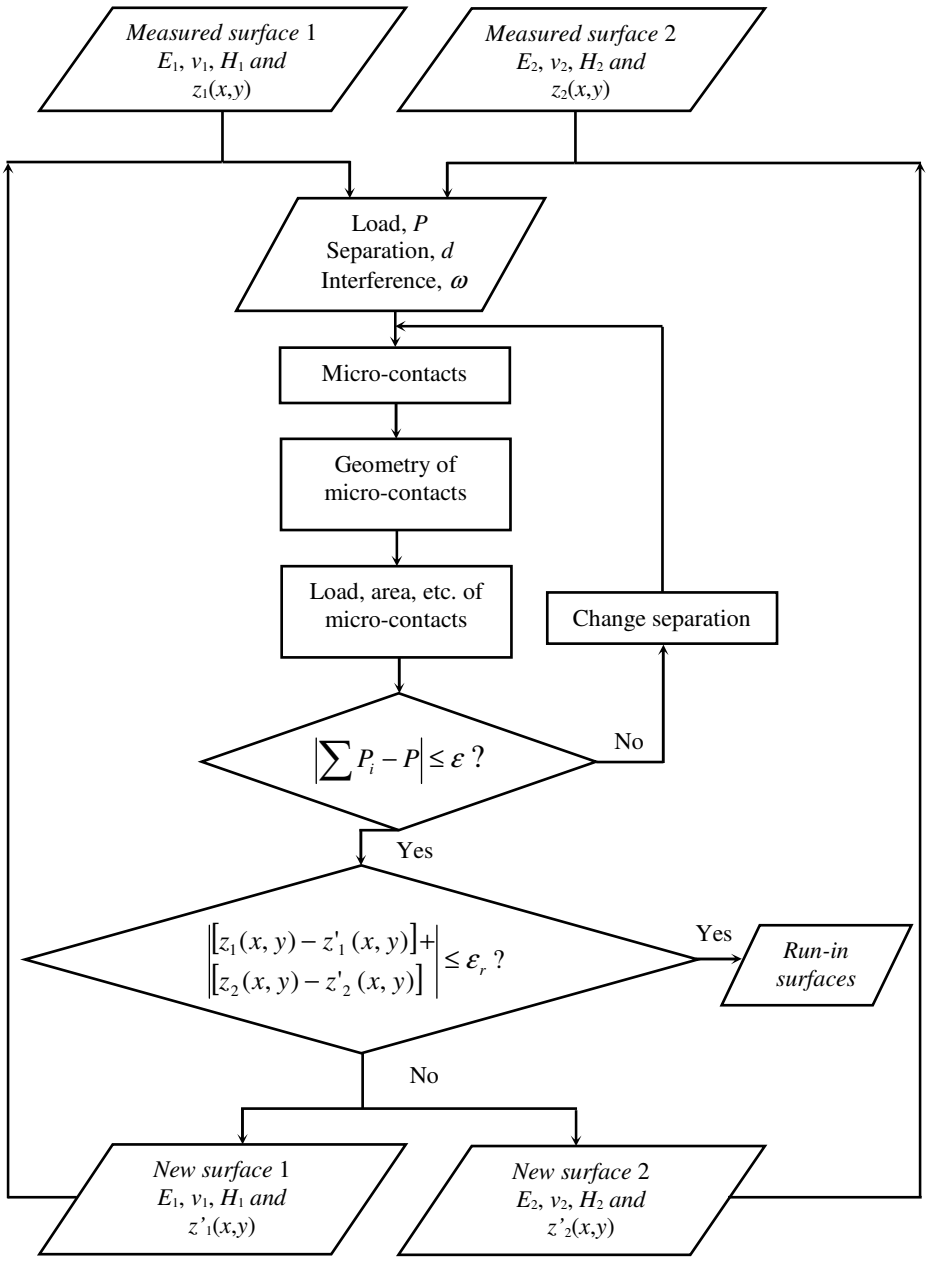

FIGURE 5.3: *Flow diagram of the calculation of repeated contacts.*

possible. This multiple-indentation process is described schematically in Fig. 5.4. Basically, the model of the repeated static contact is applied to the rolling contact model, only for the rolling contact model, the contact position has to be shifted or translated according to the rolling direction for the next loading. Firstly, as can be seen in Fig. 5.4a, Body 2 is normally loaded by Body 1. Here, the routine to calculate the deterministic elastic-plastic contact of rough surfaces as was presented in Fig. 4.24 is applied, which results into a new topography of the surfaces when there is plastic deformation. Secondly, Body 1 is unloaded and shifted in rolling direction to the position over a distance equal to one pixel size and then again loaded against Body 2 (the movement of one pixel size is chosen because of the

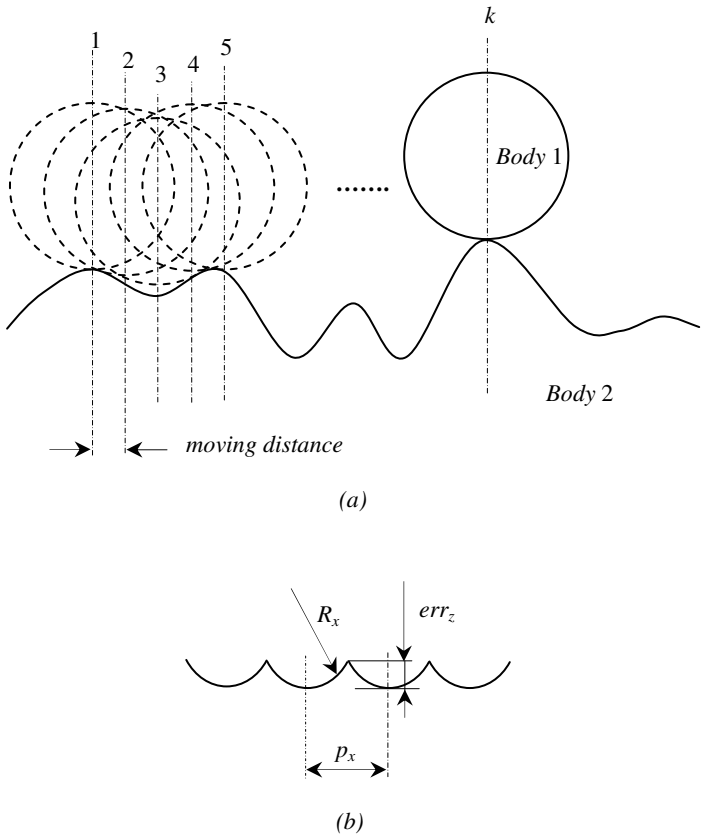

FIGURE 5.4: *Schematic representation of a rolling contact by multiple-indentation (a) and its error in height, err_z (b).*

available minimum distance from the measured surface). In this stage the output of the surface topography from the previous contact loading is used as input for the next calculation steps. These steps are repeated *k* times until the desired rolling contact distance is achieved. The method is schematically shown in Fig. 5.4a. The introduced error in height is shown in Fig. 5.4b and shows that the error becomes smaller when the radius of the

indenter increases. As an example, by using an indenter with radius R_x of 3.175 mm and the pixel size in x-direction p_x is 1 μm, due to the used magnification of the interference microscope, as is used in the present experiments, the error in height err_z is about 0.04 nm which is much less than the height resolution of the interference microscope, i.e. 1 nm, so that in the present experiments the introduced error in height is negligible.

The same procedures are used for the next cycle of multiple-indentations with a translating contact position. The cycles are repeated until there is no more change in surface topography of the rolling surfaces between the last cycle and the previous one which indicates that the contacting surfaces are run-in.

5.3 Experimental procedure

The setup, as was shown in Fig. 4.4, is utilized to perform tests for stationary repeated contacts and pure rolling or 'moving' repeated contacts. Another setup which is also utilized to perform rolling contact experiments is a 'semi on-line measurement setup' [21]. Photographical impression of these setups can be seen in Appendix D.

5.3.1 Specimens

Silicon carbide ceramic balls SiC (H = 28 GPa, E = 430 GPa and ν = 0.17) with a diameter of 6.35 mm were used as hard spherical indenters. The center line average roughness R_a of the ceramic ball of 0.01 μm was chosen to comply with the assumption of a perfectly smooth surface. Elastic-perfectly plastic aluminium (H = 0.24 GPa, E = 75.2 GPa and ν = 0.34) and mild-steel (H = 3.55 GPa, E = 210 GPa and ν = 0.3) were used for the rough flat surface specimens. The center line average roughness of the flat specimens varied from 0.7 to 2 μm.

5.3.2 Experimental details

5.3.2.1 Repeated stationary contact experiments

In principal, the test for the repeated stationary contact is the same as the test for the static contact in Chapter 4. Prior to any test, the spherical and flat specimens were cleaned with acetone and dried in air. Referring to Fig. 4.4, the cleaned flat surface is positioned in **A'** where the interference microscope is statically located. After the 3D surface topography is measured by the interference microscope, the flat specimen is moved by an X-Y table for a predetermined distance, to point **A** where the loading position stands stationary. The first loading cycle is executed in this point by screwing down the spherical indenter until it touches the surface and subsequently putting the dead weight/load system in its location on top of the center of the spherical indenter. The contacting area was lubricated to reduce the friction during loading. The load is applied for 30 seconds and then unloaded by lifting up the loading arm manually (without screwing up the loading screw). The loading arm is very stiff so that the error which can be affected by lifting up the loading arm is very small. At the same time, by using the X-Y table, the flat specimen is repositioned to point **A'** for

measuring the surface topography after the first loading. The flat surface is cleaned again with acetone, dried and subsequently the surface is acquisitioned for surface topography data by the interference microscope. With this last step, the first loading cycle is finished.

To continue the test for the next loading cycle, the same procedure is applied. It must be noted that when the flat surface is moving from position **A'** to **A**, the loading arm should be lifted up in order to avoid a sliding action between the spherical indenter and the flat surface. When position **A** is reached, the load is gently reapplied. To investigate the change of surface topography accurately for the sequence loading cycles, the matching and stitching was applied (see Appendix C). All the stitched images from every loading cycle are matched with the first stitched images. This was done separately by a personal computer.

5.3.2.2 Repeated moving contact experiments

The setup for the repeated moving contact experiments is an extension of the repeated stationary contact setup. The only difference between those setups is the loading stage. In the repeated moving contact setup, when the flat surface specimen is positioned in point **A**, the loading is performed more than once and the loading position is changed for every loading.

First, the multiple-indentation distance should be determined, say x_r. From point **A** the flat specimen is moved along $x_r/2$ in opposite *x* direction according to the 'rolling' direction by the X-Y table where the indentation of the flat by the sphere is started. After 5 seconds, the loading arm is manually lifted for unloading and then the flat is moved forward by the X-Y table over a distance of 1 pixel size in the rolling direction and then starts loading again. This process is repeated until the distance x_r is achieved. If the final loading position is finished, the loading arm is lifted up and the flat specimen is moved backwards over a distance $x_r/2$ so that the position **A** is reached. Subsequently, with the loading arm still in the lifting up position, the flat specimen is moved to position **A'** for measuring surface roughness. With this step, the first loading cycle of repeated moving contacts is finished. The same procedures are applied again for the next cycle.

5.3.2.3 Repeated rolling contact experiments

Another setup to perform the rolling contact experiments is the semi on-line measurement setup [21]. Details of the arrangement of the setup are presented in Fig. 5.5. The spherical indenter is held by the same loading arm as in the repeated stationary and moving contact setups. A disk is mounted on a rotating table which is controlled by a stepper motor. The loading arm and the rotating table are positioned on the X-Y table such that the spherical indenter is located on one side of the disk, whilst the interference microscope is positioned on the other side of the disk and stands separately from the X-Y table. The setup allows a range for the diameter of the disk specimen from 70 to 100 mm.

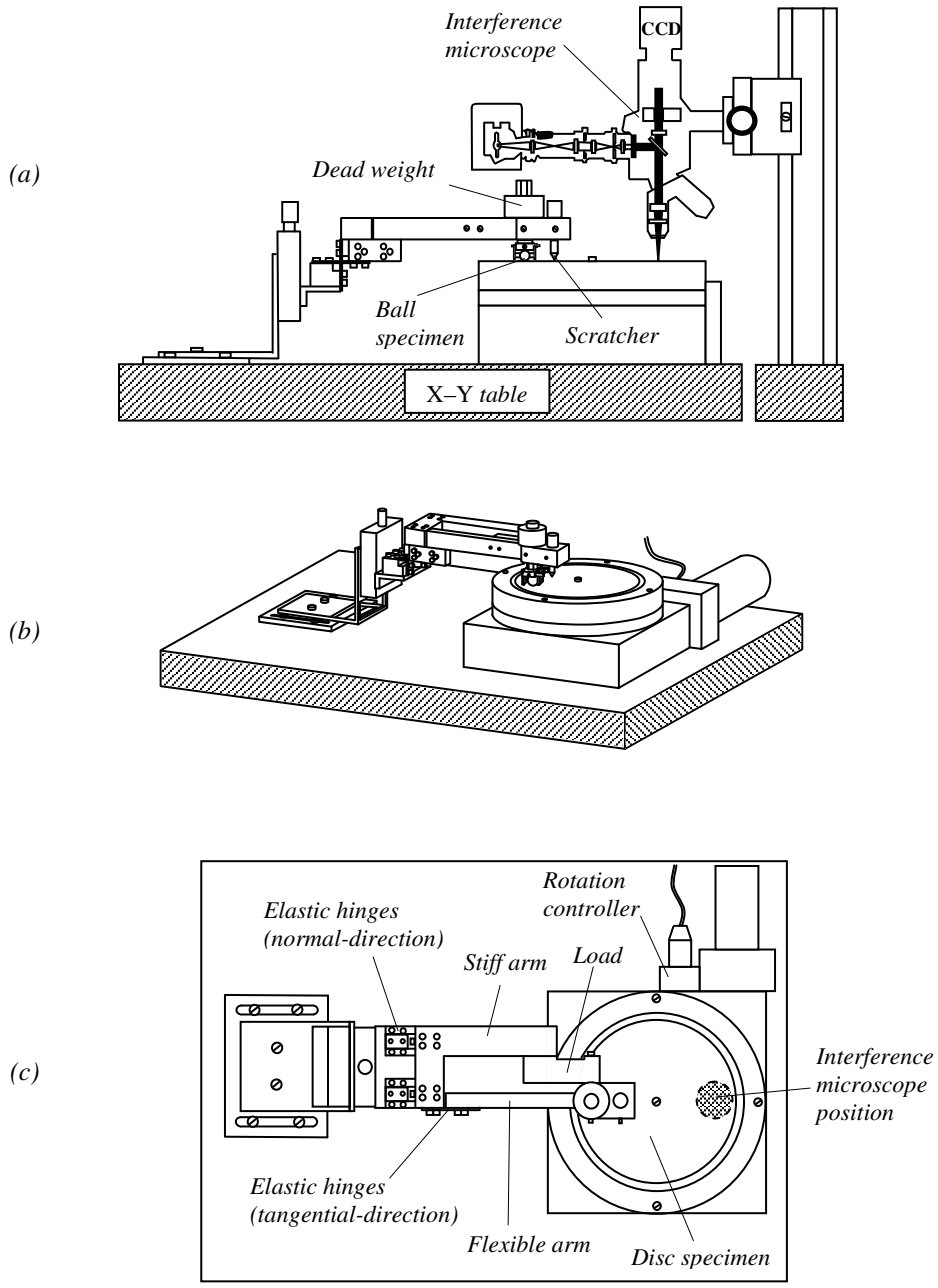

FIGURE 5.5: *Semi on-line measurement setup. (a) Main view, (b) isometric view of (a) without interference microscope and (c) top view of (b).*

In order to make a rolling condition of the sphere or ball possible, a special holder was designed as is shown in Fig. 5.6. This holder consists of three major parts: a horizontal slider, a clamping unit and miniature ball bearings. The maximum load which can be borne by the miniature ball bearings is about 7 N and therefore the maximum load which can be applied to this setup is less than 7 N. The clamping unit is designed to increase the capability of the holder by allowing different diameters of the ball. The diameters of the ball which can be used in this holder range from 6 to 12 mm. To adjust the relative position between the center of the ball and the center of the dead weight position, the horizontal slider is moved. The aim of the adjustment is to minimize the inclining effect of the loading system.

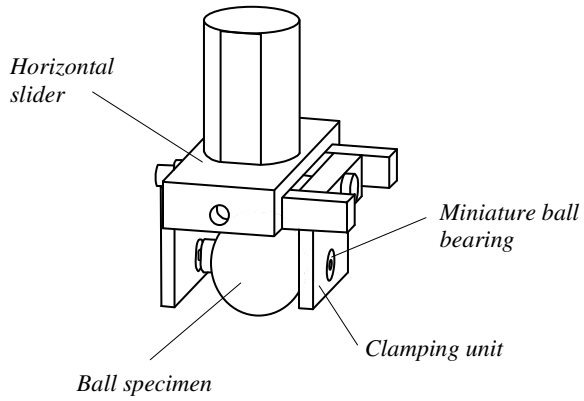

FIGURE 5.6: *Rolling ball holder.*

Sequences of the rolling contact measurement in this setup according to [21] are as follows. The relative position between the ball specimen and the disk is fixed on the X-Y table. A scratcher is positioned lower than the ball specimen. The loading arm is screwed down until the tip of the scratcher touches the disk surface and then the dead load is used, which is enough to indent the disk surface. The disk is rotated until the scratched disk surface appears. The X-Y table is utilized to move the disk so that the other side of the scratched disk is located under the interference microscope. The relative position of the ball specimen, the center of the disk and the interference microscope are set in a line of the x or y axis. When such positions are achieved, the scratcher is taken off and the X-Y table is moved in the opposite x or y direction, along the predetermined distance between the scratcher and the ball specimen. By this procedure, the disk surface which was in contact with the ball specimen will pass the point where the interference microscope is positioned. Load is applied by using the same procedure as was discussed earlier and the sample of the surface is measured by the interference microscope. For a one cycle measurement the disk is rotated for 360 degrees, stopped and then the surface roughness is measured. There are some disadvantages using this procedure such as the difficulty in determining the distance between the center of the ball specimen and the tip of the scratcher. The difficulty is the positioning of the ball specimen, the scratcher and the interference microscope in one line.

Moreover, the disk specimen is damaged by the scratcher which could be used for another experiment. Therefore, in the present experiments a modified procedure is applied.

In the present rolling experiments the scratcher is excluded. Measurements in the surface topography in the area of the disk surface should be done nearly at the same spot before and after rolling contact. A sufficient load which can deform the surface plastically is applied and then the disk is rotated with a low angular velocity. For a certain distance of rolling contact, the system is unloaded so that there is still a remaining area which was not in contact. The disk is rotated so that the plastic deformed surface stays at the opposite side of the ball indenter and is then moved by the X-Y table to position the interference microscope on the plastic deformed track. The disk is rotated again to measure the original area of the disk. When this arrangement is achieved, the same procedure is used as was described above. The velocity of the present experiment is about 7 mm/s and the system is unlubricated. Eldredge and Tabor [22] have shown that in the rolling contact condition its behavior is the same for the velocity range of 0.5 to 100 mm/s. Experiments on a new fresh surface of the same disk can be performed by adjusting the relative position between the ball specimen and the disk in x or y direction.

5.4 Results and discussion

5.4.1 Repeated stationary contact

For the repeated stationary contact experiments isotropic and anisotropic aluminium surfaces and an anisotropic mild-steel surface were used. The r.m.s. roughness is respectively 1.3 and 1.4 μm for the isotropic and the anisotropic aluminium surfaces and 0.7 μm for the anisotropic mild-steel surface. For each loading a load of 0.2 N has been applied to the aluminium contact system and 2.5 N to the mild-steel contact system. Fig. 5.7 to Fig. 5.12 show the results for the aluminium specimen where the local contact condition dominantly operates in the fully plastic contact regime.

Elastic perfectly plastic aluminium was used (see also Appendix B for the fully plastic single asperity experiments) as flat isotropic and anisotropic surface specimens. The hardness constant for full plasticity c_h of this material was 0.71 and the inception of fully plastic deformation ω_2 equals 80 times the inception of the deformation where the first yield occurs ω_1, or $c_A = 160$. Figure 5.7a shows the initial isotropic surface which was in contact with a hard smooth ball. A load of 0.2 N was applied to the contact. The position of the asperities in contact due to the applied load is presented in Fig. 5.7b. The location (not size) of the corresponding asperities is represented by dot markers in this figure. Together with the r.m.s. roughness value of R_q is 1.3 μm and its material properties yields a C_m value for the criterion of Eq. (4.12) of 0.16 which means that deformation of the surface on asperity level is expected.

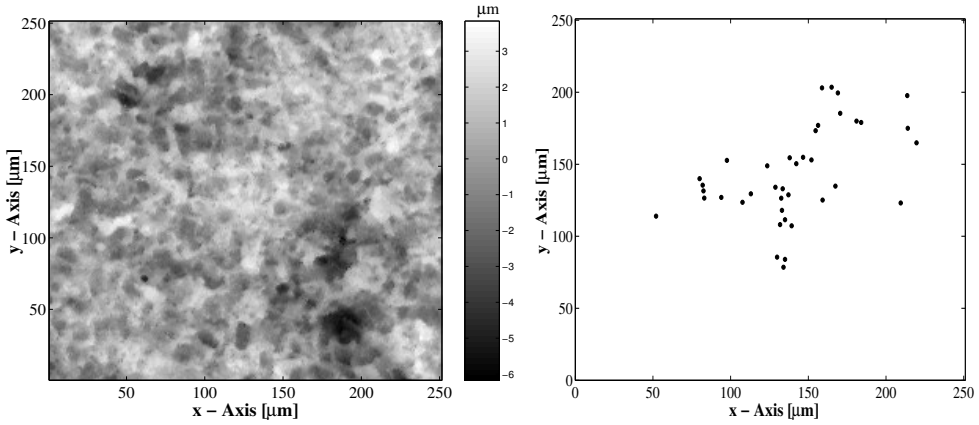

(a) *(b)*

FIGURE 5.7: *Isotropic aluminium surface before contact is applied (a) and location (not size) of the corresponding asperities (b).*

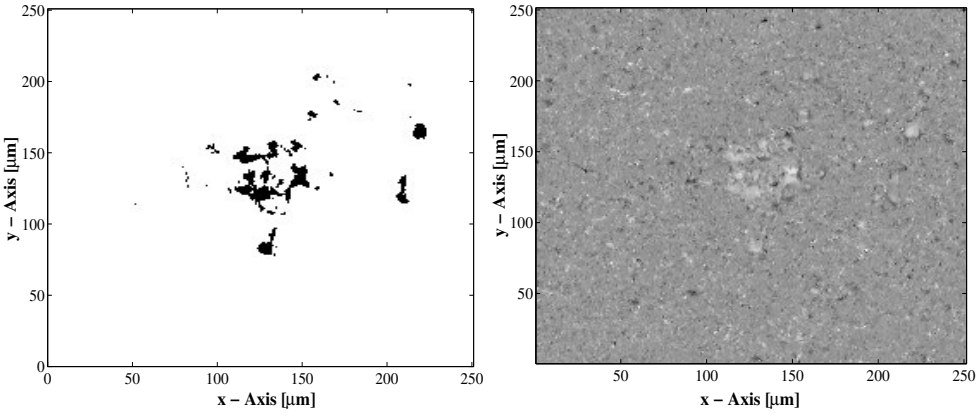

(a) *(b)*

FIGURE 5.8: *Contact area of the isotropic aluminium surface for n = 1: (a) model and (b) experiment.*

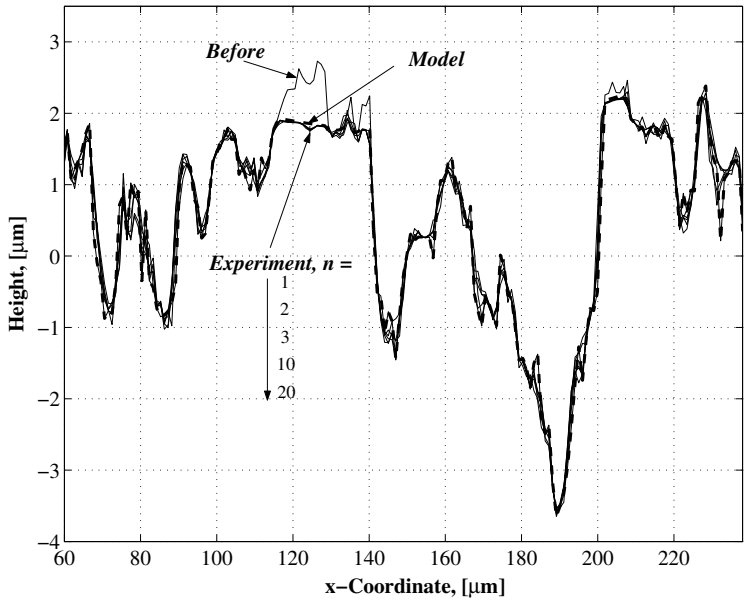

(a)

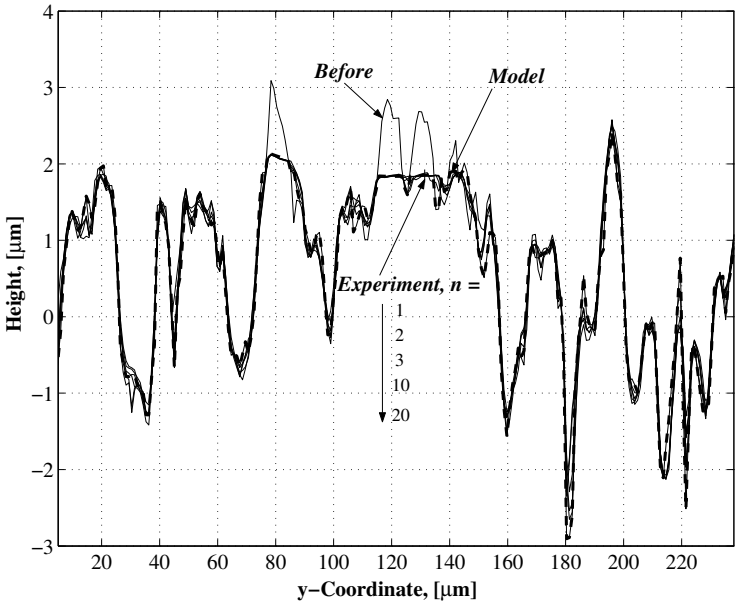

(b)

FIGURE 5.9: *Profile of the matched and stitched isotropic aluminium surface: (a) x-profile at y = 120 μm and (b) y-profile at x = 129 μm.*

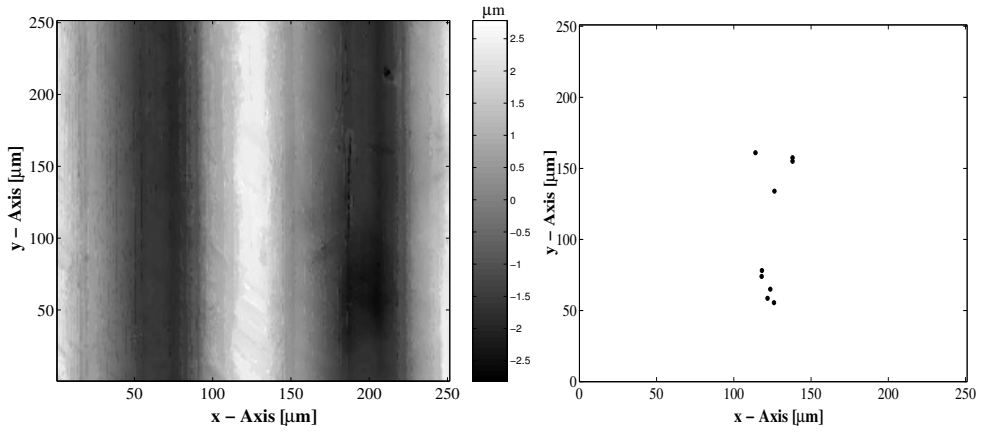

(a) *(b)*

FIGURE 5.10: *Anisotropic aluminium surface before contact is applied (a) and location (not size) of the corresponding asperities (b).*

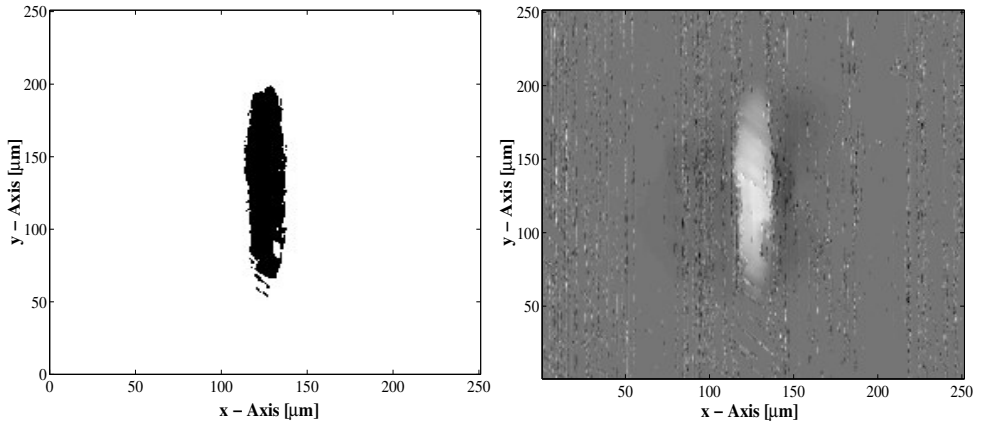

(a) *(b)*

FIGURE 5.11: *Contact area of the anisotropic aluminium surface for n = 1: (a) model and (b) experiment.*

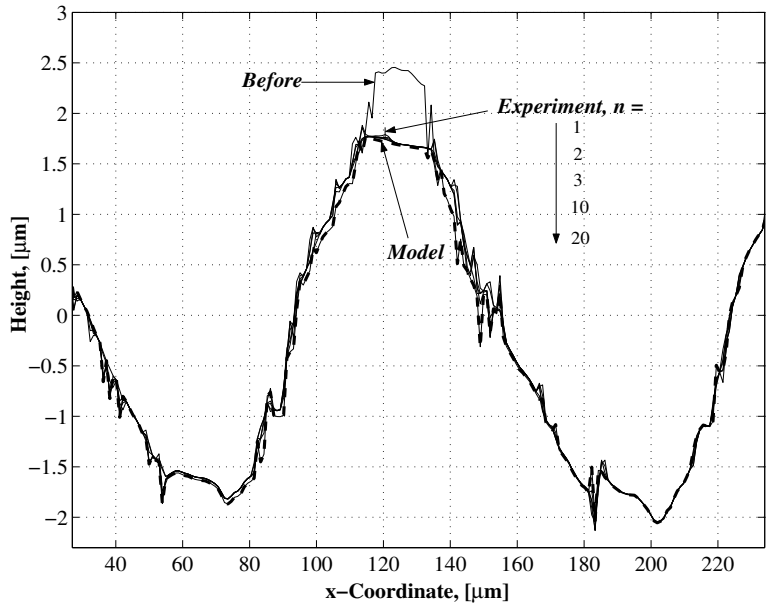

(a)

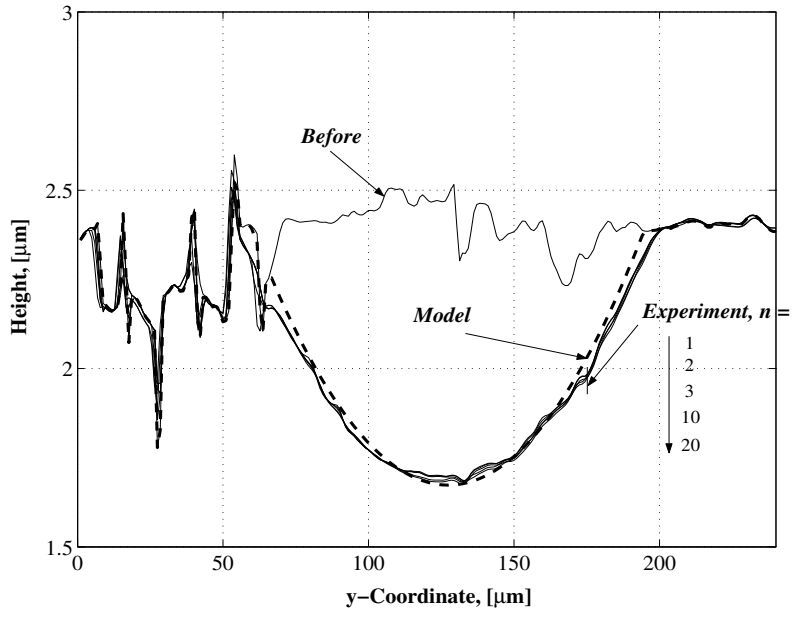

(b)

FIGURE 5.12: *Profile of the matched and stitched anisotropic aluminium surface: (a) x-profile at y = 118 μm and (b) y-profile at x = 126 μm.*

The contact area prediction by the model for the cycle n = 1 is depicted in Fig. 5.8a. Impression of the size of the geometry of the asperities is given in this figure. The experimental results of the contact area from the contact system are presented in Fig. 5.8b. As can be seen, the model predicts the contact area very well. More insight in the model prediction and the measured results may be seen in the plot of the asperities in x and y direction as presented in Fig. 5.9. The model predicts the change of the surface topography accurately. Experimental results show that there is almost no difference between the profile for cycle 1, 2, 3, 10 and 20. In the first loading cycle the asperity deforms elastic, elastic-plastic or fully plastic depending on its geometry, location and height. The contact area is developed to support the load. When the load is removed, plastic deformation will modify the surface geometry due to elastic-plastic and fully plastic deforming asperities which normally increase the degree of conformity to the counter-surface (indenter). If the same load is reapplied at exactly the same position, the same contact area as for the first loading will be developed. In this second loading the asperities deform elastically as a result of the residual stresses and geometrical changes induced by the first loading, therefore there is no change of the surface topography or of the contact area. Residual stresses will increase the yielding stress and the change of the geometry will reduce the level of applied stresses. In the present model the change of the surface geometry is the only factor. Since the same loading condition is applied for cycle 1, 2, 3, 10 and 20 the same phenomena are observed.

Results of the anisotropic aluminium surface are presented in Fig. 5.10 to Fig. 5.12. The initial anisotropic aluminium surface and its asperity location is shown in Fig. 5.10. The same load as was applied to the isotropic aluminium surface is used for the anisotropic surface. Figure 5.11 presents the result of the contact area of the model prediction and of the experimental investigation for the first cycle. From this figure it can be seen that the surface is dominantly represented by a single elliptic asperity. With a r.m.s. roughness R_q value of 1.4 μm, it yields a C_m value of 0.15 so that asperity deformation is expected. This is confirmed by the experimental results of Fig. 5.12 where the plot of the x and y profile are drawn. Results for cycle 1, 2, 3, 10 and 20 are similar to the isotropic aluminium surface i.e. there are almost no differences in the contact area and the surface topography. Small deviations between the model prediction and the experimental results are observed for the y profile in Fig. 5.12b. This behavior will be discussed further in Chapter 6.

Results of the repeated stationary contact for the mild-steel material, where most of the local contacts operate in the elastic-plastic contact regime, are presented in Fig. 5.14 to Fig. 5.17. In the elastic-plastic contact regime, instead of truncating the asperity by the hard indenter as for the case in the fully plastic contact regime, the shape of the asperity after unloading is determined as follows. Suppose the radius of the asperity in the x-direction is R_x, the normal plastic deformation as was defined in Eq. (3.84) is ω_{uep} after loading for an interference ω, the corresponding radius after unloading is defined by:

$$R_x^* = \frac{2R_x\omega - 2\omega\omega_{uep} + \omega_{uep}^2}{2(\omega - \omega_{uep})} \tag{5.2}$$

The new radius of the asperity after unloading as was defined in Eq. (5.2), is derived based on a simple analysis as presented in Fig. 5.13.

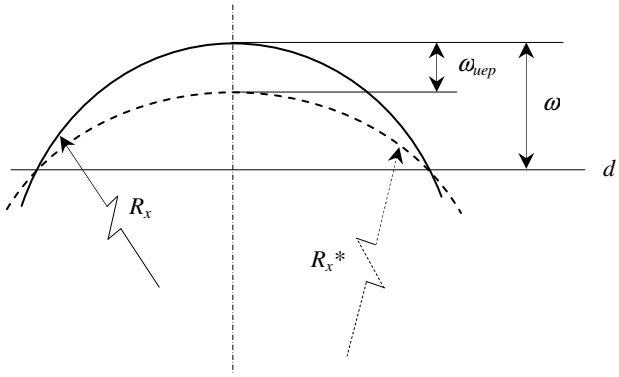

FIGURE 5.13: *Profile change before and after loading.*

Results for the mild-steel specimen are similar to the results for the aluminium specimen. The r.m.s. roughness of the mild-steel is about 0.7 μm, this combined with a 2.5 N load results into a C_m value of about 0.11 so solely asperity deformation is expected. The contact area prediction of the model in the elastic-plastic contact regime as shown in Fig. 5.15(a) is a bit larger than the measured one; this is caused by the overestimation of the contact area by expression (3.85), especially in the regime close to elastic regime. Small differences were also found in the profiles between the model and the experimental results, Figs. 5.16 and 5.17.

In general, it can be concluded that for the repeated stationary contact, the proposed elastic-plastic contact model is able to predict the contact area and the surface topography change for both isotropic and anisotropic surfaces accurately.

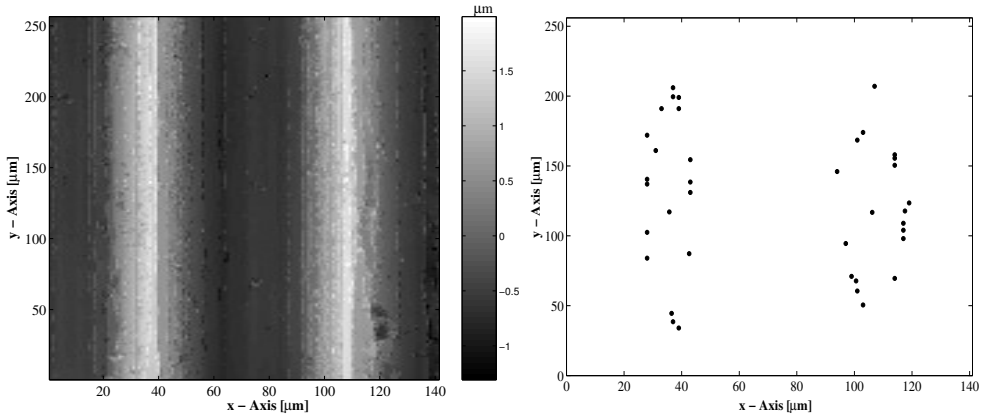

(a) *(b)*

FIGURE 5.14: *Anisotropic mild-steel surface before contact is applied (a) and location (not size) of the corresponding asperities (b).*

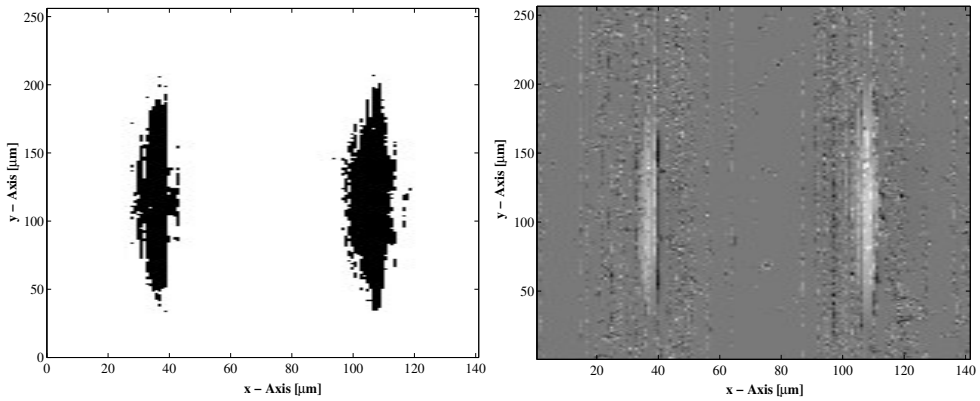

(a) *(b)*

FIGURE 5.15: *Contact area of the anisotropic mild-steel surface for n = 1: (a) model and (b) experiment.*

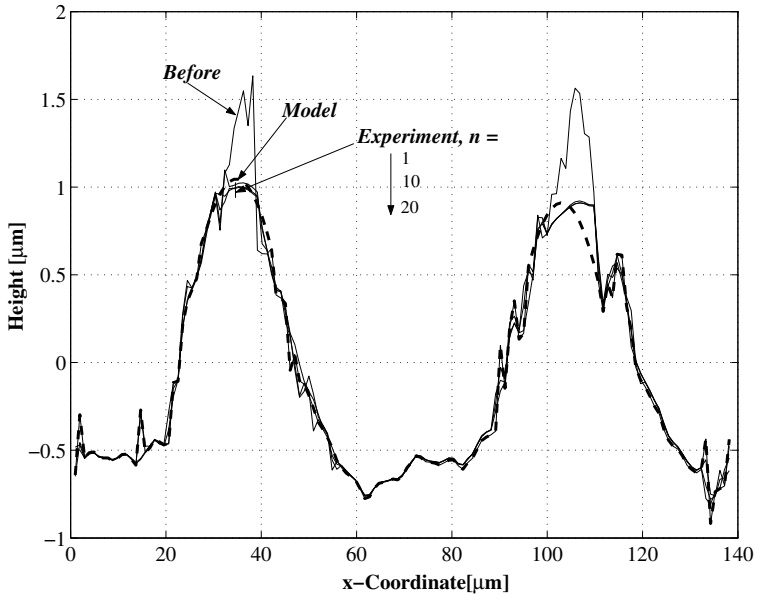

FIGURE 5.16: *x-profile of the matched and stitched anisotropic mild-steel surface at y = 110 μm.*

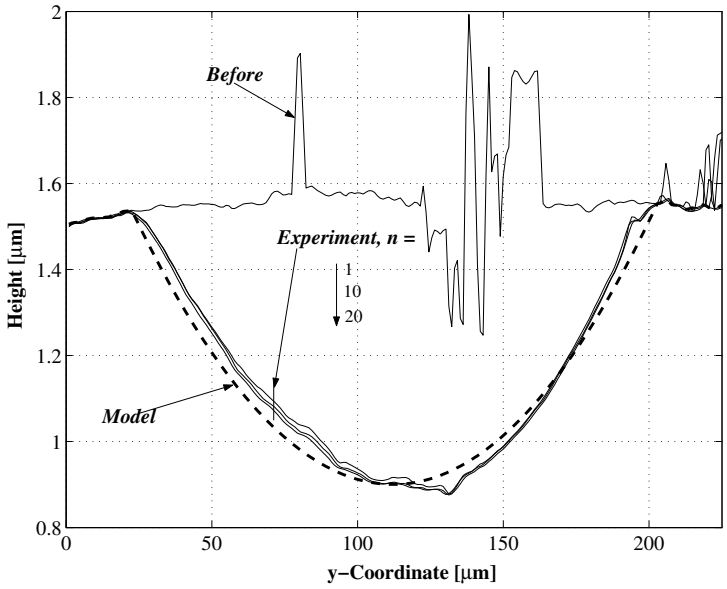

FIGURE 5.17: *y-profile of the matched and stitched anisotropic mild-steel surface at* $x = 108\ \mu m$.

5.4.2 Repeated moving contact

The contact condition for the repeated moving contact is the same as was used in the repeated stationary contact. The roughness value is almost the same and therefore solely asperity deformation is to be expected in this case.

The initial aluminium surface in the repeated moving contact experiment is presented in Fig. 5.18a, and Fig. 5.18b shows the location of the corresponding asperities as well as the sample area of the repeated moving contact and the moving direction. Results of the contact area prediction and measured contact area of aluminium after the first cycle are presented in Fig. 5.19a and Fig. 5.19b, respectively. A good prediction is observed from these figures. Figure 5.20 to Fig. 5.22 show the good ability of the model to predict the change of the surface topography for a repeated moving contact for respectively cycle 1, 2 and run-in cycle 3. A small deviation between the model and the experiment for the run-in cycle ($n = 3$) is observed, because the surface show a change due to volume conservation. The present model does not take such phenomenon into account.

Similar results are found in the mild-steel surface case. Plots of the theoretical model prediction and the measurement in the elastic-plastic contact regime are presented as profiles for cycle 1 and for run-in cycle 5 in Fig. 5.23 and Fig. 5.24, respectively. Small deviations between the model and the measurements are also found in the repeated elastic-plastic moving contact as was discussed earlier in the elastic-plastic repeated stationary contact.

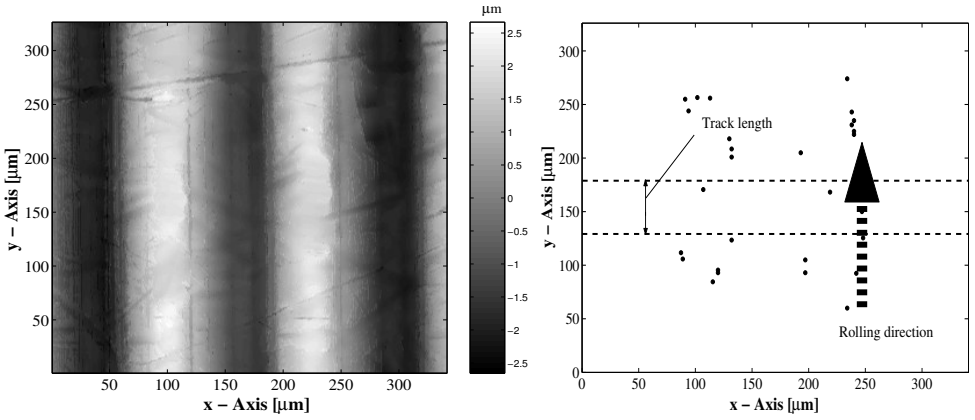

(a) *(b)*

FIGURE 5.18: *Initial aluminium surface for the repeated moving contact experiment (a) and location (not size) of the corresponding asperities with the rolling or moving sample direction (b).*

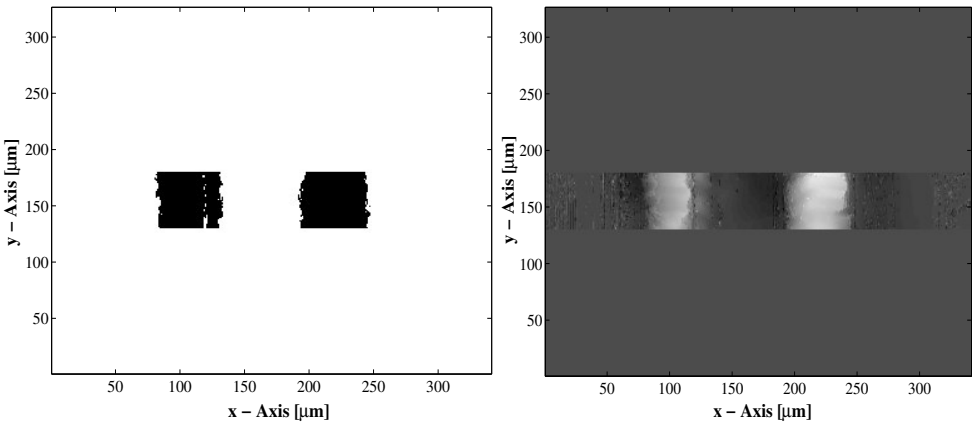

(a) *(b)*

FIGURE 5.19: *Contact area of aluminium surface for n = 1: (a) model and (b) experiment.*

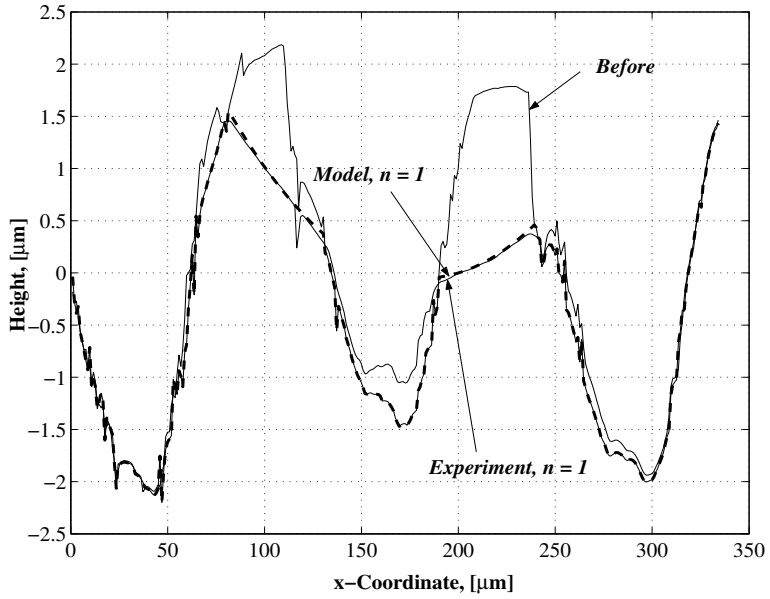

FIGURE 5.20: *Profile of the matching and stitching result of aluminium surface at* $y = 155$ μm *for cycle* $n = 1$.

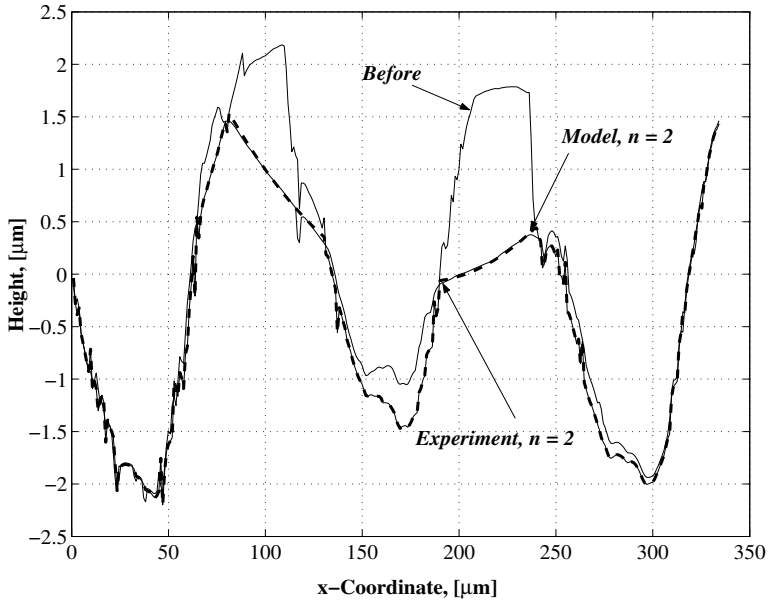

FIGURE 5.21: *Profile of the matching and stitching result of aluminium surface at* $y = 155$ μm *for cycle* $n = 2$.

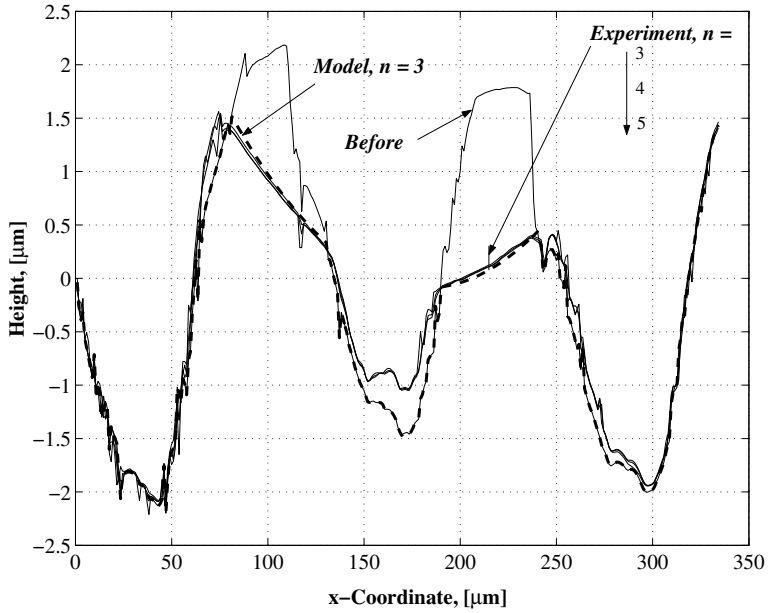

FIGURE 5.22: *Profile of the matching and stitching result of aluminium surface at* $y = 155$ μm *for cycle* $n = 3$, 4, *and* 5.

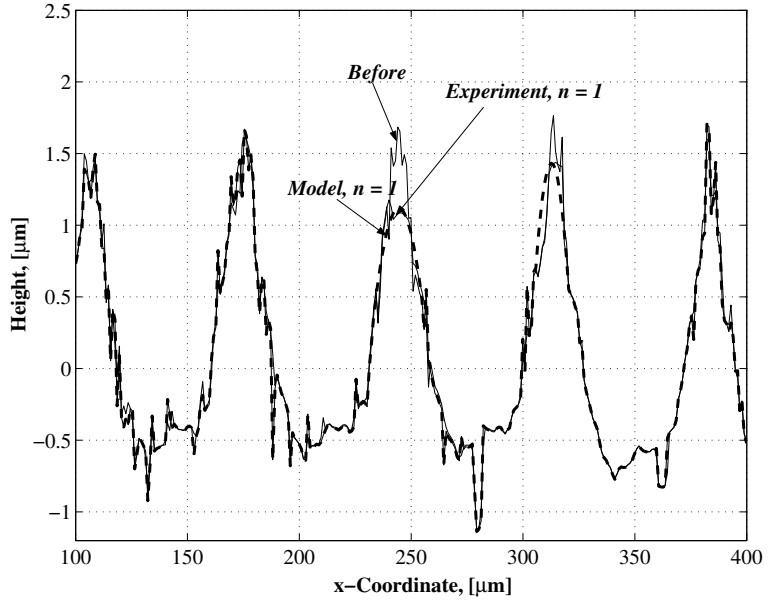

FIGURE 5.23: *Profile of the matching and stitching result of mild-steel surface at* $y = 160$ μm *for cycle* $n = 1$.

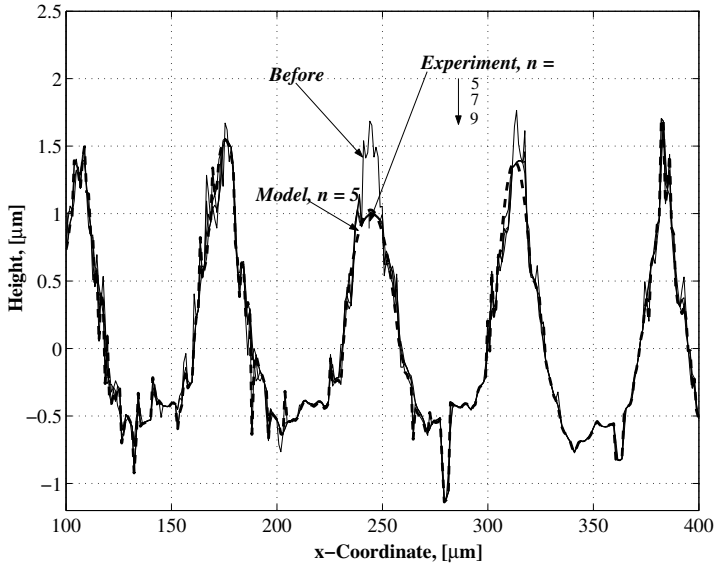

FIGURE 5.24: *Profile of the matching and stitching result of mild-steel surface at* $y = 160\ \mu m$ *for cycle* $n = 5$, 7 and 9.

Compared to the repeated stationary contact, the repeated moving contact exhibits the development of the shape of the contact area and the asperity deformation. These phenomena can be explained as follows. A deformable smooth surface in contact with a rigid sphere with high load is considered for explanation purposes, see Fig. 5.25. For the loading-unloading of a static indentation, the developed plastic contact area is circular (Fig. 5.25a). For the rolling contact situation, when rolling starts, plastic flow leads to the permanent groove in the rolling track direction. With successive traversals of rolling the track width and the normal plastic deformation gradually increases. This occurs because a line or wide elliptical contact is formed by the contact between the groove in the surface and the sphere and it is not sufficient to support the applied load. This process continues until a state of equilibrium is reached where no appreciable change in the track width and normal plastic deformation occurs. This equilibrium state is referred to as the run-in state of the contacting surfaces. In the absence of work-hardening, this effect of increasing track width or contact area (change of contact geometry) is the main factor influencing the equilibrium state. Elredge and Tabor [22] showed that when the equilibrium of the plastic deformation is reached the coefficient of friction also reaches a stable and lower value which implies that the running-in period is finished so that the contacting surface starts to operate in the steady state period.

5.4.3 Repeated rolling contact

The same contact condition as was used in the repeated moving contact was used in the repeated rolling contact. Results of the rolling contact experiment, along with the model

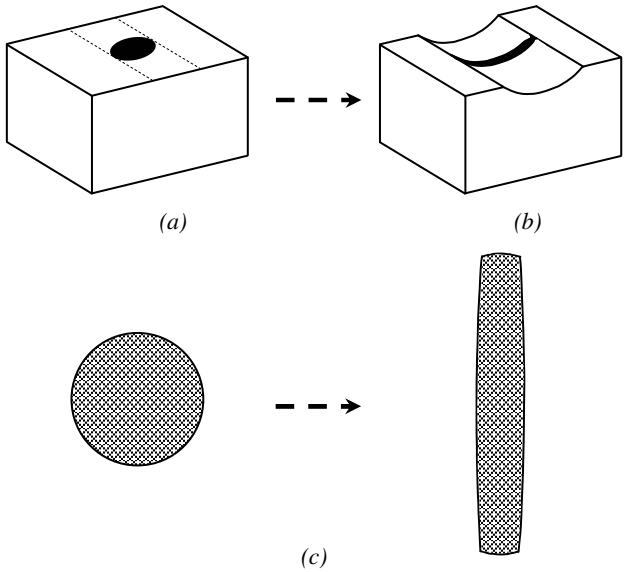

FIGURE 5.25: *Development of contact area during plastically rolling contact. (a) Static contact (b) run-in condition and (c) contact area and track width development.*

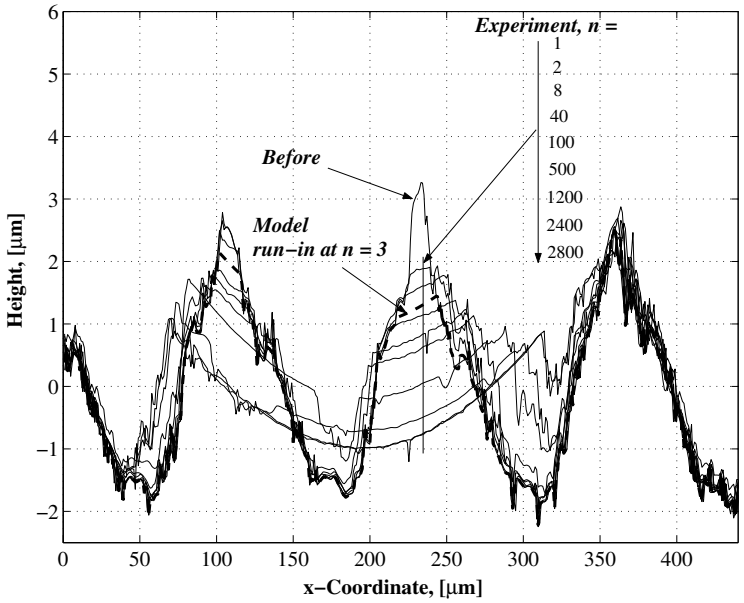

FIGURE 5.26: *Profile of the matching and stitching result of aluminium surface at* $y = 160\ \mu m$ *(perpendicular to the rolling direction).*

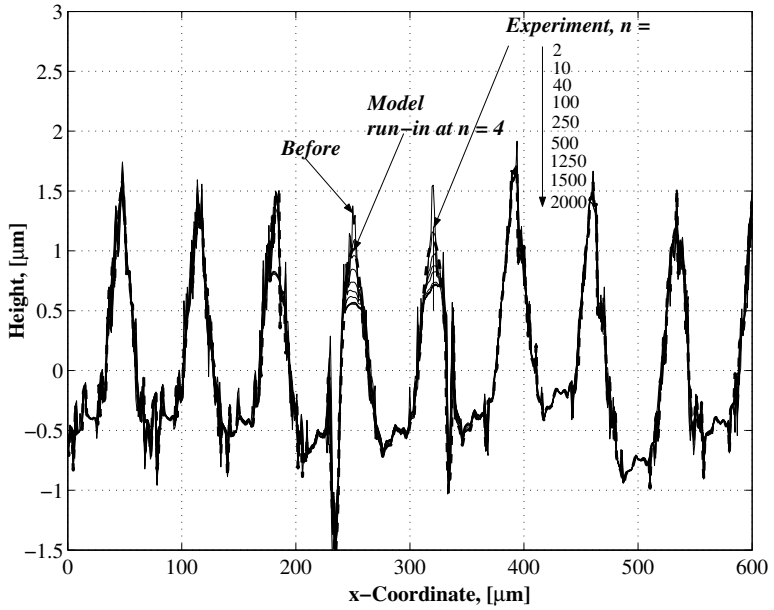

FIGURE 5.27: *Profile of the matching and stitching result of mild-steel surface at y = 158 μm (perpendicular to the rolling direction).*

prediction for the aluminium and mild-steel surfaces are presented in Fig. 5.26 and Fig. 5.27, respectively. It can be seen from Figs. 5.26 and 5.27 that there is much deviation between the predicted run-in profile and the measured run-in profile. The model predicts the surface to be run-in at cycle n = 3 for the aluminium surface and at cycle n = 4 for the mild-steel surface, but the experimental result show that the aluminium surface is run-in at cycle n = 2400 and the mild-steel surface is run-in at cycle n = 1250. The magnitude of the plastic deformation is also significantly different. Interestingly, even with the very high plastic deformation, bulk deformation is not observed as predicted. The velocity of this setup, 7 mm/s, is much higher compared to the repeated moving contact where loading and unloading is executed every 5 seconds for 1 μm translation. This high velocity may contribute to the wear of the surface. This phenomenon has been reported by Morgan [23] where a smooth deformable plate is rolled by a rigid smooth ball. Results showed that for the same number of over-rolling cycle, plastic deformation for the higher frequency (higher velocity) is higher than the lower one, which is also observed in the present experiment.

To investigate the presence of slip, an experiment was done by measuring the number of revolution of the ball and the total distance of the track on the disk. For the experiments with an aluminium surface, high slip was observed. Every 10 revolutions of the disk ($10\pi D_{track} \approx 2.89$ m) the ball rotates for about 50 revolutions ($50\pi D_{ball} \approx 0.99$ m). The rolling condition for the mild-steel surface is much better. For the first 10 rotations of the disk, the number of revolution of the ball is about 143 ($143\pi D_{ball} \approx 2.85$ m). However, when the number of over-rolling increases (the surface start to conform) the amount of slip increases. This was observed by measuring the number of revolution of the ball in the range of 40 to 50 cycles. In this range, the number of revolution of the ball is about 140

($140\pi D_{ball} \approx 2.79$ m) which is lower than the first 10 revolutions of the disk. It can be concluded that in this experiment setup, the pure rolling contact condition is hardly achieved.

5.5 Concluding remarks

In this chapter, study of the repeated stationary contact, the repeated moving contact and the rolling contact was carried out theoretically and experimentally. The experimental results were compared with the theoretical predictions and it was found that the theoretical model predicts the contact area and the change of the surface topography due to plastic deformation for the repeated stationary contact and the repeated moving contact very well. It was also shown that the run-in cycle of the contacting surface can be well predicted by the developed model.

For the rolling contact experiment the model underestimates the contact area and the plastic deformation. Wear is expected to be the main factor which affects the deviation from the model.

References

[1] Blau, P.J., 1989, *Friction and Wear Transitions of Materials: Break-in, Run-in, Wear-in*, Noyes Publications, Park Ridge, NJ, USA.

[2] Blau, P.J., 1996, *Friction Science and Technology*, Marcel Dekker, New York, USA.

[3] Lin, J.Y. and Cheng, H.S., 1989, "An analytical model for dynamic wear," *ASME-Journal of Tribology* **111**, pp. 486 – 474.

[4] Hu, Y.Z., Li, N. and Tønder, K., 1991, "A dynamic system model for lubricated sliding wear and running-in," *ASME-Journal of Tribology* **113**, pp. 499 – 505.

[5] Shirong, G. and Gouan, C., 1999, "Fractal prediction models of sliding wear during the running-in process," *Wear* **231**, pp. 249 – 255.

[6] Wang, W. and Wong, P.L., 2000, "Wear volume determination during running-in for PEHL contacts," *Tribology International* **33**, pp. 501 – 506.

[7] Kumar, R., Prakash, B. and Sethuramiah, A., 2002, "A systematic methodology to characterize the running-in and steady-state wear processes," *Wear* **252**, pp. 445 – 453.

[8] Jeng, Y.R., Lin, Z.W. and Shyu, S.H., 2004, "Changes of surface topography during running-in process," *ASME-Journal of Tribology* **126**, pp. 620 – 625.

[9] Blau, P.J., 1987, "A model for run-in and other transitions in sliding friction," *ASME-Journal of Tribology* **109**, pp. 537 – 544.

[10] Merwin, J.E. and Johnson, K.L., 1963, "An analysis of plastic deformation in rolling contact," *Proc. Instn. Mech. Engineers* **177**, pp. 676 – 685.

[11] Bhargava, V., Hahn, G.T. and Rubin, C.A., 1985, "An elastic-plastic finite element model of rolling contact. Part 1: Analysis of single contacts," *ASME-Journal of Applied Mechanics* **52**, pp. 67 – 74.

[12] Bhargava, V., Hahn, G.T. and Rubin, C.A., 1985, "An elastic-plastic finite element model of rolling contact. Part 2: Analysis of repeated contacts," *ASME-Journal of Applied Mechanics* **52**, pp. 75 – 82.

[13] Ham, G., Rubin, C.A., Hahn, G.T. and Bhargava, V., 1988, "Elasto-plastic finite element analysis of repeated, two-dimensional rolling-sliding contacts," *ASME-Journal of Tribology* **110**, pp. 44 – 49.

[14] Kulkarni, S.M, Hahn, G.T., Rubin, C.A. and Bhargava, V., 1991, "Elasto-plastic finite element analysis of three-dimensional pure rolling contact above the shakedown limit," *ASME-Journal of Applied Mechanics* **58**, pp. 347 – 353.

[15] Van Dang, K. and Maitournam, M.H., 1993, "Steady state flow in classical plasticity: applications to repeated sliding and rolling contact," *Journal of Mech. Phys. Solids* **41**, pp. 1691 – 1710.

[16] Yu, M.M.H., Moran, B. and Keer, L.M., 1993, "A direct method of 2-D elastic-plastic rolling contact," *ASME-Journal of Tribology* **115**, pp. 227 – 236.

[17] Yu, M.M.H., Moran, B. and Keer, L.M., 1995, "A direct analysis of 3-D elastic-plastic rolling contact," *ASME-Journal of Tribology* **117**, pp. 234 – 243.

[18] Yu, M.M.H., Moran, B. and Keer, L.M., 1996, "A simplified direct method for cyclic strain calculations: repeated rolling sliding contact on a case-hardened half-space," *ASME-Journal of Tribology* **118**, pp. 329 – 334.

[19] Sakae, C. and Keer, L.M., 1997, "Application of direct method for a non-linear kinematic hardening material under rolling/sliding contact: constant ratcheting rate," *Journal of Mech. Phys. Solids* **45**, pp. 1577 – 1594.

[20] Johnson, K.L., 1985, *Contact Mechanics*, Cambridge University Press, Cambridge, UK.

[21] Tasan, Y.C., 2005, Measurement of Deformation in Rolling and Sliding Contacts, PhD Thesis, University of Twente, Enschede, The Netherlands.

[22] Eldredge, K.R. and Tabor, D., 1954, "The mechanism of rolling friction: 1. The plastic range," *Proc. R. Soc. London* **A229**, pp. 181 – 198.

[23] Morgan, J.E., 1999, "Cumulative plastic deformation observed during cyclic testing in rolling ball-cylinder and static ball-flat plate experiments," *Wear* **231**, pp. 249 – 255.

Chapter 6

Conclusions and recommendations

This chapter summarizes the main conclusions of the previous chapters and provides a number of open problems for future research based on the work as described in this thesis.

6.1. Conclusions

Chapter 2: Running-in: a literature review

- Running-in is a very complex phenomenon and most of the studies have been conducted experimentally.
- Most of the time theoretical studies performed on running-in are statistical approaches, assuming a Gaussian distribution.
- Plastic deformation in normal direction and mild wear are the two dominant mechanisms during running-in of lubricated contacts. The plastic deformation in normal direction is more dominant than the mild wear and is expected to be the key factor; therefore, in the present study the analysis is focused on the plastic deformation due to normal loading and omitting the wear mechanism. In this case the pure rolling contact situation is the best selection. To study the plastic deformation due to normal loading, a contact model is needed.

Chapter 3: Elastic-plastic single asperity contact

- An asperity micro-contact model was considered due to its analytical nature. In order to select the best asperity contact model available in literature, experiments have been performed. Results showed that there is no agreement between the measured deformation and the prediction by the models. Therefore, a new contact model should be developed.

- A new elliptic elastic-plastic asperity contact model has been developed based on the knowledge gained from experimental investigation. The developed model was also examined by the experimental results presented in literature. The contact model predicts the contact parameters very well.
- An unloading elliptic elastic-plastic asperity contact model has been developed as an extension of the developed asperity contact model. The model predicts the elastic recovery and plasticity of the deformation and contact area after unloading. The model agrees well with the measured plastic deformation and plastic contact area.

Chapter 4: Deterministic elastic-plastic multi asperity contact

- Running-in changes the surface roughness height, hardly changes the surface wavelength and bulk deformation of the contacting surfaces has to be avoided since it changes the macro-geometry. Therefore, a contact condition where the deformation occurs on asperity level must be designed. A theoretical criterion to predict the deformation behavior of the contacting surfaces has been developed. A good correlation was found between the developed deformation criterion and the performed experimental results. The criterion is simple and is easy to be used for practical engineers.
- The local change of the surface topography is the point of interest of the present study which cannot be employed in the statistical contact model of rough surfaces. Instead of the statistical contact model, a deterministic elliptic elastic-plastic contact model of rough surfaces has been constructed by utilizing the developed single asperity contact model. This model excludes the bulk deformation. Geometrical contact parameters such as height and curvatures of the asperities are determined locally as the input of the model. The summit method is widely used so far in order to determine such parameters rather than the volume conservation method. The superiority of the later method to the former has been demonstrated. The model has been applied to the real contact of rough surfaces and results show that the model simulates the change of the surface topography very accurately. Deviation between the model prediction and the measured plastic deformation and plastic contact area is very small.

Chapter 5: Running-in of rolling contacts

- The developed deterministic elliptic elastic-plastic contact of rough surfaces was extended to the repeated contact situation. Three types of repeated contact were studied, namely the repeated stationary contact, the repeated moving contact and the rolling contact.
- For the repeated stationary contact model, the contacting surfaces are loaded and unloaded with the same load and at the same location. The model has been verified by experimental results and was found to be in a good agreement. Results also show that the surfaces are run-in after the first cycle of loading-unloading in this type of repeated contact.
- A running-in model was developed based on repeated moving contacts. In this model, the contacting surfaces are loaded, unloaded, translated over a distance and then again

loaded, unloaded, translated and so on until a certain 'rolling' distance is achieved. Two types of experiments were utilized for verifying the model, i.e. the repeated moving contact setup and the rolling contact setup. In the repeated moving contact setup the contacting surfaces are loaded and unloaded exactly as was described by the proposed model, whilst in the rolling contact setup a stationary rolling surface was in contact with a moving surface. Experimental results show that the model predicts the surface topography changes and the run-in cycle for the repeated moving contacts very well, whilst this is not the case for the rolling contact setup. Wear was expected to be the main factor influencing the experimental results.

6.2. Discussion

In this section two interesting findings related to this thesis will be discussed, namely (1) plastic deformation of two deformable contacting bodies and (2) plastic deformation for a very high load.

Johnson and Shercliff [1] hypothesized that when two contacting asperities have the same hardness, the depth of plastic deformation is expected to be the same for each body, independent of the geometries used. Based on this hypothesis, experiments have been performed on the contact between two hardened steel balls (H = 8.3 GPa, E = 210 GPa and ν = 0.3). A number of contact pairs with different ratio of radii of the contacting balls have been selected and the results are presented in Fig. 6.1. The method to determine the amount

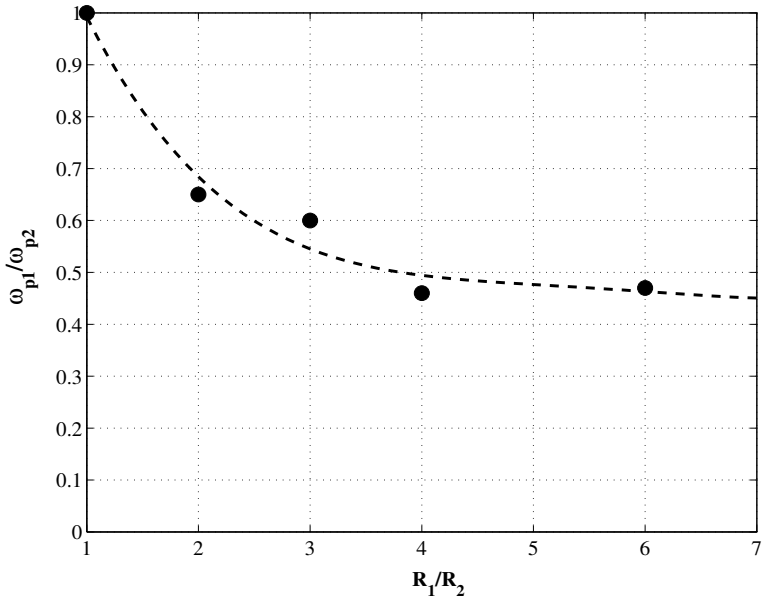

FIGURE 6.1: *The ratio of plastic deformation as a function of the ratio of radii of the contacting bodies. ● experimental results and the fitting curve (dash-line).*

of plastic deformation is the same as was applied in Section 3.5 of Chapter 3. Obviously, it is observed that even in the bodies in contact having the same hardness, the degree of plastic deformation of the bodies in contact differs significantly, which contradicts the hypothesis of [1]. The ratio of the plastic deformation of the bodies in contact ω_{p1}/ω_{p2} decreases as the ratio of the radii of the bodies R_1/R_2 increases. The body with a higher contact radius deforms plastically less than the body with a lower contact radius. This phenomenon may be explained by the flow of displaced material of the contacting bodies, see Fig. 6.2. Here, the contact between a flat half-space and a ball is considered. When a high load is applied, such that plastic deformation occurs, the material of the ball near the contact area is radially free displaced (lateral). This does not happen to the material of the half-space, because the displacement of the material due to the plastic flow is confined by the elastic-plastic bulk. Consequently, the plastic deformation for the ball is higher than for the half-space.

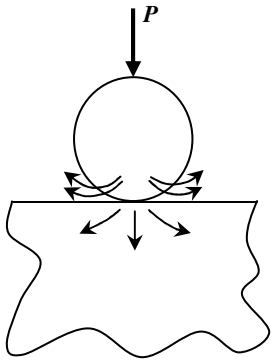

FIGURE 6.2: *Material displacement (schematically) of the contact between two deformable bodies.*

The second discussion is about the deformation behavior of the asperity at the very high load. An elastic-perfectly aluminium (H = 0.24 GPa, E = 75.2 GPa and v = 0.34) surface has been compressed repeatedly with a load of 1 N by a smooth hard SiC ceramic (H = 28 GPa, E = 430 GPa and v = 0.17) ball with radius of 5 mm. Results are presented in Fig. 6.3 along with the model prediction as was discussed in Chapter 5. As can be seen, the model predicts the change of the surface topography well for the asperities which are far away from the center of the spherical (ball) indenter, but not for the asperity close to the center of the indenter. This implies that the model is valid for moderate full plasticity and starts to deviate when it operates deeply in the full plasticity region. In the deep full plasticity region the model overestimates the plastic deformation. It is clear from the figure that the very high loaded asperity in the center, exhibits volume conservation behavior. The deformed material is displaced laterally of the asperity, which leads to the increase of the contact area and as a result the applied pressure decreases. The volume conservation phenomenon of the deformed asperity is not included in the present model, therefore the

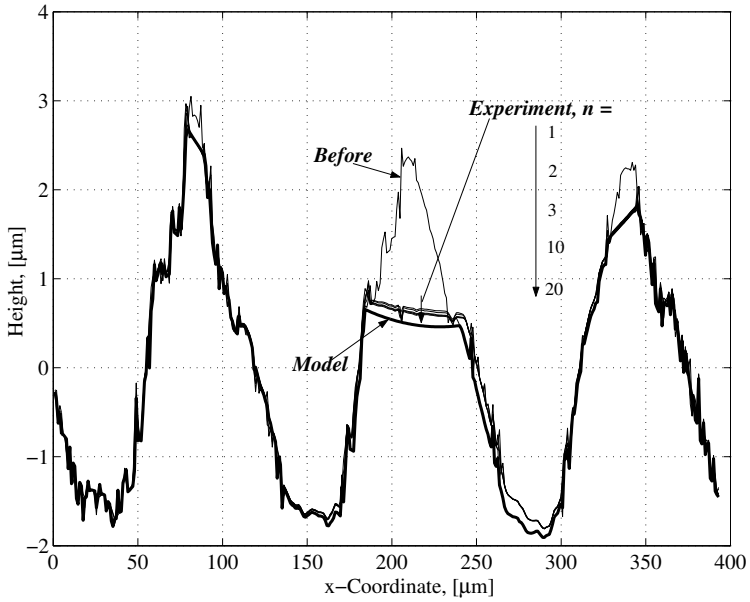

FIGURE 6.3: *Change of the aluminium profile due to repeated simple contacts.*

deviation is observed for the very high load. The behavior of the contact operating deeply in the full plasticity region has also been studied by Mesarovic and Fleck [2] by finite element analysis. They showed that for the very high load, the mean contact pressure starts decreasing. This regime, according to them, is referred to as the finite deformation regime.

6.3. Recommendations

The following offers several open problems which may be explored for future study.

- Based on the previous discussions, further investigation into the plastic deformation of the contact between two elastic-plastic deformable bodies should be conducted.
- Deep into the fully plastic regime or finite deformation regime, the behavior of the asperity shape and the mean contact pressure are changing. More research which copes with these phenomena is needed. Furthermore, strain hardening should be taken into account.
- Incorporating wear will extend the rolling running-in model to sliding or rolling/sliding running-in.

References

[1] Johnson, K.L. and Shercliff, H.R., 1992, "Shakedown of 2-dimensional asperities in sliding contact," *Int. Journal of Mech. Sciences* **34**, pp. 375 – 394.

[2] Mesarovic, S.D. and Fleck, N.A., 2000, "Frictionless indentation of dissimilar elastic-plastic spheres," *Int. Journal of Solids and Structures* **37**, pp. 7071 – 7091.

Appendix A

Critical interference

As was mentioned in Chapter 3 the critical interference, $\omega_{1\text{-}KE}$, of the *KE* model [A1] is defined in terms of contact interference ω as:

$$\omega_{1-KE} = \left(\frac{\pi K_{KE} H}{2E} \right)^2 R \tag{A.1}$$

If the value of $K_{KE} = 0.6$ then Eq. (A.1) becomes the critical interference for the *CEB* model [A2] and the *ZMC* model [A3].

The von Mises failure criterion with zero shear stresses has the following form:

$$J = \frac{1}{6}\left\{(\sigma_1 - \sigma_2)^2 + (\sigma_2 - \sigma_3)^2 + (\sigma_3 - \sigma_1)^2\right\} = k^2 = \frac{Y^2}{3} \tag{A.2}$$

where σ_1, σ_2 and σ_3 denote the three principal stresses, k represents the material yield stress in simple shear and Y represents the material yield stress in simple tension or compression. According to Johnson [A4], the principal stresses for a Hertzian contact along the z-axis (the axis that passes through the center of the contact area) can be expressed as:

$$\frac{\sigma_r}{p_0} = \frac{\sigma_\theta}{p_0} = -(1+\nu)\left[1 - s\tan^{-1}\left(\frac{1}{s}\right)\right] + \left(1+s^2\right)^{-1} \tag{A.3}$$

$$\frac{\sigma_z}{p_0} = -\left(1+s^2\right)^{-1} \tag{A.4}$$

where $s = z/a$, ν is the Poisson's ratio of the material, a is the radius of the contact area and p_0 is the maximum Hertzian contact pressure. In this case, σ_r, σ_θ and σ_z are the principal

stresses. Substituting Eqs. (A.3) and (A.4) into Eq. (A.2) and rearranging give the following expression:

$$k = \frac{1}{\sqrt{3}} f(v,s)\, p_0 \tag{A.5}$$

where

$$f(v,s) = -(1+v)\left[1 - s\tan^{-1}\left(\frac{1}{s}\right)\right] + \frac{3}{2}\frac{1}{1+s^2} \tag{A.6}$$

Since p_0 in Eq. (A.5) does not depend on s, the point where yield will occur first is where f, Eq. (A.6), has its maximum. s^*, the point where the first yield occurs, is a function of v, rather than a function of p_0. s^* can thus be found by solving

$$\left.\frac{\partial f(v,s)}{\partial s}\right|_{s=s^*} = (1+v)\left[\tan^{-1}\left(\frac{1}{s^*}\right) - \frac{s^*}{1+(s^*)^2}\right] - \frac{3s^*}{\left[1+(s^*)^2\right]^2} = 0 \tag{A.7}$$

At incipient yield $k^2 = Y^2/3$ so that Eq. (A.5) can be rewritten as:

$$k = \frac{1}{\sqrt{3}} f(v,s^*)\, p_0 = \frac{Y}{\sqrt{3}} \tag{A.8}$$

where

$$f(v,s^*) = -(1+v)\left[1 - s^*\tan^{-1}\left(\frac{1}{s^*}\right)\right] + \frac{3}{2}\frac{1}{1+(s^*)^2} \tag{A.9}$$

Rearranging Eq. (A.8) yields:

$$p_0 = \frac{1}{f(v,s^*)} Y \tag{A.10}$$

According to the work of Tabor [A5], the hardness H of a metal in simple compression can be related to its yield stress Y by $H \approx 2.8Y$, hence Eq. (A.10) can be expressed as:

$$p_0 = \frac{1}{2.8\, f(v,s^*)} H = KH \tag{A.11}$$

where K is the maximum contact pressure factor, or:

$$K = \frac{1}{2.8 f(v, s^*)} \tag{A.12}$$

This equation is solved numerically for a range of Poisson's ratios to find the location z at initial yielding. The locations of the maximum contact pressure were derived by [A6] using an approximate expression, so that K in Eq. (A.12) becomes:

$$K_{KE} = 0.454 + 0.41v \tag{A.13}$$

Similarly, [A7] used the curve fitting method to define K as:

$$K_v = 0.4645 + 0.3141v + 0.1943v^2 \tag{A.14}$$

JG [A8] proposed that the relation between the hardness of the material with its yield stress is not constant, but depends on the contact interference. Accordingly, [A8] used yield stress as a parameter rather than hardness, because yield stress is constant. Similar procedures were used and the *KH* value in Eqs. (A.1) and (A.11) are replaced by:

$$CY = 1.295 \exp(0.736v) \tag{A.15}$$

References

[A1] Kogut, L. and Etsion, I., 2002, "Elastic-plastic contact analysis of a sphere and a rigid flat," *ASME-Journal of Applied Mechanics* **69**, pp. 657 – 662.

[A2] Chang, W.R., Etsion, I. and Bogy, D.B., 1987, "An elastic-plastic model for the contact of rough surfaces," *ASME-Journal of Tribology* **109**, pp. 257 – 263.

[A3] Zhao, Y., Maietta, D.M. and Chang, L., 2000, "An asperity microcontact model incorporating the transition from elastic deformation to fully plastic flow," *ASME-Journal of Tribology* **122**, pp. 86 – 93.

[A4] Johnson, K.L., 1985, *Contact Mechanics,* Cambridge University Press, Cambridge, UK.

[A5] Tabor, D., 1951, *The Hardness of Metals,* Oxford University Press.

[A6] Chang, W.R., Etsion, I. and Bogy, D.B., 1988, "Static friction coefficient model for metallic rough surfaces," *ASME-Journal of Tribology* **110**, pp. 57 – 63.

[A7] Lin, L.P. and Lin, J.F., 2005, "An elastoplastic microasperity contact model for metallic materials," *ASME-Journal of Tribology* **127**, pp. 666 – 672.

[A8] Jackson, R.L. and Green, I., 2005, "A finite element study of elasto-plastic hemispherical contact against a rigid flat," *ASME-Journal of Tribology* **127**, pp. 343 – 354.

Appendix B

Comparison between the proposed asperity contact models with the experimental data

B.1. Fully plastic contact

B.1.1 Present experiments

Results of the contact between aluminium spheres against hard SiC flats are presented in Fig. B.1 to Fig. B.4. In the fully plastic contact regime, profile of the deformed spheres showed almost a flat following the shape of the flat indenter.

Figure B.1 shows the profile after indentation for a normal load of 206 N. This typical form applies for all the experimental results. Therefore, the plastic contact area ($A = 2\pi R\omega$) is just the truncation of the sphere as is shown in Fig. B.2. For aluminium, the mean contact pressure in the fully plastic contact regime in the present experiments is about $0.71H$, see Fig. B.3. These results confirm the experimental work of Chaudhri [B4] where the mean contact pressure in the fully plastic contact regime for elastic-plastic aluminium spheres with a diameter of 3 mm in contact with a sapphire flat is about $0.69H$. The plot of the contact area as a function of the load for the aluminium case can be seen in Fig. B.4.

B.1.2 Experiments by Johnson

Normal compression experiments of Johnson [B1] were performed with two equal copper spheres (H = 0.86 GPa, E = 115 GPa, ν = 0.34) of 127 mm diameter. The stress-strain behavior of the work-hardened copper specimens is shown in Fig. B.5. It can be seen from this figure that the copper shows an elastic-perfectly plastic material behavior.

Figure B.6 presents the results of the mean contact pressure as a function of the contact area, which were obtained by Johnson's experiment, along with the results from the *CEB* model, the *AF* model and the *JG* model as were discussed in Chapter 3. The dashed line is the best fit for the *AF* model for the mean contact pressure $p = 0.79H$. Similar

analysis is presented in Fig. B.7 for the plot of the contact area as a function of the contact load.

B.1.3 Experiments by Chaudhri

Chaudhri [B2] has performed a compression test on a copper sphere (H = 1.32 GPa, E = 120 GPa, v = 0.37) of 1.5 mm radius in contact with a sapphire plate (H = 190 GPa, E = 430 GPa, v = 0.26). The stress-strain curve of the work-hardened copper in compression is depicted in Fig. B.8.

The comparison of Chaudhri's experimental results with the proposed asperity contact models is presented in Fig. B. 9 and Fig. B.10, for the mean contact pressure versus the contact area and the contact area versus the contact load, respectively. The dashed line is the best fit for the AF model for the mean contact pressure $p = 0.68H$.

B.2. Elastic-plastic contact

The setup for the elastic-plastic contact experiments is as was mentioned in Chapter 3. The proposed elastic-plastic asperity contact models are compared. The results of Tabor's experiments [B3] are presented in Fig. B.11 and B.12 and the results of Chaudhri's experiments [B4] are presented in Figs. B.14 to B.17. In these figures the models of *JG*, *KE* and *ZMC* are plotted, as well as the experimental results. Figure B.13 shows the schematic drawing of the arrangement for observing and measuring the contact area directly from Chaudhri's test.

B.3. Conclusions

The present experiments show that for the contact between aluminium spheres and rigid flats, the mean contact pressure in the fully plastic contact regime results in about $0.71H$. Whilst the experimental results of Johnson [B1] and Chaudhri [B2, B4] are best fitted with the simple relation: $p = c_h H$, in which c_h = 0.79, 0.68 and 0.69 for the copper/copper system, the work hardened copper/sapphire system and the aluminium/sapphire system, respectively. c_h is the coefficient of the mean contact pressure in the fully plastic contact regime to the hardness.

If the mean contact pressure in the fully plastic contact regime is assumed to be as $c_h H$, the model of *ZMC* predicts the contact behavior best among the other models in the elastic-plastic contact regime.

References

[B1] Johnson, K.L., 1968, "An experimental determination of the contact stresses between plastically deformed cylinders and spheres," Engineering Plasticity, Cambridge University Press, Cambridge, pp. 341 – 361.

[B2] Chaudhri, M.M., 1987, "The plastic deformation of single asperities by hard flats," Inst. Mech. Eng. Conference Publications **C158**, pp. 1003 – 1012.

[B3] Tabor, D., 1951, *The Hardness of Metals,* Oxford University Press.

[B4] Chaudhri, M.M., Hutchings, I.M. and Makin, P.L., 1984, "Plastic compression of spheres," *Philosophical Magazine* **A49**, pp. 493 – 503.

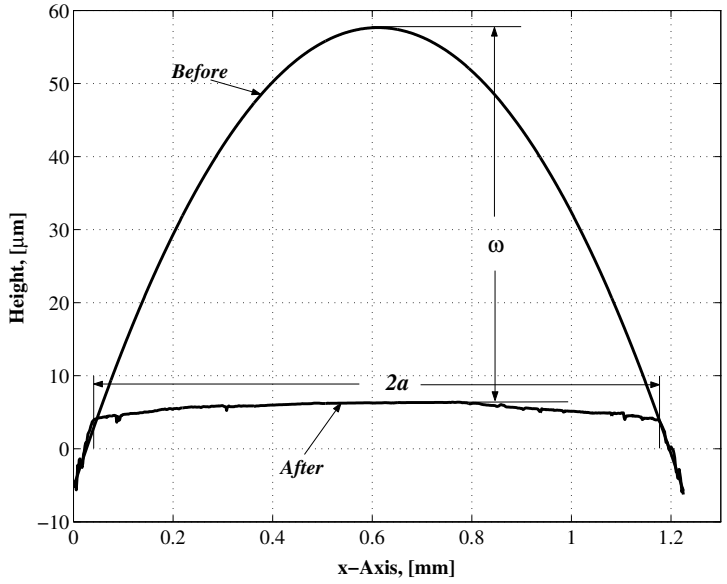

FIGURE B.1: *Profile of the matching and stitching results for 206 N normal load of an aluminium sphere.*

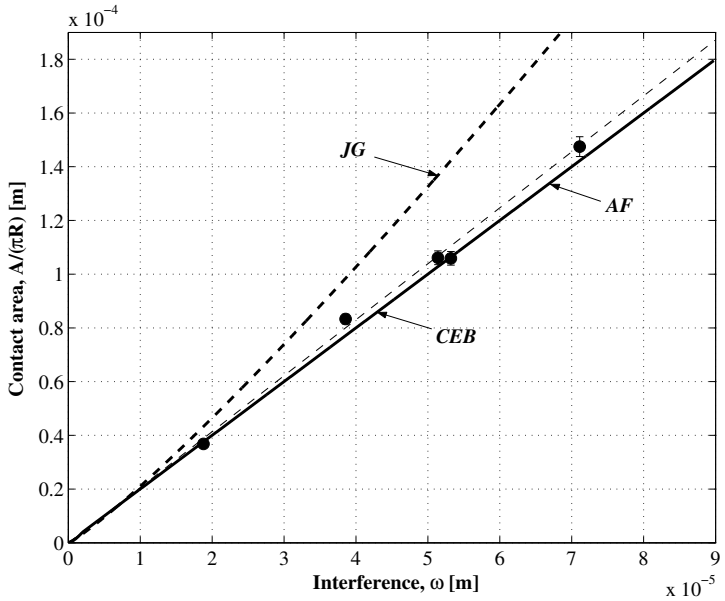

FIGURE B.2: *Plastic contact area vs interference of aluminium spheres. ● are experimental data.*

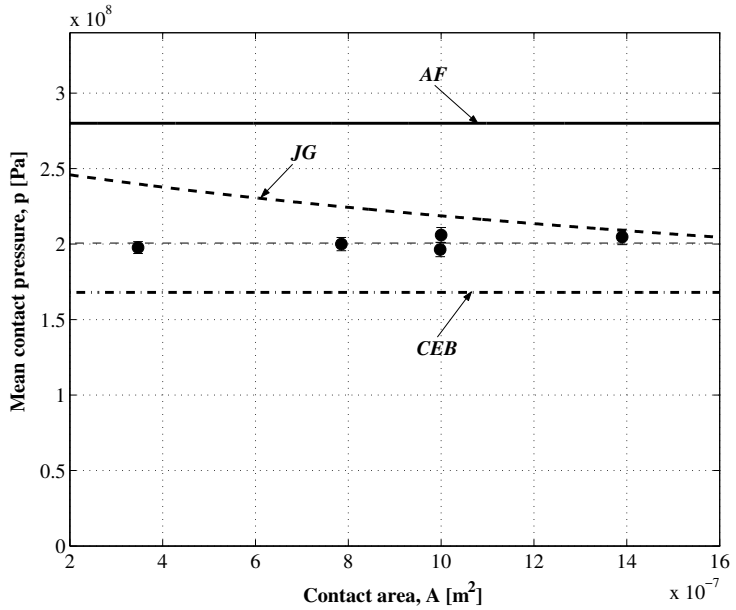

FIGURE B.3: *Mean contact pressure vs contact area of aluminium spheres. ● are experimental data.*

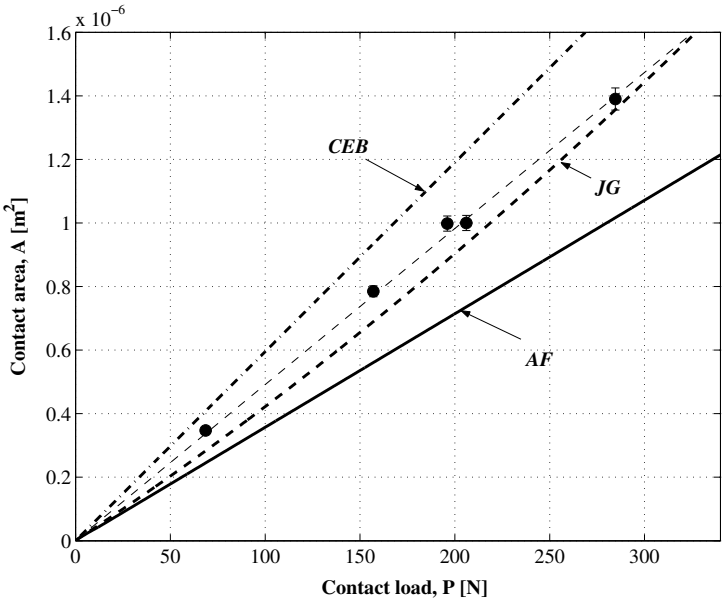

FIGURE B.4: *Contact area as a function of normal load of aluminium spheres. ● are experimental data.*

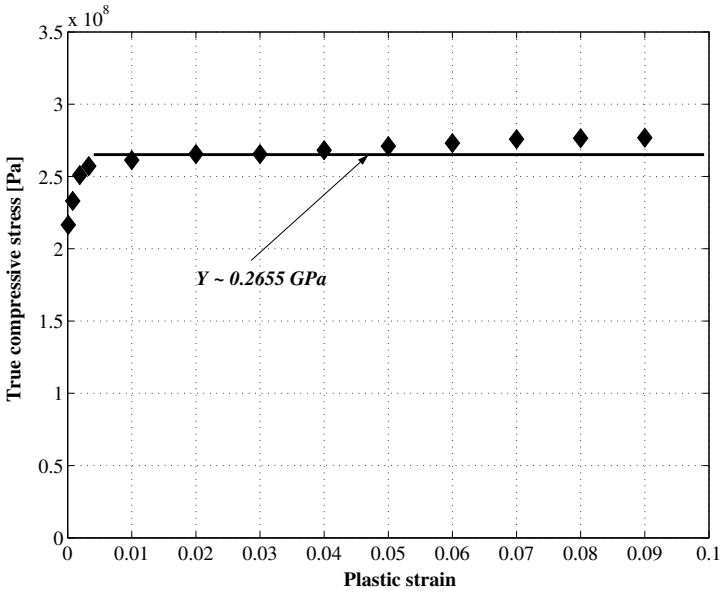

FIGURE B.5: *Compression tests of hard-drawn copper specimens* [B1].

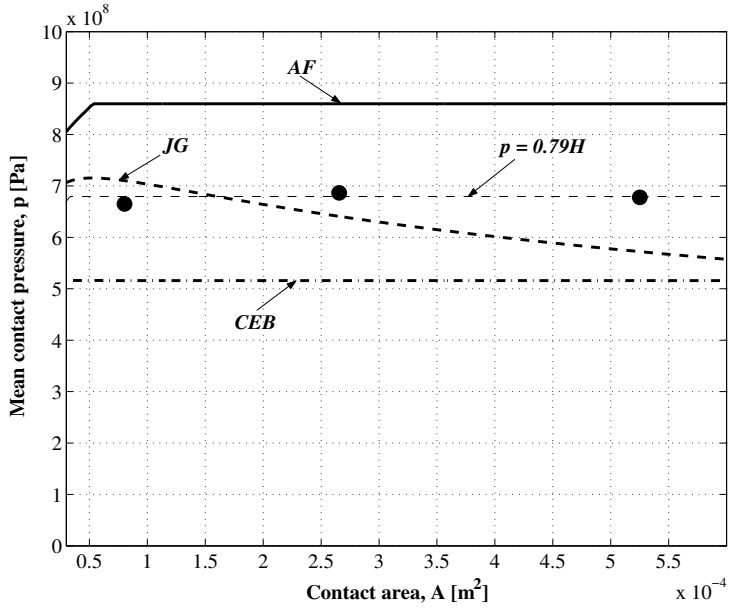

FIGURE B.6: *Mean contact pressure vs contact area of copper spheres.* ● *Johnson's experimental results* [B1].

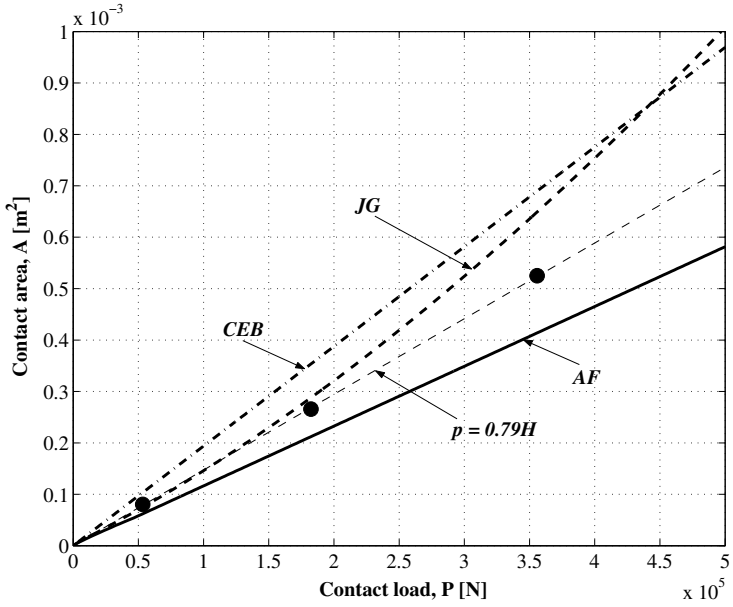

FIGURE B.7: *Contact area vs contact load of copper spheres.* ● *Johnson's experimental results* [B1].

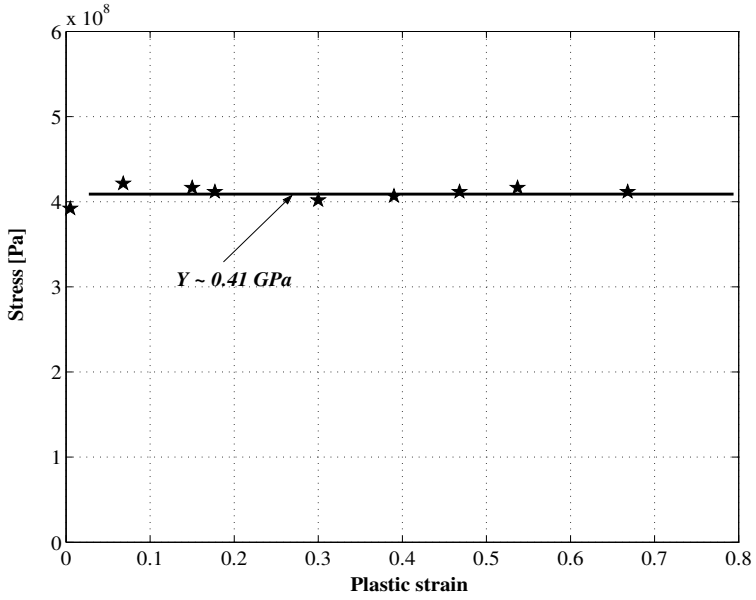

FIGURE B.8: *The stress-strain curve of the work-hardened copper in compression* [B2].

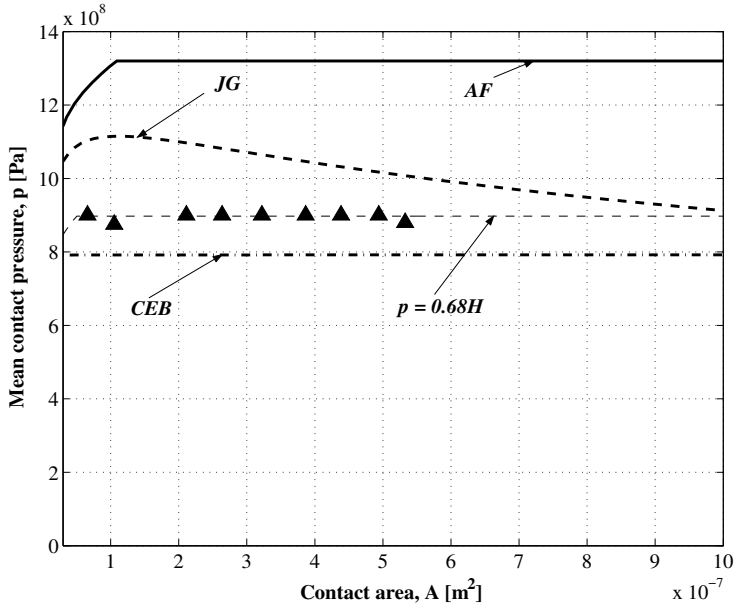

FIGURE B.9: *Mean contact pressure vs contact area of copper spheres.* ▲ *Chaudhri's experimental results* [B2].

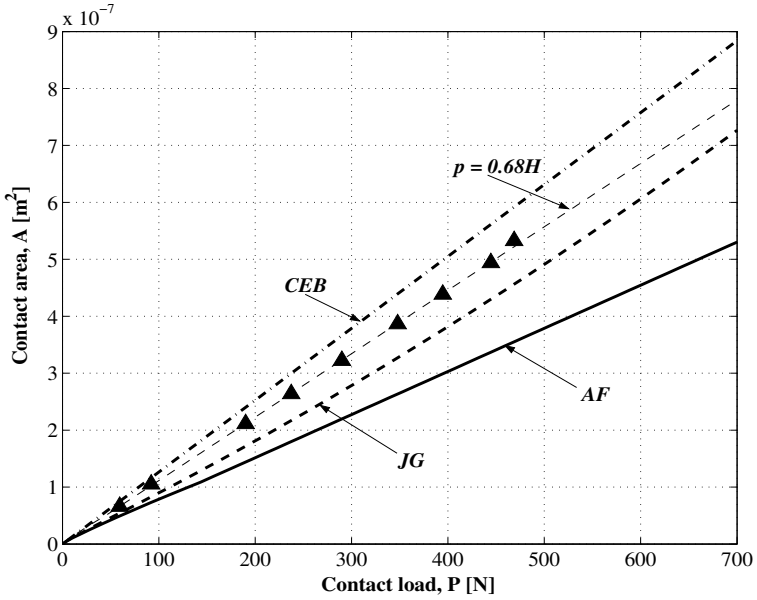

FIGURE B.10: *Contact area vs contact load of copper spheres.* ▲ *Chaudhri's experimental results* [B2].

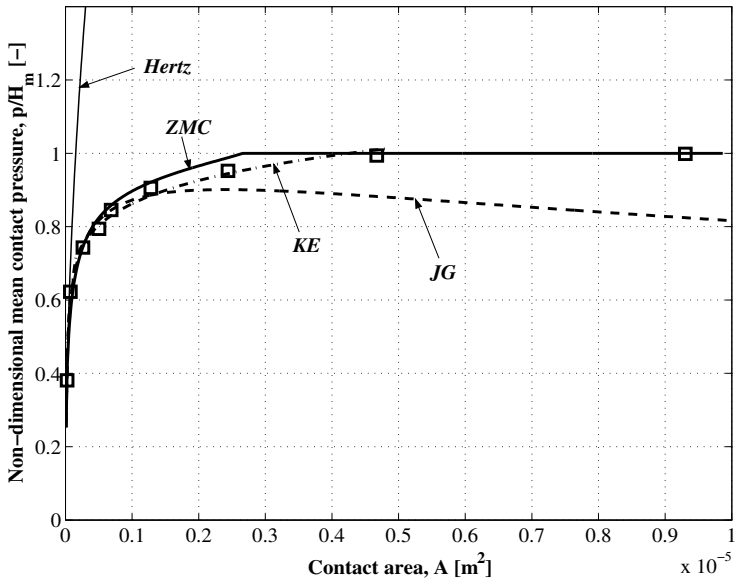

FIGURE B.11: *Non-dimensional mean contact pressure vs contact area of steel spheres.* □ *Tabor's experimental results* [B3].

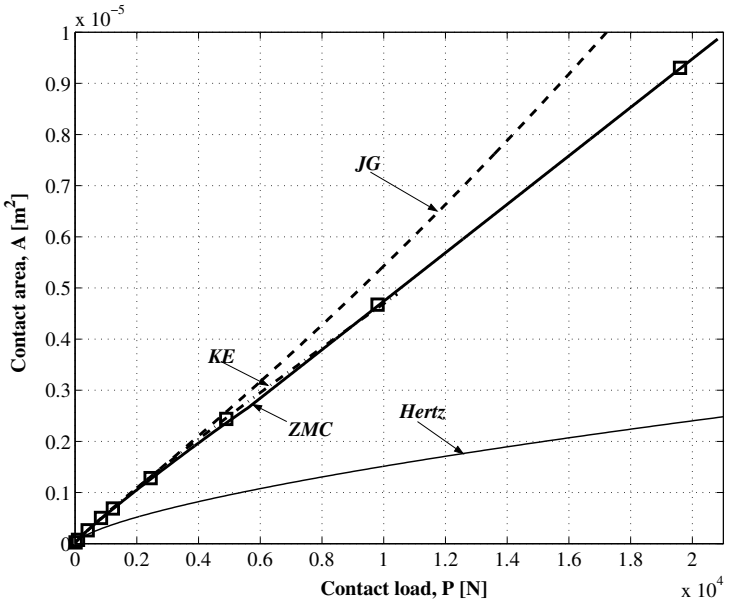

FIGURE B.12: *Contact area vs contact load of steel spheres. □ Tabor's experimental results* [B3].

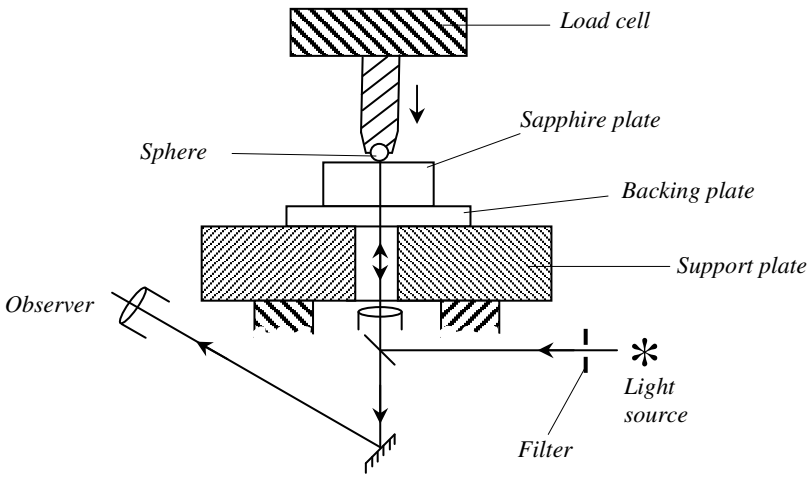

FIGURE B.13: *Schematic drawing of the arrangement for measuring the contact area* [B4].

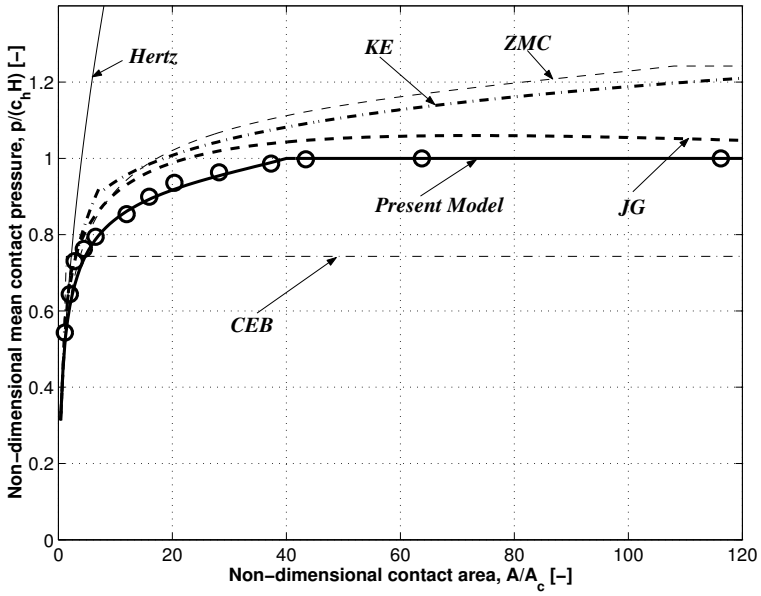

FIGURE B.14: *Non-dimensional mean contact pressure vs contact area of phosphor-bronze spheres.* ○ *Chaudhri's experimental results* [B4].

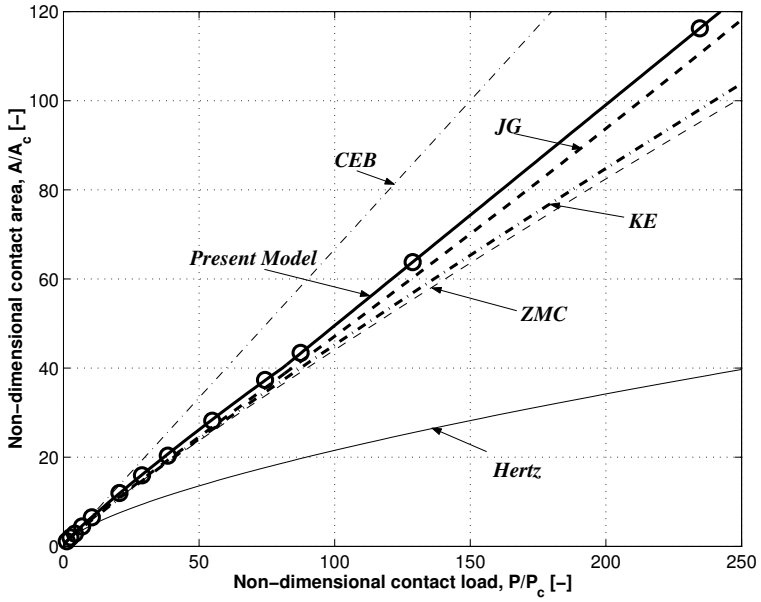

FIGURE B.15: C*ontact area vs contact load of phosphor-bronze spheres.* ○ *Chaudhri's experimental results* [B4].

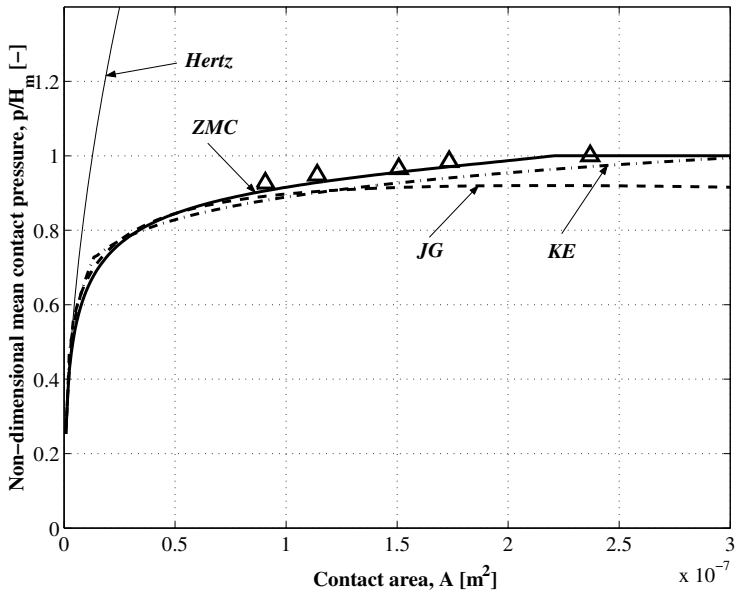

FIGURE B.16: *Non-dimensional mean contact pressure vs contact area of brass spheres.* Δ *Chaudhri's experimental results* [B4].

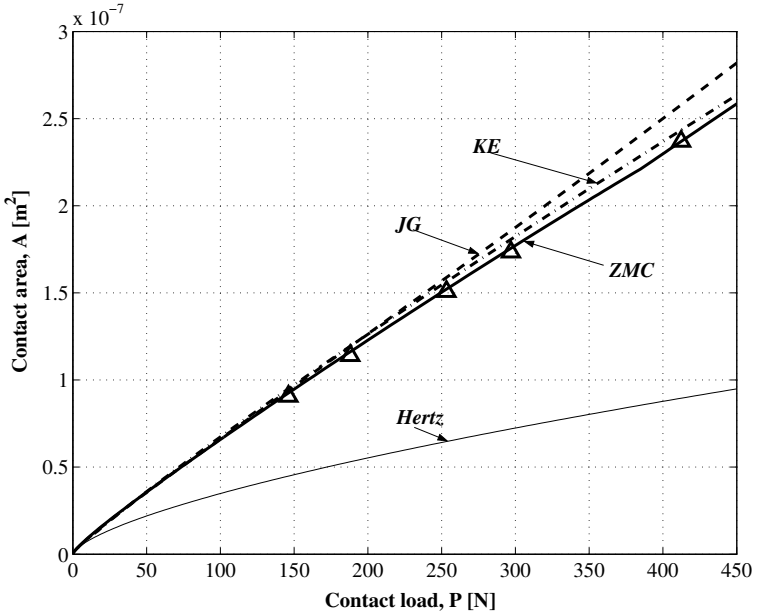

FIGURE B.17: C*ontact area vs contact load of brass spheres.* Δ *Chaudhri's experimental results* [B4].

Appendix C

Matching and stitching

C.1. Introduction

The relation between surface micro-geometry and its function is very important. For characterizing the surface micro-geometry, the statistical approach is widely used. However, in order to understand the effect of surface micro-geometry on its performance, it is important to evaluate not only the surface micro-geometry itself, but also the changes in performance as the surface micro-geometry changes in time. It is thus necessary to compare the changes of surface micro-geometry before and after a period of time or throughout the course of a process.

Omitting the concern of measurement position, it is relatively easy to study the changes in micro-geometry before and after a running process. However, studying the characteristics of the changes in micro-geometry at the same position is more desirable, especially when studying the process of change. This makes it possible to explore the detailed microscopic phenomena. It is necessary to establish special techniques to ensure measuring and observing at the same position the changes of the micro-geometry and its characteristics.

Wear and plastic deformation measurements have been presented by [C1, C2] on the comparison of local surface heights. Based on the image processing technique, they are able to measure and characterize wear of very wear-resistant materials like hard coatings. The information about local height differences at the surfaces caused by wear or material transfer is given by using this method. Basically, the method can be described as finding the best correlation and subsequently subtracting two 3D surface measurements before and after the experiment at the same spot. The 3D surface measurements are made by using a non-contacting interference microscope. The method proved to give good results but its capability is limited by hardware, in this case the capability of the optical interference microscope. In most of the practical situations it is not possible to get a detailed image of a complete section across a wear track in one measurement. Since the detailed information across the wear track is very important, the hardware limits must be overcome by software.

Sloetjes *et al.* [C3, C4] proposed a new technique, by matching and stitching a number of small but detailed images together from sequence measurements. The detailed method can be seen further in the next section.

C.2 Matching and stitching

C.2.1 Basic concept

The matching process of two images can be defined as aligning or repositioning the overlapping part of two successive images. One of the approaches which can be followed to obtain the 'best fit' between the matching images is by identifying certain distinctive features such as sharp edges or corners, contours, et cetera. However, such an approach is generally difficult to apply in roughness surface images, due to its stochastic properties. De Rooij and Schipper [C2] used the template method and obtained very good results for matching the roughness images. This method extracts a certain neighborhood (template) from one image and determines the position which gives the best fit to the other image. Instead of using several small templates [C2], the complete region of overlap is used by [C3, C4].

In order to get a detailed image of a complete section across a wear track, the stitching process has to be performed. Several measurements are taken in the stitching process and each one has a certain overlap area with the previous one. For every stitching of the subsequent two images, the mutual translation and rotation has to be determined based on the overlapping area. This process is referred to as matching. Once all images are matched, one large image is created to complete the stitching process (Fig. C.1).

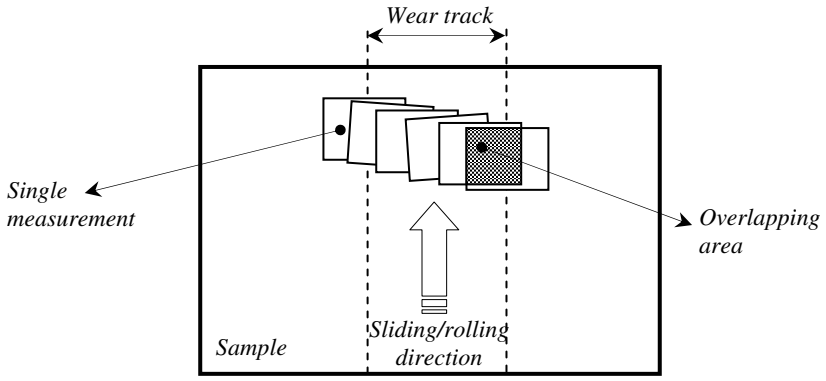

FIGURE C.1: *Matching and stitching process.*

C.2.2 Preprocessing

Data obtained by optical interferometer generally suffers some errors such as noise, outliers and bad/missing points. Before performing the matching and stitching process, the errors should be reduced as much as possible. Reduction of noise can be realized by simply applying a low pass filter. The height data for missing points are determined by using an interpolation procedure which uses measured neighboring points. A detailed description of the preprocessing step can be found in [C3].

C.2.3 Correlation

It is very difficult to maintain exactly at the same position of subsequence measurements. Therefore the correlation between the images is needed. In a 3D coordinate system, the mutual fit consists of three translations and three rotations (Fig. C.2) which yields a 6 degrees of freedom (DoF) correlation function.

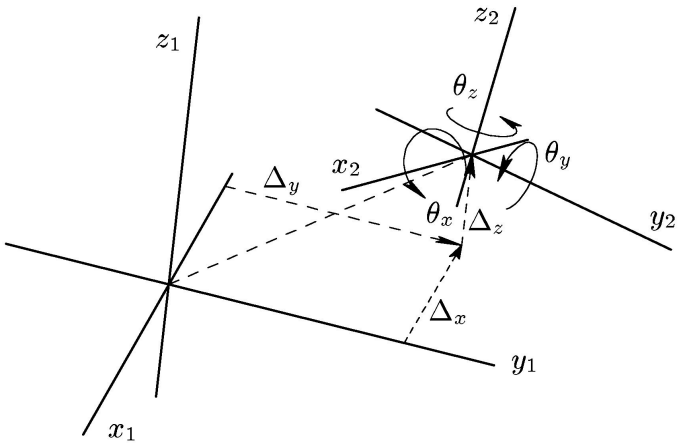

FIGURE C.2: *Coordinate systems and DoF's* [C3].

In general, a correlation function can be written as:

$$cor_i\left(\Delta_x, \Delta_y, \Delta_z, \theta_x, \theta_y, \theta_z\right) = \frac{1}{N} \sum F_i(d) \tag{C.1}$$

where the subscript i is the correlation function type, N is the number of data points and

$$d = z_2{}^t\left(x_2{}^t, y_2{}^t\right) - z_1(x_1, y_1) \tag{C.2}$$

The superscript t indicates a transformation of the second image for the specific values of the DoF's into the first image coordinate system. The difference or distance d is the

subtraction between the first and the subsequent image. There are many types of correlation functions (detailed information can be found in [C4]).

The least square correlation function minimizing the sum of the square of the distance:

$$F_{lsq}(d) = d^2 \tag{C.3}$$

while the weighted distances correlation function summing the weighted distance of the two overlapping images:

$$F_{wgt}(d) = \exp\left[-\frac{1}{2}\left(\frac{d}{R_{q,diff}}\right)^2\right] \tag{C.4}$$

where $R_{q,diff}$ is the R_q (r.m.s.) of the difference image. It was shown in [C3] and [C4] that the weighted distances correlation function gives better results compared to the least square correlation function.

C.2.4 Solvers and the matching procedure

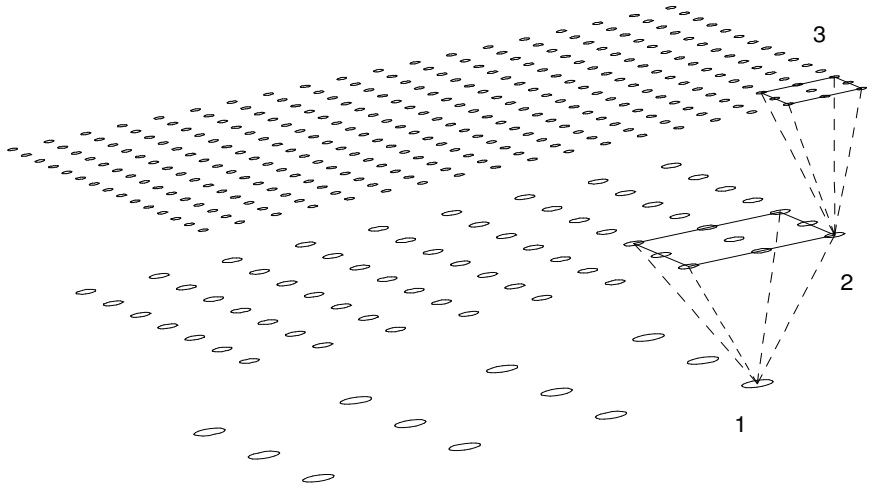

FIGURE C.3: *Coarse grids* [C4].

There are many types of solvers [C4] to find the global extreme of the cost or correlation function. The robust solver [C3] for instance, works with a search window, i.e. for every DoF only for the so-called master DoF's an interval is defined, centered around the main initial guess. Initial guess on the shifted in *x* and *y*-direction and rotated in *xy*-plane images

at first is done by just looking at the roughness itself. The initial guess of the remaining DoF's and its intervals are determined by the software. A coarse grid (Fig. C.3) was used in the robust solver to limit the search window and accordingly speed up the calculation process. While for the other solver, downhill simplex for example, this coarse grid allows larger search intervals and avoids getting stuck in local extremes on the finer grids. The optimal fit on the coarse grid is a proper estimation of the best fit on the next finer grid and the search interval can be reduced to the finer grid. This because the difference between the high resolution (fine grid) image and the low resolution (coarse grid) image is high frequency related and therefore information is localized.

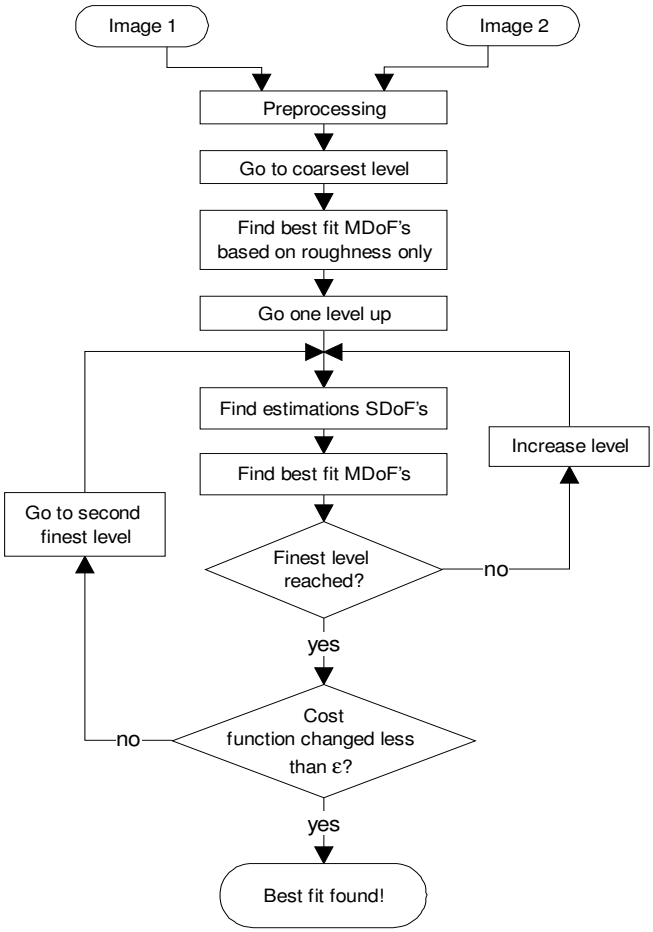

FIGURE C.4: *Flow chart of the matching process* [C3].

The matching procedure of the matching of two surfaces is shown in Fig. C.4. After preprocessing, the search for a first approximation of the master DoF's is started on the

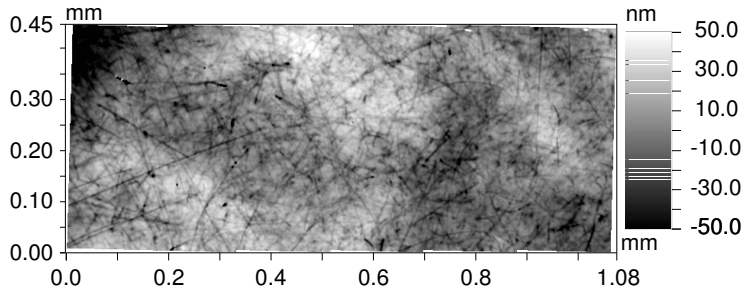

(a)

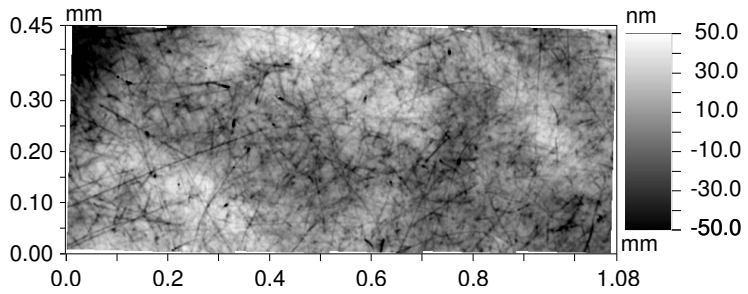

(b)

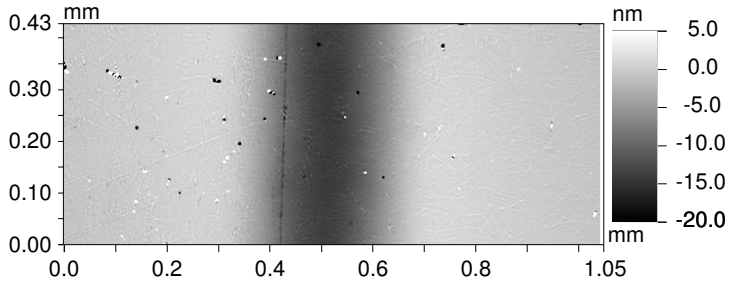

(c)

FIGURE C.5: *Matching and stitching of 6 images and its difference (c) before (a) and after (b) experiment* [C3].

coarsest level. The macro-geometry is removed only in this level. Next, the level is increased by one and followed by entering the level loop. This loop is repeated until the fit on the finest level is achieved. The difference stop criterion, ε, to the cost function must be applied after the last loop, in order to get convergence. The complete cycle from the second coarsest level up to the value of the cost function on the finest level must be repeated at least once to be able to calculate the stop criterion. If this is not satisfying, the cycle begins again at the second finest level. There is no need to start at a coarser level, since the changes of the DoF's take place mostly on the scale of the finest level. Therefore the loop is started at the second finest level for 'safety' reasons.

C.3 Application example

The matching and stitching has been applied to determine the change of a steel surface topography on a ball-on-disc sliding experiment [C3]. By the naked eye, it is very difficult to distinguish the image between before and after an experiment (Fig. C.5a and C.5b). From the difference image (Fig. C.5c) it is clear that deformation/wear occurred. A 15 nm deep groove is already visible. This concludes the robustness of the method for determining the changes in micro-geometry of surfaces.

References

[C1] De Rooij, M.B., 1998, A wear measuement method based on the comparison of local surface heights, PhD thesis, University of Twente, Enschede, The Netherlands.

[C2] De Rooij, M.B. and Schipper, D.J., 1998, "A wear measurement method based on the comparison of local surface heights," *Wear* **217**, pp. 182 – 189.

[C3] Sloetjes, J.W., Schipper, D.J., Lugt, P.M. and Tripp, J.H., 2000, "The determination of changes in surface topography using image processing techniques," in *Proceeding of the International Tribology Conference*, Nagasaki, Japan.

[C4] Sloetjes, J.W., Tasan, Y.C., De Rooij, M.B. and Schipper, D.J., 2002, "Algorithm for determining changes in micro-geometry using image processing techniques," in *Proceeding of the 2nd Asia International Conference on Tribology, Asiatrib '02*, Cheju Island, Korea.

Appendix D

Photographic impression of the experimental equipment

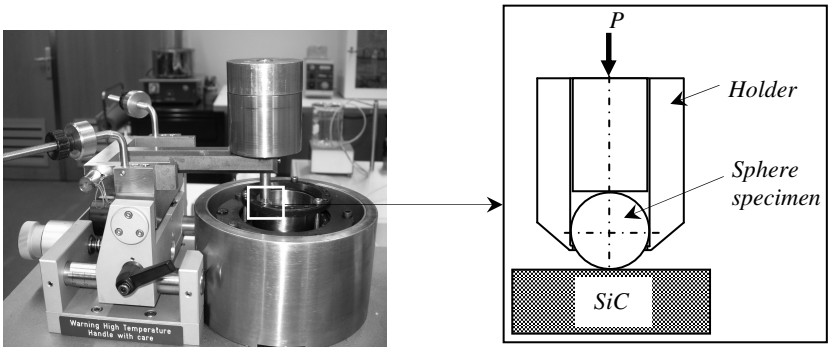

FIGURE D.1: *Pin-on-disk machine.*

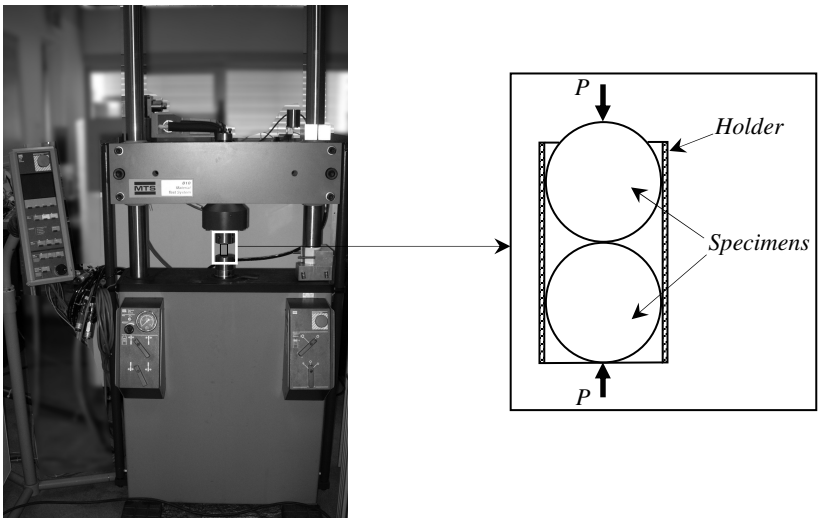

FIGURE D.2: *Tensile testing machine.*

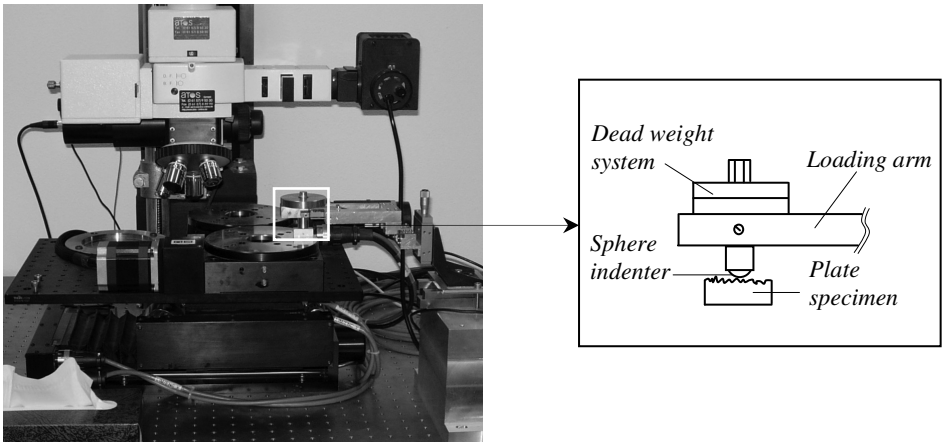

FIGURE D.3: S*tatic indentation (x-y table) setup.*

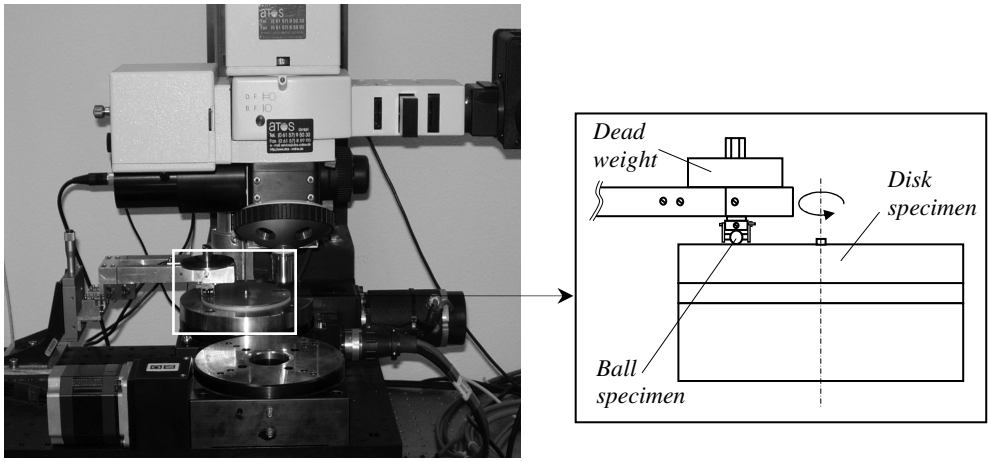

FIGURE D.4: *Rolling contact running-in setup.*

Appendix E

Thickness effect on the pressure required in surface bulk compression

The condition for compression of a bulk specimen by hard dies is illustrated in Fig. E.1a. In this case, a circular blank specimen is assumed to be reduced in thickness after compression. It is also assumed that the volume is conserved so that the radius of the blank increases and the thickness decreases as the load increases, see Fig. E.1b. In general, the pressure required for the compression depends upon: (a) the inherent flow stress of the material; (b) the strain pattern as determined by the configuration of the part; and (c) the effects of friction [E1].

In analyzing the effect of friction, three mechanisms are recognized as follows. Firstly, relative sliding (slip) occurs between the blank specimen and the die surface at all points, except in the center of the specimen. Secondly, relative motion does not happen and the spreading action results from shear strain in the blank surface parallel to the die surface (stick). Thirdly, the intermediate condition between the stick and slip condition. In the following analysis, the first mechanism is assumed.

The differential equation for stress distribution based upon the stress state in Fig. E.1c can be expressed as:

$$\frac{\partial \sigma_r}{\partial r} + \frac{\sigma_r - \sigma_c}{r} = -\frac{2f}{t} \tag{E.1}$$

where σ_r is the principal stress in radial direction, σ_c is the tangential stress, r is the variable radius, f is the unit friction force and t is the thickness of the specimen. By using the shear-strain energy of von Mises as a criterion for yielding, the yield stress, Y, can be related to the applied stresses as:

$$(\sigma_n - \sigma_r)^2 + (\sigma_r - \sigma_c)^2 + (\sigma_c - \sigma_n)^2 = 2Y^2 \tag{E.2}$$

where σ_n is the principal stress in normal or thickness wise direction. In this simple compression situation the general stress state is that of uniaxial compression combined with a hydrostatic pressure σ_h, thus:

$$\sigma_n = Y + \sigma_h \text{ and } \sigma_r = \sigma_c = \sigma_h \tag{E.3}$$

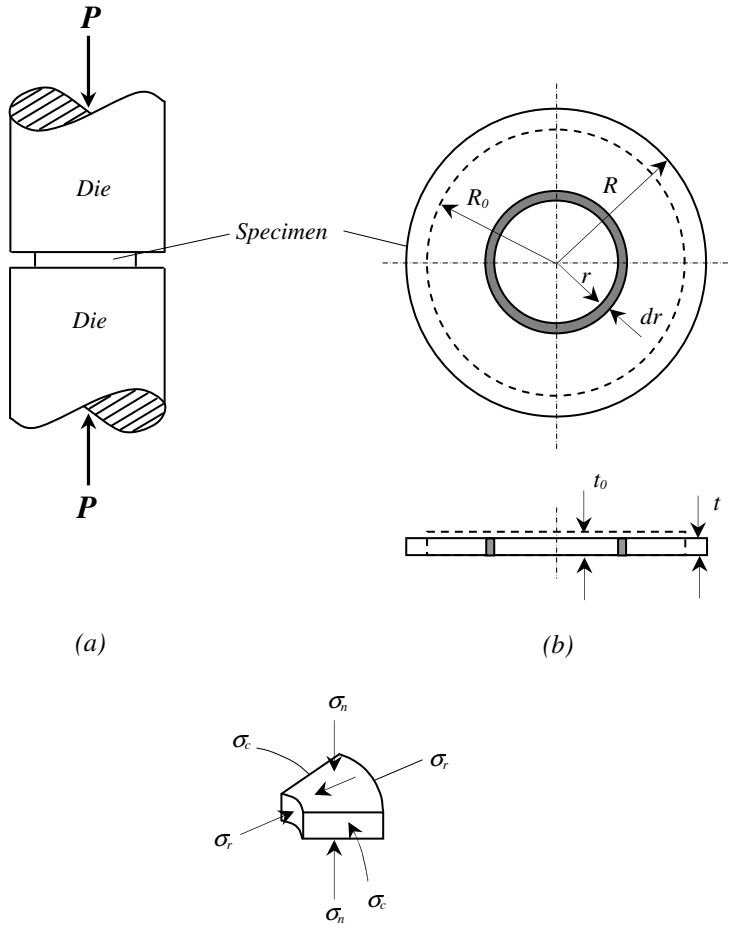

FIGURE E.1: *Compression of a blank specimen: (a) compression configuration, (b) geometry of the blank and (c) the stress state on an element, after* [E1].

By the principal of transmissibility of forces it may be recognized that:

$$\sigma_n = p \tag{E.4}$$

where p is the normal pressure applied by the die to the element. The friction force can be related to the normal pressure as:

$$f = \mu p \tag{E.5}$$

where μ is the coefficient of friction. Combining Eqs. (E.1) to (E.5) yields:

$$\frac{dp}{p} = -\frac{2\mu}{t} dr \tag{E.6}$$

Integrating Eq. (E.6) yields the expression for the pressure with the boundary conditions $p = p$ at $r = r$ and $p = Y$ at $r = R$ as:

$$\frac{p}{Y} = e^{2\mu(R-r)/t} \tag{E.7}$$

where R is the blank specimen radius after compression. According to Eq. (E.7) the maximum pressure p_{max} occurs at $r = 0$ as:

$$p_{\max} = Ye^{2\mu R/t} \tag{E.8}$$

The average required or die pressure may be obtained by the basic expression below:

$$p_a \int_a^b 2\pi r dr = \int_a^b 2\pi r p dr \tag{E.9}$$

where a and b are any conditions for lower and upper limits of a variable radius r. In this analysis $a = 0$ and $b = R$ so that by substituting these values and Eq. (E.7) into Eq. (E.9) and integrating between the given limits yields:

$$\frac{p_a}{Y} = \frac{2}{C^2}\left(e^C - C - 1\right) \tag{E.10}$$

where

$$C = \frac{2\mu R}{t} \tag{E.11}$$

Reference

[E1] Schroeder, W. and Webster, D.A., 1949, "Press-forging thin sections: effect of friction, area, and thickness on pressure required," *ASME-Journal of Applied Mechanics* **16**, pp. 289 – 294.

Appendix F

Asperities determination of real rough surfaces

A method to model the micro-contacts of real rough surfaces by elliptical paraboloids will be described in this appendix. The model is based on a volume conservation method.

An elliptical paraboloid is defined as a paraboloid having an elliptical cross-section in the *xy*-plane and paraboloids in the *xz*- and the *yz*-plane respectively. In a mathematical form, this elliptical paraboloid is expressed by [F1]:

$$\frac{x^2}{a^2}+\frac{y^2}{b^2}-\frac{z}{c}=0 \tag{F.1}$$

where x, y, and z are the coordinate system and a, b, c are constants. The volume displaced, V, due to contact of this elliptical paraboloid is the same as the volume above a certain cut-off height (volume conservation), hence:

$$V=\int_{x_{low}}^{x_{high}}\int_{y_{low}}^{y_{high}}\int_{z_{low}}^{z_{high}} dxdydz \tag{F.2}$$

The limits of integral in Eq. (F.2) are determined as follows. For the z-coordinate, the upper integration limit is the cut-off height ω of the micro-contact as:

$$z_{low}=\omega \tag{F.3}$$

and the lower limit is determined rearranging Eq. (F.1) into:

$$z_{high}=\frac{c}{a^2b^2}\left(x^2b^2+y^2a^2\right) \tag{F.4}$$

For the *y*- coordinate, the following equations are valid at the edge of the contact:

$$\frac{c}{a^2b^2}\left(x^2b^2 + y^2a^2\right) = \omega \tag{F.5}$$

and by solving *y* in Eq. (F.5) gives:

$$y_{low} = -\frac{b}{ac}\sqrt{c\left(a^2\omega - cx^2\right)} \tag{F.6}$$

$$y_{high} = \frac{b}{ac}\sqrt{c\left(a^2\omega - cx^2\right)} \tag{F.7}$$

Now, the integration limits for *x* are left to consider. These can be determined by substituting $y_{low} = y_{high} = 0$ into Eqs. (F.6) and (F.7) which results:

$$x_{low} = -a\sqrt{\frac{\omega}{c}} \tag{F.8}$$

$$x_{high} = a\sqrt{\frac{\omega}{c}} \tag{F.9}$$

By substituting Eqs. (F.3) – (F.9) into Eq. (F.2) prior to integration and simplifying yields:

$$V = \frac{\pi}{2}\frac{ba}{c}\omega^2 \tag{F.10}$$

The length of the micro-contact area in *x*-direction L_x is calculated by subtracting Eq. (F.9) by Eq. (F.8) as:

$$L_x = 2a\sqrt{\frac{\omega}{c}} \tag{F.11}$$

and the length of the micro-contact area in *y*-direction L_y is calculated by subtracting Eq. (F.7) by Eq. (F.6) at $x = 0$ as:

$$L_y = 2\frac{b}{ac}\sqrt{ca^2\omega} \tag{F.12}$$

Substituting Eqs. (F.11) and (F.12) into Eq. (F.10) results into a new expression for the volume as:

$$V = \frac{1}{8}\pi L_x L_y \omega \tag{F.13}$$

Curvature is defined as the second derivative of the elliptical paraboloid, thus the curvature κ_x in x-direction and the curvature κ_y in y-direction are found by applying the second derivative to Eq. (F.1) as:

$$\kappa_x = \frac{2}{a^2} c \tag{F.14}$$

$$\kappa_y = \frac{2}{b^2} c \tag{F.15}$$

A combination is made by rearranging Eqs. (F.10) – (F.15):

$$\sqrt{\kappa_x \kappa_y} = 2\frac{c}{ab} = \frac{8\omega}{L_x L_y} = 4\pi \frac{V}{A^2} \tag{F.16}$$

$$\frac{\kappa_x}{\kappa_y} = \frac{L_y^2}{L_x^2} \tag{F.17}$$

Substituting Eq. (F.17) into Eq. (F.16) and rearranging gives the final expressions for the elliptic paraboloid that will be used for 'fitting' the real micro-contact region as:

$$\kappa_x = 4\pi \frac{V}{A^2} \frac{L_y}{L_x} \tag{F.18}$$

$$\kappa_y = \kappa_x \frac{L_x^2}{L_y^2} \tag{F.19}$$

The volume V and the contact area A in Eq. (F.18) are determined from the micro-geometry measurement, therefore, the fitting elliptic paraboloid has the same volume and contact area as the as measured micro-contact region.

Reference

[F1] de Rooij, M.B., 2005, Handout Solids and Surfaces, University of Twente, Enschede, The Netherlands.

Summary

Running-in is a phenomenon which occurs shortly after the start of the contact between fresh solid surfaces. Before the contacting solid surfaces reach a steady-state operation situation there is a running-in period for enhancing the surface contact performance. Changes in the surface topography, friction, temperature and wear rate are commonly observed. The properties of two mating surfaces are continuously and monotonously changing during this initial stage of operation. These changes are advantageous when the running-in process succeeds, i.e. the degree of the conformity increases so that the load-carrying capability and its reliability and life improves. Running-in is a fundamental behavior of newly manufactured surfaces and is beneficial. Ignoring the running-in aspects means overlooking the important clues to the evolution of conjoint processes which leads to the final long-term steady-state friction and wear behavior. Running-in is a very complex and vast problem area. The running-in period depends upon many factors, chemically or mechanically, such as surface topography, macro-geometry, material and the operating conditions. However, for a given contact situation with the same operating conditions, the running-in performance is mostly determined by the initial surface topography. Plastic deformation in normal direction (perpendicular to the surface), and mild wear, are the two dominant mechanisms. For pure rolling contact situations the mild wear contribution is omitted.

This thesis deals with running-in of the pure rolling contact situation operating in the boundary lubrication regime, so that normal plastic deformation due to the contact between asperities is the main aspect. The change of the surface topography during the running-in process and the run-in surfaces are predicted locally. The main theme concerns the elastic-plastic asperity contact model.

An asperity micro-contact model was considered due to its analytical nature and a well-ploughed study. A new single elliptic elastic-plastic asperity contact model has been proposed and demonstrated as the best prediction to the experimental results among the other models. Plastic deformation appears when the applied load is removed; therefore, the developed asperity contact model was extended to the unloading case.

Most engineering surfaces are rough on micro-scale. This roughness is developed from the population of asperities with different heights and curvatures. It turns out that ideas from the single asperity contact may be adapted to the multiple asperity contact. Surface asperities do not perfectly follow certain shape geometry like spherical or

paraboloidal, but protrude randomly in the three-dimensional space instead. Hence, a new method, the volume conservation method, was adapted to determine the asperity geometry and height. Once all the asperity contact parameters are determined, a deterministic elliptic elastic-plastic contact of rough surfaces is applied. In the contact of rough surfaces, another phenomenon is revealed, namely bulk (macro-geometry) deformation, whereas the running-in concerns with micro-geometry or roughness only. To overcome this problem, a new criterion has been developed to maintain the running-in of the contacting surfaces so that it operates in the regime in which bulk deformation does not occur.

Rolling contact of rough surfaces was modeled by loading-unloading-translating the contacting surfaces. The run-in surfaces are indicated by the elastic deformation of all the asperities in contact during subsequent loading-unloading. The proposed theoretical prediction agrees well with the experimental results.

Samenvatting

Inlopen is een verschijnsel dat optreedt vlak nadat twee oppervlakken voor de eerste keer met elkaar in contact komen. De totale inloopperiode, dat wil zeggen vanaf het eerste contact totdat er een stationaire situatie is bereikt, heeft meestal tot doel de contactsituatie te verbeteren. Tijdens het inlopen worden vaak veranderingen in oppervlakte geometrie, wrijving, temperatuur and slijtage waargenomen. Deze veranderingen vinden continu plaats en vaak op een monotone wijze. Wanneer het inloopproces succesvol wordt doorlopen, leiden deze veranderingen tot een verbeterde conformiteit van de oppervlakken. Hierdoor worden de belastbaarheid, betrouwbaarheid en levensduur van het contact verhoogd.

Inlopen is een fundamenteel aspect van nieuwe (in de zin van ongebruikte) oppervlakken en heeft een positief effect op het functioneren van de oppervlakken. Het verwaarlozen van dit proces heeft tot gevolg dat belangrijke aspecten die het verloop bepalen van de gezamelijke processen die leiden tot het uiteindelijke wrijvings- en slijtagegedrag, onopgemerkt blijven.

Inlopen is een zeer complex proces en een enorm probleemgebied. De totale inloopperiode hangt af van factoren van zowel mechanische als chemische aard, zoals oppervlakte geometrie, macro geometrie, het materiaal en de operationele condities. Voor een gegeven contact situatie en operationele condities is de oppervlakte geometrie de bepalende factor. Plastische deformatie loodrecht op het oppervlak en milde slijtage zijn de twee dominante processen die verantwoordelijk zijn voor de verandering in oppervlakte geometrie. In geval van puur rollen kan de milde slijtage achterwege worden gelaten.

Dit proefschrift behandelt inlopen van contacten verandering in micro-geometrie, onder condities van puur rollen. Dit heeft tot gevolg dat plastische deformatie loodrecht op het oppervlak het belangrijkste onderwerp is. De verandering in oppervlakte geometrie wordt op lokaal niveau voorspeld. Een elatisch-plastich contact model is hierbij onontbeerlijk.

Er is gekozen voor een contact model op ruwheidsniveau vanwege het anlytische karakter. Op basis hiervan is een elastisch-plastisch contact model ontwikkeld dat geschikt is om de vervorming van een enkel elliptisch gevormde ruwheidstop te beschrijven. In het algemeen blijft een top na belasten plastisch gedeformeerd. Om ook dit goed te kunnen beschrijven, is het model uitgebreid met de ontlastfase.

Het merendeel van de oppervlakken is ruw op microschaal. Deze ruwheid kan worden beschreven door middel van een verzameling ruwheidstoppen, met ieder een eigen

hoogte en kromming. Het blijkt dat het model dat ontwikkeld is voor een enkele top, ook kan worden gebruikt om de vervorming van een verzameling van toppen te beschrijven. Op deze manier is simulatie van de vervorming van een compleet ruw oppervlak binnen handbereik.

Helaas hebben ruwheidstoppen niet altijd een perfect parabolische vorm, vaak zijn het min of meer willekeurige uitstulpsels. Naar aanleiding hiervan is een model ontwikkeld op basis van behoud van volume. Dit model kan globaal worden omschreven voor het bepalen van een equivalente parabolische vorm van de top met willekeurige vorm. Daarbij zijn de volumes van beide vormen gelijk. Wanneer alle willekeurig gevormde toppen die het oppervlak vormen op deze manier beschreven zijn, wordt het deterministische contact model op ieder individueel equivalent parabolische topje toegepast.

Wanneer twee oppervlakken met elkaar in contact komen kan naast de deformatie van de ruwheid ook bulk deformatie optreden. Het huidige model kan dit type deformatie niet simuleren. Om af te schatten onder welke condities ruwheids deformatie optreedt, is een criterium afgeleid dat aangeeft wanneer ruwheids deformatie een significante rol gaat spelen. Daarmee is ook het geldigheidsgebied van het huidige model vastgelegd.

Rollend contact van twee oppervlakken is gemodelleerd aan de hand van belasten-ontlasten-transleren van oppervlakken. Ingelopen oppervlakken worden gekenmerkt door uitsluitend elastische deformatie tijden een belasten-ontlasten cyclus. De theorie komt vrij goed overeen met experimentele resultaten.

Acknowledgements

The process of making of this thesis has not been completely easy and smooth. Many people have contributed to this thesis, in different ways, by their physical or intellectual support. I would like to thank them who supplied a significant contribution in the evolution of this study.

I am enormously grateful to Dik Schipper, my promoter, my mentor, a friend and sometimes 'a father'. I would like to thank him for sharing his ideas and knowledge, his encouragement and his generosity. He supported me throughout the whole process of my study, ranging from the correction of typing errors, valuable comments/suggestions and numerous other things which always helped me to more in the right direction. I might not have survived my study and would not have produced these scientific results without his help and support. I also definitely owe my gratitude to Matthijn de Rooij for his valuable discussions and advice.

Next, I would like to thank the graduation committee members: D.J. Schipper, R. Akkerman, P.P.L. Regtien, P. Vergne, M.C. Elwenspoek and A. van Beek for reading the final thesis draft and subsequently giving me their valuable advice and suggestions to improve the quality of my thesis.

I am indebted to Wijtze ten Napel for introducing me to the Tribology Group, University of Twente which leads to the opportunity to carry out the research project during my study.

In the first two years of my study I was involved in the 'bi-weekly' meeting held at SKF-ERC B.V. and UT. For this I would like to thank John Tripp and Piet Lugt for their useful discussions, comments and advice.

I am grateful to Jan Willem Sloetjes for his patience and guidance in introducing me to the Matching and Stitching tool and the experimental procedures. He also translated the summary of this thesis into Dutch. Erik 'the real engineer' de Vries is also gratefully acknowledged for helping me in developing all the experimental setup.

I also thank Willie Kerver for making parts and preparing the samples for my experiment, Walter Lette for solving all kinds of computer problems and Belinda Bruinink for carrying out administrative work.

During my research study I considered myself very fortunate to work in a very pleasant environment created by my fellow (ex-) staff members of the Tribology Group (now Laboratory for Surface Technology and Tribology): Wijtze ten Napel, Dik Schipper,

Kees Venner, Matthijn de Rooij, Erik de Vries, Walter Lette, Belinda Bruinink, Willie Kerver, the (former) PhD students: Ako, Bert, Bernd, Caner, Ellen, George, Gerrit, Isaias, Irinel Faraon, Jan Willem, Loredana, Marc, Mark, Radu, Rihard and Quiang, and the (former) MSc students: Bart, Bas, Evert, Freddy, Justin, Karen, Koen and Tom. I would like to thank them for providing a nice working atmosphere.

There was a transient period to 'run-in' into my joyful stay in Enschede. In this sense I would like to thank Bu Nung, Bang Anto, Reza, Rihard and many others. Those who are not mentioned, surely will not be forgotten. Many thanks also go to The Alfian family: Pak Dedy, Bu Ella and Defan (Abang Dipang). They provided me, not only the 'energy' but also a fresh insight and a lot of fun, especially during the last period of my study. Many help from Cak Irwan, Mbak Ina and Venda is also fully acknowledged. Not to forget, I also want to thank Anggoro and Adit for helping me to design a nice cover of this thesis. Pak Kyai Hadi Susanto, in the University of Massachusetts, thanks for the mathematical discussion and everything we have had.

I have been lucky to have built up a very colorful life in a foreign country and I very much appreciate the friendship I share with all members of IMEA, ISUT and PPIE. They have been my mates in pray, sports, chat, and *minta makan*.

I wish to pronounce my sincere and very grateful thanks to my *guru* Pak Darmawan Harsokoesoemo and all members of EDC (Engineering Design Centre) Laboratory, ITB (Institute of Technology Bandung): Pak Bagus, Pak Satryo, Pak Wayan, Pak Wirat and Bu Esih for their help and support.

And last, but certainly not least, I would like to thank Tuan Putri Martha Ardiaria for her patience, her support, her great understanding and her unfailing love. She encourages me continuously even though she does not know what I do or why I do what I do.

Publications

Jamari, J. and Schipper, D.J., 2006, "Experimental Investigation of Fully Plastic Contact of a Sphere Against a Hard Flat," *ASME Journal of Tribology*, accepted, printed April.

Jamari, J. and Schipper, D.J., 2006, "An Elastic-Plastic Contact Model of Ellipsoid Bodies," *Tribology Letters*, accepted.

Jamari, J. and Schipper, D.J., 2006, "Deformation Due to Contact Between a Rough Surface and a Smooth Ball," *Wear*, submitted.

Jamari, J. and Schipper, D.J., 2006, "Plastic Deformation and Contact Area of an Elastic-Plastic Contact of Ellipsoid Bodies after Unloading," *Tribology International*, submitted.

Jamari, J. and Schipper, D.J., 2006, "The Effect of Component Thickness on the Flattening of Surface Asperities," *Tribology International*, submitted.

Jamari, J., de Rooij, M.B. and Schipper, D.J., 2006, "Plastic Deterministic Contact of Rough Surfaces," *ASME Journal of Tribology*, submitted.

Jamari, J. and Schipper, D.J., 2006, "Deterministic Repeated Contact of Rough Surfaces," *Tribology Letters*, submitted.

Jamari, J. and Schipper, D.J., 2006, "Point and Line Contacts Deformation of Rough Surfaces," *Tribology Letters*, submitted.

Jamari, J. and Schipper, D.J., 2006, "Plastic Deterministic Model of Rolling Contacts: Analysis of Single Contacts," *ASME Journal of Applied Mechanics*, submitted.

Jamari, J. and Schipper, D.J., 2006, "Criterion for Surface Deformation," *TriboTest*, submitted.

Jamari, J. and Schipper, D.J., 2006, "Plastic Deterministic Model of Rolling Contacts: Analysis of Running-in Contacts," *ASME Journal of Applied Mechanics*, to be submitted.